Subsynoptic extratropical weather systems: observation, analysis, modeling and prediction: notes from a colloquium, summer 1974

QC
883.4
C64
1974
v.1

PB-247 285

SUBSYNOPTIC EXTRATROPICAL WEATHER SYSTEMS: OBSERVATION, ANALYSIS, MODELING, AND PREDICTION. NOTES FROM A COLLOQUIUM: SUMMER 1974. VOLUME I. PRINCIPAL LECTURES

Melvyn Shapiro

National Center for Atmospheric Research

Prepared for:

National Science Foundation

1974

DISTRIBUTED BY:

NTIS

National Technical Information Service
U. S. DEPARTMENT OF COMMERCE

NCAR/ASP-CQ-3
Vol.I

PB 247 285

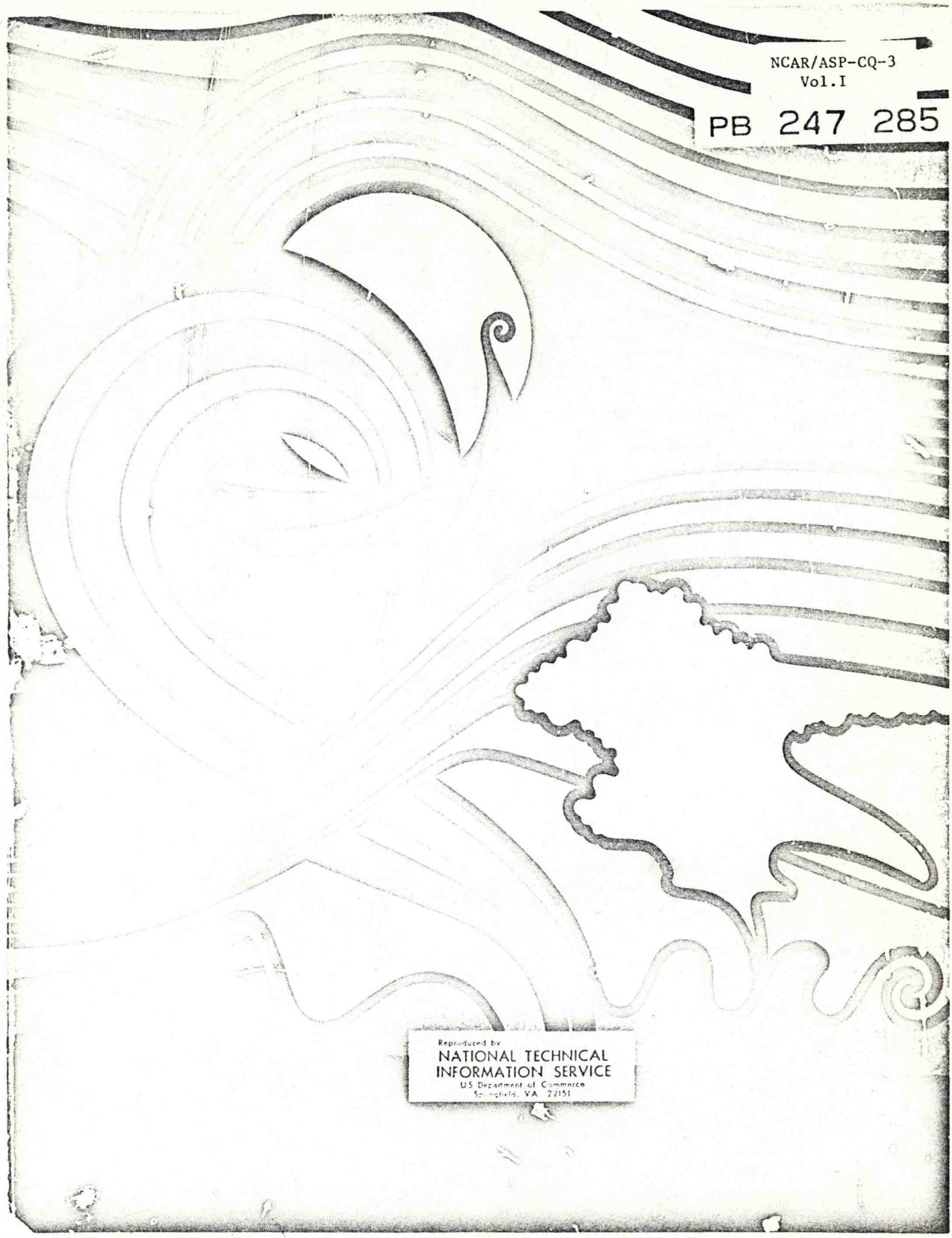

Reproduced by
NATIONAL TECHNICAL
INFORMATION SERVICE
US Department of Commerce
Springfield, VA 22151

Colloquium on Subsynoptic Extratropical Weather Systems, Boulder, Colo., 1974.

QC 883.4 C64 1974 V.1

BIBLIOGRAPHIC DATA SHEET	1. Report No. NCAR/ASP-CQ-3-V.1	2.	3. Recipient's Accession No. PB247285
4. Title and Subtitle: Subsynoptic Extratropical Weather Systems: Observation, Analysis, Modeling, and Prediction. Notes from a Colloquium: Summer 1974 (2 vols)			5. Report Date: Summer 1974 (prep)
			6.
7. Author(s): Coordinator: Melvyn Shapiro			8. Performing Organization Rept. No.
9. Performing Organization Name and Address: National Center for Atmospheric Research, P.O. Box 3000, Boulder, Colo. 80303			10. Project/Task/Work Unit No.
			11. Contract/Grant No.
12. Sponsoring Organization Name and Address: National Science Foundation, 1800 G. Street, Washington, D.C. 20550			13. Type of Report & Period Covered
			14.

15. Supplementary Notes

16. Abstracts: The colloquium on Subsynoptic Extratropical Weather Systems was jointly conducted by the Advanced Study Program and the Small-Scale Analysis and Prediction Project of NCAR. The colloquium notes are divided into four sections: 1) A series of lectures by Noel LaSeur on the structure and dynamical aspects of atmospheric frontal zones, jet streams, squall lines, convective clouds, and tornadoes. A brief discussion of numerical modeling of atmospheric fronts and cumulus convection is included. (2) A series of lectures by Arnt Eliassen on the theoretical aspects, both analytical and numerical, of fronts and jet streams, mountain waves, small amplitude gravity wave oscillations, and Ekman layer theory. (3) Special one-week workshop on current work in developing and improving upon limited-area, short-range numerical weather prediction models. Presentations by the British Meteorological Office, Swedish Meteorological and Hydrological Institute, Japan Meteorological Agency, Drexel University, NWS and NMC of NOAA, and NCAR are included. (4) Twenty-six supplemental afternoon seminars on topics relating to the colloquium, in the areas of symoptics, dynamics, numerical techniques, observing systems, objective analysis, and social impact assessment were also presented.

17. Key Words and Document Analysis. 17a. Descriptors

fronts (meteorology)
jet streams (meteorology)
tornadoes
atmospheric models
weather forecasting
squalls

17b. Identifiers/Open-Ended Terms

dynamic meteorology
numerical weather prediction
convective clouds

17c. COSATI Field Group 0402

PRICES SUBJECT TO CHANGE

18. Availability Statement "Unlimited"	19. Security Class (This Report) UNCLASSIFIED	21. No. of Pages 235
	20. Security Class (This Page) UNCLASSIFIED	22. Price 8.00-2.25

FORM NTIS-35 (REV. 10-73) ENDORSED BY ANSI AND UNESCO. THIS FORM MAY BE REPRODUCED USCOMM-DC 8265-P74

QC
883.4
.C64
1974
v.1

343158

SUBSYNOPTIC EXTRATROPICAL WEATHER SYSTEMS: OBSERVATION, ANALYSIS, MODELING, AND PREDICTION

NOTES FROM A COLLOQUIUM: SUMMER 1974

ATMOSPHERIC SCIENCES
LIBRARY
MAR 1978
N.O.A.A.
U. S. Dept. of Commerce

VOLUME I

PRINCIPAL LECTURES

Conducted Jointly by:
The Advanced Study Program and Small-Scale Analysis and Prediction Project
National Center for Atmospheric Research *
Boulder, Colorado

Coordinator: Dr. Melvyn Shapiro
Principal Lecturers: Professor Arnt Eliassen
Professor Noel LaSeur

The National Center for Atmospheric Research is operated by the University Corporation for Atmospheric Research under sponsorship of the National Science Foundation.

Preceding page blank

78 0730

These Colloquium Notes are dedicated to the memory of my former classmate and colleague, Ben Ceselski. His last publication, which was scheduled for presentation during the Colloquium, is reproduced on pages 797-821. We miss you, Ben.

COVER LEGEND

The concept for the cover design for these lecture notes came as an apparition while working on a case study of upper-level frontogenesis over Northern Europe during my visit with Arnt Eliassen in Oslo this fall. It was subsequently executed in collaboration with Howard Crosslen of the NCAR Graphics Group with additions to encompass further aspects of the colloquium subject matter. The design shows isentropes turning into isotachs as they encircle the sun to emerge from an egg as an isobaric surface depiction of isentropes within an upper level frontal zone which narrows, extending upward to turn anticyclonically and vanish. The upper front is in the form of a Viking ship with its oars formed by the isentropes as they exit the entrance region of the front. The sun and the egg are a dual symbol of creation and the Viking ship the vehicle of the creators, for it was the Scandinavians who conceived what we now call modern meteorology and it was they who then left their native lands to propagate this knowledge throughout the world, in true Viking fashion. The sail of the ship enters into the wind distribution for a jet stream core which passes in back of the vertical section depiction of the isentropes within upper level frontal zone and then emerges as a low-level frontal zone that enters the earth. In the cold air behind the front one finds a mountain range and its related mountain wave. Ahead of the cold front are turbulent breaking waves in an atmospheric boundary layer and a severe convective storm which has penetrated the stratosphere and spawned a tornado from its base. The color scheme for the cover is representative of the vibrant visions of the Norwegian autumn time, with the darkness of the earth browns contrasted by the the transitions of aspen and birch. If you look closely you will see the trolls as they return to the Eliassen's summer cottage on the upper pasture to herald the coming of winter. Var so god.

Melvyn A. Shapiro
Colloquium Coordinator

PREFACE

May I introduce you to the lecture notes from the Colloquium on Subsynoptic Extratropical Weather Systems which was held during the summer of 1974 at the National Center for Atmospheric Research in Boulder, Colorado. This Colloquium was jointly sponsored by the NCAR Advanced Study Program and the Small Scale Analysis and Prediction Project. It was formally attended by predoctoral and postdoctoral students whose responsibility it was to prepare the notes contained herein in collaboration with the Colloquium lecturers. Although some editing of the notes has been done, they are not intended to be publications, and should not be quoted as such.

The subject of this year's Colloquium was selected because it represents one of the next frontiers at which observational and theoretical atmospheric scientists will expend considerable effort to obtain increased understanding and more accurate short-range prediction of small-scale weather systems. It was our intent to give the attending students sufficient background material and supplemental seminars by active researchers to provide them with a comprehensive account of the current state of the science on the Colloquium subject, thus enhancing their awareness of the problems that remain to be solved in this area.

For this purpose, two principal lecturers were invited to present lectures on selected aspects of the subject. The first lecture series was presented by Professor Noel LaSeur, Chairman of the Department of Meteorology at Florida State University. Because of my association with Noel as one of his students, I was aware of his ability to integrate and develop subject matter illustrating the structural and diagnostic aspects of mesoscale weather systems. Though Noel is known mostly for his contributions to tropical meteorology, these lectures attest to his expertise in frontal and extratropical convective-scale processes which previously had been shared only with his university students.

The second lecture series on selected theoretical aspects of the Colloquium subject was presented by Professor Arnt Eliassen, Chairman of the Department of Geophysics at the University of Oslo, Norway. We were most fortunate in that Arnt was able to come to Boulder to present

this lecture series. His experience at operational weather forecasting, pioneering work in numerical weather prediction, and classical work in frontal theory and boundary layer meteorology formed the basis for a most interesting lecture series and stimulating discussions and commentaries on other presentations.

The supplemental afternoon seminars were presented by invited representatives of the university community, federal government agencies, and the NCAR scientific and facilities support staff. Here we were exposed to subject matter spanning a wide variety of topics relating to the Colloquium theme. The areas of synoptics, dynamics, numerical techniques, observing systems, objective analysis, and social impact assessment were all represented.

The final aspect of the Colloquium centered upon a special one-week workshop during which representatives from four international operational numerical prediction groups, the university community, and NCAR presented their current work in developing and improving upon limited-area short-range numerical weather prediction models.

I would like to thank the principal lecturers, the supplemental seminar lecturers, the workshop participants, and Colloquium students for their contributions to what we shall all remember as an exciting summer of science and newfound friendships.

I hope through these notes we have shared with you that you too will sense the excitement of these days and the challenges of this aspect of atmospheric science.

Melvyn A. Shapiro
Colloquium Coordinator

ACKNOWLEDGEMENTS

This Colloquium represents the efforts of many NCAR people. Specifically, we wish to thank Christine Gerhardt for technical editing; Anthony Galván III for photographing the events and participants; Peter Gilman for administrative advice; Betty Wilson for administrative and editorial assistance; Lois Gries, Betsy Holdsworth, Gloria Parker, Judith Prangley, and Ursula Rosner for typing and assembling the contents of the notes; Ray Walling, Carl Edwards, Clarence Cook, Don Green and Bob Bryan for printing the notes; Howard Crosslen and William Hemphill for advice and art work on the cover design; Randi Opsahl for visual aids assistance; Rose Bridgewater for arranging the reception and banquet; and Leslie Doukas for taking messages for the participants and assisting with the meeting room in the Fleischmann Building.

COLLOQUIUM PARTICIPANTS

Coordinator

Melvyn A. Shapiro, NCAR

Principal Lecturers

Arnt Eliassen, University of Oslo
Noel LaSeur, Florida State University

Seminar Speakers

Richard Anthes, Pennsylvania State University
Stanley L. Barnes, National Severe Storms Laboratory
William R. Bergen, NCAR
Rainer Bleck, NCAR
Lance F. Bosart, State University of New York at Albany
Rodger Brown, National Severe Storms Laboratory
Edwin F. Danielsen, NCAR
James W. Deardorff, NCAR
James C. Fankhauser, NCAR
Jack L. Fishman, Saint Louis University
Gerald W. Grams, NCAR
Brian Hoskins, University of Reading, England
Donald R. Johnson, University of Wisconsin
Patrick J. Kennedy, NCAR
Joseph B. Klemp, NCAR
Douglas K. Lilly, NCAR
Joseph Oliger, Stanford University
Harold D. Orville, South Dakota School of Mines & Technology
James W. Purdom, NOAA/NESS
Melvyn A. Shapiro, NCAR
M. Steven Tracton, Naval Postgraduate School
Kenneth E. Wilk, National Severe Storms Laboratory

Workshop Speakers

David P. Baumhefner, NCAR

Rainer Bleck, NCAR

Svante Bodin, Swedish Meteorological & Hydrological Institute

Joseph P. Gerrity, Jr, National Meteorological Center, NOAA

David E. Jones, Meteorological Office, England

Michael L. Kaplan, Air Weather Service, USAF

Carl W. Kreitzberg, Drexel University

Yasushi Okamura, Japan Meteorological Agency

Douglas A. Paine, Cornell University

Donald J. Perkey, NCAR

Wilson A. Shaffer, NOAA/NWS

Melvyn A. Shapiro, NCAR

Arne Sundström, F.O.A. (Research Institute of Swedish National Defence)

David L. Williamson, NCAR

Participants

John J. Cahir, Pennsylvania State University

Len-Fu Walter Chang, University of Oklahoma

Thomas B. Curtin, University of Miami

Zon-hwa Grace Feng, State University of New York at Albany

Jack L. Fishman, Saint Louis University

Arnold L. Friend, Texas A&M University

Kee-Ying Fung, Cornell University

Louis T. Gidel, University of Illinois

Martin J. Leach, Drexel University

Richard L. Livingston, University of Missouri

C. Henry McComas, Johns Hopkins University

James F. Price, University of Miami

Ronald B. Smith, Johns Hopkins University

David W. Stuart, Florida State University

M. Steven Tracton, Naval Postgraduate School

Louis W. Uccellini, University of Wisconsin

Margaret C. Wheldon, Harvard University

SUBSYNOPTIC EXTRATROPICAL WEATHER SYSTEMS:
OBSERVATION, ANALYSIS, MODELING, AND PREDICTION

CONTENTS

Reproduced from best available copy.

Reproduced from
best available copy.

Reproduced from
best available copy.

LECTURES BY PROFESSOR NOEL LASEUR, FLORIDA STATE UNIVERSITY

SELECTED SUBSYNOPTIC FEATURES OF PARTICULAR INTEREST: AN INTRODUCTION

Lecturer: Dr. N. LaSeur Notes by: J. Cahir

Date: June 17, 1974

Subsynoptic and mesoscale structures have attracted increased attention from atmospheric dynamicists and numerical modelers in recent years, but synopticians have long been interested in them. Structures such as fronts, squall lines, wind shear lines, cloud bands and jet streams, all of which have at least one characteristic horizontal length scale that is subsynoptic, are of everyday concern to those involved in weather forecasting.

The presentations to follow will emphasize the structure and behavior of two classes of mesosystems: strong frontal (hyperbaroclinic) zones, and intense organized convective systems. Although a great deal of information about these systems is available in routine observations, much of it is lost in conventional analysis and data processing.

A continuing point of emphasis will be the relationship and interaction of these mesoscale features with other scales of motion, both larger and smaller. Larger, synoptic-scale patterns, provide the setting for the development of mesoscale features which in turn influence smaller scales. These, in turn, can have important feedback effects on larger scale systems.

Consider first the intense upper front, or hyperbaroclinic zone. Its formation usually occurs in connection with significant cyclonic development at the surface (defined here as an increase in surface vorticity), and important forecasting errors have been related to these

factors. The evidence is persuasive that these errors result in part from a failure to adequately resolve the intense gradients associated with the zones; they must be observed, comprehended, and modeled appropriately in any general weather forecasting scheme. Reed and Sanders (1953), Newton (1954), Reed (1955), Staley (1960), and Bosart (1970) have all dealt with examples of intense fronts, where discontinuities of first order and even (on rather small scales) of zero order can be found in potential vorticity, the vertical component of vorticity, vertical motion, and related fields. First order discontinuities in pressure, potential temperature, and wind have been emphasized.

Certain typical aspects of intense hyperbaroclinic zones associated with cyclogenesis should be noted. The formation, maintenance, and decay of these zones are intrinsically and intimately related to strong vertical motions which have large spatial variations. They are, then, dynamic in nature and closely related to vigorous wind systems, or jet streams. All characteristically involve descending currents of dry air, plunging downward and southward from the upper troposphere, and indeed, the stratosphere, in the rear of cold upper troughs in the westerlies. These cases fall into the category of katafronts (Sansom, 1951); that is, the warm air above the front is descending. There is often descent on both sides of such fronts, as the large scale flows suggest; however, relative upward motion in the cold air, which can be associated with an indirect thermal circulation, is a common feature on the shorter scales.

The vertical temperature gradient in these zones is very large, being of order 10 C km^{-1}, and a typical scaling height H is of order one km. Clearly, these are regions which are very stable in the static sense.

Across the current, the channel width W of the intense horizontal temperature gradient is 100-200 km, so that a representative slope is:

$$\delta = \frac{H}{W} \cong 10^{-2} \qquad (1)$$

corresponding to the average slope of cold fronts.

Alongstream scaling lengths depend on the details of the flow, but may be considerably greater. In any event, it is clear that the air motion is considerably faster than the phase speed associated with the zone of maximum baroclinicity. This suggests that whatever the alongstream dimensions are, the air undergoes frontogenesis in the entrance region and frontolysis in the exit region, in rapid succession.

The phase speed C is usually progressive (C>0), which means that the zone propagates downstream and rotates about the long-wave trough. Maximum intensity, as measured by the thermal gradient, is usually reached near the southernmost penetration, and rapid cyclogenesis typically occurs concurrently at somewhat downstream locations under the diffluent flow east of the trough. This is summarized schematically in Fig. 1.

The hyperbaroclinic zone can easily be detected on cross sections of the upper troposphere when it is located to the west of the long-wave trough position. Thus, the upper front can be a valuable diagnostic feature, and the cross section a valuable diagnostic tool for those who would predict cyclogenesis.

When the representation involves analysis on cross sections, every

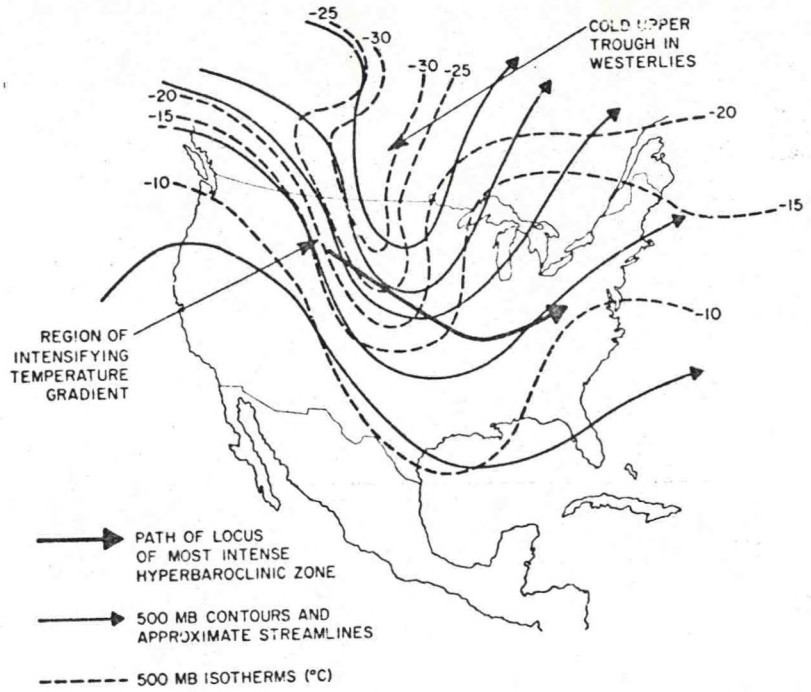

Fig. 1. Schematic 500 mb chart typifies the case of an intensifying upper front involving stratospheric air of high potential vorticity. Zone usually attains maximum strength at southernmost penetration during period of major cyclogeneses in diffluent exit region.

piece of information in the radiosonde is optimally utilized. Further, if surfaces of equal potential temperature are analyzed, the sense of adiabatic vertical motion in the plane of the section is easily visualized.

Fig. 2 (Duquet, et. al., 1966) is an example of an actual cross-section through one of these zones. The upper front stands out, but, as is often the case, there is little or no connection with a surface front until the structure moves to the east of the long-wave trough, where surface winds are usually convergent and fronts more detectable. In fact, although there may be a link-up with pre-existing surface fronts during those later stages, several authors have noted that they see no

necessity for such linking, nor that it has any bearing on the cyclogenesis process.

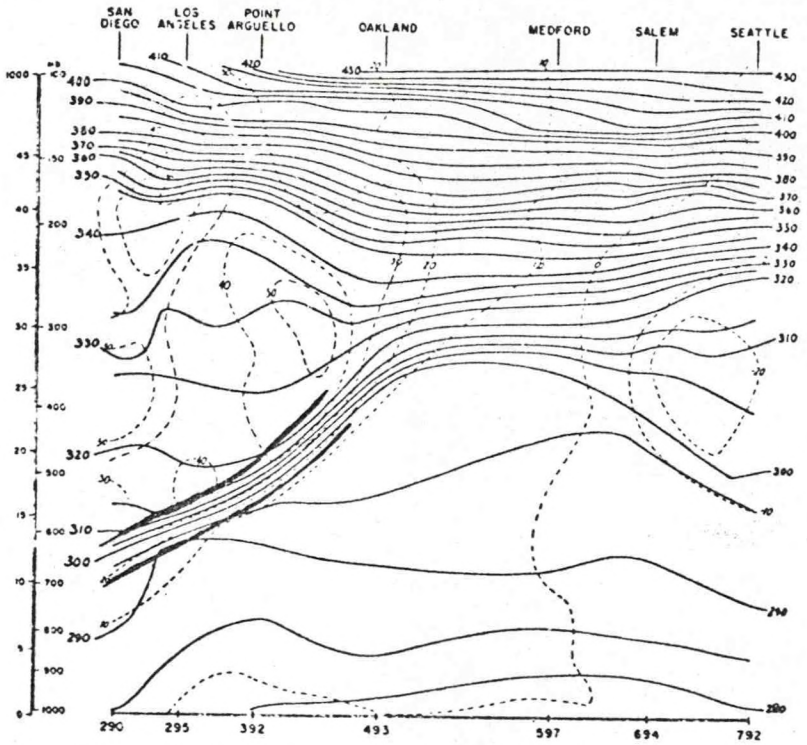

Fig. 2. Subjectively analyzed cross section for 21 April 1963 at 1200 GMT.

On the cross section, the region of greatly magnified values of the quantity $\nabla_p \theta$ or alternatively, $\nabla_p T$ are bounded by heavy lines where the gradient, rather than θ or T itself, is taken to be discontinuous. Although the degree to which a particular atmospheric variable can be treated as discontinuous is largely a matter of scale, the hyperbaroclinic zone boundaries are marked as first-order discontinuities, and in the case of potential vorticity and vertical motion, probably by real zero-order discontinuities. The use of potential vorticity on isentropic surfaces to identify these zones, first sug-

gested by Reed and Sanders (1953), is readily applicable because, to the extent that the air is of stratospheric origin, the quantity:

$$\underline{P} = -\left(\zeta_\theta + f\right)\frac{\partial \theta}{\partial p} \qquad (2)$$

the product of absolute vorticity on a θ-surface with the static stability, which is conserved for adiabatic inviscid flow, has much larger values in the stratosphere than in the troposphere. While notable amounts of mixing and diabatic effects are known to occur in frontal regions over reasonable time frames, potential vorticity maxima will occur within the front. The higher stratospheric values of potential vorticity can be attributed to the greater mean static stability of the stratosphere and also to the fact that:

$$\zeta_\theta = \left(\frac{\partial v}{\partial x}\right)_\theta - \left(\frac{\partial u}{\partial y}\right)_\theta \qquad (3)$$

where the variables have their usual meteorological meanings, tends to be positive in the stratosphere but negative in much of the troposphere as a result of the contribution of the poleward shear term. All this has led Danielsen (1959) to suggest that the tropopause be considered the barotropic level where the potential vorticity characteristically takes on stratospheric values. This is in contrast to the usual definition, which considers only the static stability, and is therefore often ambiguous. The advantage of looking at the tropopause as Danielsen suggests is that it lends itself to the visualization of the ready exchange across the tropopause under adiabatic motion.

What can be seen in cross-sections of this type does not, however, depend upon the definition of the tropopause. The relatively unstable troposphere bounding the stable frontal zone; a strong vertical shear of the normal geostrophic (and actual) wind component being concentrated in the frontal zone between a mound of cold, lower level air and warm air to its west; a high, cold tropopause over warm air, and a low, warm tropopause over cold air; the reversing temperature gradient and related reversing shear in the stratosphere ordaining the jet near the tropopause; all tell their interesting structural story in clear terms.

References

Bosart, L. F., 1970: Mid-tropospheric frontogenesis. Quart. J. Royal Met. Soc., 96, 442-471.

Danielsen, E. F., 1959: The laminar structure of the atmosphere and its relation to the concept of a tropopause. Archiv. Meteor. Geophys. Bioklim. Series A, 11, 293-332.

Duquet, R. T., E. F. Danielsen and N. R. Phares, 1966: Objective cross section analysis. J. Appl. Meteor., 5, 233-245.

Newton, C. W., 1954: Frontogenesis and frontolysis as a three-dimensional process. J. Meteor., 11, 449-461.

Reed, R. J., and F. Sanders, 1953: An investigation of the development of a mid-tropospheric frontal zone and its associated vorticity field. J. Meteor., 10, 338-349.

_____, 1955: A study of a characteristic type of upper-level frontogenesis. J. Meteor., 12, 226-237.

Sansom, H. W., 1951: A study of cold fronts over the British Isles. Quart. J. Royal Met. Soc., 77, 96-120.

Staley, D. O., 1960: Evaluation of potential vorticity changes near the tropopause and related vertical motions, vertical advection of vorticity, and transfer of radioactive debris from stratosphere to troposphere. J. Meteor., 17, 591-620.

CHARACTERISTICS OF UPPER LEVEL BAROCLINIC ZONES

Lecturer: Dr. N. LaSeur Notes By: A. Friend

Date: June 18, 1974 K.-Y. Fung

I. Introduction

Two case studies of upper-level baroclinic zones are described, and calculations of the contributing terms in the frontogenetic equation of Miller (1948) and the vorticity equation are presented. Following Miller (1948), the intensity of frontogenesis is defined as the rate of change of the horizontal gradient of potential temperature following the three-dimensional motion, and may be written:

$$\frac{d}{dt}(\theta_y) = \frac{\partial}{\partial y}\left(\frac{d\theta}{dt}\right) - \frac{\partial w}{\partial y}\theta_z - \frac{\partial v}{\partial y}\theta_y \qquad (1)$$

where

θ = potential temperature

$\theta_y = \partial\theta/\partial y$

v = horizontal velocity components in y direction

w = vertical velocity

t = time

y = horizontal coordinate perpendicular to the flow.

The first term on the right of equation (1) represents changes due to diabatic effects, and being very small, may be neglected. The second term is the tipping term, representing changes in the gradient of θ due to differential vertical motion along the y coordinate. The last term is the diffluence effect, which represents the change in the horizontal gradient of θ due to variations of v along the y coordinate.

After Reed and Sanders (1953), the generation of cyclonic vorticity following the three-dimensional motion and neglecting the effect of curvature, may be written:

$$\frac{d}{dt}\left(-\frac{\partial u}{\partial y}\right)_p = -g\left\{\left[f-\left(\frac{\partial u}{\partial y}\right)_p\right]\frac{\partial}{\partial p}(\rho w) + \frac{\partial u}{\partial p}\frac{\partial}{\partial y}(\rho w)\right\} - \frac{df}{dx} \qquad (2)$$

where

ρ = density of the air

g = acceleration due to gravity

f = Coriolis parameter

u = horizontal velocity in x direction

$( )_p$ = evaluated on a pressure surface.

The first term on the right of equation (2) represents the effect of divergence on the vorticity, while the second (tipping) term represents the effect a horizontal gradient of vertical velocity has in transforming vorticity about a horizontal axis to vorticity about a vertical axis. The last term, called the Rossby term, represents changes in vorticity due to latitudinal displacement.

II. Lecture Notes

The Reed and Sanders (1953) case study involves a distinct example of frontogenesis at the 500-mb level during the period 1500 GCT 27 January 1953 to 0300 GCT 28 January 1953. The 500-mb chart at initial time, Fig. 1, (Reed and Sanders, 1953) does not contain a distinct baroclinic zone. At the final time the 500-mb chart, Fig. 2, shows that a distinct baroclinic zone exists from the west side of the 500-mb trough, across the bottom of the trough, and partially along its

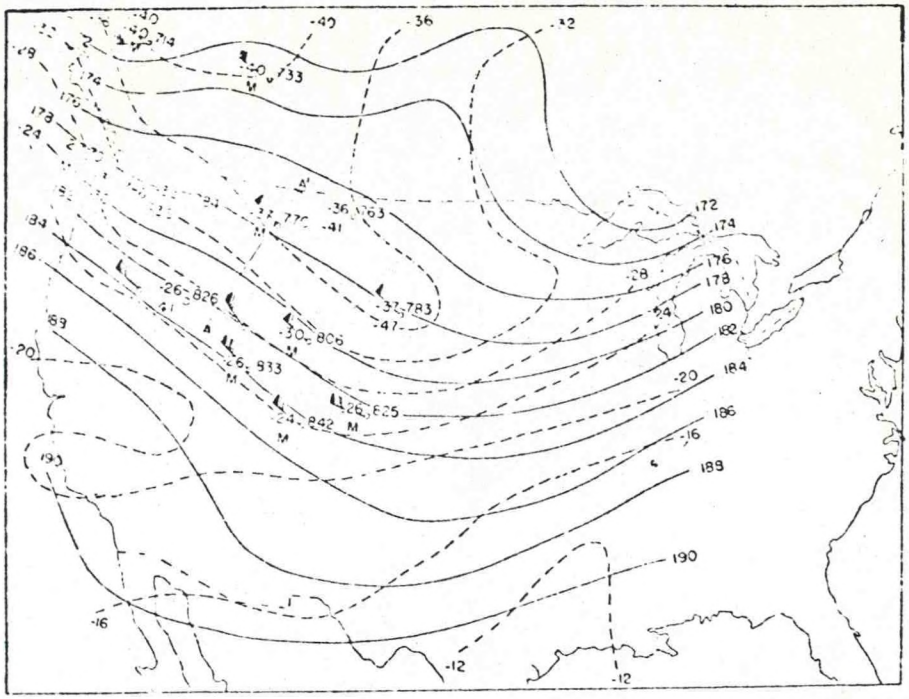

FIG. 1. 500-mb surface for 1700 GCT 27 January 1953 showing contours (thin solid lines) and temperatures (dashed lines). Observed radiosonde and rawin reports have been added in critical areas. Each half barb represents wind speed of 5 kn, each full barb 10 kn, and each solid wedge 50 kn. Contour height in ft and temperature in deg C.

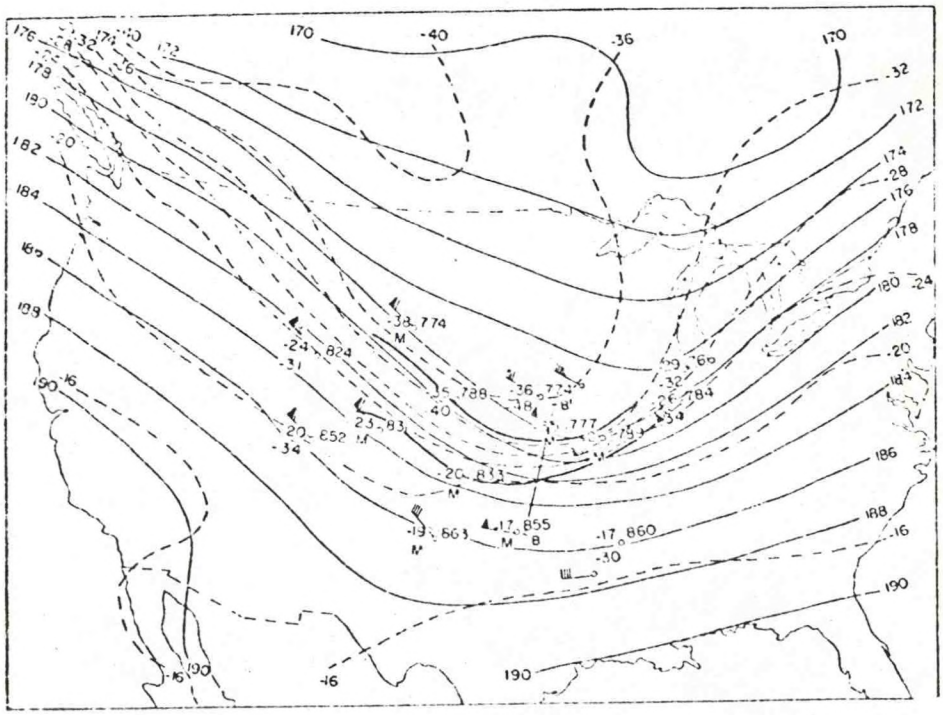

FIG. 2. 500-mb surface for 0300 GCT 28 January 1953. Heavy solid lines are frontal boundaries; otherwise representation is same as in fig. 1.

east side. Figs. 3 and 4 are vertical cross sections showing the distribution of geostrophic wind speed and potential temperature from 700 to 300 mb, as well as the boundaries of the tropopause and the baroclinic zone. The cross section in Fig. 4 is taken along BB' in Fig. 2, and is normal to the strong portion of the baroclinic zone at the final time. The cross section in Fig. 3 is taken in the region shown as AA' in Fig. 1, which is the origin of the air that reaches 500 mb at the later time. The point M in Figs. 1-4 represents a particle originating in Fig. 1 with θ = 300K and p = 370 mb. In the subsequent 12 hours, this particle experiences frontogenesis as it moves to its position in Fig. 2 with θ = 300K and p = 500 mb. To evaluate the terms in equations (1) and (2), a vertical cross section, representing the 2100 GCT position of the air parcels that terminate on the 500-mb surface, Fig. 5, is constructed. Instantaneous values for the terms in equations (1) and (2) at the point M are determined from Fig. 5 and multiplied by 12 hours to give the contribution for the period. One exception is w, which cannot be obtained directly from Fig. 5, but is instead plotted as average vertical motion on the isentropic surfaces over the 12-hour period. The calculations tabulated in Tables 1 and 2 show that for both the frontogenetic and vorticity equations, the tipping term is the most significant. Fig. 6 shows how differential vertical motion tips the isentropic surfaces to increase the baroclinicity of the horizontal temperature field despite diffluence in the horizontal motion.

In Newton's (1954) article, a baroclinic zone extending along the west side of the 500-mb trough (but not on the east side) is considered at one time, 1500 GCT 3 April 1950, Fig. 7. Two separate baroclinic zones

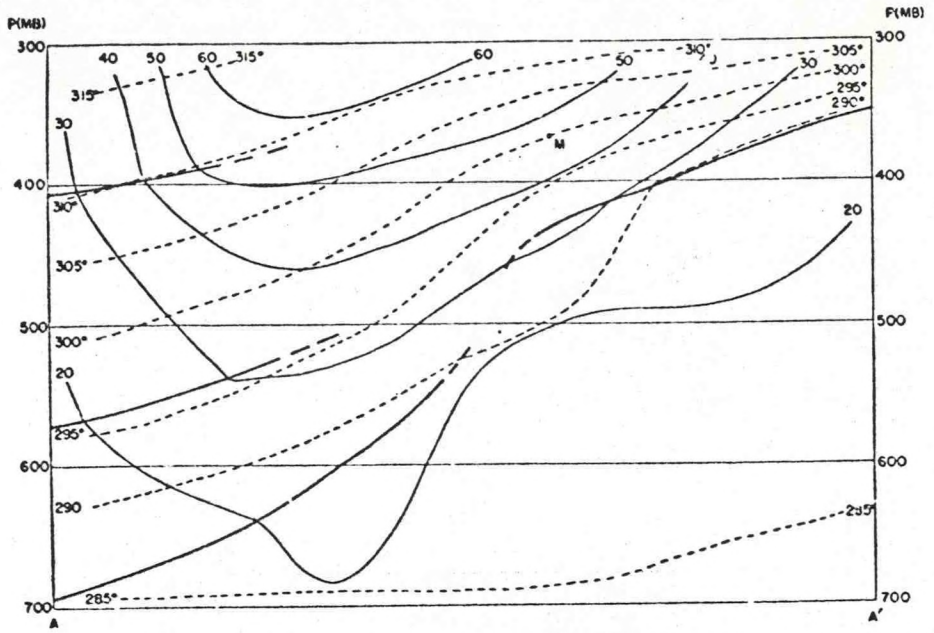

FIG. 3. Cross section along A–A′ in fig. 1. Thin solid lines give geostrophic wind speed (m/sec) normal to section; heavy solid lines are tropopause or frontal boundaries; dashed lines are isentropes.

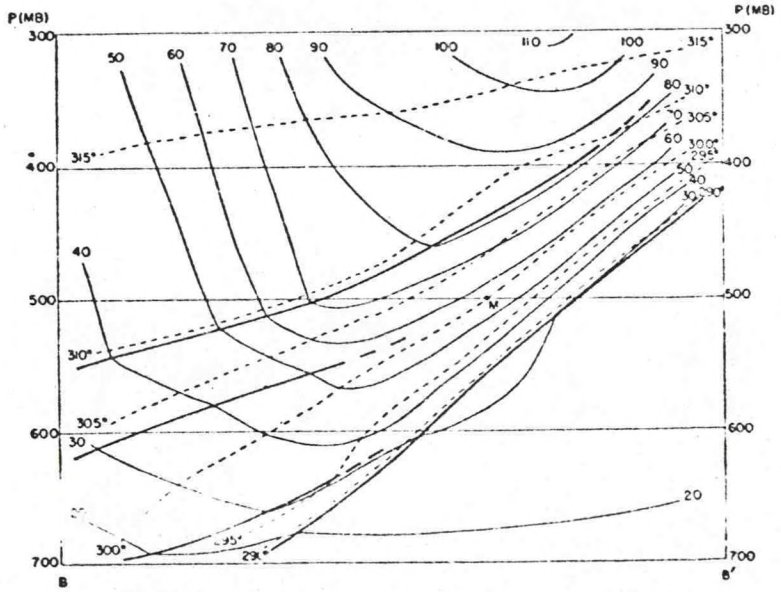

FIG. 4. Cross section along B–B′ in fig. 2. Notation as in fig. 3.

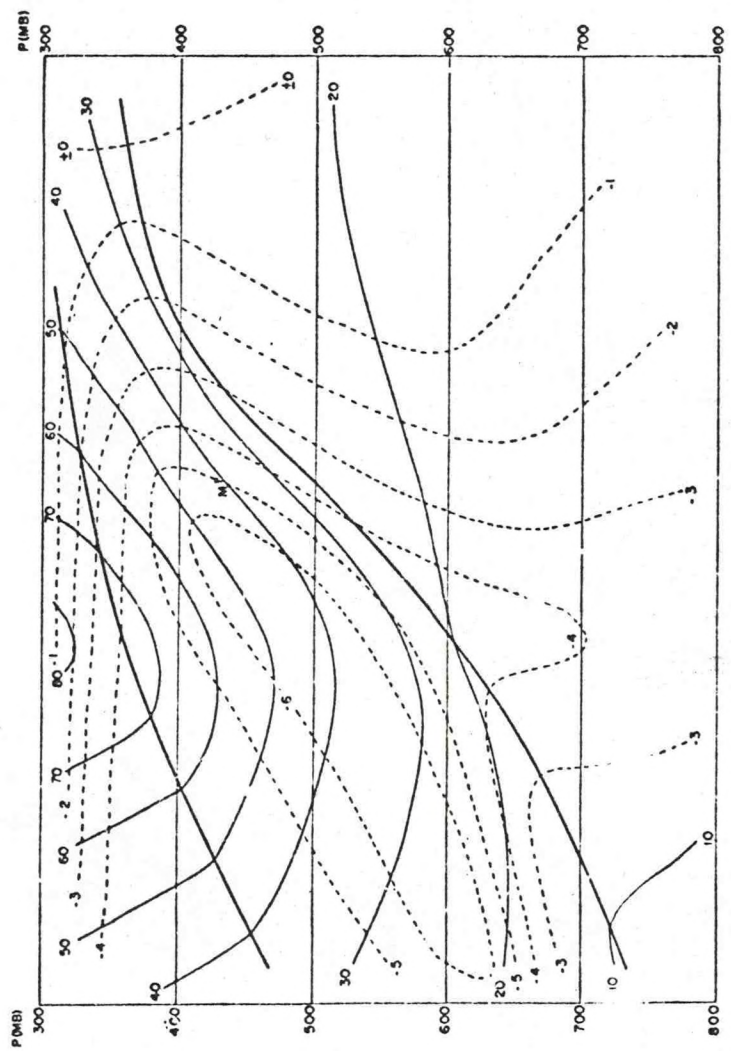

FIG. 5. Cross section from Bismarck, N.D. to Pueblo, Colorado at 2100 GCT 27 January 1953. Thin, solid lines give wind speed (m/sec); heavy, solid lines are frontal boundaries; dashed lines represent average 12-hr vertical velocities (cm/sec).

TABLE 1.
Changes in temperature gradient at point M due to various terms in frontogenetical equation expressed in deg C per 100 km per 12 hr.

	$\Delta(-\partial\theta/\partial y)$
Tilting effect	+9
Confluence effect	-2
Total (computed)	+7
Total (observed)	+7
Two-dimensional (observed)	+9

TABLE 2.
Changes in vorticity at point M due to various terms in the vorticity equation expressed in sec^{-1} per 12 hr.

	$\Delta\zeta$
Divergence effect	-2×10^{-5}
Vertical shear effect	+13
Rossby effect	+ 1
Total (computed)	+12
Total (observed)	+13
Two-dimensional (observed)	+18

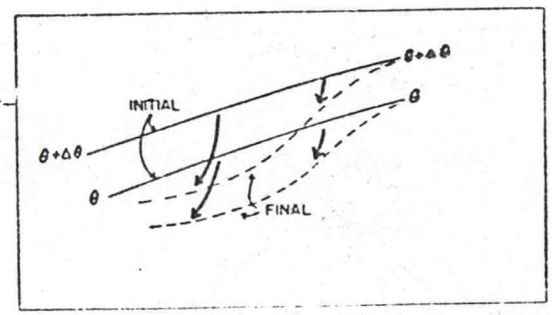

FIG. 6. Schematic diagram illustrating opposing effects of diffluence and vertical motion in producing frontogenesis in temperature field. Solid lines show initial positions of isentropes (θ) in plane normal to flow; dashed lines show final position. Heavy arrows represent displacement of selected points on isentropic surfaces.

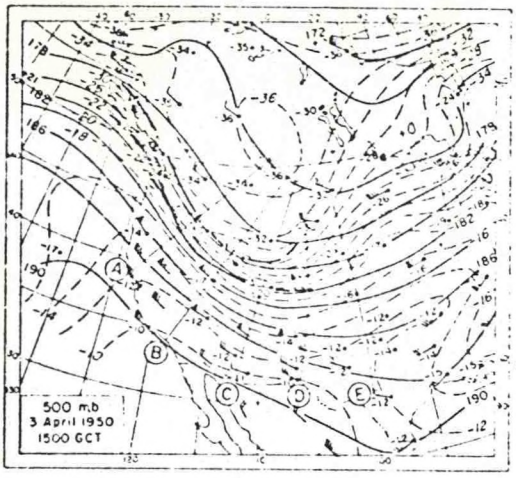

FIG. 7. 500-mb chart, 1500 GCT 3 April 1950. Light solid lines A to E indicate locations of cross-sections.

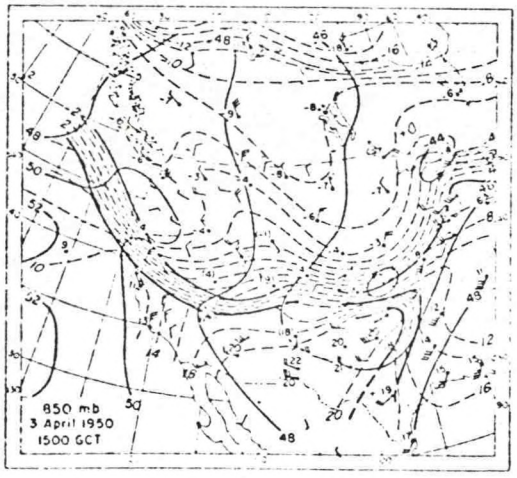

FIG. 8. 850-mb chart, 1500 GCT 3 April 1950. At stations, full wind barb-10kn, triangle-50kn (dashed for winds at somewhat lower level); temperature in deg. C. Thin solid lines: contours (interval: 200 ft.); dashed lines: isotherms (interval: 2C); heavy lines: frontal boundaries. Only south (upper) boundary of main front east of Rocky Mountains is shown, since lower boundary does not intersect 850-mb surface.

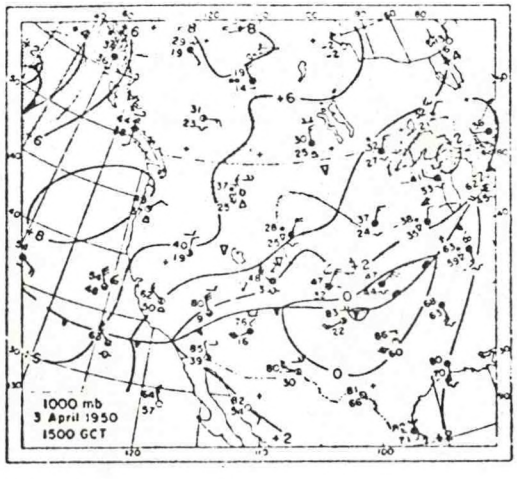

FIG. 9. 1000-mb chart, 1500 GCT 3 April 1950. Contour interval: 200 ft. Precipitation areas stippled.

are shown at lower levels on the 850-mb chart, Fig. 8 (Newton, 1954). The first extends from the west coast to Colorado, and the second covers the Arkansas-Oklahoma area. The 1000-mb chart, Fig. 9, shows a front in this second area, but no fronts in the western U.S. Figs. 10 and 11 are vertical cross sections along lines C and D in Fig. 7. They show the rapid decline in baroclinicity while moving around the base of the trough since they are only 275 miles apart at point A. Based on the progression of this exit region of the baroclinic zone over the previous 24 hours, Newton has determined that 8 hours are required for a particle leaving point A in Fig. 10 to arrive at a point where the structure is equivalent to that at point A in Fig. 11. Figs. 12 and 13 show the distribution of potential temperature and shearing vorticity for these two cross sections. In these figures the shearing vorticity is drawn with a zero order discontinuity at the boundary of the baroclinic zone.

To calculate the contributions of the terms in equations (1) and (2), Newton sets up a system of simultaneous equations for the individual changes in the horizontal and vertical potential temperature changes and the components of vorticity about the y- and z-axes. Due to the choice of coordinate axes, equation (1) contains the additional term $-\partial w/\partial y\, \theta_x$. Since z is used as the vertical coordinate instead of p, equation (2) is in a slightly different form. To solve the set of simultaneous equations for $\partial v/\partial y$, $-\partial w/\partial z$, $\partial v/\partial z$ and $\partial w/\partial y$, all other quantities of the system are measured on the cross sections, Figs. 12 and 13. The initial and final value of each quantity is averaged. The mean values are then used to obtain the solution of the system. For this case, the horizontal

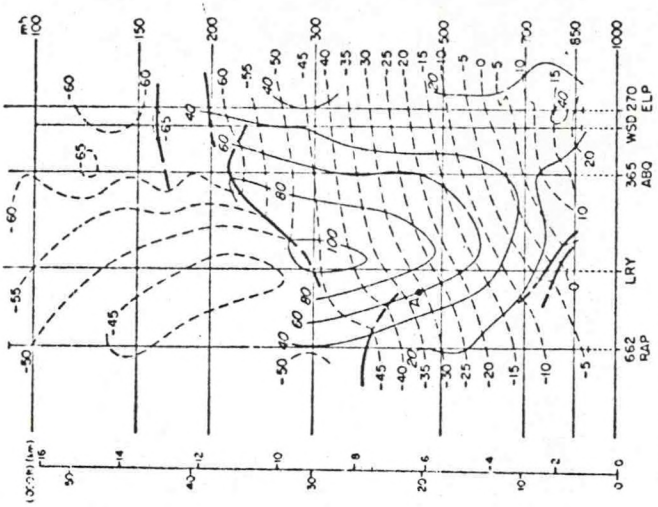

FIG. 10. Cross section along line C in Fig. 9, 1500 GCT 3 April 1950.

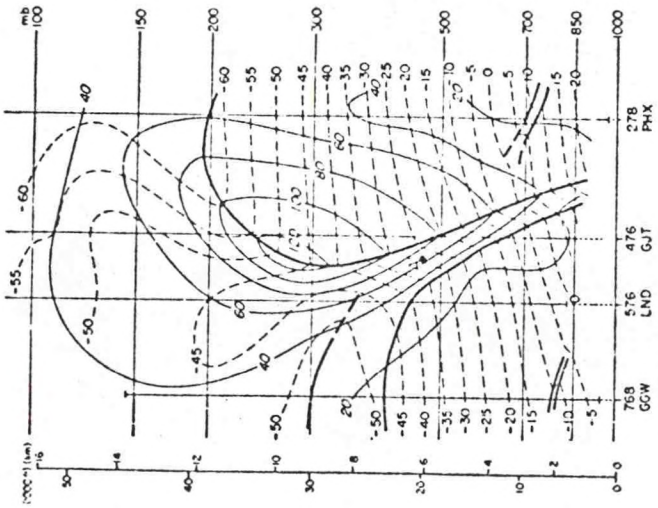

FIG. 11. Cross section along line D in Fig. 9, 1500 GCT 3 April 1950.

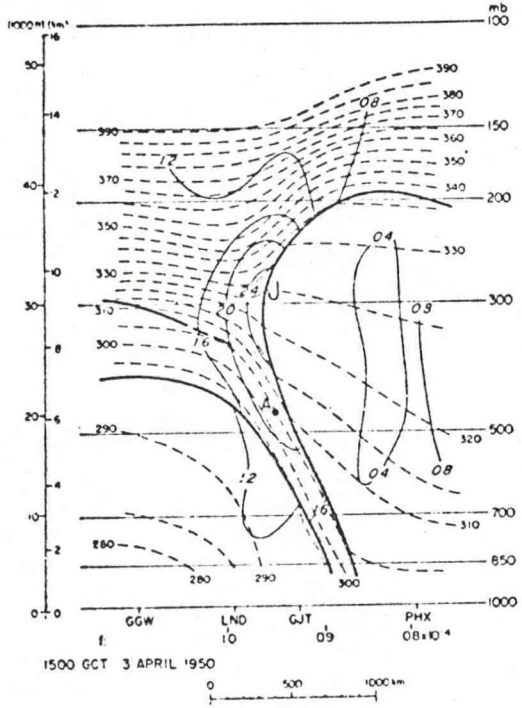

FIG. 12. Potential temperature (deg K, dashed lines) and shearing vorticity (10^{-4} sec^{-1}, thin solid lines) corresponding to Fig. 10. At maximum value, absolute vorticity is about 10 per cent greater than shearing vorticity. J indicates the center of the stream.

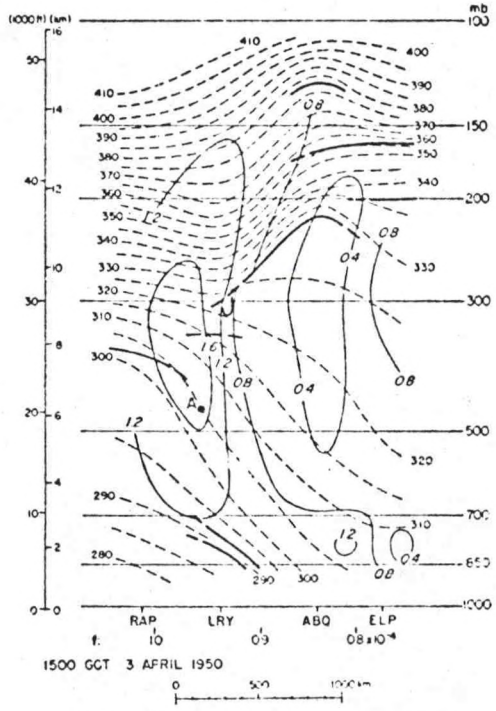

FIG. 13. Potential temperature and vorticity corresponding to Fig. 11.

advection, confluence, and tipping terms all contribute about equally to the frontalysis a particle would experience following the path of point A for the eight hours required to travel from Fig. 12 to Fig. 13. The results for equation (2), neglecting the very small contribution of the Rossby term, indicate that the decrease in vorticity about the vertical axis is due mainly to the tipping term, with slightly more than one third of the change coming from the divergence term.

The results of these two papers indicate that the tipping terms make significant contributions in both the frontogenetic and the vorticity equations. It is, in fact, concluded that the tipping term is of primary importance in these upper-level baroclinic zones. The fact that the tipping terms have opposite signs between the two equations suggests that they can be combined in terms of potential vorticity on isentropic surfaces. This potential vorticity will be a conservative quantity as a particle moves adiabatically through a baroclinic zone.

References

Miller, J. C., 1948: On the concept of frontogenesis. J. Meteor., 5, 169-171.

Newton, C. W., 1954: Frontogenesis and frontalysis as a three-dimensional process. J. Meteor., 11, 449-461.

Reed, R. J., and F. Sanders, 1953: An investigation of the development of a mid-tropospheric frontal zone and its associated vorticity field. J. Meteor., 10, 338-349.

THE ROLE OF VERTICAL MOTION IN THE DEVELOPMENT OF UPPER TROPOSPHERIC HYPERBAROCLINIC ZONES

Lecturer: Dr. N. LaSeur Notes By: L. Gidel

Date: June 19, 1974 M. Leach

In this lecture the vertical motion associated with mid- and upper-tropospheric frontogenesis is presented, with observational case studies of Shapiro (1970) and Staley (1960) serving as examples. The role of the vertical motion in the adiabatic and vorticity equations is discussed as it relates to frontogenesis, and the two equations are combined with the continuity equation to obtain Ertel's (1942) potential vorticity equation.

In the case of adiabatic, frictionless flow, the potential vorticity is conservative and its form suggests θ- coordinates as the natural system for resolving cases of mid- and upper-tropospheric frontogenesis.

Fig. 1 (Shapiro, 1970) is an example of the mid-troposheric thermal structure. A primary baroclinic zone is positioned on the western side of the trough together with additional secondary baroclinic zones. Line A designates the cross section shown in Fig. 2. An important feature of this cross section is the intense packing of the isotachs in the primary baroclinic zone, and the tendency of these isotachs to align themselves parallel to the boundaries of the frontal zones. This behavior is very similar to that of the isentropes in the same zone. The lower boundary of the primary zone is continuous with the tropopause at the lower edge. The secondary zones are similar to

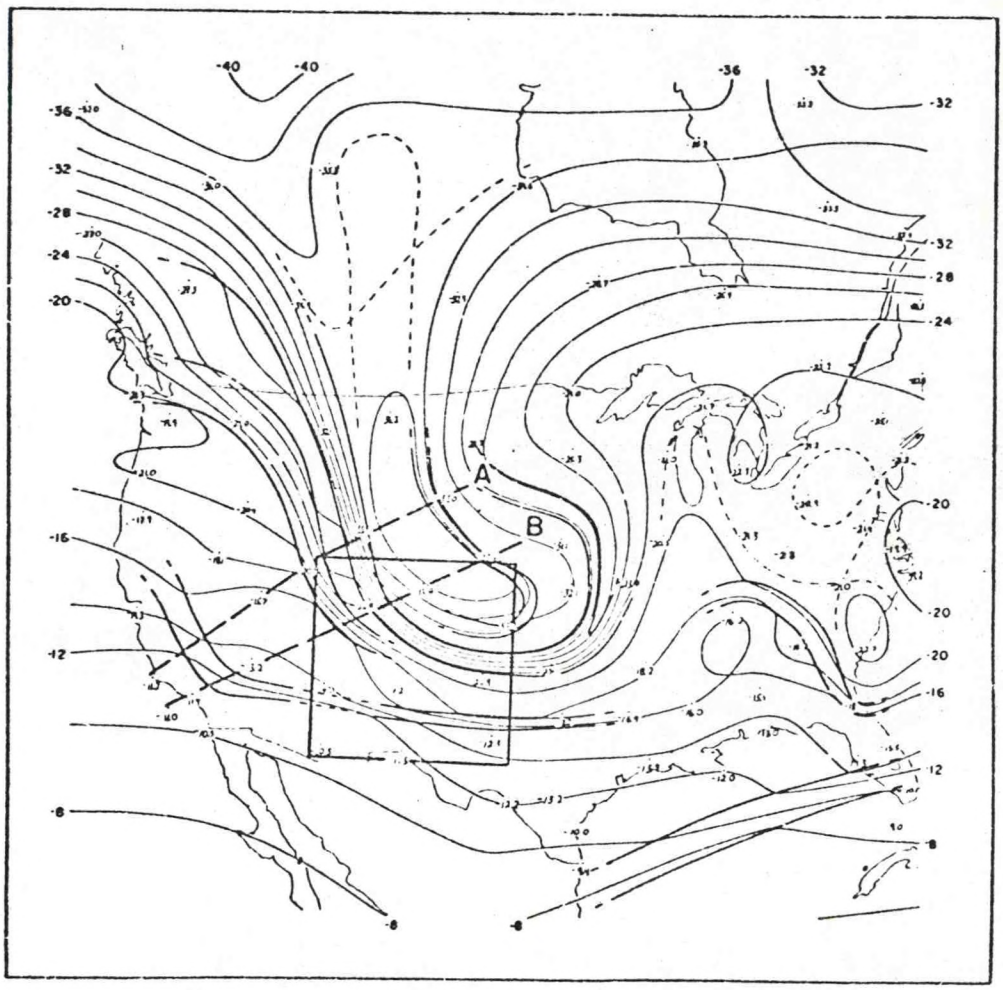

FIG. 1. 500-mb temperature analysis for 0000 GMT 8 December. Thin lines, isotherms (°C); heavy lines, intersections of frontal and secondary baroclinic zone boundaries with the 500-mb surface; square outlined area over southwestern United States, area of frontal-scale numerical calculations.

the stable laminae discussed by Danielsen (1959).

The vertical velocity used by Shapiro (1970) and Staley (1960) is calculated from the thermodynamic equation. This method is particularly suited to upper-level frontal zones because these zones are characteristically located in non-precipitating, subsident regions and hence experience minimal diabatic heating. Thus:

$$\omega = \frac{\frac{\partial \theta}{\partial t} + V_p \cdot \nabla \theta}{-\frac{\partial \theta}{\partial p}} \qquad (1)$$

Because of the difficulty of obtaining an instantaneous value for the tendency term, the local temperature change is calculated in a coordinate system moving at a constant velocity on an isobaric surface, i.e.:

$$\frac{\delta \theta}{\delta t} = \frac{\partial \theta}{\partial t} + \mathbb{C} \cdot \nabla_p \theta \qquad (2)$$

If $\mathbb{C}$ is set equal to the translational velocity of the semi-permanent frontal zone, $\frac{\delta \theta}{\delta t}$ is sufficiently small that the potential temperature field remains unchanged in the moving system. Substitution of (2) into (1) yields the form used by Shapiro (1970):

$$\omega = \frac{(V_p - \mathbb{C}) \cdot \nabla \theta + \left(\frac{\delta \theta}{\delta t}\right)_{\mathbb{C}}}{-\frac{\partial \theta}{\partial p}} \qquad (3)$$

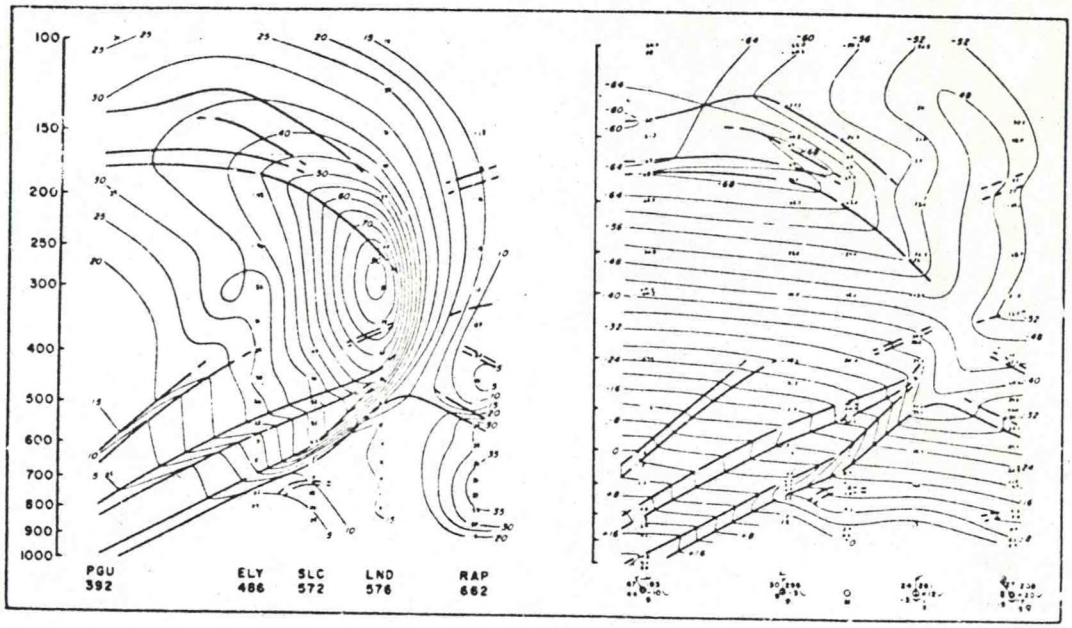

FIG. 2. Cross section analysis of wind speed and temperature along line A of Fig. 1 at 0000 GMT 8 December. Heavy solid lines denote tropopause, frontal and secondary layer boundaries.

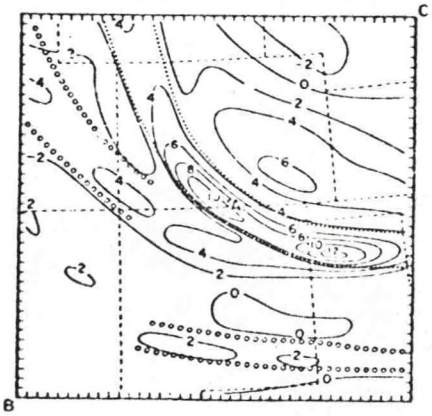

FIG. 3. 500-mb vertical velocity. Solid lines, isolines of vertical velocity at 2 X 10^{-3} mb sec^{-1} intervals; dotted lines, frontal boundaries; open circle lines, boundaries of secondary baroclinic zones; dashed lines, state borders.

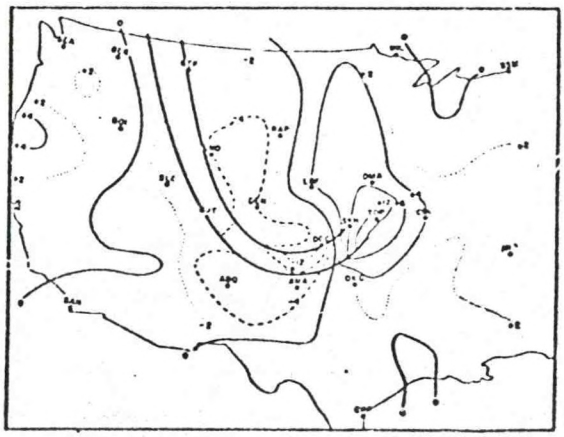

FIG. 4. Vertical velocity at 500 mb for 1500 GMT 14 March 1957. Thin solid (dashed) lines denote positive (negative) values at 4 cm sec^{-1} intervals. Dotted lines denote selected intermediate values. Heavier solid lines represent frontal boundaries.

A similar expression was used by Staley (1960):

$$w = -\frac{(\mathbf{v} - \mathbf{c}) \cdot \nabla\theta + \left(\frac{\partial\theta}{\partial t}\right)_c}{(\gamma_d - \gamma)}$$

Computations demonstrate that the tendency term calculated in the moving system is generally smaller than the first term in each of the above equations and up to one order of magnitude smaller in the frontal zone.

In Fig. 3 (Shapiro, 1970), the maxima of sinking motion are located within the baroclinic zones. Compare the zero order discontinuities at the frontal zone boundaries in Fig. 3 to those in Fig. 4 (Staley, 1960). In both cases, there exists a maximum of sinking motion in the frontal zone and zero order discontinuities at the frontal boundaries. In Fig. 4, note also the position of the maximum positive vertical velocity, which corresponds to the area of maximum frontolysis as discussed in an earlier lecture and by Newton (1954).

The frontogenetical effect of this field of vertical motion is illustrated by the frontogenesis equation of Miller (1948):

$$-\frac{d}{dt}\left(\frac{\partial\theta}{\partial y}\right) = -\frac{\partial}{\partial y}\left(\frac{d\theta}{dt}\right) + \frac{\partial w}{\partial y}\frac{\partial\theta}{\partial z} + \frac{\partial v}{\partial y}\frac{\partial\theta}{\partial y} \qquad (4)$$

where the y-axis is parallel to the temperature gradient and points toward cold air. The second term on the right side represents the horizontal variation of adiabatic heating or cooling resulting from

the horizontal gradient of the vertical motion.

The vorticity equation in P-coordinates is:

$$\frac{d}{dt}(\zeta_p + f) = -(\zeta_p + f)\nabla_p \cdot V - \frac{\partial \omega}{\partial x}\frac{\partial v}{\partial p} + \frac{\partial \omega}{\partial y}\frac{\partial u}{\partial p} \qquad (5)$$

The second and third ("tilting") terms on the right side represent the effect a horizontal gradient in the vertical velocity field has in transforming vorticity about a horizontal axis (i.e., the vertical shear of the horizontal wind) to vorticity about a vertical axis. The individual derivative of the absolute vorticity on the left side contains the vertical advection of the absolute vorticity.

Figs. 5 and 6 (Staley, 1960) show, respectively, the vertical advection of the vertical component of geostrophic vorticity, and the sum of the vertical motion terms in the vorticity equation. Again, the position of the positive and negative maxima and the discontinuity existing at the frontal boundaries should be noted, as well as the order of magnitude difference between the values within the frontal zone and those outside it.

Fig. 7 (Staley, 1960) is a simplified composite of what has been shown in the preceding figures. In Figs. 7a and 7b, the relative positions of the positive and negative centers of vertical velocity are shown. The positive center is northeast of the negative center and in the area of the increasingly diffuse frontal zone. Fig. 7d is a schematic representation of the orientation of the isentropic surfaces within the frontal zone and Fig. 7c is a representation of the

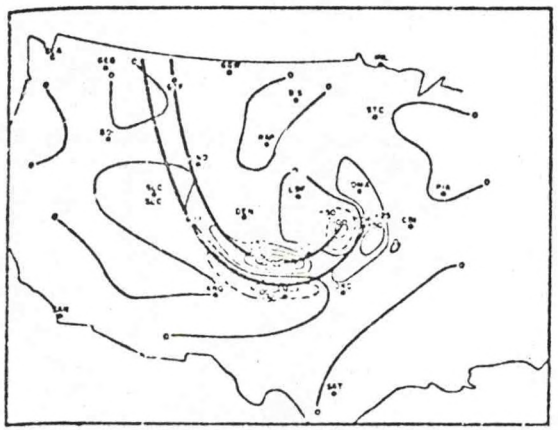

FIG. 5. Vertical advection of the vertical component of geostrophic vorticity, $-w\partial\zeta_g/\partial z$, in units of 10^{-5} sec^{-1} day^{-1}, at 500 mb for 1500 GMT 14 March 1957. Solid (dashed) lines denote positive (negative) values. Heavy solid lines denote frontal boundaries.

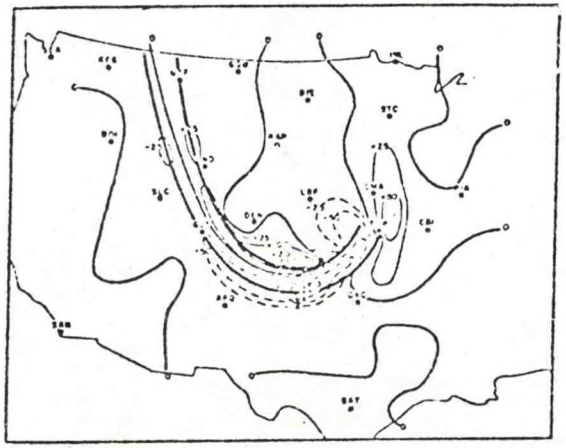

FIG. 6. Sum of vertical-motion terms in the vorticity equation, $-g(fT)^{-1}\nabla_p(u\nabla_p T)$, in units of 10^{-5} sec^{-1} day^{-1}, at 500 mb for 1500 GMT 14 March 1957. Otherwise conventions same as in fig. 5.

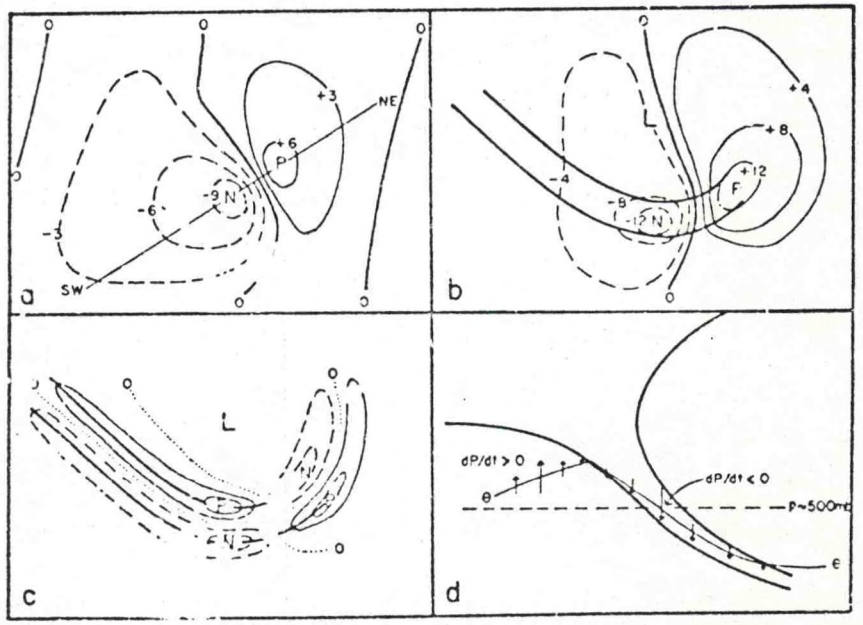

FIG. 7. Schematic idealizations in relation to upper-air front and potential-vorticity discontinuity, of vertical motion, vertical-motion terms in the vorticity equation, and sign of potential-vorticity changes for an upper-air front on the south and southwest side of the trough or vortex. a: Vertical motion in cm sec^{-1} on an isentropic surface, such as θ in d, passing upward through the frontal or baroclinic zone and out into the high troposphere on the cold side of the front. Solid (dashed) lines denote positive (negative) values; P and N denote positive and negative centers respectively. Magnitudes are only suggestive. Thin, straight line indicates the southwest-northeast orientation of the centers. b: Vertical motion in cm sec^{-1} at 500 mb in relation to frontal boundaries (heavy solid lines) and vortex center L. c: Qualitative distribution, relative to front or zone of large temperature gradient of any of the vertical-motion terms in the vorticity equation or their sum. P and N denote positive and negative centers respectively. d: Qualitative distribution of vertical velocity and potential-vorticity change $d\zeta_\theta/dt$ in vertical cross-section relative to the potential vorticity discontinuity and a selected isentrope θ passing through the frontal zone. Vertical velocities are denoted by arrows, with speeds proportional to length. Cross-section orientation along SW to NE line in diagram a.

vertical motion terms within the frontal zones.

The potential absolute vorticity is described by: (1) the three dimensional vorticity equation, (2) the equation of continuity, and (3) the thermodynamic equation. These can be combined to give:

$$\frac{dP}{dt} = \frac{\alpha}{g}\left[\vec{\eta}\cdot\nabla\left(\frac{d\theta}{dt}\right) + \nabla\theta\cdot(\nabla\times F)\right] \qquad (6)$$

where

$$P = \left(-\frac{\partial\theta}{\partial p}\right)\left(\zeta_\theta + f\right)$$

and where ζ_θ is vorticity in isentropic coordinates. For adiabatic frictionless flow $\frac{dP}{dt} = 0$.

The first term on the right side of equation (6) represents the effects of the gradient of diabatic heating along the vorticity axis. The remaining term on the right side is the frictional stress term.

Since frontal zones are characteristically regions of densely packed isentropes, the form of the potential vorticity suggests that an isentropic coordinate system would provide greater resolution of these zones. Isentropic coordinates thus appear to be the natural system for frontal zone analysis.

As seen before, the conservation of potential vorticity can be written in Θ-coordinates as:

$$(\zeta_\theta + f)\left(\frac{\partial \theta}{\partial p}\right) = C$$

or in p coordinates as:

$$(\zeta_p + f)\left(\frac{\partial \theta}{\partial p}\right) + \hat{k} \cdot \left(\frac{\partial V}{\partial p} \times \nabla_p \theta\right) = C$$

By manipulating these equations and the thermal wind equation, it can be shown that ζ_θ is typically less than ζ_p :

$$\zeta_\theta = \zeta_p - \left|\frac{\partial p}{\partial \theta}\right| \frac{R}{f} \frac{1}{p} \left(\frac{p_0}{p}\right)^{R/c_p} \left|\nabla_p T\right|^2$$

or

$$\zeta_\theta = \zeta_p - \frac{\partial u}{\partial p}\left(\frac{\partial p}{\partial y}\right)_\theta$$

Observationally, ζ_θ was found to change less than ζ_p and could be resolved with a horizontal scale of 300 km. This is an important advantage of θ-coordinates over p - coordinates, because ζ_p changes more rapidly in time, and can be properly resolved only with a much finer grid.

While prediction in θ-coordinates may be the best way to forecast cyclogenesis associated with mid- and upper- tropospheric frontogenesis, it is still an unproven method for predicting cyclogenesis associated with convergence of the moisture field, in which case there is less resolution in θ-coordinates than in p-coordinates. Deaven (1974) has

proposed a numerical model that employs σ-coordinates in the lower troposphere and θ-coordinates in the upper troposphere as an alternative.

References

Danielsen, E.F., 1959: The laminar structure of the atmosphere and its relation to the concept of a tropopause. Arch. Meteor. Geophys. Bioklim., A, 11, 293-332.

Deaven, D.G., 1974: A solution for boundary problems in isentropic coordinate models. Ph.D. dissertation, Pennsylvania State University.

Ertel, H., 1942: Ein neuer hydrodynamischer wirbelsatz. Meteor. Z., 59, 277-281.

Miller, J.E., 1948: On the concept of frontogenesis. J. Meteor., 5, 169-171.

Newton, C.W., 1954: Frontogenesis and frontolysis as a three dimensional process. J. Meteor., 11, 449-461.

Shapiro, M.A., 1970: On the applicability of the geostrophic approximation to upper-level frontal scale motions. J. Atmos. Sci., 27, 408-420.

Staley, D.O., 1960: Evaluation of potential vorticity changes near the tropopause and the related vertical motions, vertical advection of vorticity, and transfer of radioactive debris from stratosphere to troposphere. J. Meteor., 17, 591-620.

SOME OBSERVED PROPERTIES OF UPPER-LEVEL AND LOWER-LEVEL FRONTS

Lecturer: Dr. N. LaSeur Notes by: R. Livingston

Date: June 20, 1974 H. McComas

I. Upper-Level Fronts

In previous lectures it has been established that narrow zones of intense baroclinicity associated with strong jetstreams form and propagate in the upper troposphere. Although the association between baroclinic zones and strong jetstreams is obvious and understandable in terms of quasi-geostrophic and hydrostatic balance, frontogenesis or frontolysis must be a result of some degree of dynamic imbalance.

Some indication of the frontogenetic properties of the upper-tropospheric, baroclinic zones have been established through the work of Reed and Sanders (1953), Newton (1954), Reed (1955), and Staley (1960). The conclusions expressed by Reed and Sanders (1953) and Reed (1955) concerning the origin of the air found in the frontal zone are of some interest. Reed and Sanders (1953) suggest that the lower stratosphere undergoes strong, differential subsidence, and Reed (1955) implies that the subsidence is manifest in a folding tropopause process which allows a tongue of stratospheric air to descent to mid-tropospheric levels.

The work of Reed and Danielsen (1959) also suggests that the upper-level frontal zone air is of stratospheric origin. They investigated five separate cases where pronounced fronts were evident aloft. Cross-sections were analyzed and composite figures were drawn. The analyses suggest that the intense baroclinic zone is on the order of 180 km wide and extends down to about 700 mb (Fig. 1). The frontal zone is terminated

at 700 mb because, in three out of the five cases analyzed, it became quite diffuse below this level.

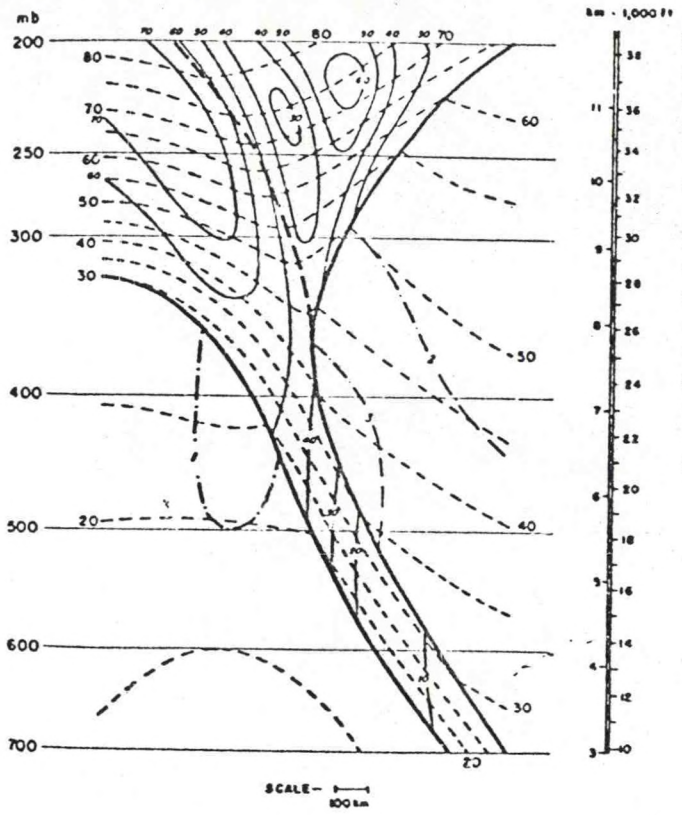

Fig. 1. Composite section showing frontal boundaries and tropopauses, (heavy solid lines); axis of warm air, (heavy broken line); isopleths of potential vorticity in units of 10^{-9} cgs, (light solid and dash dot lines); and isentropes in deg C (light broken line). (From Reed and Danielsen, 1959).

The analysis also shows that first order discontinuities exist in the potential temperature field, and zero order discontinuities are found in the potential vorticity field. The potential vorticity field within the frontal zone has the same high values characteristic of the lower stratosphere. Since tropospheric values are much lower, and since potential vorticity is a quasi-conservative air mass property, it is clear that the potential vorticity field (Fig. 1) identifies the air in the frontal zone as being of stratospheric origin.

In lower tropospheric regions (or on the θ surface), the frontal zone

is not readily distinguishable. However, potential vorticity defined in previous lectures as:

$$(\zeta_\theta + f)\left(-\frac{\partial \theta}{\partial p}\right) = P \qquad (1)$$

can also be expressed as:

$$(\zeta_p + f)\frac{\partial \theta}{\partial p} + k \cdot \frac{\partial V_2}{\partial p} \times \nabla_p \theta = P \qquad (2)$$

where ζ_p is the relative vorticity evaluated on the pressure surface, and the other terms have their usual meanings. The first term of Eq. (2) is sometimes called the partial potential vorticity, P', or:

$$(\zeta_p + f)\frac{\partial \theta}{\partial p} = P' = P - \left[k \cdot \frac{\partial V_2}{\partial p} \times \nabla_p \theta\right].$$

P' varies more in space and time than P. Thus, P' is not a conservative parameter and cannot be used as an air mass tracer.

The isotherm pattern in Fig. 2 (Reed and Danielsen, 1959) shows that the frontal zone is very stable, but the surrounding regions are much less stable. Fig. 2 also indicated that the jet stream core is located almost directly over the intersection of the upper frontal boundary and the 500-mb surface. This is in good agreement with the observations of Palmén and Newton (1948).

Further evidence that stratospheric-tropospheric interaction occurs during upper-level frontogenesis is given by Danielsen (1968). Comparisions are made of ozone concentration, radioactivity, and potential

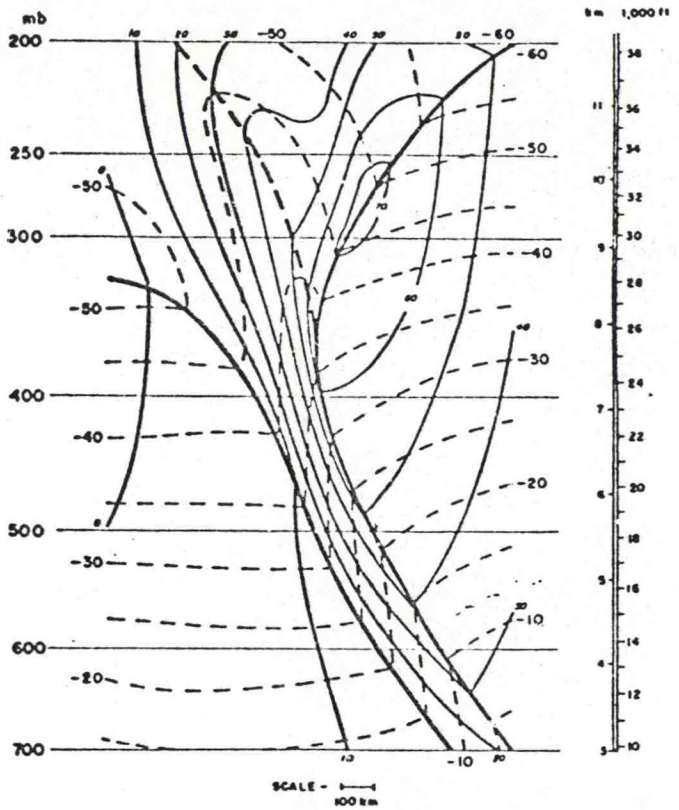

Fig. 2. Same as Fig. 1, except isotachs of normal geostrophic wind component in m/sec (light solid lines) and isotherms (light broken lines).

vorticity values of the lower-stratospheric upper-tropospheric region and the frontal zone. Fig. 3 (Danielsen, 1968) is derived from data collected by aircraft which penetrated the frontal zone. Again, the indication is that a tongue of stratospheric air is descending into the troposphere. There is also a positive correlation between potential vorticity and radioactive decay of strontium 90 (Sr90), part of the radioactive debris injected into the stratosphere by weapons tests. In addition, there is a second maximum of potential vorticity-radioactivity which is quite distinct. The double maxima, with lower tropospheric values between them, strongly suggest that not only is strato-

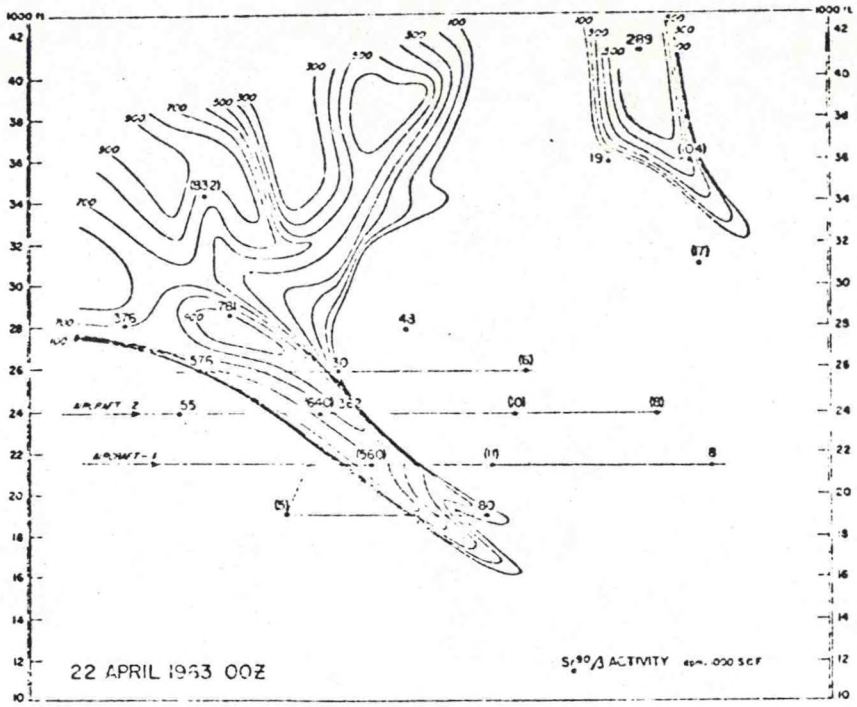

Fig. 3. Potential vorticity (contoured at intervals of 100 x 10^{-10} cm sec (°K) gm^{-1}) and Sr90 activity.

spheric air descending, but also that tropospheric air is rising and mixing into the stratosphere.

The implication that frequent and continued mass exchange occurs through the tropopause does suggest that the tropopause is not a substantial surface. Using all of the data available on the original radiosonde trace (National Weather Service guidelines were not used for linear interpolation and identification of significant levels), Danielsen (1959) found several stable laminae that had spatial and temporal continuity. He concluded that there is no distinct discontinuous surface which separates the stratosphere and troposphere. Rather, it is suggested that the tropopause is a barotropic surface which is quite permeable to

atmospheric motion. In fact, Danielsen (1968) suggests that on the average, stratospheric mass outflow into the upper-level frontal zone is compensated for by a quasi-steady inflow from the troposphere through the barotropic tropopause layer.

In summary, it has been found that the formation of the upper-level front (zone of hyperbaroclinicity) is first detectable in the northwest flow behind an upper-level trough. Stratospheric air subsides into tropospheric regions, either by a folded-tropopause type mechanism or by some other means. In time, the hyperbaroclinic zones propagate around the trough. Often surface frontogenesis occurs as the upper-level fronts move into the southeast region of the trough. In most instances there is a coupling of the two fronts. The physics of the coupling mechanism is still unclear.

II. Lower-Level Fronts

A notable feature of surface fronts is their ability to form and propagate in the absence of any such upper-level feature. One such case has been investigated by Sanders (1955). The front is clearly defined at the surface, but becomes quite weak between 700 and 600 mb (Fig. 4). After rising several thousand feet, the frontal boundaries become almost parallel to the earth's surface.

A cross-sectional view of the front shows the surface convergence pattern with air rising ahead of and immediately within the front at the surface.

The frontogenetic properties of the frontal zone are examined by use of the frontogenesis equation (Miller 1949) and the vorticity equation for adiabatic frictionless flow. These equations can be

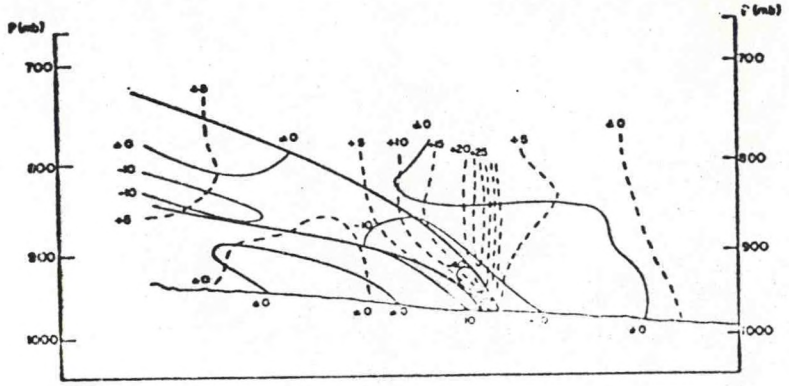

Fig. 4. Distribution of horizontal divergence and veri
Boundaries of frontal zone (heavy solid lines), isopleths of divergence in units of 10^{-5} sec^{-1} (light solid lines), vertical velocity at intervals of 5 cm/sec (dashed lines). (From Sanders, 1955)

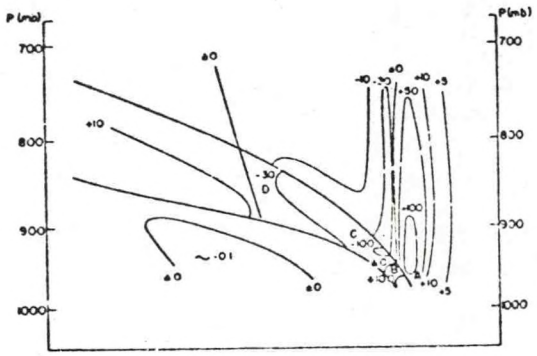

Fig. 5. Net frontogenetical effect for all terms in units of 3-hour changes in horizontal temperature gradient (°C/100 km). Positive values indicate frontogenesis.

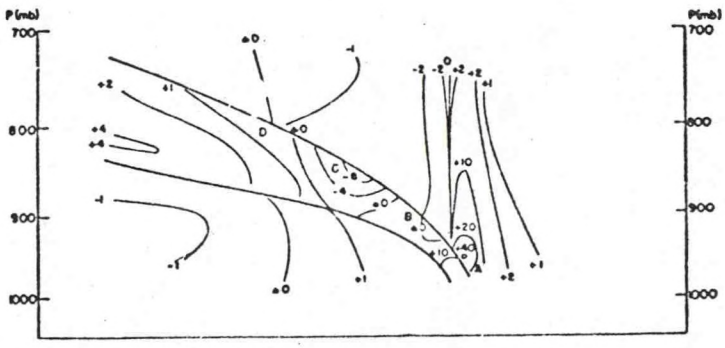

Fig. 6. Net frontal effect in units of 3-hour changes of 10^{-4} sec^{-1}. Positive values indicate frontogenesis in the field of motion.

expressed, respectively, as:

$$-\frac{d}{dt}\left(\frac{\partial\theta}{\partial y}\right) = -\frac{\partial}{\partial y}\left(\frac{d\theta}{dt}\right) + \frac{\partial v}{\partial y}\frac{\partial\theta}{\partial y} + \frac{\partial w}{\partial y}\frac{\partial\theta}{\partial z} \qquad (3)$$

$$-\frac{d}{dt}\left(\frac{\partial u}{\partial y}\right) = \frac{\partial v}{\partial y}\frac{\partial u}{\partial y} + \frac{\partial w}{\partial y}\frac{\partial u}{\partial z} - f\frac{\partial v}{\partial y} - \frac{df}{dt} \qquad (4)$$

The x-axis is oriented parallel to the θ field. (The individual terms have been defined in previous lecture notes.) The frontogenesis effects of each term have been determined and the net influence of equations (3)-(4) are presented in Fig. 5 and 6. [See Sanders, 1955, for the influence of each term of Eqs. (3) and (4).]

Both figures indicate frontogenesis ahead of and in the lower portion of the frontal zone. It seems apparent that the frontal surface is not a substantial or material boundary; rather, air parcels on the warm side of the front move into the frontal zone at the surface while undergoing frontogenesis, pass upward, remaining within the frontal boundaries, and eventually experience frontolysis aloft. There is no indication that air from the cold side of the front is entrained into the frontal zone.

:le is known on how the surface and upper-level fronts become co nor is there any clear picture of the physical structure of such a coupling. It is suspected, however, that there is no unique

model that adequately describes the observed properties of upper-level and lower-level fronts and their coupling.

References

Danielsen, E. F., 1959: The laminar structure of the atmosphere and its reference to the concept of a tropopause. Arch. Meteor. Geophys. Bioklim., A, 11, 293-332.

_____, 1968: Stratospheric-tropospheric exchange based on radioactivity, ozone, and potential vorticity. J. Atmos. Sci., 25, 502-518.

Miller, J. E., 1949: On the concept of frontogenesis. J. Meteor., 5, 169-171.

Newton, C. W., 1954: Frontogenesis and frontolysis as a three-dimensional process. J. Meteor., 11, 449-461.

Palmén, E., and C. W. Newton, 1948: A study of mean wind and temperature distribution in the vicinity of the polar front in winter. J. Meteor., 5, 220-226.

Reed, R. J., 1955: A study of a characteristic type of upper-level frontogenesis. J. Meteor., 12, 226-237.

_____, and E. F. Danielsen, 1959: Fronts in the vicinity of the tropopause. Arch. Meteor. Geophys. Bioklim., A, 11, 1-17.

_____, and F. Sanders, 1953: An investigation of the development of a mid-tropospheric frontal zone and its associated vorticity field. J. Meteor., 10, 338-349.

Sanders, F., 1955: An investigation of the structure and dynamics of an intense surface frontal zone. J. Meteor., 12, 542-552.

Staley, D. O., 1960: Evaluation of potential vorticity changes near the tropopause and the related vertical motions, vertical advection of vorticity, and transfer of radioactive debris from stratosphere to troposphere. J. Meteor. 17, 591-620.

THEORIES OF FRONTOGENESIS

Lecturer: Dr. N. LaSeur Notes by: R. Smith

Date: June 24, 1974 J. Price

I. Introduction

In addition to the descriptive work on the structure of surface- (Type I) and upper-level (Type II) fronts, there has been some attempt, notably by Sawyer (1956) and Hoskins (1971, 1972) to construct simple mathematical models of these processes. This lecture gives a brief account of the results of the two simplest models of Hoskins (1971).

II. The Models

Hoskins' simplest model is a Boussinesq, rotating, inviscid fluid model bounded by rigid surfaces at $z = 0$ and $z = H$, where H is a potential density scale height, 8 km, and z is a function of pressure. The fluid extends to infinity in the horizontal, and the long front direction is parallel to y. The initial potential temperature field is given by:

$$\theta(x,z,0) = Cz + \frac{2\Delta\theta}{\pi} \tan^{-1} x/L_o$$

where C is a constant stability parameter = $2\Delta\theta/H$,

$\Delta\theta = 12°C$

$L_o >$ internal radius of deformation ~ 800 km

L_o, the initial length scale of the temperature field in the cross front direction, is chosen to be large enough to make the associated thermal wind negligible. The response of this system to an imposed horizontal deformation field

$$u = -\alpha x \quad , \quad v = \alpha y$$

is then considered.

The deformation field compresses the horizontal temperature field, reducing its length scale L according to:

$$L = L_0 \exp\left(-\int_0^t \alpha \, dt\right)$$

This, in turn, increases the horizontal gradients of hydrostatic pressure. The fluid particles initially respond by moving down the pressure gradient (i.e., the ageostrophic response). Eventually, they are turned by the Coriolis force in the direction paralled to the isobars. The final cross-front displacement of a fluid particle is simply proportional to the imposed pressure gradient at a given level. In this analysis, the assumption of cross front geostrophy is crucial, for without it the response of the fluid particles would be oscillatory and much more difficult to analyze.

As the process continues, the potential temperature field is distorted further due to advection both by the imposed deformation field and ageostrophic displacements. There is, in fact, a "snowballing" effect in which each increment of potential temperature advection sharpens the gradients and increases the sensitivity of the system to the succeeding increment of deformation. Near a solid boundary this can produce a discontinuity in finite time.

III. The Results

For the case of a single rotating stratified fluid adjacent to a horizontal rigid boundary, Hoskins finds isotherm and isotach patterns qualitatively similar to those of a surface front (Fig. 1). The calculated front has moved about 400 km to the warm side of its initial position and is strongly tilted, less concentrated with altitude, and has strong cyclonic shear across it.

In general, there is a direct circulation (i.e., cold air sinking, warm air rising) in agreement with observations of cloudiness. Near the surface, there is a region where the Richardson number, calculated with geostrophic assumptions, is small, suggesting intense local turbulence.

Hoskins briefly discusses the effects of latent heat release and surface friction. Latent heat release serves to enhance frontogenesis by providing bouyant lift to the already rising warm air, thus increasing the vertical velocity on the cyclonic side of the front. Ekman boundary layer flow is convergent at low levels on the cyclonic side of the front and is frontogenetic. However, the associated divergence at higher levels is frontolytic. The net effect of surface friction is therefore not clear.

In an attempt to study the upper-level hyperbaroclinic zone, Hoskins has used a two-fluid system with a "stratosphere" having a potential vorticity nine times that of the "troposphere". In response to the applied deformation field, both surface-and upper-level frontogenesis occurs. The tropopause, not being as rigid as the ground surface, starts to kink and draw down (Fig. 2), while a wind maximum develops

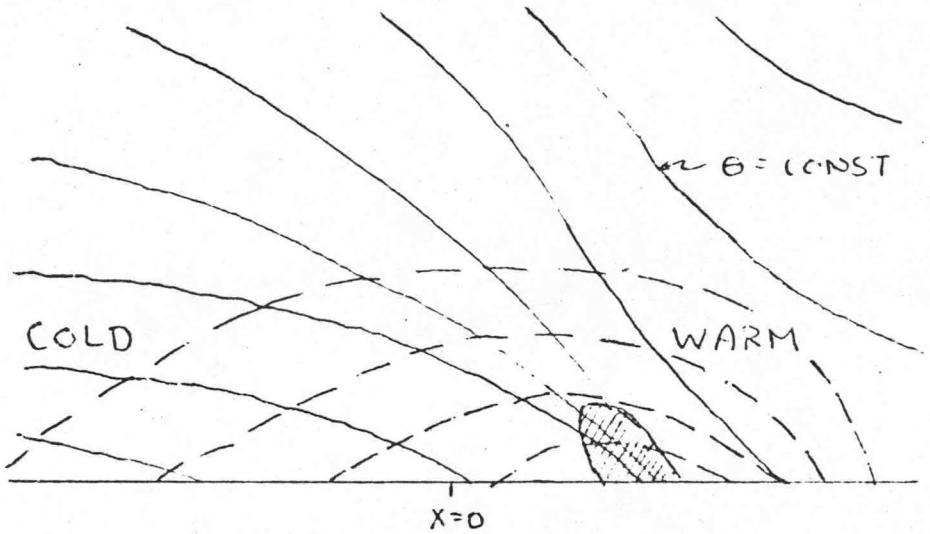

Fig. 1. Single fluid model from Hoskins (1971). Dashed lines are lines of constant along-front velocity. Hatched region has low Richardson number.

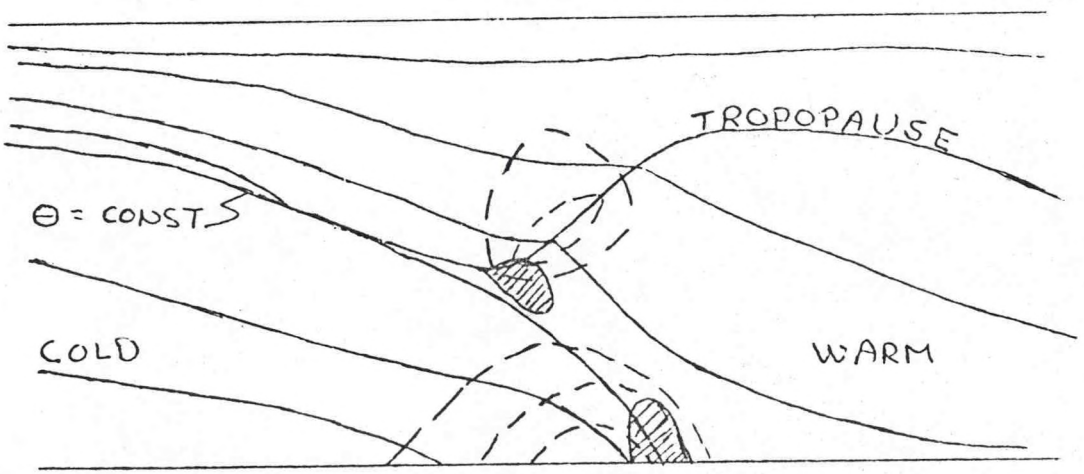

Fig. 2. Two fluid model from Hoskins (1971). Dashed lines are contours of equal along-front velocity. Low Richardson number regions are hatched.

near the tropopause. The general pattern of circulation is direct everywhere but in the extruded stratospheric air. This agrees with the findings of Reed and Sanders (1953), who stressed the indirect circulation observed in the hyperbaroclinic zone composed of stratospheric air. In this case, two regions of low Richardson number were found; one at the surface, as before, and one at the tip of the stratospheric intrusion.

Hoskins' models are in surprisingly good agreement with observations, but there are still discrepancies. It is questionable whether the imposed deformation field corresponds to conditions in the atmosphere described in case studies. The penetration of stratospheric air and the strength of the wind maximum are both underestimated in the model. Removal of the Boussinesq approximation only partially solves the problem.

References

Hoskins, B. J., 1971: Atmospheric frontogenesis models--some solutions. Quart. J. Meteor. Soc., 97, 139-153.

_____, and F. P. Bretherton, 1972: Atmospheric frontogenesis models: mathematical formulation and solution. J. Atmos. Sci., 29, 11-37.

_____, 1972: Non-Boussinesq effects and further development in a model of upper tropospheric frontogenesis. Quart. J. Meteor. Soc., 98 532-541.

Reed, R. J., and F. Sanders, 1953: An investigation of the development of a mid-tropospheric frontal zone and its associated vorticity field. J. Meteor., 10, 338-349.

Sawyer, J. S., 1956: The vertical circulation at meteorological fronts and its relation to frontogenesis. Proc. R. Soc. A234, 348-362.

MIDDLE LATITUDE CONVECTIVE SYSTEMS —AN INTRODUCTION

Lecturer: Dr. N. LaSeur Notes by: M.S. Tracton

Date: June 25, 1974

I. Introduction

There is currently considerable interest among meterologists concerning the nature of middle latitude convective systems. The interest is motivated in part by the fact that significant weather in extra-tropical regions is often due to organized convection. As noted by Palmén and Newton (1969), a large percentage of the total annual precipitation in mid-latitudes is attributable to convective showers, and in many areas convection accounts for the greatest amount of weather-induced damage.[1] Mid-latitude convection is also of interest because it is perhaps the most obvious manifestation of the interaction between circulations of differing scales of motion. Significant convection is largely a consequence of the thermal structure and dynamical influence of the synoptic-scale system in which it is embedded. In turn, the convection presumably influences its larger-scale environment through the release of latent heat and vertical transports of various physical quantities.

This lecture is the first of a series which concern organized convective systems in middle latitudes.[2] In these presentations,

---

[1] According to Sanders (1971), convective storms kill more people in the United States and result in greater financial loss than do extra-tropical storms and tropical cyclones.

[2] The presentations begin with the synoptic-scale conditions necessary for the development and maintenance of organized convection, and

emphasis is placed upon the descriptive aspects of the structure and behavior of the intense convection associated with synoptic disturbances over the United States. Such convection is typically organized into quasi-linear patterns of intense cells (e.g., pre-frontal squall lines) and should be distinguished from the less organized and less intense "air mass" convection associated predominantly with surface heating.

The characteristic dimensions of organized convective systems (i.e., the characteristic scale of the associated wind, pressure, and thermal patterns) are:

Height $\sim$ 10 km.

Length $\sim$ 100 km.

Width $\sim$ 10-100 km.

Systems with such dimensions, commonly referred to as mesoscale systems, occupy the middle ground in the heirarchy of scales between individual convective clouds and synoptic-scale disturbances.

A fundamental point that must be continually stressed is the concept of scale interaction and interdependence. Systems of one scale

---

proceed down the heirarchy of scales with discussion of the descriptive aspects of systems on each scale, and the pertinent interrelationships between systems of different scales.

There are a number of survey papers which synthesize and organize background material and work concerned with convective systems in middle latitudes. The principal reviews are cited in the bibliography.

It should be noted that the data and methods utilized to resolve and describe subsynoptic phenomena necessarily differ from those emphasized in standard analyses of synoptic-scale systems. For example, use is made of radar data, instrumented aircraft, special networks of surface and upper-air observations, and time-space conversions. Since these data methods of analysis are not a primary concern in this series of lectures, particular reference should be made to the reviews by Fujita, et. al., (1956) and Fujita (1963) for further information.

cannot be taken out of context from the temporal and spatial aspects of systems of other scales. A description of the formation, structure, and behavior of mesoscale systems should be presented in the framework of the synoptic-scale environment necessary for their development. The nature of individual cloud systems, in turn, should be considered from the perspective of the mesoscale features in which they are embedded. Finally, sub-scale cloud systems (i.e., funnel scale systems) should be considered in terms of various aspects of the cloud-scale systems favorable to their existence. Thus, even the smallest and most intense of all weather systems, the tornado, should be viewed not as a random phenomenon, but rather the ultimate consequence of complex temporal and spatial interrelationships between systems of all scales.

II. The Synoptic-Scale Setting

The sounding type which most commonly precedes significant outbreaks of convection is shown in Fig. 1. The structure of the sounding is that of a low-level moist layer capped by an inversion with much drier air above. Considering the overall depth of the troposphere, the sounding is characterized by the presence of both conditional and convective instability. As in the usage of Palmén and Newton (1969), an air mass which is both conditionally and convectively unstable ($\gamma > \gamma_m$ and $\frac{\partial \sigma_w}{\partial z} < 0$, respectively) is referred to as potentially unstable.

The Great Plains of the United States, as a result of a unique combination of geography and orography, is a region particularly susceptible to the generation of potential instability. The Gulf of Mexico to the south and elevated desert regions to the southwest provide the necessary ingredients for the creation of a low-level moist layer

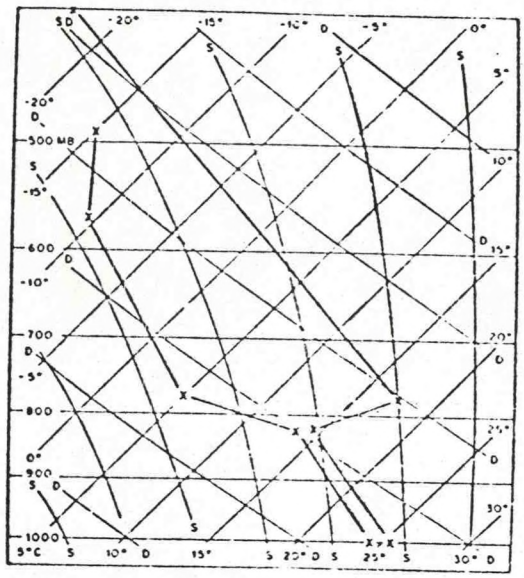

FIG. 1. Mean temperature (right hand curve) and dewpoint (left) shortly before the occurrence of tornadoes, after Fawbush and Miller (1953).

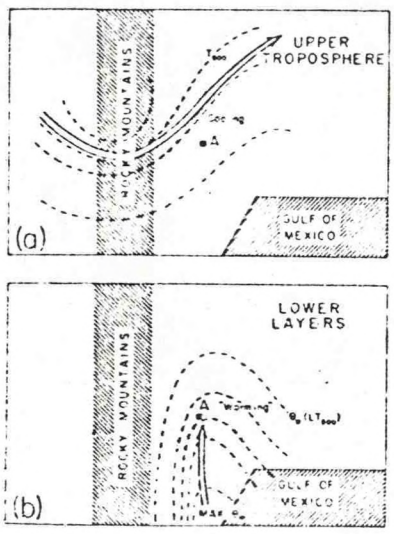

FIG. 2. Schematic illustration of processes in formation of a potentially unstable air mass. In (a) and (b), arrows are axes of high tropospheric and low-level jets. In (a), isolines of wet bulb potential temperature are indicated (from Newton, 1963).

overlain by much drier air a few thousand feet above the surface. The essential features of the synoptic conditions favorable for the development of the instability are summarized in Fig. 2. Increasing low-level southerly flow ahead of a cold trough approaching from the west advects warm moist air northward from the Gulf. Largely as a consequence of orographic features, the southerly flow is not a broad uniform current, but rather, a pronounced low-level wind maximum. As a result, a pronounced tongue of warm moist air at low levels is produced. Aloft, the advection of drier and cooler air from the southwest by the mid-to upper- tropospheric jet stream provides the additional requirements for generation of instability. It should be noted here that the presence of the inversion above the moist layer (Fig. 1.) plays an important role in the degree of instability which is produced (Fulks, 1951). The inversion effectively prevents deep convective overturning so that a progressive increase of instability can occur in response to the differential thermal and moisture advections just described.

A high degree of potential instability is a necessary but not a sufficient condition for the occurrence of significant convection: a mechanism for releasing the instability is required as well. That "triggering mechanism" is the upward vertical motion connected with the mid- to upper- troposphere jet stream and associated pattern of positive vorticity advection. Cold frontal lifting and surface heating may in some instances also initiate the convection.

Note that although vertical wind shear (associated here with bands of strong winds in lower and upper levels veering with height) and dry air aloft might <u>a priori</u> be considered inhibiting factors in the growth

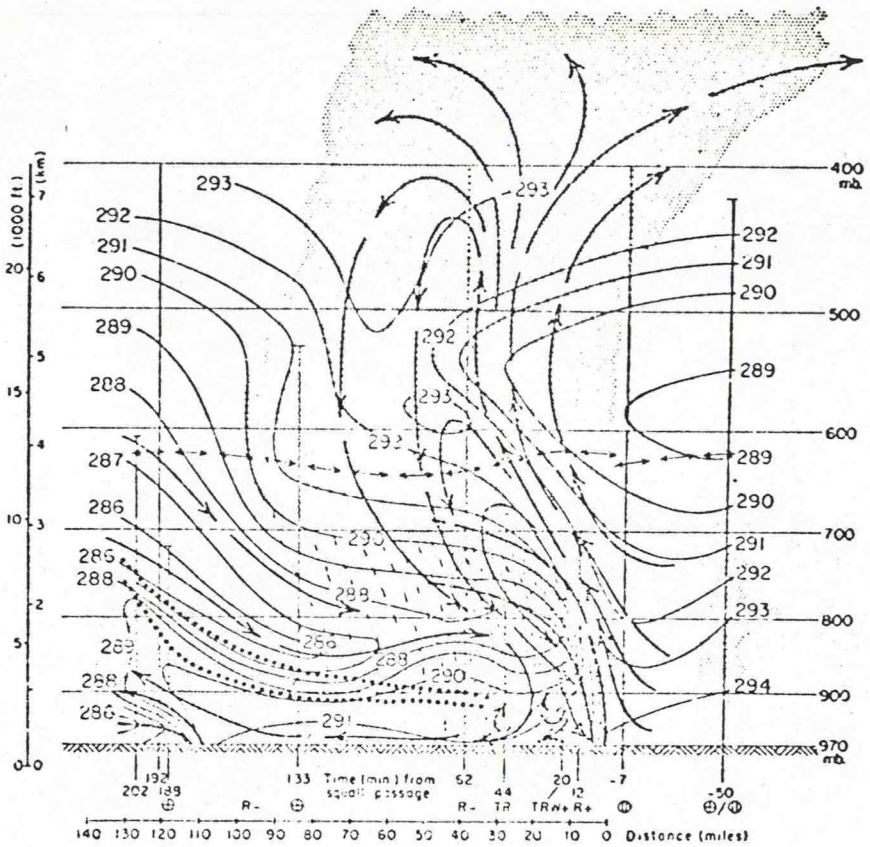

FIG. 3. Time section through a squall line passing over Ohio 0730 - 1139 CST 29 May 1947. Surfaces of stable layers, heavy lines (polar front at left); dotted lines are boundaries of stable layer in squall sector with relatively dry air above it; isopleths of σ_w, thin lines. Arrows showing circulation are schematic (After Newton, and Newton, 1959).

of convective cells, the foregoing discussion indicates that they are, in fact, necessary for the occurrence of intense convection.

III. Introduction to the Structure of Mesoscale Systems

The most characteristic mesoscale system is the pre-frontal squall line. Time sections illustrating the well-defined thermodynamic and streamline patterns in the mesoscale associated with such systems

are presented in Figs. 3 and 4. These time sections, produced from serial radiosonde ascents, can be converted to space sections normal to the squall line by assuming it is a quasi-steady system travelling at some constant speed.

Of particular interest in Figs. 3 and 4 is the evident lifting of warm moist air (high θ_e) from low levels over the squall front and the descent of cooler drier air (low θ_e) behind it. The sloping upward and downward flows take place simultaneously, although separated in space. Collectively these observations are our first indication of physical mechanisms cooperating to enhance convection. More specifically, because the rising moist air slopes in the vertical, the updraft is relieved of the weight of hydrometeors; consequently the buoyancy of the

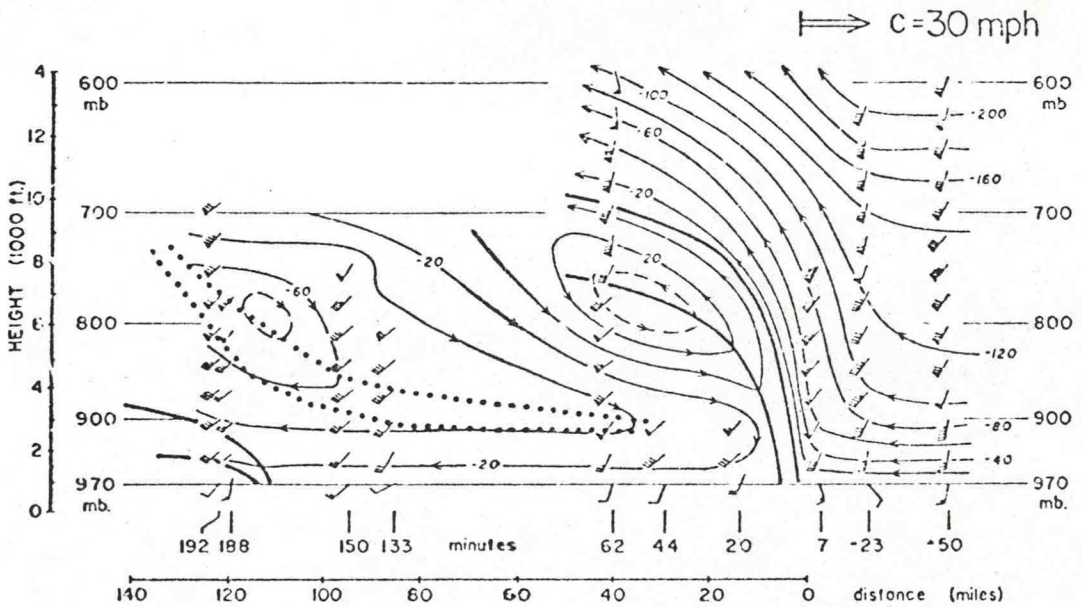

FIG. 4. Streamlines relative to moving squall front (heavy lines on right), on 29 May 1947 (after Newton, 1963).

updraft is enhanced. In addition, since the hydrometeors must fall into the descending drier air, the intensity of the downdraft is increased through evaporative cooling. The increased outflow at the surface then provides a mechanism for triggering further convection. Thus, dry air aloft and vertical wind shear can provide a self-cooperating mechanism for the development of intense convection that can continue to propagate as long as the proper kinematic and thermodynamic conditions are met.

References

Fawbush, E. J., and R. C. Miller, 1953: A method for forecasting hailstone size at the earth's surface. Bull. Am. Meteor. Soc., 34, 235-244.

Fujita, Tetsuya, 1963: Analytical mesometeorology: A review by Tetsuysa Fujita. In Meteorological Monographs, Vol. 5, No. 27, 77-125.

Fujita, T., H. Neustein, and M. Tepper, 1956: Mesoanalysis, an important scale in the analyses of weather data. USWB Research Paper No. 39, U.S. Dept. of Commerce.

Fulks, J. R., 1951: The instability line. In Compendium of Meteorology, (T. F. Malone, ed.) pp. 647-654, Amer. Meteor. Soc., Boston,

Ludlam, F. H., 1963: Severe local storms. In Meteorological Monographs, Vol. 5, No. 27, 1-30.

Newton, C. W., 1963: Dynamics of severe convective storms. In Meteorological Monographs, Vol. 5, No. 27, 33-58.

Newton, C. W., 1967: Severe convective storms. Advances in Geophysics, 12, 257-398.

Newton, C. W., and H. R. Newton, 1959: Dynamical interactions between large convective clouds and environment with vertical shear. J. Meteor., 16, 483-496.

Palmén, E., and C. W. Newton, 1969: Atmospheric Circulation Systems, Academic Press, New York.

Sanders, J., 1971: Toward defining human needs: How does the atmosphere hurt us. Bull. Amer. Meteor. Soc., 50, 446-449.

MESOSCALE ANALYSIS OF SEVERE CONVECTIVE STORMS

Lecturer: Dr. N. LaSeur Notes by: L.W. Uccellini

Date: June 26, 1974 M. Wheldon

I. Introduction

The techniques of mesoanalysis were developed, principally through the efforts of Dr. Tetsuya Fujita, to make maximum use of all available surface data in describing the lifetime of organized convective storm systems and their effects upon surface wind, temperature, and pressure fields.

The most important aspect of the analysis technique is the transformation of data from time series to spatial form. The process begins with the preparation of station time sections for temperature, pressure, winds, clouds, and rainfall. The velocity of the system itself is then determined, either through the use of radar or isochrone analyses. Assuming that changes in the system are small for a short period of time, tendencies in the time section are converted to gradients in space. For example, if the maps are analyzed every hour, data from up to one-half hour prior to and one-half hour after map time could be taken from the time section and placed up or downstream from the station at a distance determined by the rate of movement of the system. This transformation has the effect of filling the gaps between reporting stations and thus converting the analysis to the mesoscale.

The data from Fujita's analyses was derived from many sources. Fujita (1955) utilized hourly data from Weather Bureau reporting stations, autographic stations (including nearly 200 accelerated barograph traces maintained in the Midwest), and the climatic rainfall network.

Fujita and Brown (1958) restricted the data sources to the hourly Weather Bureau station reports, thereby determining that this type of analysis is possible within a regular network.

This lecture deals with the results of this analysis technique as applied to convective storms by Fujita (1955) and Fujita and Brown (1958). A model of the evolution of the mesosystems attending organized convective storms is included along with alternatives to this model. The debate over "pressure jump lines", which resulted from this and Tepper's work,(1950) is also discussed.

II. Lecture

Fig. 1 illustrates the effects of a mature convective storm upon surface pressure, temperature, and wind fields. The schematic represents a summary of many case studies, seven of which are presented in Fujita (1955) and Fujita and Brown (1958).

The organized convective storm systems in these studies were shown to have the following distinguishable features:

1) Shallow pool of cold air located at the surface directly beneath the storm cloud.

   As the drier downdraft air is incorporated into the thunderstorm, water droplets evaporate into it, resulting in much cooler air within the downdraft area. The cooling process acts to accelerate the downdraft through buoyancy forces, resulting in a shallow mass of cold air diverging at the surface. The leading edge of this air is known as the meso-cold front, and temperatures may fall as much as 25-30° with its passage.

2) Pressure surge line

   Within the diverging cold air mass beneath the cloud, a meso-high pressure system rapidly develops. This excess pressure is essentially a hydrostatic reflection of the denser rain-cooled air. The rapidly diverging nature of this air mass results in a pressure surge line. Across this line the

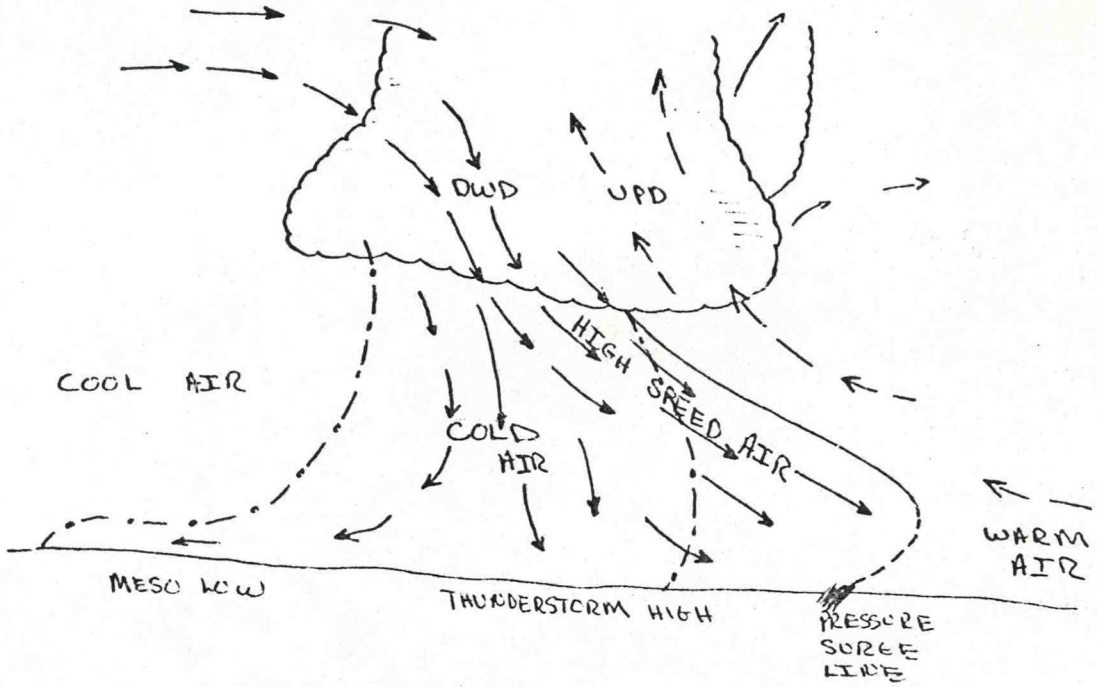

Fig. 1. Schematic section through a squall line thunderstorm and illustration of mesoscale systems as presented by Fujita (1955).

pressure tendency reaches the order of 1 mb/min with gradients of 1 mb/km. The pressure surge line does not necessarily coincide with the meso-cold front. In cases of frontally-induced squall lines, the pressure surge line acts to distort the synoptic-scale frontal boundaries.

3) Gust front

The downdraft air usually originates in the middle troposphere where wind speeds are usually large. Thus, as this air descends, there is a transport of momentum downward to the surface. The leading edge of air is known as the gust front, which may or may not coincide with the pressure surge line or the meso-cold front.

4) Meso-low

As the thunderstorm develops, and after the formation of the meso-high, a meso-low forms behind the storm. This low was formerly called the "wake" low, but the terminology has since been discontinued.

The analyses reveal how convective storms and the characteristic meso-features evolve, translate, and interact with synoptic-scale features. Fujita and Brown (1958) presented a model of three distinct stages in the life of mesosystems attending convective storms (Fig. 2).

Stage 1: Formative Stage is characterized by the organization of the pressure surge line by the diverging surface wind field and by the first appearance of thunderstorms and rainfall.

Stage 2: Mature Stage is distinguished by the rapid expansion of the colder downdraft air and increase in the magnitude of the meso-high. A very distinct pressure surge line, windshift line, and a rapid decrease in the surface temperature are evident during this stage. A meso-low behind the system is also apparent. Strong surface winds are divergent within the high pressure area and convergent along the leading edge.

Stage 3: Dissipating Stage is characterized by the continuing areal expansion of the system and a marked decrease in the magnitude of the meso-high, ending with its disappearance. The meso-low is the dominant feature at this stage.

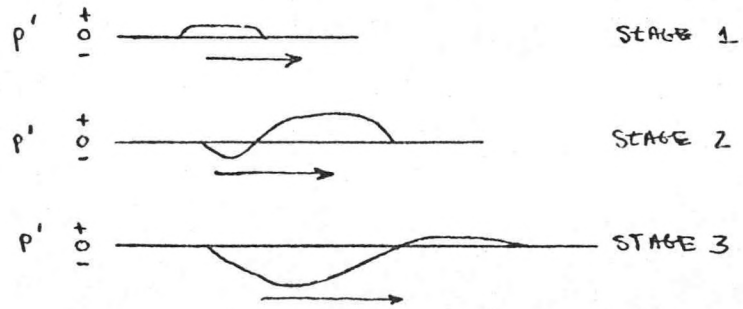

Fig. 2: Surface pressure perturbations (p') associated with organized convective storms as proposed by Fujita and Brown (1958).

These distinct pressure fields increase in magnitude and expand radially during the mature stage. This expansion, coupled with the movement of the cell and squall systems in different directions,

results in a complex translation pattern of the mesosystems with respect to both the cell and a ground-based observer. An example of this pattern is provided by Fig. 3 where the tracks of the squall line system, individual cells, pressure excess area, and pressure deficit area all differ.

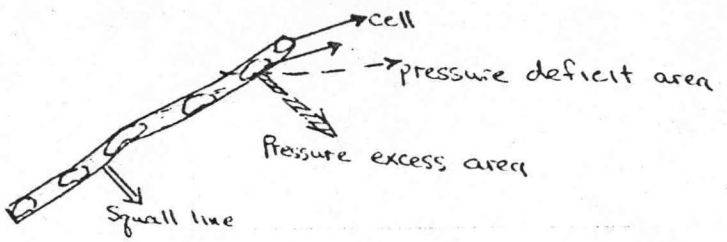

Fig. 3. Illustration of the different tracks of the squall system and attending meso-features that have been observed.

The interaction of the pressure surge line with the ambient wind and moisture fields was noted by Fujita as a possible mechanism for the development of new storm cells (Fig. 4). This idea has received renewed attention with recent satellite pictures revealing the development of new cells along the intersection of pressure surge lines with other mesosystems and synoptic-scale frontal boundaries (Purdom, 1973).

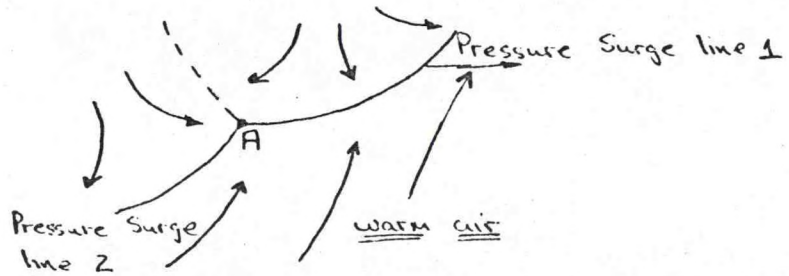

Fig. 4. The interaction of pressure surge lines with warm ambient wind flow. Point A is where convergence is strongest and where redevelopment has been observed.

III. An Alternative Model

Where the model developed by Fujita and Brown indicates one meso-low behind the storm system, more recent observations have revealed, and numerical models have confirmed, the common existence of meso-lows on either side of the high (Fujita, 1963; Fig. 5). Schlesinger (1973) has attributed the development of these meso-lows to heating of the atmosphere, either by latent heat release or by adiabatic warming resulting from compensating downward motion outside the cloud.

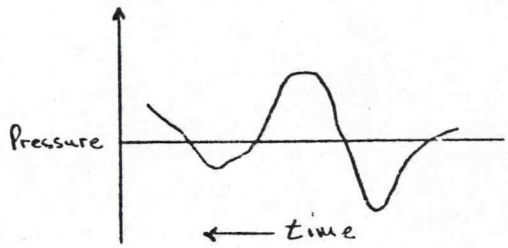

Fig. 5. Pressure trace in thunderstorm situations illustrating an alternative model with meso-lows on both sides of the meso-high.

IV. Pressure Surge vs. Pressure Jump

The completion and results of Fujita's initial mesoanalysis, provoked a heated debate over the coincidence of intense convective systems and characteristic surface pressure perturbations. The rapid increase in pressure observed before and during the lifetime of a storm has been incorporated into various models, between which causal sequences are completely reversed. Tepper (1950, 1954) proposed that a pressure jump, caused by an accelerating cold front (an analogy to a hydraulic jump was drawn) and traveling along an inversion, initiated squall-line development by lifting the lowest layers of a convectively unstable atmosphere.

Fujita insisted that no pressure jumps were apparent before development in his case studies, and that the pressure surge line was a result of the convective storms. Tepper did produce some examples of dry pressure jump lines which appeared to initiate squall lines. The general outcome of the debate, however, was that mesoscale pressure patterns resulting from convection are observed more frequently, and convection can therefore be considered the more probable cause.

Recent case studies indicate that gravity waves may indeed play a role in initiating the development of convective storms (Matsumoto and Akiyama, 1969; Uccellini, 1973). Uccellini's analysis of a convective storm system which underwent periodic intensification and redevelopment revealed a surface pressure perturbation field having the characteristics of gravity waves. The waves were tracked over a few cycles with thunderstorms occurring after the passage of the wave trough. These observations agreed with a theoretical model which implied that the maximum upward vertical motion lags the wave trough by 90°.

There are many questions concerning the nature of the waves which were left unresolved by Matsumoto's and Uccellini's analyses. For example, how are the waves generated? Or, how was the wave pattern maintained for such a long period of time, given that internal gravity waves of the observed frequency could well propagate energy vertically as well as horizontally? However, the fact that a cause-and-effect relationship between gravity waves and thunderstorm initiation has once again been observed may mean that the crucial question is not <u>if</u> this happens, but <u>how often</u> it occurs.

References

Fujita, T., 1955: Results of detailed synoptic studies of squall lines. Tellus, VIII, 405-436.

-----, 1963: Analytic mesometeorology: A review. Meteor. Monographs, 5, 77-128.

-----, and h. A. Brown, 1958: A study of mesosystems and their radar echoes. Bull. Amer. Met. Soc., 39, 538-554.

Matsumoto, S., and T. Akiyama, 1969: Some characteristic features of the heavy rainfalls observed over western Japan on July 9, 1967. Part 1: Mesoscale structure and short period pulsation. J. Meteor. Soc. Japan, 47, 255-266.

Purdom, J. F., 1973: Satellite imagery and the mesoscale convective forecast problem. Eighth Conf. on Severe Local Storms, Oct. 15-17, Denver, Colorado, 244-251.

Schlesinger, R. E., 1973: A numerical model of deep moist convection: Part 1: Comparative experiments for variable ambient moisture and wind shear. J. Atmos. Sci., 30, 835-856.

Tepper, M., 1950: A proposed mechanism of squall lines: The pressure jump line. J. Meteor., 7, 21-29.

-----, 1954: Pressure jump lines in midwestern United States, January-August 1951. Research Paper No. 37, U. S. Weather Bureau, Washington, D. C., 70 pp.

Uccellini, L. W., 1973: A case study of apparent gravity wave initiation of severe convective storms. Project Report 73-2 of Grant No. GI-31278X (National Science Foundation), University of Wisconsin, 70 pp.

INDIVIDUAL CLOUD SCALE MOTIONS

Lecturer: Dr. N. LaSeur Notes By: L.-F. Chang

Date: June 27, 1974 A. Friend

The concept of scale interaction and interdependence has led from the study of synoptic-scale motions to mesoscale and then to individual cloud-scale motions. This lecture focuses on the most intense individual cloud circulations and their interaction with systems on other scales.

The typical dimensions of an individual intense cloud are 5-10 mi. in diameter and up to 50,000 feet in height. Several of these intense clouds may occur around a single meso-high, sometimes called a "thunderstorm" high. Browning (1964) suggests the name SR storm (S for severe, R for right) for these intense clouds, because large hail and tornadic storms typically occur in their right rear quadrants. The evidence presented in this lecture shows that these storms, composed of coexisting up- and down-drafts, exist in a quasi-steady state for several hours.

Fujita (1958) described the development of intense clouds as typically occurring in convective areas ahead of the cold front in a synoptic-scale cyclone having a cyclonic vorticity field. In one case described by Fujita, two hours after the first intense convective cloud appeared, the intense clouds were aligned behind the gust front and pressure surge line in the meso-high. In a similar case, Browning (1965) describes a family of storms which developed in Oklahoma on 26 May 1963. These storms also organized along the leading edge of a meso-high. The positions of several of these storms at successive times are connected

with dashed lines in Fig. 1.

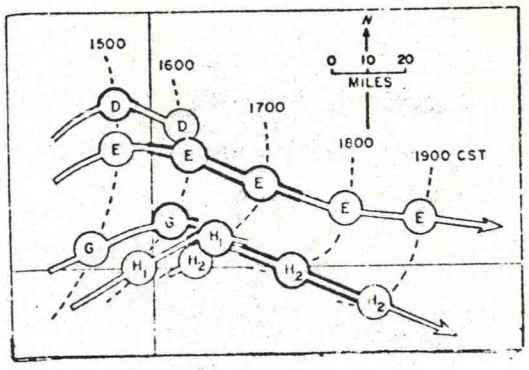

Fig. 1. Schematic diagram illustrating the organization and motion of storm cells on 26 May 1963, as observed by radar at Weather Radar Laboratory, Norman, at the intersection of the cross-lines. Tracks of storms in their SR Mature Stage are denoted by thick lines, and positions of storms at the same time are connected by dashed lines.

Fig. 1 also illustrates a prime characteristic of the SR storm, which is to travel to the right of its original path after reaching the SR stage. Associated with this deviation is cyclonic rotation on the scale of the cloud itself. Fujita (1965) found that the embedding of the meso-high in a synoptic-scale cyclonic circulation is a favorable condition for the development of the rotation of individual cloud cells. Fujita (1958 and 1965) also found that clouds deviate about 25° to the right of the mean flow as soon as cloud-scale cyclonic rotation develops, and that these clouds return to the original direction of motion when rotation stops.

Fujita and Grandoso (1968) examined a case where an initial echo split into two separate echoes (see Fig. 2). One echo deviated 20° to the right of the original path, and the other deviated over 30° to the left of the path. The evidence presented by Fujita and Grandoso for this case suggests that the echo deviating to the left has anticyclonic rotation, and that the echo deviating to the right has cyclonic rotation. It also appears that these two storms move with different translational speeds. The occurrence of anticyclonic rotation of an intense cloud,

however, needs to be verified by better observations using Doppler radar.

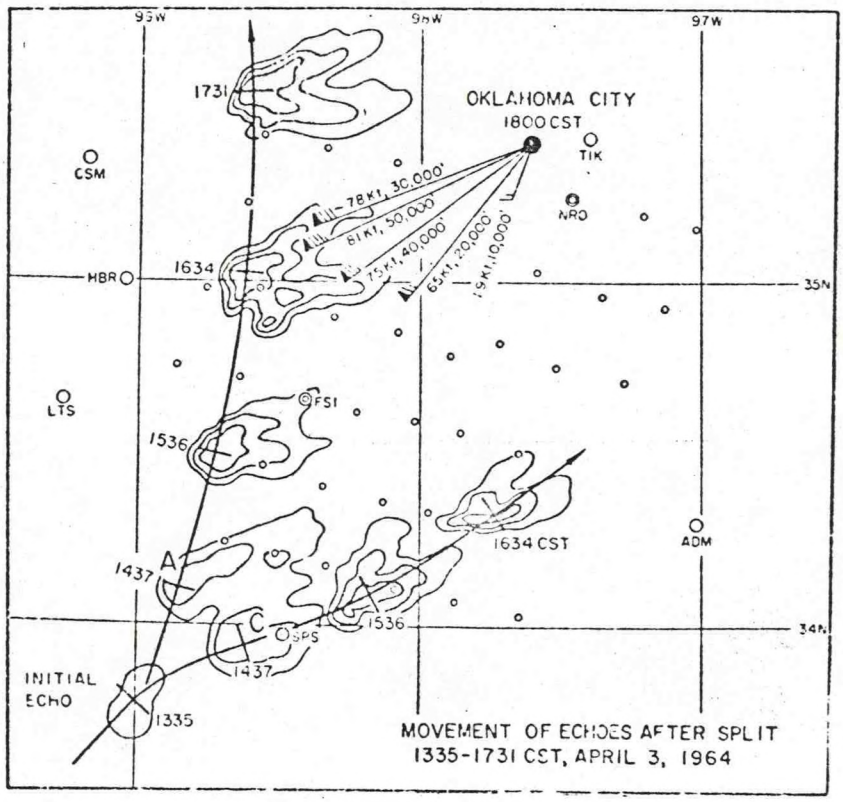

Fig. 2. Hourly positions and features of a split-echo couplet of 3 April 1964. Similar split echoes were observed on 23 April 1964.

Attempts to explain the deviation of the SR cloud motion from the mean flow are based on an analogy to a cylindrical object embedded in a fluid. Newton and Newton (1959) proposed a model in which strong vertical shear induces a large vertical hydrodynamic pressure gradient near the edge of the cloud. This gradient favors a new updraft on the right flank of the cylindrical cloud. In contrast, Fujita (1965) explains the right-veering of the storms in terms of the "Magnus" force, which tends to pull the central core circulation in the direction perpendicular

to the general flow. This force is expressed by $F = \rho u \Gamma$ where F is the force toward the side of the highest resultant speed obtained by superimposing the rotational and translational speeds, ρ is the density of the environmental air, u is the speed of the environmental air, and Γ is the circulation around the rotating cylinder. Thus, if the circulation is cyclonic, F will be directed toward the right of the geostrophic wind, but if the circulation is anticyclonic, F will be directed toward the left (see Fig. 3). This explanation does allow for the existence of anticyclonic rotation in left-deviating storms, as described by Fujita and Grandoso (1968).

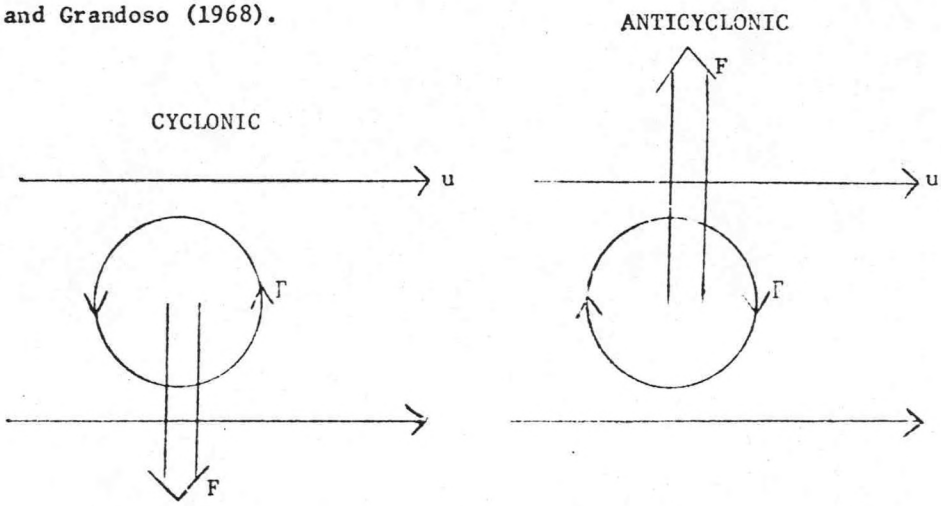

Fig. 3. Schematic illustration of the resultant Magnus force, F for cyclonic and anticyclonic-rotating cylinders imbedded in a geostrophic flow u.

The circulation within the severe right cloud storm is described by Browning (1964). Fig. 4 (Browning, 1964) depicts the environmental air flow relative to a SR storm. Fig. 4a shows the winds relative to the ground and 4b shows them relative to the storm. Fig. 4c shows a plan view of the up- and down-drafts within the storm. The updraft is

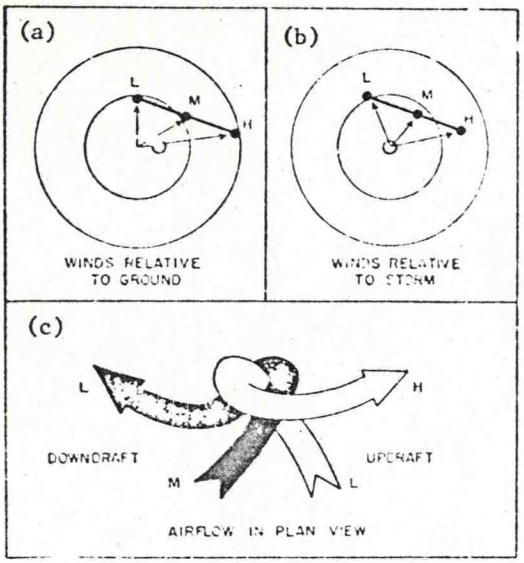

Fig. 4. Diagrams illustrating how the airflow within an SR storm is governed by the environmental wind field and its own direction of travel. Wind directions in the hodographs are represented as directions toward which the wind is blowing. In each case, the velocity of the wind is denoted by an open circle.

accelerated into the storm in lower levels from the right forward quadrant. After rising at speeds up to tens of meters per second and turning cyclonically within the updraft, the air leaves the updraft at high levels to become the anvil of the storm. The downdraft originates in middle levels, where the cold and dry air is situated. Further cooling of this air by evaporation of precipitation falling from the down shear edge of the updraft creates negative buoyancy, inducing a vigorous downdraft. The middle level air has a significant velocity component relative to the right flank of the storm. The downdraft turns cyclonically as it descends, leaving the storm at low levels from the left rear flank. Upon reaching the ground, the downdrafts diverge in all directions under the updraft and may actually enhance the updraft motion. The co-existing up- and down-drafts continuously provide the mechanism to gain kinetic energy not only from a conversion of potential energy,

but also directly from the kinetic energy of the relative horizontal inflow. This may explain the severeness of the SR storms.

Two features of the development of SR storms revealed by radar are the hook echo and the echo-free vault described by Browning (1965) and Browning and Donaldson (1963). The development of the hook echo is shown in Fig. 5. (Browning, 1965) for storm E on 26 May 1963. Development starts as a pendant to the rear of the storm, then grows and turns cyclonically relative to the storm, forming a hook. The entire process occurs in about 30 minutes. The echo-free vault region, as shown in Fig. 5, is interpreted as the core of the updraft. This region is filled with clouds composed of droplets too small to be detected by radar.

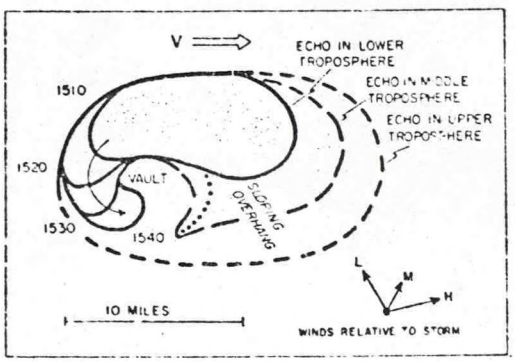

Fig. 5. Schematic diagram illustrating the development of the hook echo within Storm E, successive positions of the hook being shown at times 1510, 1520, 1530 and 1540 CST.

The distribution of precipitation at the surface has been related to the above features of the SR storm by Browning (1964, 1965). In Fig. 6 (Browning, 1964), it can be seen that relative to the motion of the storm, rain occurs on the left side and hail occurs predominantly in the right rear quadrant. The largest hail falls immediately behind the vault, decreasing in size to the rear of the storm.

Browning (1964) analyzes a situation where precipitation from a

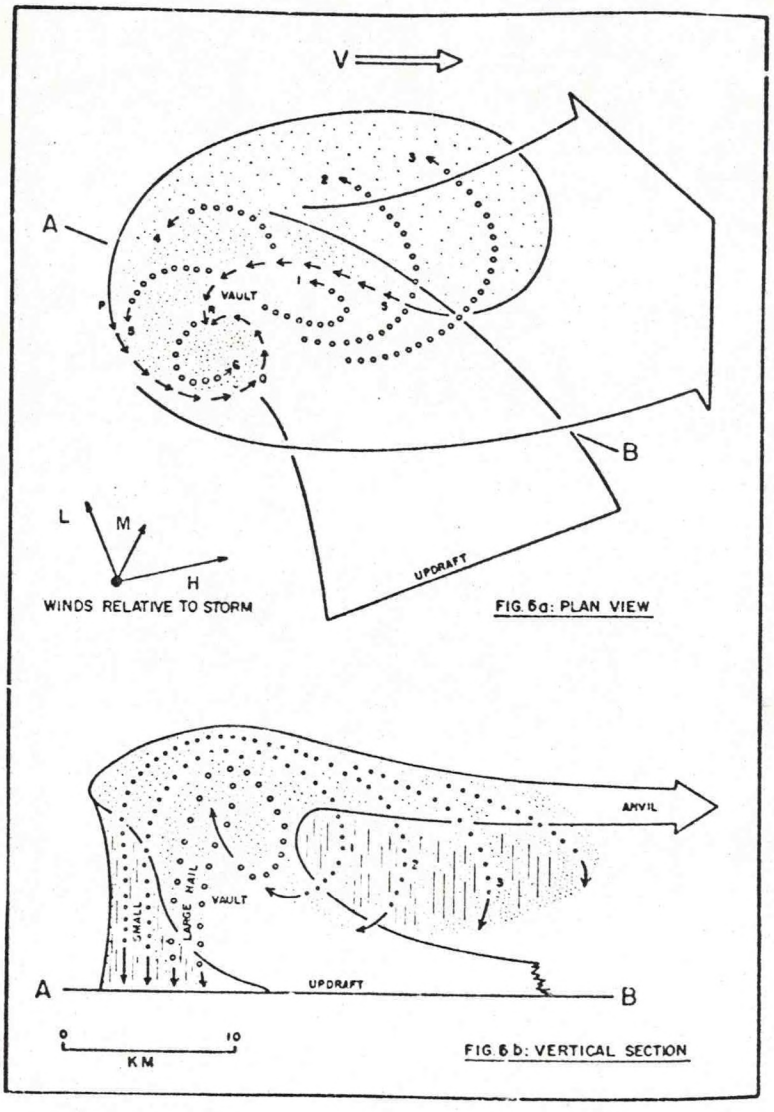

Fig. 6. Schematic horizontal (Fig. 6a) and vertical (Fig. 6b) sections qualitatively illustrating precipitation trajectories in different parts of an SR storm traveling at a velocity V. In both figures the extent of the updraft is represented by solid curves and precipitation trajectories are represented by dotted curves. In the horizontal section the extents of rain and hail close to the surface are represented by light and heavy shading, respectively, and the arrows around PQRS indicate the direction of motion of protuberances on the edge of the low-level radar echo. The vertical section along AB is oriented in the direction of the mean wind shear, into which the updraft is inclined at low and medium levels. In the vertical section the presence of downdrafts with strong normal components of motion is indicated by broken vertical hatching. On the downshear side of the updraft (right side of page) these components are directed into the page; beneath the updraft, on its upshear side, they are directed out of the page.

neighboring storm is drawn into the updraft of a well-developed vault. This case indicates that as new cells form to the right of old cells, they may tend to cut off the low level in-flow to the old cells. This case alsc verifies the sloping updraft required for the cooperative up- and down-draft system that sustains the SR storm.

The SR storm may also spawn one or more funnels and one or more may become tornadoes.

References

Browning, K. A., 1964: Airflow and precipitation trajectories within severe local storms which travel to the right of the winds. J. Atmos. Sci., 21, 634-639.

_____, 1965: The evolution of tornadic storms. J. Atmos. Sci, 22, 664-668.

_____, and R. J. Donaldson, Jr., 1963: Airflow and structure of a tornadic storm. J. Atmos. Sci., 20, 533-545.

Fujita, F., 1958: Mesoanalysis of the Illinois tornadoes of 9 April 1953. J. Meteor., 15, 288-296.

_____, 1965: Formation and steering mechanisms of tornado cyclones and associated hook echoes. Mon. Wea. Rev., 93, 67-78.

_____, and H. Grandoso, 1968: Split of a thunderstorm into anticyclonic and cyclonic storms and their motion as determined from numerical model experiments. J. Atmos. Sci., 25, 416-439.

Newton, C. W., and H. R. Newton, 1959: Dynamical interactions between large convective clouds and environment with vertical shear. J. Meteor., 16, 483-496.

OBSERVATIONAL ASPECTS OF MOTION ON THE CLOUD AND FUNNEL SCALES

Lecturer: Dr. N. LaSeur Notes by: T. Curtin

Date: July 1, 1974 K.-Y. Fung

This lecture focuses on certain observed aspects of tornado-cyclone and funnel scales of motion. Through careful study of the characteristics of each successive downscale system, the generating and propagating mechanisms responsible for the observed motions can be inferred and studied further.

As has been previously noted, a mesoscale high embedded in a strong synoptic vorticity field characteristically produces the most intense convection. Associated with this convection are cumulonimbus clouds which move both to the right (cyclonic) and left (anticyclonic) relative to the moving convective system. The right-moving clouds have been observed more frequently, and have come to be known as "severe right" (SR) clouds. Certain properties of these tornado-cyclone clouds are observationally well documented by radar echoes, and may be best summarized by the following sketches in the x-y and x-z planes:

x-y plane:

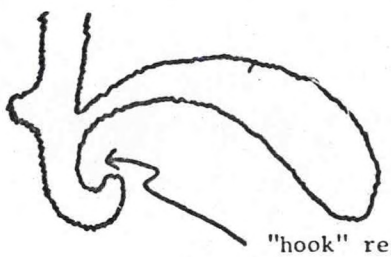

x-z plane:

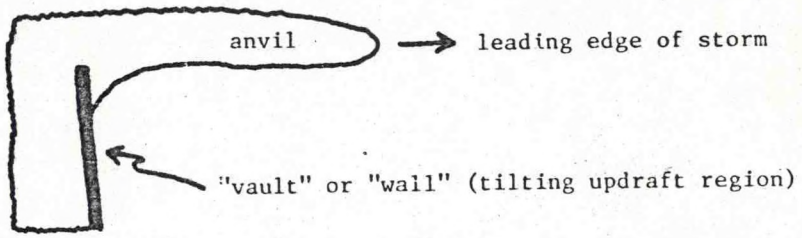

There is a characteristic 3-to 5-mb drop in pressure associated with tornado-cyclone clouds. The "hook" region is a mesoscale low accompanied by strong convergence with vertical velocities in the "vault" or "wall" zone, reaching tens of meters per second. Precipitation is usually observed beneath the leading "anvil". Occasional observations have verified a significant rotation of the cloud itself. More systematic documentation of this feature is expected to emerge from observations made with the use of Doppler radar.

Some of the more significant features of these cloud and funnel-scale systems can be examined through the study of detailed case studies of the following storms:

1. the Illinois tornadoes of 9 April 1953;
2. the Fargo tornado of 20 June 1957;
3. the Dallas tornado of 2 April 1957;
4. the Palm Sunday tornadoes of 11 April 1965.

1. The Illinois tornadoes of 9 April 1953 are illustrated in Figs. 1 - 3 (Fujita, 1958). Fig. 1 shows the typical protrusion emanating from an echo-free region, or "hook". The curvature of the tornado-related echo implies cyclonic rotation. Subsequently, a tornado funnel, spinning off at 40-50 mph, emerged from the right-hand side of the echo-free region.

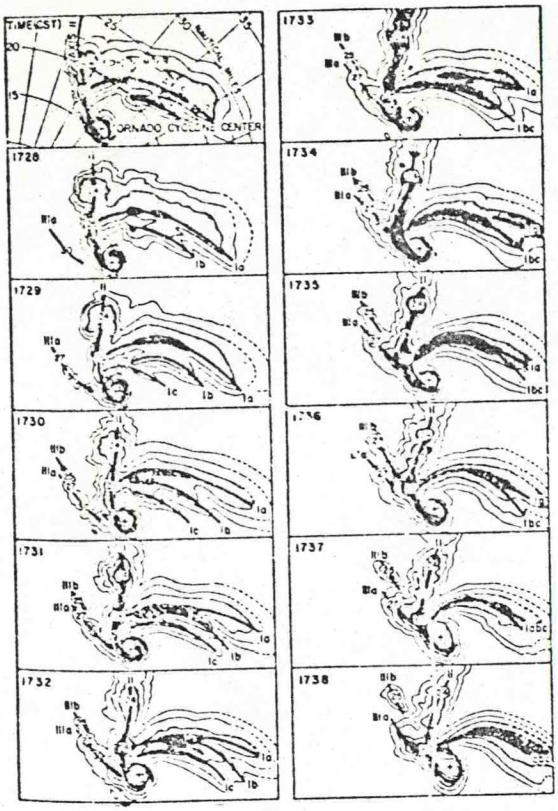

Fig. 1. Contour representation of tornado-related echo.

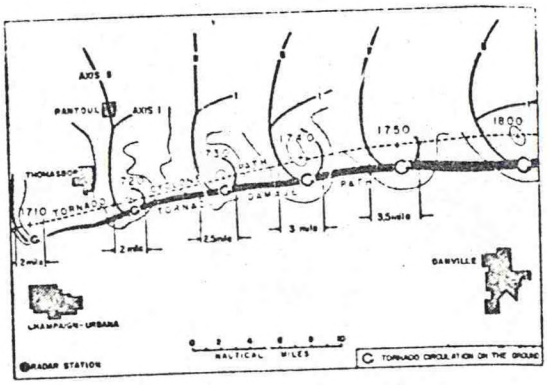

Fig. 2. Tornado-cyclone path fixed by Champaign radar and the tornado damage path surveyed by the Illinois State Water Survey.

Fig. 2 shows the path traversed by this funnel. The funnel emerged along an intensified ring of radar echo as can be seen in Fig. 3. This is the characteristic location of tornado-scale phenomena for this type of tornado-cyclone.

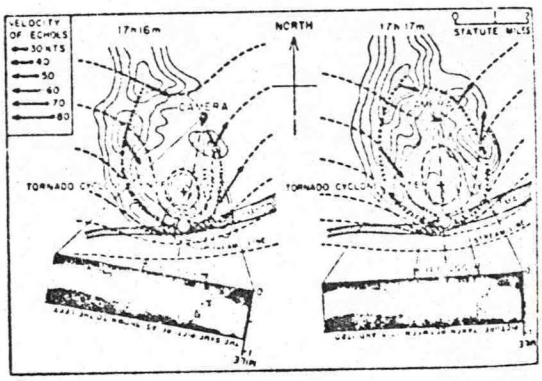

Fig. 3. Location and size of the surface tornado based upon the picture taken by Capt. J. H. Yancy.

2. The Fargo tornado of 20 June 1957 is illustrated in Figs. 4 - 7 (Fujita, 1960). Figs. 4a, 4b, and 4c show the well-defined annular ring of elevated pressure associated with this tornado-cyclone. Fujita attributes the embedded high in the overall mesoscale low to the hydrostatic weight of large amounts of condensed water. Fig. 5 shows the paths of five tornado funnels spawned by this system. The point of emergence is again to the right of the cloud, and the path is cyclonic relative to the cyclonically-rotating cloud. Ultimately, each cloud reaches the left hand side and then weakens.

Fujita has used two methods to estimate the wind speed associated with the funnel. In the first method, he assumes that the funnel wall is an isobaric surface and that the radius of curvature is the geometric radius of the funnel. The tangential component is then taken to be in cyclostrophic balance, that is:

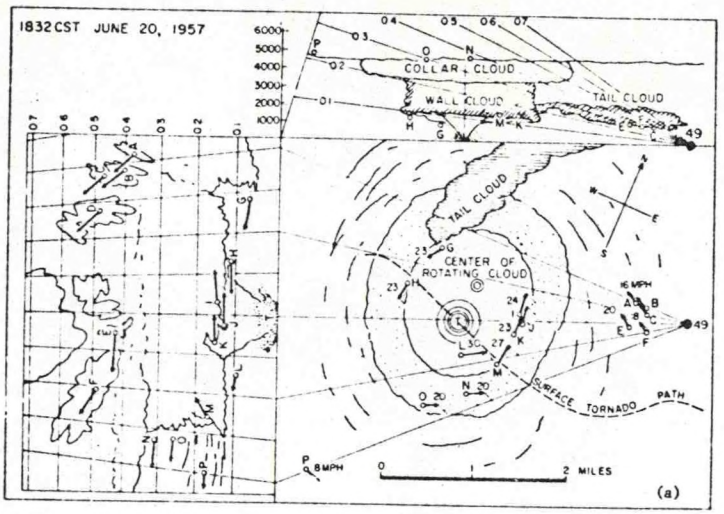

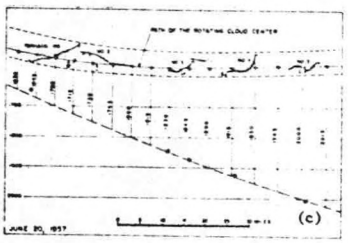

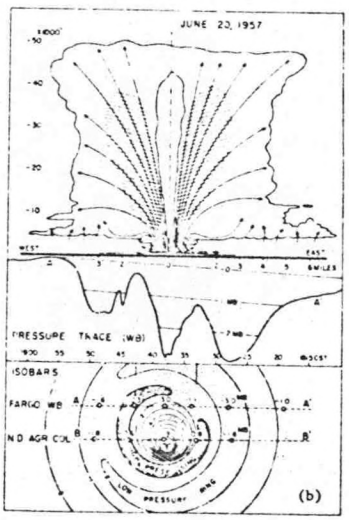

Fig. 4. (a) Determination of the rotational speed of the rotating cloud, (b) Relative position of the Fargo tornadoes and the center of the rotating cloud, (c) Pressure field beneath the rotating cloud.

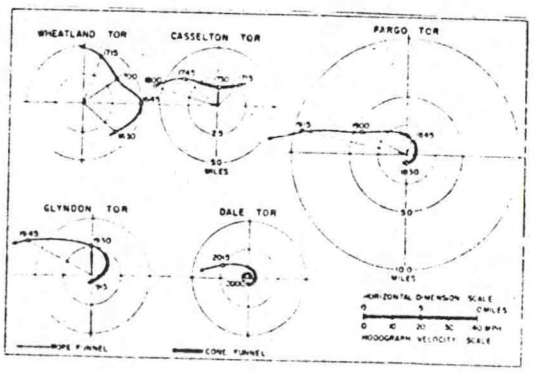

Fig. 5. Relative movement of the surface tornado center with respect to the center of the rotating cloud.

$$\frac{V_0^2}{R} = \frac{\partial \varphi}{\partial R} \qquad (1)$$

The second method is based on direct observation (photographic tracking with motion pictures) of identifiable moving objects or features. The results of calculations based on both methods are shown in Fig. 6. Due to the general level of uncertainty inherent in these calculations, the order of magnitudes, rather than the specific values, should be noted.

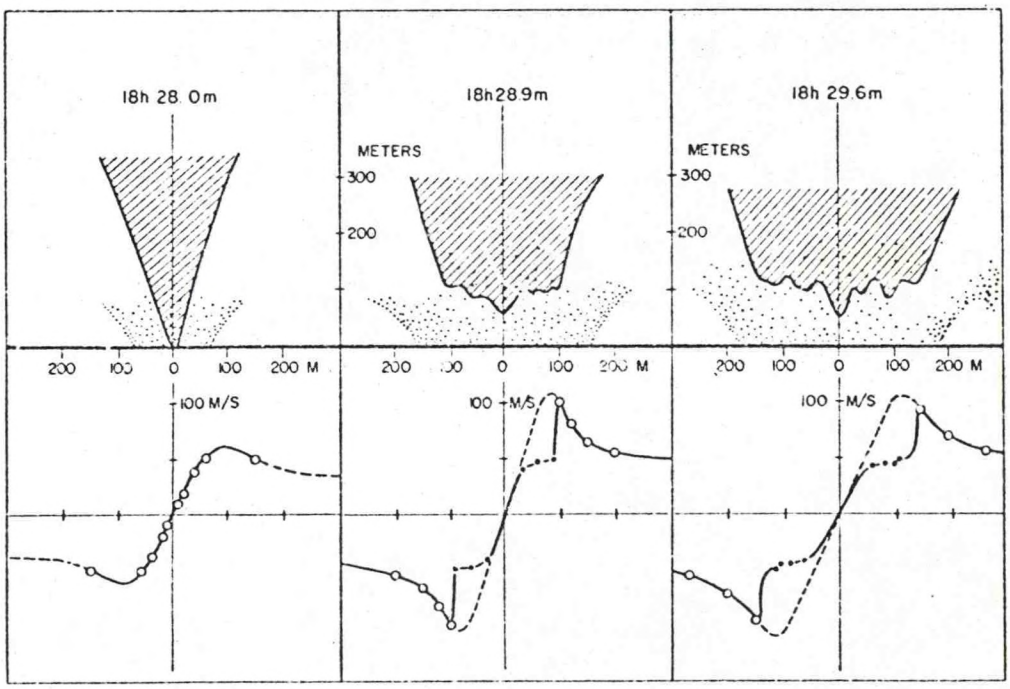

Fig. 6. Rotational speed of the funnel. Open and solid circles indicate the speed obtained by the two different methods described.

The maximum value of the tangential wind speed is about 100 meters per second, and the funnel diameter characteristically varies between 0 and

400 meters (although some funnels as wide as 1 mile have been observed). More details of the cloud characteristics are given in Fig. 7.

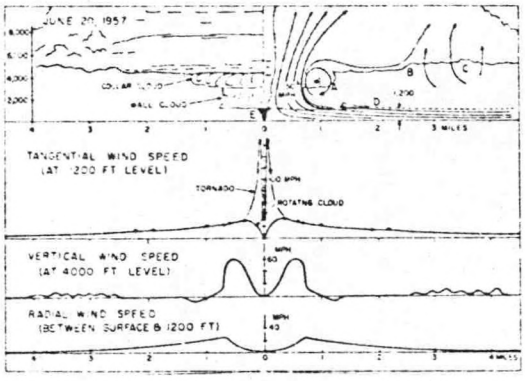

Fig. 7. Schematical diagram showing the wind distribution beneath the rotating cloud.

Such clouds typically move from west to east and have a lifetime of several hours. The five tornado funnels spawned by this cloud occurred quasi-periodically at about 45-minute intervals. Although the funnel path is cyclonic relative to the cloud trajectory, the path is not necessarily cyclonic relative to the ground.

3. The Dallas tornado of 2 April 1957 is illustrated in Figs. 8 - 11 (Hoecker, 1960, 1961). Fig. 8 schematizes the various types of elements used as air flow tracers. From the movement of solid debris particles and cloud and dust parcels, estimates of both the tangential and vertical wind components are made and these are given, respectively, in Figs. 9 and 10. The isotachs calculated indicate that the funnel did not extend to the ground, and as shown in the insert in Fig. 9, the vortex is of fairly small scale--on the order of trees and houses. The maximum tangential velocity is 175 mph, and the maximum vertical velocity, 150 mph. The suggestion is one of increasing upward vertical motion

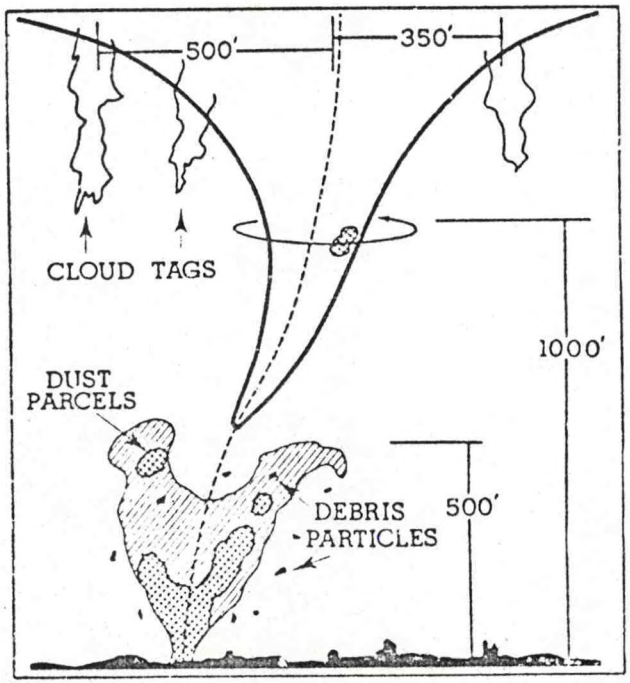

Fig. 8. The various types of elements used as air flow tracers in the wind speed measurements of the Dallas tornado of April 2, 1957.

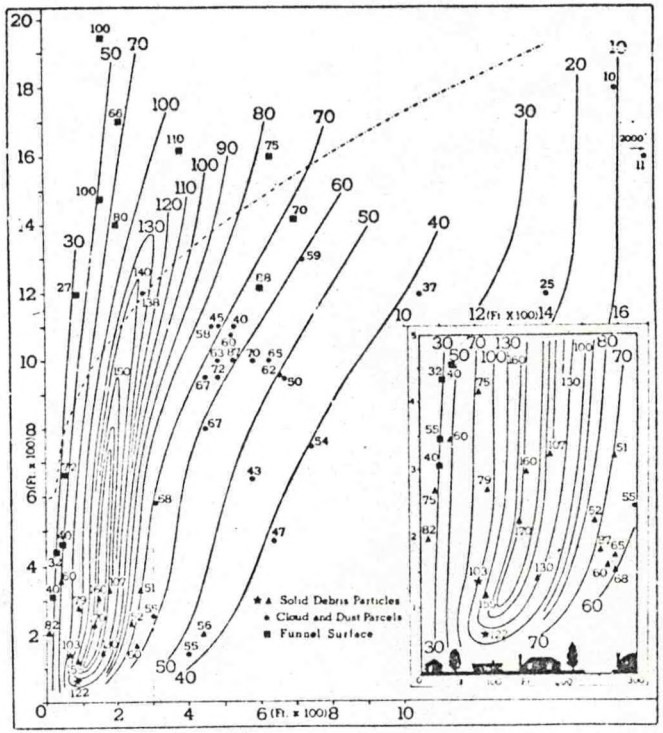

Fig. 9. Distribution of derived tangential speed from the center of the tornado to a radius of 2000 ft. and from near the ground to about 1800 ft. in elevation.

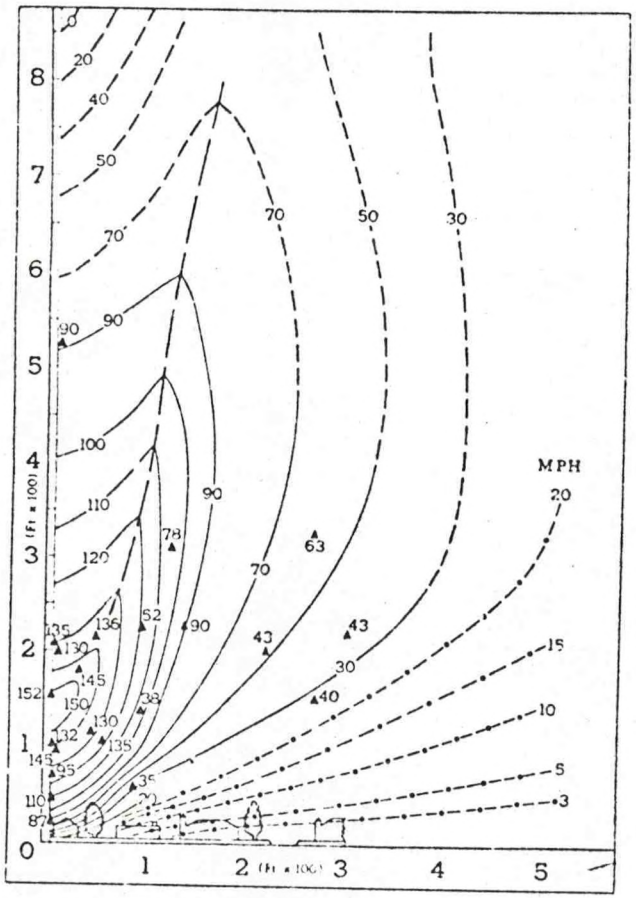

Fig. 10. Detailed version of distribution of upward speeds. Only the lower 900 ft. and the inner 500 ft. are shown.

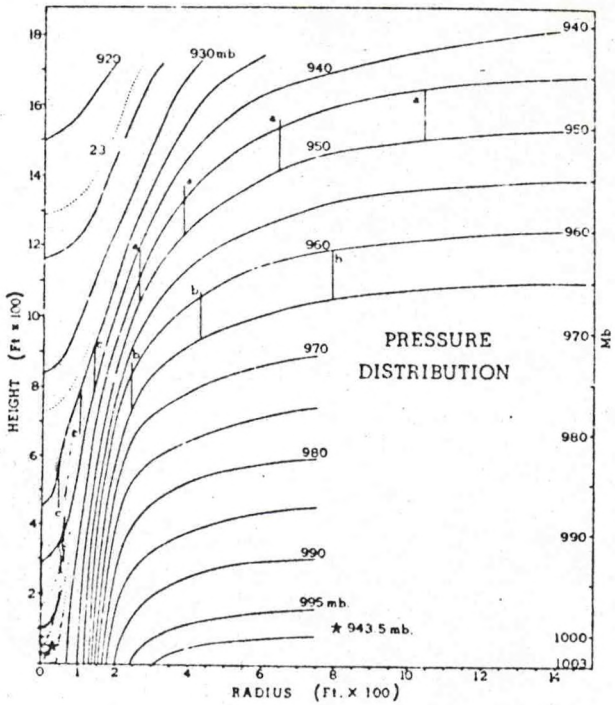

Fig. 11. The derived pressure field of the Dallas tornado in the vertical plane. Symmetry in the horizontal plane is assumed, giving pressure distribution in three dimensions. The derived central pressure at the ground is 943.5 mb, or 59.5 mb below the undisturbed pressure of 1003.0 mb.

close to the axis, with a spreading out at the top. Very little vertical velocity is observed along the surface of the funnel itself. Fig. 11 contains an additional interesting feature in the derived pressure field, which shows a 60-mb drop from the local environment to the center of the tornado. By tracing a particular inter-isobaric separation through the system, the resultant vertical acceleration can be inferred. The departure from hydrostatic equilibrium, indicated by a spreading apart of the isobars, implies a local downward acceleration (a contraction of isobars would imply a local upward acceleration).

4. The Palm Sunday tornadoes of 11 April 1965 are illustrated in Fig. 12 - 16. (Fujita, et. al., 1970). Fig. 12 shows an anemometer record registering a peak gust of 150 mph, a characteristic value.

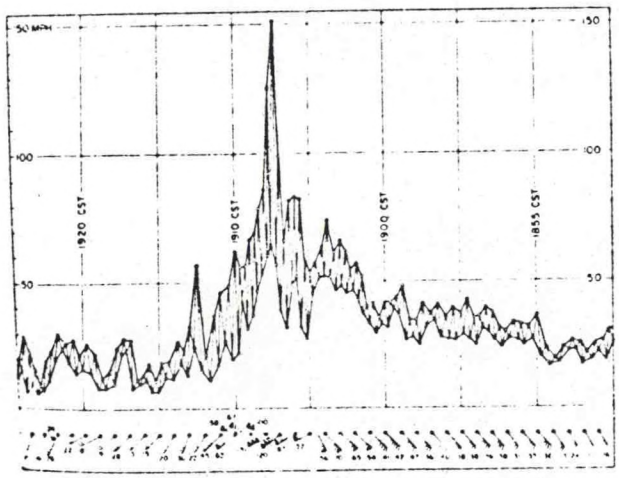

Fig. 12. Enlargement of the wind recorder trace. For the wind speed chart, both time and speed of all visible maximum and minimum values were read from the recorded trace and then connected with straight lines. At the same time, successive maximum and minimum values were separately joined to show the range in the variation of gusty winds. Wind velocities plotted at the bottom represent 1-min means of maximum values in miles per hour.

Also typical of this type of storm and shown in Figs. 13, 14, and 15, are the familiar "hook", "vault", or "eye"; funnel generation on the right side of the cloud; and cyclonic relative winds (maximum approaching 100 m/sec). After careful analysis of damage patterns, as well as streamline patterns impressed upon low-growing vegetation ("suction-marks"), Fujita delineated the fine structure inherent in the funnel wall.

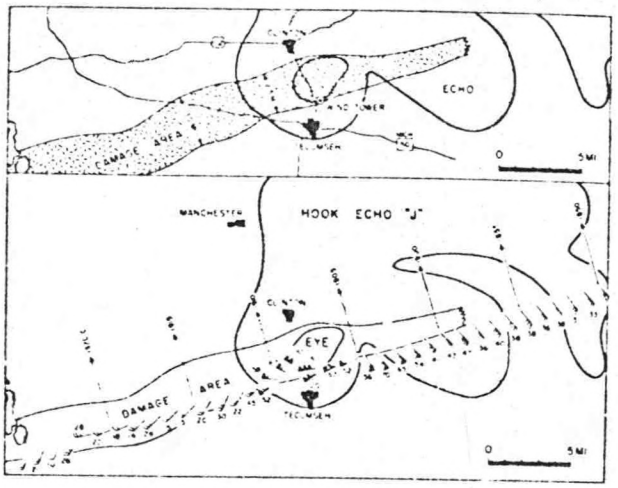

Fig. 13. Damage area in relation to the hook echo at the time of the highest recorded wind (upper chart) and to the space section of the mean maximum winds (lower chart).

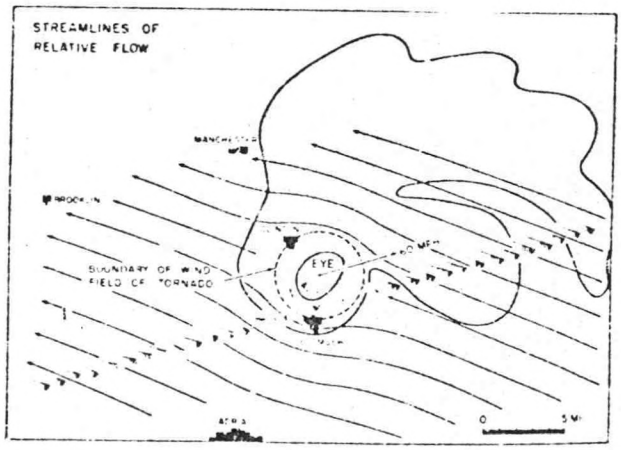

Fig. 14. Space section of relative winds obtained by subtracting 60 mi hr^{-1}, the translational velocity of the storm, from the 1-min means of maximum winds. Due to the rapid motion of the tornado cyclone, the relative winds computed tend to blow through the tornado-cyclone near the ground. Inside the tornado area, as indicated by the dashed circle, the relative winds are circulating around the tornado center.

Fig. 16 illustrates the change in shape of the tornado core as determined from the analysis of cycloidal suction marks. In addition, further concentrations of vorticity have been noted in regions of the wall itself, which Fujita has called "suction spots". An average of four "suction spots" are observed in the wall of a typical tornado. Fujita assumes that their translational speed is the same as that of the wall itself, and that a superposition of the translational and rotational speeds leads to the expected and observed cycloidal trajectory patterns.

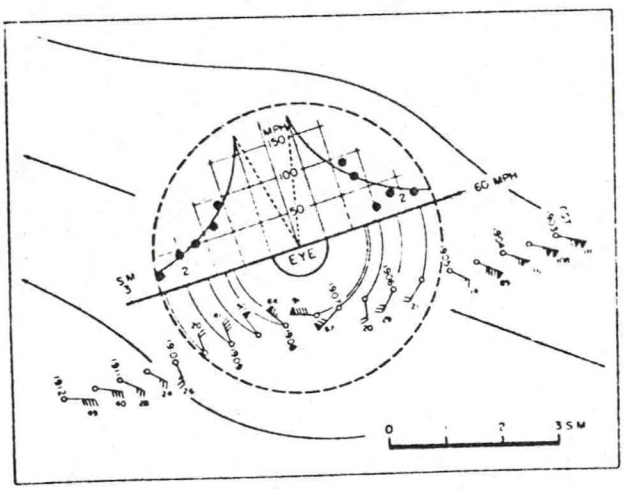

Fig. 15. Enlargement of the field of relative winds shown inside the dashed circle in Fig. 14. The area within the circle, 5 mi in diameter, is characterized by a tangential wind speed inversely proportional to the radius. From the widespread damage path, the radius of the circle of maximum wind is estimated to be about half a mile. The wind around this radius would be over 175 mi hr^{-1}.

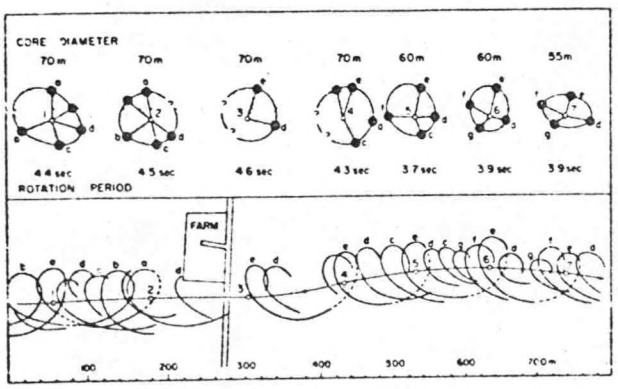

Fig. 16. Change in the shape of the tornado core as determined from the analysis of the cycloidal suction marks. Core diameter in meters, rotation periods, and funnel positions 1 through 7 are given in the upper part. Note that the rotational rate increased as the core diameter decreased, suggesting a conservation of angular momentum.

Laboratory studies have demonstrated that it is relatively easy to produce tornado-like motions. Whether these artifically-produced cyclones are mechanically analogous to those observed in nature is, however, an open question. To model the atmospheric generation processes, it is not necessary to find mechanisms that generate circulation, but rather to find mechanisms that concentrate circulation down the scale.

One simple model that has been proposed for tangential velocity on the funnel scale is the Rankine vortex, which has a tangential velocity distribution (and analogous surface pressure distribution) as follows:

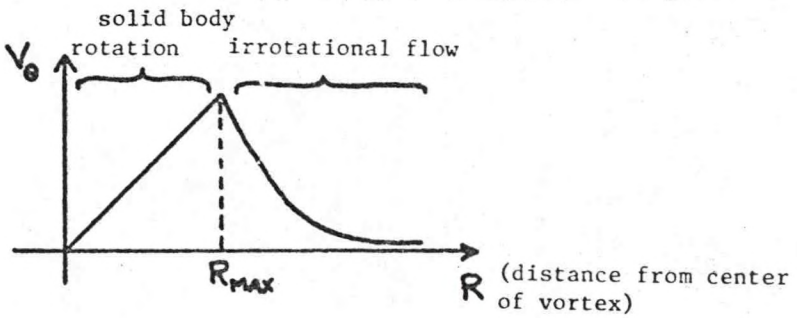

The pressure difference between the environment and the vortex center is given for cyclostrophic flow by:

$$p_\infty - p_0 = \rho V_{max}^2 \qquad (2)$$

The basic elements of the Rankine vortex model are solid body rotation ($V_\theta = \Omega r$) from r = 0 to $r = R_{max}$, and irrotational flow outside R_{max} (i.e., $V_\theta = \Omega R_{max}^2 / r$). From cyclostrophic balance ($\partial p / \partial r = \rho V_\theta^2 / r$), equation (2) is easily verified. In the Rankine model, circulation is conserved outside the region $r = R_{max}$.

The sense of rotation for geophysical vortices is variable, but a pattern which appears to be a function of scale has been observed. The following table summarizes the range of these observations:

Description	Sense of Rotation (% cyclonic)	Pressure Contrast (mb)	Velocity Maximum (m/sec)
dust devils	50	1-4	10-20
water spouts	70	36-100	60-100
tornadoes	100	50->100	70->100

Although 100% is given for the percentage of tornado rotation observed to be cyclonic, anticyclonic rotation is not impossible; as yet, it has not been documented. In conclusion, for scales of motion greater than dust devil scale, the intense vortices observed in the atmosphere are not random events; they are rather, downscale concentrations of vorticity whose net result is a preference in the sense of rotation.

References

Fujita, T. T., 1958: Mesoanalysis of the Illinois tornadoes of 9 April 1953. J. Meteor., 15, 288-296.

_____, 1960: Detailed analysis of the Fargo tornadoes of June 20, 1957. Research Paper No. 42, U.S. Weather Bureau, Washington, D.C., 67 pp.

_____, D. L. Bradbury, and C. F. van Thullenar, 1970: Palm Sunday tornadoes of April 11, 1965. Mon. Wea. Rev., 98, 29-70.

Hoecker, W. H., 1960: Wind speed and air flow patterns in the Dallas tornado of April 2, 1957. Mon. Wea. Rev., 88, 167-180.

_____, 1961: Three-dimensional pressure pattern of the Dallas tornado and some resultant implications. Mon. Wea. Rev., 89, 533-542.

NUMERICAL MODELLING OF SQUALL LINES

Lecturer: Dr. N. LaSeur Notes by: L. Gidel

Date: July 2, 1974 G. Feng

Intense line convection, commonly called squall lines, differs from shallow convection in both its environment and its quasi-steady-state configuration. The structure is two-dimensional and highly asymmetric. Such storms generally occur in environments characterized by strong vertical wind shear and by low-level moist air overlain by extremely dry mid- and upper-tropospheric air.

Schematic models of such storms have been suggested by Browning and Ludlam (1962), Browning (1964), Newton (1967) and Fankhauser (1971). This lecture reviews two anelastic, two-dimensional numerical models by Schlesinger (1973a) and Hane (1973).

Schlesinger aims to simulate basic patterns of pressure, temperature and rainfall intensity, and to assess the role of the ambient shear and the convective instability. The basic assumptions of the model are:

1. Flow is two-dimensional in x-z plane.
2. Coriolis force is neglected.
3. Liquid water exerts a drag force equal to its weight; ice is not included.
4. Pressure deviations are important to gravitational buoyancy in the vertical momentum equation, but they are not important to parcel temperature changes in the thermodynamic equation.
5. Supersaturation is instantaneously removed by the release of latent heat, and liquid water evaporates instantaneously until the air is saturated or until all liquid water has been consumed.
6. Liquid water is partitioned into cloud droplets and precipitation by the method of Takeda (1965, 1966a,b).

7. Diffusion of heat and moisture are not explicitly included and friction is neglected--except at points on or in the cloud where a hypothesis of Lettau (1967) is used for calculating Reynolds stress divergence.

The model includes prognostic equations for vorticity, temperature, and the mixing ratios of water vapor and liquid water. The vorticity equation is:

$$\frac{\partial \eta}{\partial t} = -u\frac{\partial \eta}{\partial x} - w\frac{\partial \eta}{\partial z} + g\rho_0\left(\frac{1}{P_0}\frac{\partial p}{\partial x} - \frac{1}{T_{v0}}\frac{\partial T_v}{\partial x}\right)$$
$$+ g\frac{\partial q_\ell}{\partial x} + \frac{z w}{\rho_0}\frac{\partial \rho_0}{\partial z}\left(\eta - u\frac{\partial \rho_0}{\partial z}\right) \qquad (1)$$
$$+ uw\frac{\partial^2 \rho_0}{\partial z^2} + \frac{\partial(\rho_0 F_x)}{\partial z} - \frac{\partial(\rho_0 F_z)}{\partial x}$$

where η is vorticity, q_ℓ is liquid water mixing ratio, T_v is virtual temperature, and F_x and F_z are the horizontal and vertical components of the friction force per unit mass.

The temperature equation is:

$$\frac{\partial T}{\partial t} = -u\frac{\partial T}{\partial x} - w\left(\frac{\partial T}{\partial z} + \Gamma\right) \qquad (2)$$

where Γ is the dry or moist adiabatic lapse rate, depending on whether the air is saturated or unsaturated.

The moisture prognostic equations are:

$$\frac{\partial q_v}{\partial t} = -u\frac{\partial q_v}{\partial x} - w\frac{\partial q_v}{\partial z} - \frac{c_p}{L}(\gamma_d - \Gamma)w \qquad (3)$$

and

$$\frac{\partial q_\ell}{\partial t} = -u\frac{\partial q_\ell}{\partial x} - w\frac{\partial q_\ell}{\partial z} + \frac{c_s}{L}\rho_0(\gamma_d - \Gamma)w + \frac{\partial}{\partial z}(Vq_r) + \frac{q_\ell w}{\rho_0}\frac{\partial \rho_0}{\partial z} \qquad (4)$$

where q_v, q_ℓ and q_p are, respectively, the mixing ratios of water vapor, liquid water and precipitation.

There are also three diagnostic equations. The streamfunction is defined from:

$$u = \frac{1}{\rho_0}\frac{\partial \psi}{\partial z} \qquad w = -\frac{1}{\rho_0}\frac{\partial \psi}{\partial x} \qquad (5,6)$$

The vorticity is related to the streamfunction by:

$$\eta = \nabla^2\psi \qquad (7)$$

And, finally, the equation of continuity for two-dimensional motion is:

$$\frac{\partial(\rho_0 u)}{\partial x} + \frac{\partial(\rho_0 w)}{\partial z} = 0 \qquad (8)$$

The grid on which the numerical integrations are performed is a 55 x 21 rectangular grid having a width of 172.8 km (ΔX = 3.2 km) and a depth of 14 km (Δz = 700 m). The finite difference scheme used is forward-time, upstream-space for the advective terms, and centered-space for other spatial derivatives, with the exception of the horizontal pressure gradient. The truncation error of the forward-upstream scheme

numerically diffuses all advected fields. This pseudo-diffusion is proportional to the grid mesh separation and fluid speed, and may be up to an order of magnitude greater in this model than might be expected in a real thunderstorm. No other diffusion is included in the model.

A movable grid is used in order to keep the main convective circulation within the domain of the model. Inflow lateral boundary conditions are specified, but the outflow variables are defined in terms of interior information transmitted from upwind. There is no flow allowed through the top or bottom boundary.

The initial perturbation is a symmetric streamfunction perturbation 51.2 km wide and 4.2 km high. The center of the impulse has an updraft 12.8 km wide with a thermally-buoyant saturated region in the interior of the updraft. Maximum values of temperature excess (1° C), updraft velocity (1.5 m/sec), and liquid water content (1 gm/m^3) are located at the center point of the cloud.

Fig. 1 (Schlesinger, 1973a) shows the environmental temperature

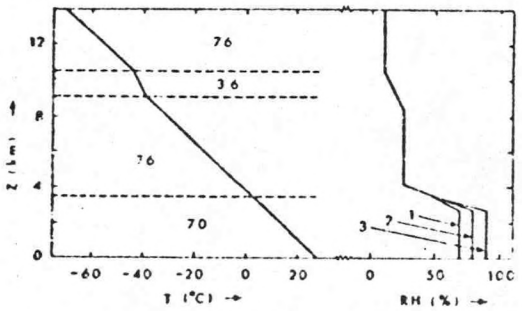

Fig. 1. Initial base states for air temperature T and relative humidity RH in the comparative experiments. Left: numbers in the layers separated by dashed lines indicate the lapse rate--$\partial T/\partial z$(°C km^{-1}) in each layer; right: cases are numbered 1, 2 or 3 according to the assumed constant value H of the relative humidity from the lower boundary to 2.8 km.

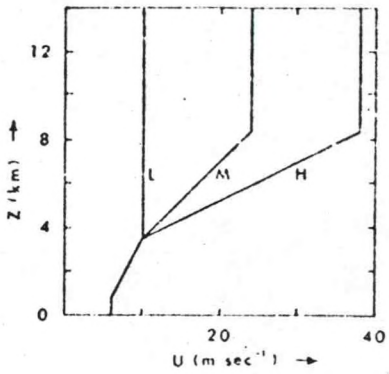

Fig. 2. Initial base states for the wind velocity u in the comparative experiments. Cases are identified by the letter L, M or H according to the value of the total wind shear between 3.5 and 8.4 km.

and relative humidity, and the environmental wind profile is shown in Fig. 2 (Schlesinger, 1973a). Three values of humidity (70%, 80%, 90%) are used in the low levels, with the air abruptly becoming dry above those levels. Three values of the horizontal wind are shown corresponding to weak, moderate and strong shear.

The effects of shear on the disturbed flow are shown in Figs. 3, 4, and 5 (Schlesinger, 1973a) for intermediate moisture (80% RH) after 50 min of integration. The weakening of the convection with increasing shear is apparent from the maximum magnitude of the disturbance streamfunction, the width of the cloud anvil, and the horizontal extent of the outermost plotted streamlines. The strongest downdraft is located at and near the cloud edges below 6 km, suggesting that after 50 min the downdraft is due primarily to negative thermal buoyancy induced by evaporation, rather than to liquid water drag. The downdraft is considerably weaker than the updraft, having maximum velocities of 2.5, 2.5 and 2 m/sec, corresponding to maximum updrafts of 12, 9 and 5 m/sec.

Finally, as the shear increases, the anvil becomes increasingly asymmetric, and the entire updraft-downdraft couplet tilts more downshear. Fig. 6 (Schlesinger, 1973a) shows the pressure deviation for case M2 after 50 minutes of integration. On the whole, the pressure has fallen in the lower part of the region and risen in the upper part. Two meso-lows are located at low levels, the main one under the leading cloud edge, and the secondary one behind the trailing edge. Contrary to the findings of Fujita (1955) and Fujita and Brown (1958), there is no meso-high at the surface. The shallow dome of relatively high pressure has developed in the cold air beneath and just behind the cold core.

Fig. 7 (Schlesinger, 1973a) shows the temperature deviation for case M2 after 50 min. of integration. A warm core updraft has developed with a temperature excess of 6° C at about 8 km. The lowest 2 km of the cloud interior has cooled. Cold tongues at the cloud edges, resulting

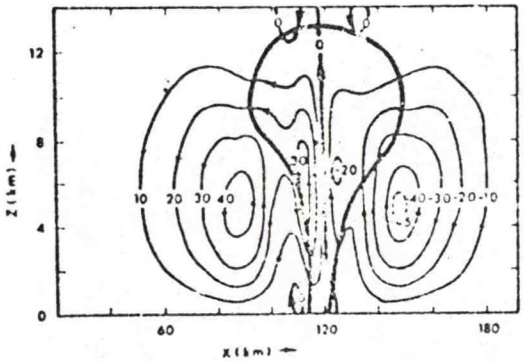

Fig. 3. Deviation of streamfunction from the initial base state (10^6 gm m^{-1} sec^{-1}) for case L2 at 50 min. The shaded region bounded by the heavy solid curve represents the cloud. In this and all subsequent figures in which the variable x appears, it denotes the distance (km) to the right of the initial left boundary (6 grid shifts).

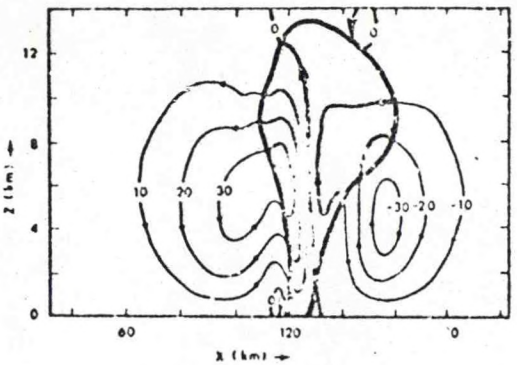

Fig. 4. Same as Fig. 3, but for case M2. (10 grid shifts).

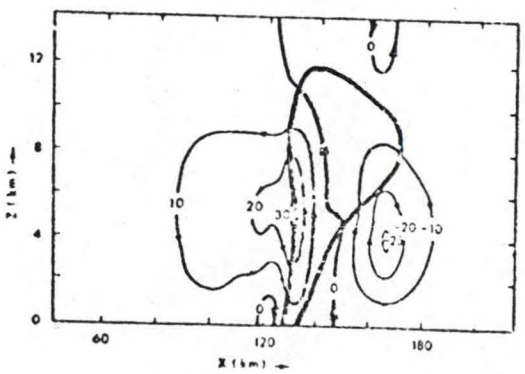

Fig. 5. Same as Fig. 3, but for case H2. (13 grid shifts).

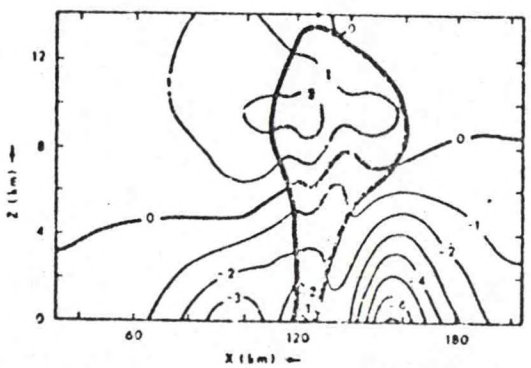

Fig. 6. Deviation of air pressure from the initial base state (mb) for case M2 at 50 min. The shaded region bounded by the heavy solid curve represents the cloud.

from evaporation into unsaturated air, are delineated by the zero is isotherm. The maximum cooling at the surface is -4^{o} C.

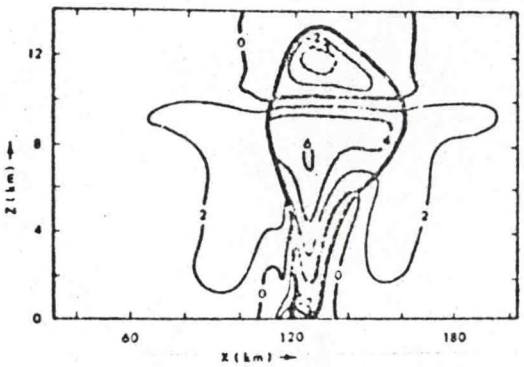

Fig. 7. Deviation of air temperature from the in tial base state (^{o}C) for case M2 at 50 min. The shaded region bounded by the heavy solid curve represents the cloud.

Figs. 8, 9, and 10 (Schlesinger, 1973a) show the effect of increasing moisture for moderate shear. The maximum strength of the storm increases with increasing moisture.

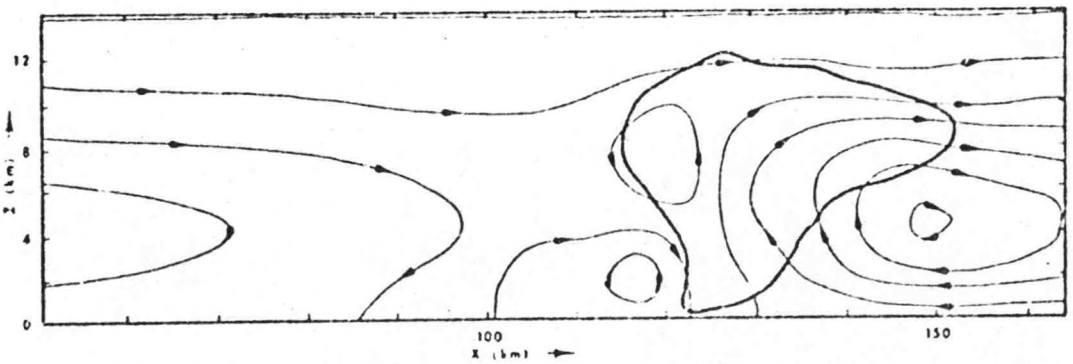

Fig. 8. Airflow streamlines relative to the moving cloud core and rainfall pattern for case M1 at 50 min. The heavy solid curve represents the cloud boundary. Thinner solid curves with arrows are streamlines at intervals of 10^{7} gm m^{-1} sec^{-1}. Dashed streamlines (if any) indicate half-intervals. Light shading represents rainfall with an intensity of at least 30 mm hr^{-1}; heavy shading (if any) represents rainfall with an intensity of at least 90 mm hr^{-1}.

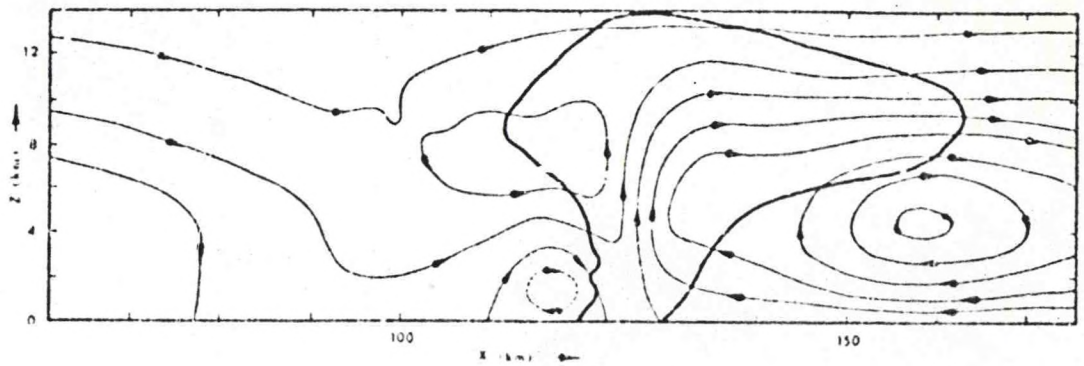

Fig. 9. Same as Fig. 8, but for case M2.

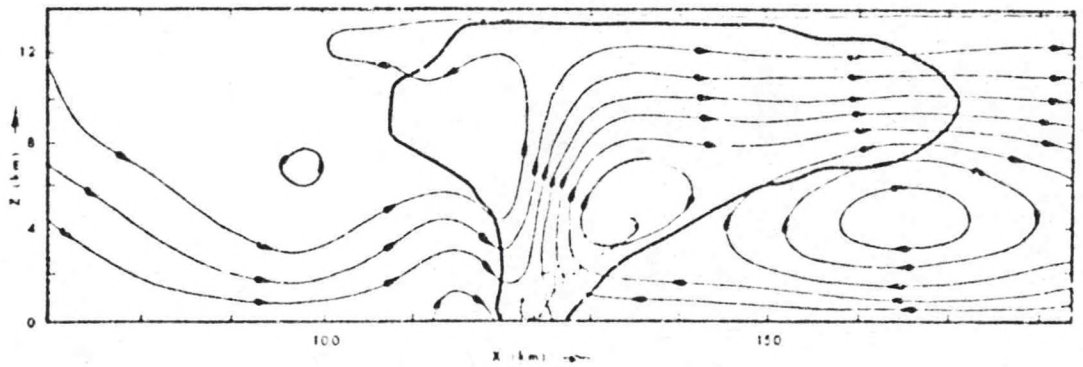

Fig. 10. Same as Fig. 8, but for case M3.

Schlesinger (1973b) investigated the relative importance of various individual forces for case M2 (moderate shear, moderate moisture) which exhibit a nearly quasi-steady-state mature stage. The results can be summarized as follows:

1. Downdraft formation is due mainly to evaporati' cooling from rainfall.

2. Thermal buoyancy is the dominant vertical force, but is strongly opposed by the vertical perturbation pressure force, which can

be up to 25% of the thermal buoyancy.

3. Liquid water drag is significant and can be up to 40% of the maximum thermal buoyancy.

The realism of Schlesinger's model is limited by its two-dimensionality, the unrepresentativeness of the pseudo-diffusion, and the lack of sophisticated micro-physical processes.

In modeling the squall line, Hane (1973) also tries to include the qualitative features of the squall line proposed by Newton (1950), Bates (1961), Browning and Ludlam (1962), and Newton (1963). His experiments are specifically aimed at attaining a quasi-steady, cooperative updraft-downdraft system which interacts continuously with the environment (or a succession of developments, each containing the ingredients for redevelopment after dissipation).

Physical processes and characteristics included in the model are:

1. The environment is convectively unstable and contains strong vertical wind shear.
2. Condensation and evaporation are included, but ice is not.
3. Horizontal changes in quantities along the direction of the squall line elongation are neglected, making this a two-dimensional model.
4. The pressure perturbation force is not included, and the only buoyancy force is thermal.
5. Sub-grid scale turbulent mixing entrainment is explicitly parameterized.
6. Liquid water is included "in bulk" with a Marshall-Palmer (1948) drop-size distribution.
7. Radiational effects are neglected.
8. Surface effects such as friction and surface evaporation are not taken into account (implicitly in the boundary conditions).

The basic model includes prognostic equations for vorticity, temperature and for the mixing ratios of water vapor, cloud water and rain water. The appropriate vorticity equation (Hane, 1972) is:

$$\frac{\partial \eta}{\partial t} = -u\frac{\partial \eta}{\partial x} - w\frac{\partial \eta}{\partial z} - \eta D_v - \frac{g}{T_v}\frac{\partial T_v}{\partial x} + g\frac{\partial}{\partial x}(q_\ell + q_c) + \frac{\partial}{\partial x}\left(\nu_x \frac{\partial \eta}{\partial x}\right) + \frac{\partial}{\partial z}\left(\nu_z \frac{\partial \eta}{\partial z}\right) \quad (9)$$

$$+ C_n\left\{\frac{\partial}{\partial z}\left[\left|\frac{\partial w}{\partial x}\right|(u''-u)\right] - \frac{\partial}{\partial x}\left[\left|\frac{\partial w}{\partial x}\right|(w''-w)\right]\right\}$$

where $\eta = \frac{\partial u}{\partial z} - \frac{\partial w}{\partial z}$, u and w are the horizontal and vertical wind speeds, $D_v = \frac{\partial u}{\partial x} + \frac{\partial w}{\partial z}$ is the two-dimensional divergence, T_v is the virtual temperature, q_ℓ the rain water mixing ratio, q_c the cloud water mixing ratio, C_n is the turbulent mixing coefficient, u'' and w'' are the time invariant motion of the environment, and ν_x and ν_z are the time-space dependent horizontal and vertical eddy viscoscity coefficients.

The temperature equation is:

$$\frac{\partial T}{\partial t} = -u\frac{\partial T}{\partial x} - w\left(\frac{\partial T}{\partial z} + \Gamma_d\right) + \frac{1}{C_p}\frac{dq}{dt} + C_n\left|\frac{\partial w}{\partial x}\right|(T''-T) + \nu_\theta \nabla^2 T. \quad (10)$$

where T is absolute temperature, Γ is the dry adiabatic lapse rate, $\frac{1}{C_p}\frac{dq}{dt}$ is the latent heating or cooling, T'' is the time invariant temperature profile of the environment and ν_θ is the constant coefficient of thermal eddy diffusion.

The moisture prognostic equations are:

$$\frac{\partial q_v}{\partial t} = -u\frac{\partial q_v}{\partial x} - w\frac{\partial q_v}{\partial z} + c_n\left|\frac{\partial w}{\partial x}\right|(q_v'' - q_v) + \nu_\theta \nabla^2 q_v \quad \text{(11)}$$

+evaporation - condensation

$$\frac{\partial q_c}{\partial t} = -u\frac{\partial q_c}{\partial x} - w\frac{\partial q_c}{\partial z} + c_n\left|\frac{\partial w}{\partial x}\right|(q_c'' - q_c) + \nu_\theta \nabla^2 q_c \quad \text{(12)}$$

- autoconversion - accretion - evaporation + condensation

$$\frac{\partial q_r}{\partial t} = -u\frac{\partial q_r}{\partial x} - w\frac{\partial q_r}{\partial z} + \frac{\partial}{\partial z}(q_r V_T) + \frac{q_r V_T}{\rho}\frac{\partial \rho}{\partial z} \quad \text{(13)}$$

+ autoconversion + accretion - evaporation

where q_v'' and q_c'' are the time-invariant profiles of water vapor and cloud water of the environment and V_T is the effective terminal velocity of the rain water distribution.

In addition to the five prognostic equations, there are three diagnostic equations. The diagnostic equation relating the streamfunction to the vorticity is:

$$\nabla^2\psi - \frac{1}{\rho}\frac{\partial \psi}{\partial z}\frac{\partial \rho}{\partial z} = \rho\eta \quad \text{(14)}$$

The diagnostic equations relating the wind components to the streamfunction are:

$$\rho u = \frac{\partial \psi}{\partial z} \qquad \rho w = -\frac{\partial \psi}{\partial x} \quad \text{(15, 16)}$$

The final diagnostic equation is the two-dimensional continuity equation:

$$\frac{\partial(\rho u)}{\partial x} + \frac{\partial(\rho w)}{\partial z} = 0 \qquad (17)$$

The time integration of the prognostic equations is carried out with the predictor-corrector scheme using a variable time step of about 15-20 seconds, depending on the magnitude of the air motion. The grid spacing is 400 m vertically and horizontally, and the domain of integration varies from 25-6 km to 38.0 km horizontally by 12.8 km vertically. Integrations are performed in a relative coordinate system.

The nine-point Arakawa-Jacobian scheme (Arakawa, 1966) is used for the advective terms and centered-space differences elsewhere. Eq. (14) was solved by successive over-relaxation.

No flow is allowed through the top or bottom boundaries, and the flow through the lateral boundaries is constant in time. The values of other variables at the boundaries are determined by an inflow-outflow condition.

The initial perturbation is a well-developed thunderstorm-like circulation.

The environmental temperature and dew point soundings are shown in Fig. 11 (Hane, 1973) and the environmental wind profile is shown in Fig. 12 (Hane, 1974) as the solid line. The environment is quite unstable, with a sharp drop in the moisture profile between 600 and 500 mb, and is similar to the moderately moist sounding used by Schlesinger. The wind profile used by Hane in experiment R1 and R6 has slightly

more shear than the moderate shear case of Schlesinger, but significantly less shear than Schlesinger's strong shear case.

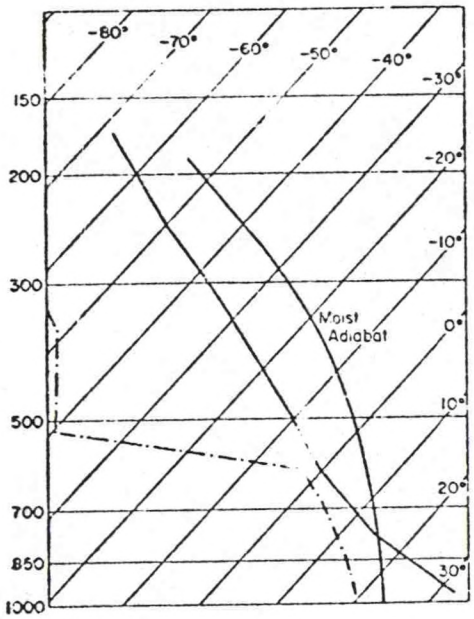

Fig. 11. Initial vertical distribution of environmental temperature (solid line) and environmental dew point dew point (dash-dotted line).

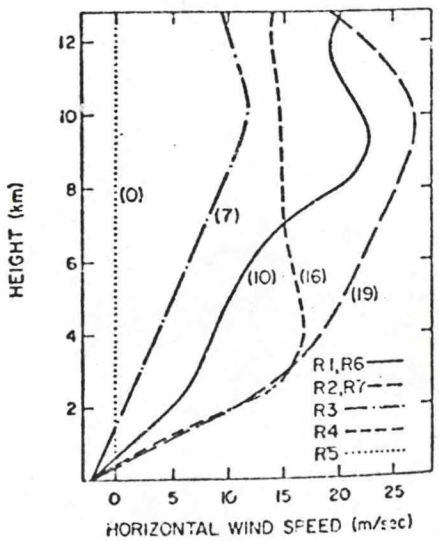

Fig. 12. The vertical distribution of the horizontal envronmental wind used in the model experiments. Numbers in parentheses denote the approximate rate of motion (m sec^{-1}) of the system.

The results after approximately 6 minutes of integration are shown in Figs. 13 and 14 (Hane, 1973). The streamfunction pattern shows the coexistence of an updraft and a downdraft. The updraft has an upshear tilt and the downdraft, which originates in the midlevels, is located beneath the updraft. There is inflow at midlevels on the upshear side of the updraft and at low levels on the downshear side. The upper portion of the cloud spreads out horizontally mainly on the downshear side, and the rain water pattern shows an increasing accummulation of rain water on the upshear edge of the updraft.

As seen in the distribution of temperature anomoly, when the downdraft hits the ground, it spreads out, forming a large pool of cold air (negative anomoly > 6C). The amount of cold air, which results from the evaporation of rain in the downdraft, is more than Schlesinger obtained. Schlesinger, however, did not allow falling rain water to evaporate as it fell through the downdraft, but rather evaporated all of the rain water instantaneously upon leaving the cloud. The temperature anomoly pattern of Fig. 13 (Hane, 1973) also shows the core of warm air (anomoly > 7^{o} C) located along the axis of the updraft.

The vertical motion field has a maximum upward motion greater than 22 m/sec at 7 km in the updraft and a maximum downward motion of 10 m/sec at 3 km in the downdraft. However, unlike Schlesinger's, Hane's model does not dilute the thermal buoyancy by including the pressure perturbation force.

The equivalent potential temperature field of Fig. 14 (Hane, 1973) shows dry air as it is brought down to the surface from the mid-troposphere, and moist air as it rises and is somewhat diluted by

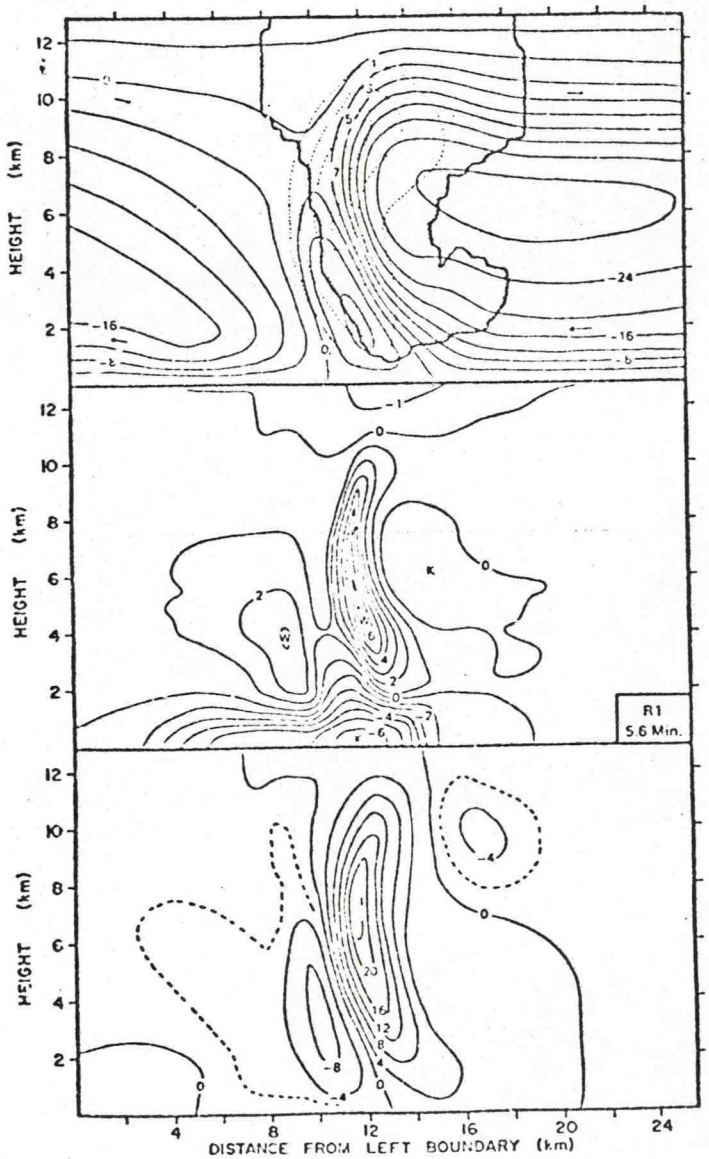

Fig. 13. Variable fields for Experiment R1 at 5.6 min. Upper: solid lines are streamfunction (10^3 kg m^{-1} sec^{-1}); dashed lines rain water mixing ratio (gm kg^{-1}); scalloped lines cloud water mixing ratio outline; middle: temperature anomaly (^oK); lower: vertical wind speed (m sec^{-1}).

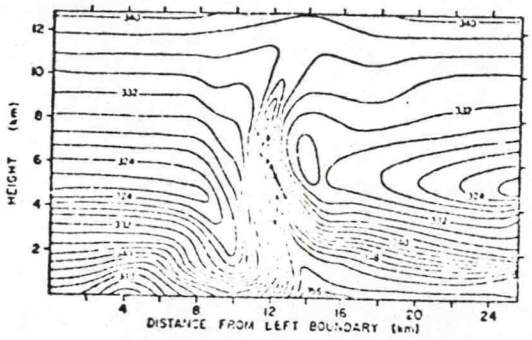

Fig. 14. The equivalent potential temperature (^{o}K) distribution for Experiment R1 at 5.6 min.

mixing in the updraft core.

The results of the integration after 16 min are shown in Fig. 15 (Hane, 1973), which indicates a lessening in intensity and a lack of organization of the system. This is most probably a result of the two-dimensionality of the model. The cold air descending in the downdraft can only spread out in front and to the rear, whereas in nature some cold air is able to spread sideways. As a result, the lower updraft undergoes excessive downshear displacement, and downward motion from midlevels on the downshear side advects too much dry air into the updraft. In the upper levels, the air cannot go around the cloud in two dimensions as it can in nature, and the model cloud experiences a strong left-to-right flow in the upper levels.

After 42 min, the model shows a significant redevelopment, a situation comparable to that found after 6 min of integration. In fact, this pattern of dissipation followed by redevelopment continues to occur in a periodic fashion for as long as the integrations are carried out. Fig. 16 (Hane, 1973) shows the time evolution of the magnitude of maximum downward motion and maximum rain water mixing ratio. The maximum

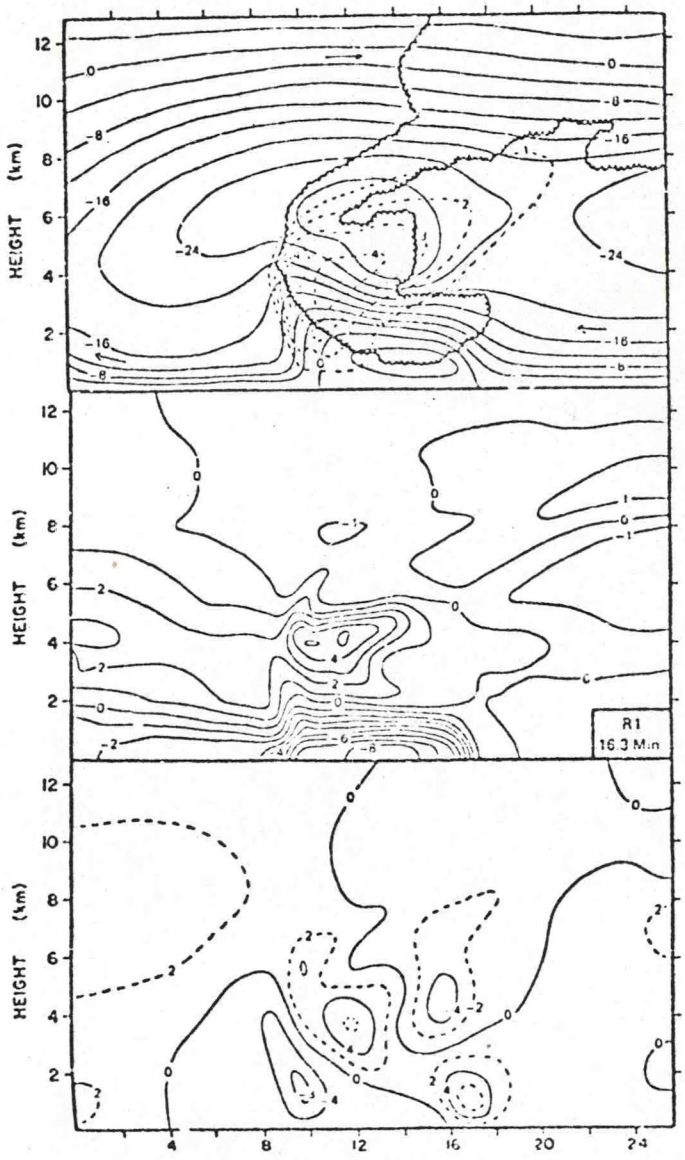

Fig. 15. Same as Fig. 13, but after 16.3 min.

downdraft lags the maximum updraft because the maximum downdraft results from the evaporation of rain water which must first be produced in the updraft.

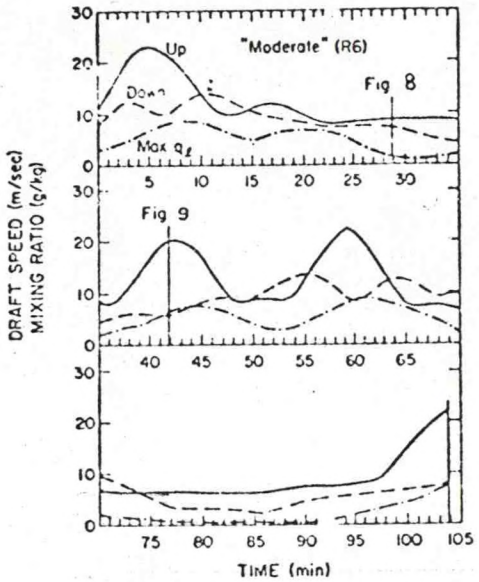

Fig. 16. For Experiment R6, the variation with time of the magnitude of the maximum upward motion (solid), maximum downward motion (dashed), and maximum rain water mixing ratio (dash-dotted).

References

Arakawa, A., 1966: Computational design for long-term numerical integration of the equations of fluid motion. Two-dimensional incompressible flow. Part I. J. Comp. Phys., 1, 119-143.

Bates, F. C., 1961: The Great Plains squall line thunderstorm - A model. Ph.D. thesis, Saint Louis University.

Browning, K. A., 1964: Airflow and precipitation trajectories within severe local storms which travel to the right of the winds. J. Atmos. Sci., 21, 634-639.

-----, and F. H. Ludlam, 1962: Airflow in convective storms. Quart. J. Roy. Meteor. Soc., 88, 117-135.

Fankhauser, J. C., 1971: Thunderstorm-environment interactions determined from aircraft and radar observations. Mon. Wea. Rev., 99, 171-192.

Fujita, T., 1955: Results of detailed synoptic studies of squall lines. Tellus, 7, 405-436.

-----, and H. A. Brown, 1958: A study of mesosystems and their radar echoes. Bull. Amer. Meteor. Soc., 39, 538-554.

Hane, C. E., 1972: Squall line structure and maintenance: Numerical experimentation. Ph.D. thesis, The Florida State University.

-----, 1973: The squall line thunderstorm: Numerical experimentation. J. Atmos. Sci., 30, 1672-1690.

Lettau, H. H., 1967: New Hypothesis for the relationship between eddy and mean states. Phys. Fluids Suppl., 579-583.

Marshall, J. S., and W. McK. Palmer, 1948: The distribution of raindrops with size. J. Meteor., 5, 165-166.

Newton, C. W., 1950: Structure and mechanism of the prefrontal squall line. J. Meteor., 7, 210-222.

-----, 1963: Dynamics of severe convective storms. Meteor. Monographs. 5, 33-58.

-----, 1967: Severe convective storms. Adv. in Geophys., 12, 257-308.

Schlesinger, R. E., 1973a: A numerical model of deep moist convection: Part I. Comparative experiments for variable ambient moisture and wind shear. J. Atmos. Sci., 30, 835-856.

-----, 1973b: A numerical model of deep moist convection: Part II. A prototype experiment and variations upon it. J. Atmos. Sci., 30, 1374-1391.

Takeda, T., 1965: The downdraft in convective-shower cloud under the vertical wind shear and its significance for the maintenance of convective systems. J. Meteor. Soc. Japan, 43, 302-309.

-----, 1966a: The downdraft in the convective cloud and raindrops: A numerical computation. J. Meteor. Soc. Japan, 44, 1-11.

-----, 1966b: Effects of the prevailing wind with vertical shear on the convective cloud accompanied with heavy rainfall. J. Meteor. Soc. Japan, 44, 129-143.

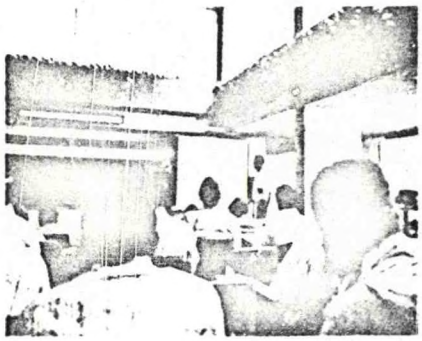

LECTURES BY PROFESSOR ARNT ELIASSEN, UNIVERSITY OF OSLO

102 b

GRAVITY OSCILLATIONS AND WAVES OF SMALL AMPLITUDE

Lecturer: Dr. A. Eliassen Notes by Z.-H. Feng

Date: July 8, 1974 L. Gidel

I. General Fluid Model

In general, the density of a sample of a fluid can be expressed as a function of pressure p, specific entropy s, and the mole fractions m_i:

$$\rho = F(p, s, m_i) \qquad \sum_i m_i = 1 \qquad (1)$$

The change in the density of an individual fluid element or parcel is given by:

$$D\rho = \frac{\partial F}{\partial p} Dp + \frac{\partial F}{\partial s} Ds + \sum_i \frac{\partial F}{\partial m_i} Dm_i \qquad (2)$$

If it is assumed that the parcel exchanges neither heat nor mass with its environment, $DS = 0$ and $Dm_i = 0$. Eq. (2) becomes:

$$\frac{D\rho}{Dp} = \frac{\partial F}{\partial p} = \frac{1}{C_s^2} \qquad (3)$$

where C_s is the speed of sound.

If this fluid is in equilibrium in a gravitational field, then each of the variables of state are a function of z only, and the pressure variation with height is hydrostatic:

$$p = p_e(z)$$

$$s = s_e(z)$$

$$m_i = m_{ie}(z) \qquad (4)$$

$$\rho = \rho_e(z) = F(p_e, s_e, m_{ie})$$

$$\frac{dp_e}{dz} = -\rho_e g$$

Consider a parcel initially a height z which is lifted a small distance ζ. By Taylor expansion, the density of the environment at $z+\zeta$ is:

$$\rho_{env}(z+\zeta) = \rho_e(z) + \left(\frac{\partial F}{\partial p}\frac{dp_e}{dz} + \frac{\partial F}{\partial s}\frac{ds_e}{dz} + \sum_i \frac{\partial F}{\partial m_i}\frac{dm_{ie}}{dz}\right)\zeta + \cdots$$

But since the parcel moves adiabatically and without mixing, and always at equilibrium with the environment,

$$\rho_{parcel}(z+\zeta) = \rho_e(z) + \frac{\partial F}{\partial p}\frac{dp_e}{dz}\zeta + \cdots$$

The buoyancy of such a parcel at $z+\zeta$ per unit mass of parcel is:

$$g\,\frac{\rho_{env}-\rho_{parcel}}{\rho_{parcel}} = \frac{g\left(\frac{\partial F}{\partial s}\frac{ds_c}{dz}+\sum_i \frac{\partial F}{\partial m_i}\frac{dm_{ic}}{dz}\right)\zeta}{\rho_c(z)+\frac{\partial F}{\partial p}\frac{d\rho_c}{dz}\zeta}$$

If ζ is small compared to the distance over which ρ_c changes appreciably,

$$g\,\frac{\rho_{env}-\rho_{parcel}}{\rho_{parcel}} \doteq \frac{g}{\rho_c}\left(\frac{\partial F}{\partial s}\frac{ds_c}{dz}+\sum_i \frac{\partial F}{\partial m_i}\frac{dm_{ic}}{dz}\right)\zeta$$

$$= -N^2\zeta$$

where N^2 is the buoyancy frequency (Brunt-Väisälä frequency)

$$N^2 = -\frac{g}{\rho_c}\left(\frac{\partial F}{\partial s}\frac{ds_c}{dz}+\sum_i \frac{\partial F}{\partial m_i}\frac{dm_{ic}}{dz}\right) \qquad (5)$$

The vertical variation of the equilibrium density is obtained from:

$$\frac{1}{\rho_c}\frac{d\rho_c}{dz} = \frac{1}{\rho_c}\left(\frac{\partial F}{\partial p}\frac{d\rho_c}{dz}+\frac{\partial F}{\partial s}\frac{ds_c}{dz}+\sum_i \frac{\partial F}{\partial m_i}\frac{dm_{ic}}{dz}\right)$$

$$\frac{1}{\rho_c}\frac{d\rho_c}{dz} = -\frac{g}{c_s^2}-\frac{N^2}{g} \qquad (6)$$

Now consider small disturbances from the equilibrium state for a statically stable fluid where $N^2 > 0$:

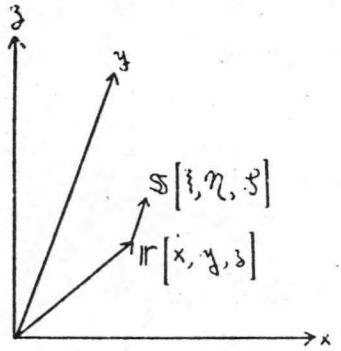

$$P = P_e(z) + p'(x, y, z, t)$$
$$\rho = \rho_e(z) + \rho'(x, y, z, t)$$
$$N = N(z)$$
$$S = S(r, t)$$
$$V = \frac{\partial S}{\partial t}$$

$r[x, y, z]$ is the position vector of the parcel in equilibrium and $S[\xi, \eta, \zeta]$ is the perturbation displacement of the parcel from its equilibrium position.

$P(r + S)$ and $\rho(r + S, t)$ can be approximated by expanding them about r and keeping only first order terms:

$$p'(r + S, t) = p'(r, t) + S \cdot \nabla p' + \cdots \simeq p'(r, t) \qquad |S| \ll L(p')$$

$$\rho'(r + S, t) = \rho'(r, t) + S \cdot \nabla \rho' + \cdots \simeq \rho'(r, t) \qquad |S| \ll L(\rho')$$

$$P_e(r + S) = P_e(r) + S \cdot \nabla P_e + \cdots \simeq P_e(z) - g \rho_e \zeta$$

$$\rho_e(r + S) = \rho_e(r) + S \cdot \nabla \rho_e + \cdots \simeq \rho_e(z) - \left(\frac{g}{c_s^2} + \frac{N^2}{g}\right) \rho_e \zeta$$

Therefore,

$$P(r + S, t) = P_e(z) - g \rho_e \zeta + p'(r, t)$$

$$\rho(r + S, t) = \rho_e(z) - \left(\frac{g}{c_s^2} + \frac{N^2}{g}\right) \rho_e \zeta + \rho'(r, t)$$

The individual change in density of the parcel in going from $\mathbf{r}$ to $\mathbf{r}+\boldsymbol{\xi}$ is given by Eq. (3):

$$D\rho = \frac{1}{c_s^2} Dp$$

$$\rho(\mathbf{r}+\boldsymbol{\xi},t) - \rho_0(\mathbf{r}) = \frac{1}{c_s^2}\left(p(\mathbf{r}+\boldsymbol{\xi},t) - p_0(\mathbf{r})\right)$$

$$\rho_0(z) - \left(\frac{g}{c_s^2} + \frac{N^2}{g}\right)\rho_0 \xi + \rho'(\mathbf{r},t) - \rho_0(z) =$$

$$\frac{1}{c_s^2}\left(p_0(z) - g\rho_0\xi + p'(\mathbf{r},t) - p_0(z)\right)$$

$$\rho'(\mathbf{r},t) = \frac{N^2}{g}\rho_0 \xi + \frac{p'(\mathbf{r},t)}{c_s^2} \qquad (7)$$

The first term on the right in Eq. (7) represents the perturbation increase in density due to heavier parcels arriving from below and the second term represents compressibility (i.e., $p'>0$ contributes to $\rho'>0$).

The <u>continuity equation</u> is:

$$\frac{D\rho}{Dt} = \frac{1}{c_s^2}\frac{Dp}{dt} = -\rho\,\nabla\cdot\mathbf{v}$$

$$\frac{1}{c_s^2}\left(\frac{Dp_0}{dt} + \frac{Dp'}{dt}\right) = -(\rho_0+\rho')\nabla\cdot\boldsymbol{\xi}_t$$

$$\frac{1}{c_s^2}\left(-g\rho_0\xi_t + p_t'\right) + \rho_0\nabla\cdot\boldsymbol{\xi}_t = 0$$

where second order terms have been dropped. Integrate in time:

$$\nabla\cdot\boldsymbol{\xi} - \frac{g}{c_s^2}\xi + \frac{p'}{c_s^2\rho_0} = f(\mathbf{r})$$

If the equilibrium case is a special case where all perturbations are zero, then $f(\ ) \equiv 0$

$$\nabla \cdot \mathbb{S} - \frac{g}{c_s^2} \rho + \frac{p'}{c_s^2 \rho_c} = 0 \qquad (8)$$

The momentum equation is:

$$\rho \left(\frac{D \mathbb{V}}{dt} + f \mathbb{n} \times \mathbb{V} \right) + g \rho \mathbb{n} + \nabla p = 0$$

where $\mathbb{n}$ is the vertical unit vector. The perturbation equation becomes:

$$\rho_c \left(\mathbb{S}_{tt} + f \mathbb{n} \times \mathbb{S}_t \right) + g \rho' \mathbb{n} + \nabla p' = 0$$

or, when ρ' is eliminated by means of (7)

$$\rho_c \left(\mathbb{S}_{tt} + f \mathbb{n} \times \mathbb{S}_t + N^2 \zeta \mathbb{n} \right) + \nabla p' + \frac{g}{c_s^2} p' \mathbb{n} = 0 \qquad (9)$$

The solutions must satisfy the following boundary conditions:

Rigid boundary: $\mathbb{S}_n = 0$

Free surface at z_F: $\dfrac{D(p_c + p')}{dt} = 0$

$$-g \rho_c \zeta_t + p_t' = 0$$

$$p' = g \rho_c \zeta \quad \text{at } z = z_F$$

Next, eliminate ρ_c from Eqs. (8) and (9) by change of variable:

$$\mathbb{S} = \rho_c^{-1/2} \tilde{\mathbb{S}} \qquad p' = \rho_c^{1/2} \tilde{p}$$

$$\mathbb{S}_z = \rho_c^{-1/2} \left(\tilde{\mathbb{S}}_z + \frac{1}{2} \left(\frac{g}{c_s^2} + \frac{N^2}{g} \right) \tilde{\mathbb{S}} \right)$$

$$p_z' = \rho_c^{-1/2} \left(\tilde{p}_z - \frac{1}{2} \left(\frac{g}{c_s^2} + \frac{N^2}{g} \right) \tilde{p} \right)$$

The continuity and momentum equations become:

$$\nabla \cdot \tilde{\mathbb{S}} - \beta \tilde{\mathbb{S}} + C_s^{-2} \tilde{p} = 0 \qquad (8')$$

$$\tilde{\mathbb{S}}_{tt} + f \mathbb{m} \times \mathbb{S}_t + N^2 \mathbb{m} \tilde{\mathbb{S}} + \nabla \tilde{p} + \beta \mathbb{m} \tilde{p} = 0 \qquad (9')$$

$$\beta = \frac{1}{2}\left(\frac{g}{C_s^2} - \frac{N^2}{g} \right) \qquad (10)$$

The <u>wave energy relation</u> is obtained by taking $p' \frac{\partial}{\partial t}(8) + \mathbb{S}_t (9)$

$$\frac{\partial E}{\partial t} + \nabla \cdot \mathbb{F}_e = 0 \qquad (11)$$

where E is the wave energy density

$$E = \frac{1}{2} \rho_0 \left(\mathbb{S}_t^2 + N^2 \zeta^2 \right) + \frac{p'^2}{2 \rho_0 C_s^2}$$

$$= \frac{1}{2} \mathbb{S}_t^2 + \frac{1}{2} N^2 \zeta^2 + \frac{1}{2 C_s^2} \tilde{p}^2 \qquad (12)$$

The terms on the right are the kinetic, potential and internal wave energies, respectively. The wave energy flux density $\mathbb{F}_e$ is:

$$\mathbb{F}_e = p' \mathbb{S}_t = \tilde{p} \tilde{\mathbb{S}}_t \qquad (13)$$

<u>Equipartition of wave energy</u> is demonstrated by taking $\frac{1}{2} p' \times (8) + \frac{1}{2} \mathbb{S} \cdot (9)$ and using the identity,

$$\mathbb{S} \cdot \mathbb{S}_{tt} = \left(\frac{1}{2} \mathbb{S}^2 \right)_{tt} - \mathbb{S}_t^2$$

$$\frac{1}{2} \rho_0 \mathbb{S}_t^2 = \frac{1}{2} \rho_0 N^2 \zeta^2 + \frac{1}{2} \frac{p'^2}{C_s^2 \rho_0} + \left(\frac{\rho_0}{4} \mathbb{S}^2 \right)_{tt} +$$

$$\nabla \cdot \left(\frac{1}{2} p' \mathbb{S} \right) - \frac{1}{2} \rho_0 f \mathbb{m} \cdot \left(\mathbb{S} \times \mathbb{S}_t \right)$$

Time and space average this equation and denote the average with an "over-bar."

$$\overline{\left(\frac{\rho_0}{4}\,\mathbb{S}^2\right)_{tt}} = 0$$ if averaged over a long time

$$\overline{\nabla\cdot\left(\tfrac{1}{2}P'\mathbb{S}\right)} = 0$$ if boundary for the space integration is a rigid box or if averaged over a large region in space

$$\overline{\tfrac{1}{2}\rho_0\,\mathbb{S}_t^2} = \overline{E}_K$$ kinetic energy

$$\overline{\tfrac{1}{2}\rho_0 N^2 \xi^2} = \overline{E}_P$$ potential energy

$$\overline{\frac{1}{2}\frac{P'^2}{c_s^2\rho_0}} = \overline{E}_i$$ internal energy

$$\overline{\tfrac{1}{2}\rho_0 f\,\mathbb{m}\cdot(\mathbb{S}\times\mathbb{S}_t)} = \overline{f\rho_0\frac{dA}{dt}}$$ if there is no rotation (i.e., f=0), this term is zero

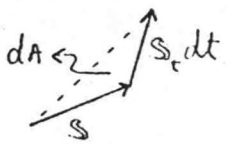

The result is

$$\overline{E}_K = \overline{E}_P + \overline{E}_i - \overline{f\rho_0\frac{dA}{dt}} \qquad (14)$$

Pure accoustic waves are the solution to Eqs. (8) and (9) if there is no gravitation field (g=0), the fiuid is homogeneous (N^2=0), and there is no rotation (f=0). Equations (8) and (9) become:

$$\nabla\cdot\mathbb{S} = -\frac{P'}{c_s^2} \qquad \mathbb{S}_{tt} = -\nabla P' \qquad P' = \frac{P'}{\rho_0} \qquad (15)$$

Eliminating $\mathbf{S}$ yields the classical, non-dispersive wave equation

$$P'_{tt} = c_s^2 \nabla^2 P'$$

The energy density for this wave is:

$$E = \frac{1}{2} \rho_0 S_t^2 + \frac{1}{2} \frac{\rho_0}{c_s^2} P'^2 = E_k + E_p$$

There is no potential energy in pure accoustic waves.

Pure gravity waves are the solution to Eqs. (8) and (9) if the fluid is incompressible ($\frac{1}{c_s^2} = 0$) and there is no rotation (f=0). Equations (8) and (9) become

$$\nabla \cdot \mathbf{S} = 0 \qquad S_{tt} = -N^2 \rho' \mathbf{n} - \frac{1}{\rho_0} \nabla P' \qquad (18)$$

The energy density for this wave is:

$$E = \frac{1}{2} \rho_0 S_t^2 + \frac{1}{2} \rho_0 N^2 \rho'^2 = E_k + E_p \qquad (19)$$

There is no internal energy in pure gravity waves.

If the change in the undisturbed density with height is small compared to the density itself, variations in the density can be ignored in the momentum equations except in the external forcing terms. Eq. (18) becomes:

$$\nabla \cdot \mathbf{S} = 0 \qquad S_{tt} = -N^2 \rho' \mathbf{n} - \nabla P' \qquad (20)$$

and the approximation is called the Boussinesq approximation.

These equations can be used to compute the frequency of oscillation of a fluid for standing oscillations. The resulting frequency formula, called Höiland's frequency formula, shows that the buoyancy frequency is an upper limit to the frequency of oscillation that a fluid can undergo.

Assume that the parcel displacement $\mathcal{S}$ is a standing oscillation in the form:

$$\mathcal{S}(r,t) = \hat{\mathcal{S}}(r)\sin\nu(t-t_0) \qquad \text{and} \quad \mathcal{S}_{tt} = -\nu^2\mathcal{S} \tag{21}$$

where the frequency ν is a constant. If the fluid is confined in a vessel, then the streamlines $\hat{\mathcal{S}} \times d\mathbf{r} = 0$ must close up on themselves, and they are fixed in space. Integrate Eq. (18) along a closed streamline L in a chosen positive direction (see figure below) to obtain:

$$\nu^2 \oint \rho_c \mathcal{S}\cdot d\mathbf{r} = \oint_L \rho_c N^2 \zeta\, dz \tag{22}$$

by using Eq. (21). Here both $\mathcal{S}$ and $d\mathbf{r}$ are tangent to L and $|\mathcal{S}| = S$, $|d\mathbf{r}| = d\ell$. The vertical displacement $\zeta = S\cos\theta$ and $dz = d\ell\cos\theta$. Hence,

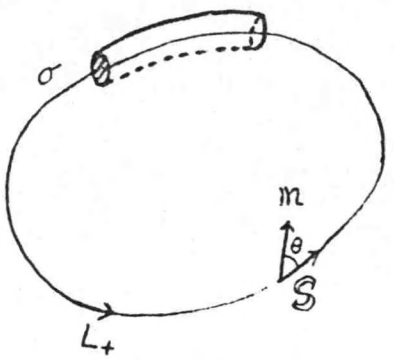

$$\nu^2 = \frac{\oint \rho_c N^2 \cos^2\theta\, S\, d\ell}{\oint \rho_c S\, d\ell} \tag{23}$$

This is called the Höiland frequency formula since Höiland (1939) gave a useful mechanical interpretation to Eq. (22). By considering the particles in a closed tubular fluid filament (streamline), we have a mechanical system for which the pressure forces have no resultant in the direction tangential to the filament. The inertial force along the filament per tubular unit cross section on the left hand side of Eq. (22) is therefore determined by the restoring force on the right hand side, i.e., buoyancy induced by gravity. Let σ be a cross section of a narrow stream tube around L. The

incompressibility demands the tubular volume element aS = constant along L at any time although a may vary along L. Eq. (23) becomes:

$$\nu^2 = N^2 \frac{\oint N^2 \frac{\rho_0}{a} \cos^2\theta \, dl}{\oint \frac{\rho_0}{a} \, dl} \qquad (23')$$

In a special case, if $N(z)$ = constant.

$$\nu^2 = \frac{\oint \cos^2\theta \, \frac{\rho_0}{a} \, dl}{\oint \frac{\rho_0}{a} \, dl} \qquad (24)$$

The formula gives ν if the flow kinematics is known (shape of the streamlines). Eq. (24) shows that $\nu < N$. If $\theta \approx 0$ along most of the streamline, the streamlines tend to be vertical (Fig. A) and $\nu \approx N$. If $\theta \approx \pm \pi/2$ along most of the streamline, the streamlines tend to be horizontal (Fig. B) and $\nu << N$.

Fig. A 

Fig. B 

Example: standing oscillations are imposed in two fluid-filled closed tubes with the same outer shapes: which shape give the higher frequency?

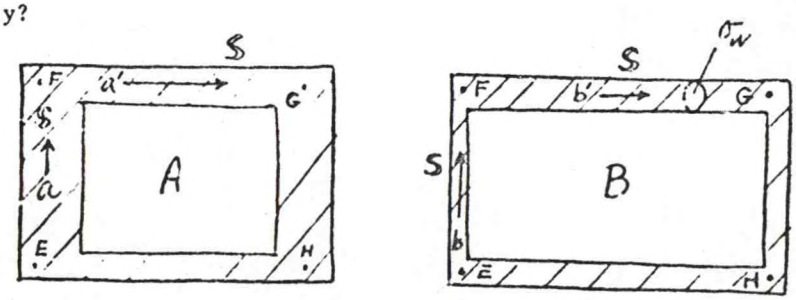

From Eq. (24),

$$\mathcal{N}^2 = N^2 \frac{\frac{1}{\bar{\sigma}_V}\int_V \rho_0\, dl}{\frac{1}{\bar{\sigma}_V}\int_V \rho_0\, dl + \frac{1}{\bar{\sigma}_H}\int_H \rho_0\, dl} = \frac{N^2}{1 + \frac{\bar{\sigma}_V}{\bar{\sigma}_H}\frac{L}{H}}$$

where subscripts V and H refer to the vertical and horizontal legs, respectively. It follows that the frequency is reduced when $\bar{\sigma}_V/\bar{\sigma}_H$ is increases. A small $\bar{\sigma}_H$ means large horizontal displacements, and large horizontal acceleration, which increase the effective inertia of the system.

References

Höiland, E., 1939: On the interpretation and application of the circulation theorems of V. Bjerkuev. Arch. Math. Naturvidermskap, 42, No. 5.

Thompson, P.A., 1972: Compressible Fluid Dynamics, Chapter 2.

GRAVITY WAVES WITHOUT ROTATION

Lecturer: Dr. A. Eliassen Notes by: L. W. Uccellini

Date: July 9, 1974 J. Fishman

I. Introduction

This lecture is a continuation of Dr. Eliassen's presentation of gravity wave theory, assuming no rotational effects. Discussion of the case of a two dimensional box shows that the particular solution for this example is a function only of the box shape. Also discussed are the concepts of transversal waves, energy density, and mean energy flux density. Properties of wave propagation and group velocity are also presented, as well as an analysis of various composite waves.

II. Two-dimensional Oscillations in a Box

Only vertical motions give rise to a restoring force. Horizontal motions must then be driven by the vertical displacements through the action of pressure forces.

Denoting the pressure perturbations by p', the system of equations becomes in the Boussinesq approximation, with $P = \frac{p'}{\rho_0}$:

$$u_{tt} = -P'_x \qquad \text{(horizontal acceleration)}$$

$$w_{tt} = -N^2 \zeta - P'_z \qquad \text{(vertical acceleration)}$$

$$u_x + w_z = 0. \qquad \text{(continuity)}$$

The schematic diagram for this case is shown in Fig. 1.

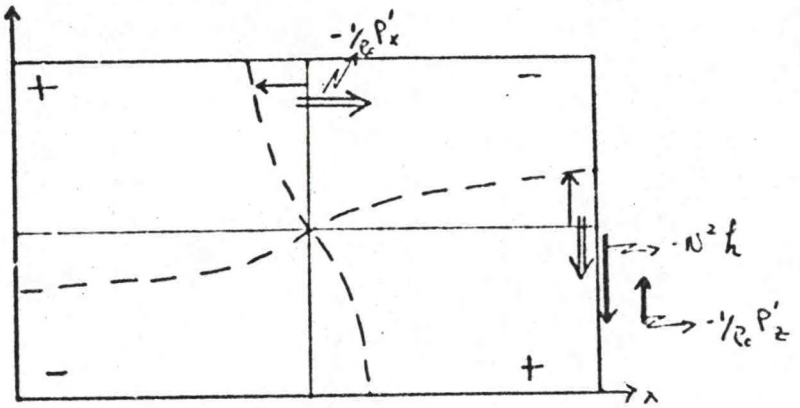

Fig. 1. Two dimensional oscillations in a box: +, −, are pressure perturbations (ρ'); ⇒ accelerations (ζ_{tt}); →, ↑ displacements (ζ).

To solve this system of equations, let:

$$\zeta = -\psi_z$$

$$\zeta = \psi_x$$

and $N^2 =$ CONSTANT

By cross-differentiation of the equations of motion, the pressure terms can be substracted, leaving:

$$\zeta_{xtt} - \zeta_{ztt} = -N^2 \zeta_x ,$$

or $$\nabla^2 \psi_{tt} = -N^2 \psi_{xx} ,$$

With the boundary conditions

$$\psi = 0 ,$$

(at x=0, x=L, z=0, Z=H), where H and L are the height and length of the box respectively.

The solutions of the partial differential equation is:

$$\psi_{m,n} = \sin \frac{m\pi x}{L} \sin \frac{n\pi z}{L} \sin \nu_{m,n}(t-t_0), \quad (25)$$

where: $$\nu^2_{m,n} = N^2 \frac{m^2/L^2}{m^2/L^2 + n^2/H^2} \quad (26)$$

Examining the first mode, where $m = n = 1$,

$$\nu^2_{1,1} = N^2 \frac{H^2}{L^2 + H^2}$$

or

$$\nu_{1,1} = N \frac{H}{\sqrt{L^2 + H^2}}$$

This shows that the frequency of the solution is a function of H/L as long as N is constant. In other words ν is a function of the shape of the box only, not its size. Note that the first mode ($\psi_{1,1}$) is not the one with lowest frequency.

The eigenfunctions $\psi_{m,n}$ represent Fourier components over the box, and hence form a complete system. Höiland has shown that no complete system of eigenmodes can be found in the case of a tilted box.

III. Simplest Gravity Waves without Rotation

Recall:

$$\nabla \cdot \mathbf{S} = 0$$

$$\mathbf{S}_{tt} = -N^2 \chi \hat{n} - \nabla P' \quad (20)$$

where N is constant. A plane wave is defined by:

$$\$(r,t) = \hat{\$}\, e^{i(k\cdot r + \nu t)}$$

$$P'(r,t) = \hat{P}\, e^{i(k\cdot r + \nu t)} \quad , \tag{28}$$

where $\hat{\$}$ and $\hat{P}$ are complex constants, and k and ν are real constants. The real part of the solution represents the physical solution; the plane wave propogates in direction k with a phase velocity

$$c = -\frac{\nu}{\kappa} \quad , \tag{29}$$

where $\kappa = |k| = (k_x^2 + k_y^2 + k_z^2)^{1/2}$, $\nu < 0$.

Using Eqs. (28) and (29), Eq. (20) can be rewritten:

$$k \cdot \hat{\$} = 0 \tag{30}$$

$$-\nu^2 \hat{\$} + N^2 \hat{\$}_L k + i k \hat{P} = 0 \quad , \tag{31}$$

where Eq. (30) shows that the waves are <u>transversal</u>. The combination of Eq. (30) and Eq. (31) shows the waves to be <u>plane polarized</u> since $\hat{\$}$ lies in the vertical plane through k (Fig. 2). The displacements $\hat{\$}$ are directed along L; the unit vector normal to k.

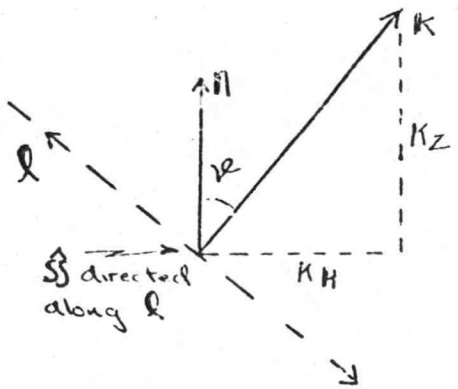

Fig. 2.
Schematic of vector plane for plane waves.

For $0 \le \alpha \le \pi$, $\cos\alpha = \frac{k_z}{k}$, $\sin\alpha = \frac{k_H}{k} \ge 0$; (31a)

$$\hat{h} = \hat{S} \cdot \hat{N} = \hat{S} \sin\alpha , \tag{31b}$$

$$\hat{S} = \hat{S} \hat{\ell} , \tag{31c}$$

where $\hat{S} = \hat{S}_r + i\hat{S}_i$ and $\hat{\ell}$ is directed along $\hat{S}$. Operating on Eq. (31) with $\hat{S}$ and applying Eqs. (31b) and (31c) yields

$$-\nu^2 \hat{S}^2 + N^2 \hat{h}^2 = 0 . \tag{31d}$$

Solving for ν^2,

$$\nu^2 = N^2 \left(\frac{\hat{h}}{\hat{S}}\right)^2 = N^2 \sin^2\alpha .$$

Therefore:

$$\nu^2 = N^2 \frac{k_x^2 + k_y^2}{k^2} ,$$

or:

$$\nu = \pm N \sin\alpha \tag{32}$$

Eq. (32) shows that the plane waves can propogate horizontally, but not vertically.

Operating on Eq. (31) with $\hat{k}$ gives:

$$N^2 \hat{h} k \cos\alpha + i k^2 \hat{p} = 0 ,$$

or

$$\hat{p} = i \frac{N^2}{k} \hat{h} \cos\alpha \tag{33}$$

That is, the pressure distribution is 90^{o} out of phase with the vertical displacement.

The energy density of a pure gravity wave is given by:

$$E = \tfrac{1}{2}\rho_0 S_t^2 + \tfrac{1}{2}\rho_0 N^2 \eta^2 \qquad (19)$$

Denoting the average energy density over one wavelength or over one period by $\bar{E}$, we arrive at:

$$\bar{E} = \tfrac{1}{2}\rho_0 \overline{S_t^2} + \tfrac{1}{2}\rho_0 N^2 \overline{\eta^2} \,. \qquad (19a)$$

Using the relationship that

$$\overline{\mathrm{Re}\left(\hat{a}\, e^{i(\mathbf{k}\cdot\mathbf{r}+\nu t)}\right)\mathrm{Re}\left(\hat{b}\, e^{i(\mathbf{k}\cdot\mathbf{r}+\nu t)}\right)} = \tfrac{1}{2}\mathrm{Re}\left(\hat{a}\hat{b}^{*}\right)$$

Eq. (19a) becomes:

$$\bar{E} = \tfrac{1}{4}\rho_0 \nu^2 |\hat{S}|^2 + \tfrac{1}{4}\rho_0 N^2 |\hat{\eta}|^2$$

Applying Eq. (31d) we get:

$$\bar{E} = \tfrac{1}{2}\rho_0 \nu^2 |\hat{S}|^2 \qquad (34)$$

The mean energy flux density, $\overline{F_e}$, is shown to be

$$\overline{F_e} = \overline{p' S_t} = \frac{\rho_0}{2}\mathrm{Re}\left(\hat{P}^{*}\, i\nu \hat{S}\right)$$

(i.e., $\overline{p' S_t}$)

$$= \tfrac{1}{2}\rho_0 N^2 c |\hat{S}| \sin 2\alpha \cos 2\alpha \ell \qquad (35)$$

Thus a wave moving in the direction $\mathbf{k}$ will have an energy flux in the direction ℓ, i.e., perpendicular to it.

IV. Group Velocity

The group velocity of a wave packet is defined as the velocity at which the entire packet and thus its energy, propagates. The group and

phase velocites differ when the wave system is dispersive, that is, when the phase velocity is wavelength dependent.

The group velocity, C_g, as it relates to a vector space ($|k|$ space) is illustrated in Figs. 3 and 4. C_g is equal to $-\nabla_k \nu$, where $\nu = \sigma \sin \alpha$ and c is in the direction of k. Note that C_g is directed along the vector l, which is perpendicular to k.

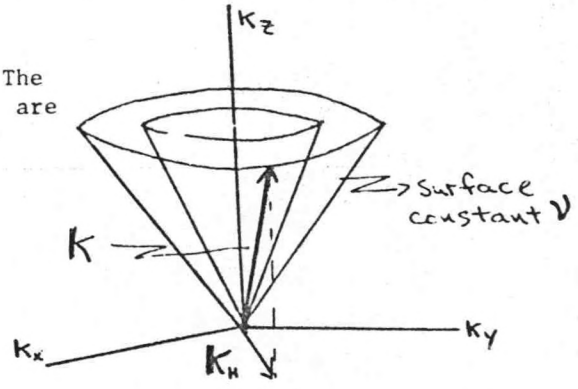

Fig. 3. Surfaces of constant frequency (ν) in k space. The components of $|k|$: k_x , k_y are horizontal; k_z is vertical.

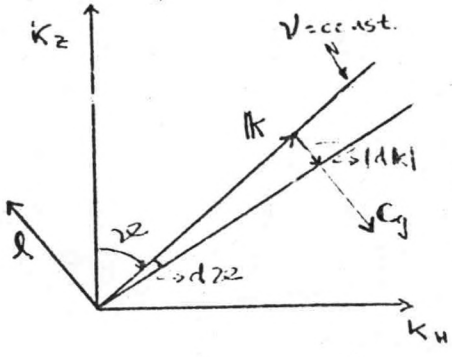

Fig. 4. Vertical cross section through surface of constant ν along k_H . l is perpendicular to k .

The relationship of C_g and C can be shown in the following manner:

$$|C_g| = \frac{|d\nu|}{|dk|} = \left| \frac{N \cos\alpha \, d\alpha}{k \, d\alpha} \right| = \left| \frac{N \cos\alpha}{k} \right|$$

Since $\nu = -N \sin 2\alpha$,

$$|C_g| = \left| \frac{\nu \cos 2\alpha}{\sin 2\alpha \, k} \right| = |c \cot 2\alpha| ,$$

and

$$\mathbf{C}_g = -C \cot 2\alpha \vec{\ell} \quad . \tag{36}$$

Therefore the group velocity is normal to the direction of propagation. Furthermore, it follows from Eqs. (34), (35), and (36) that

$$\overline{\mathbf{F}_c} = \overline{E} \, \mathbf{C}_g \tag{37}$$

The mean wave energy flux density is directed along the group velocity vector $-\vec{\ell}$.

Given that $\nu = -N \sin 2\alpha$ $\left(\nu^2 = N^2 \frac{k_H^2}{k_H^2 + k_z^2} \right)$, $C_H = \frac{-\nu}{k_H}$, $C_z = \frac{-\nu}{k_z}$, the following expressions were derived:

$$\frac{C_{gH}}{C_H} = \frac{k_H}{\nu} \frac{\partial \nu}{\partial k_H} = \frac{k_H^2}{\nu^2} \frac{\partial \nu^2}{\partial k_H^2} = \frac{k_z^2}{k^2} ,$$

$$\frac{C_{gz}}{C_z} = \frac{k_z}{\nu} \frac{\partial \nu}{\partial k_z} = \frac{k_z^2}{\nu^2} \frac{\partial \nu^2}{\partial k_z^2} = -\frac{k_z^2}{k^2} .$$

The horizontal group and phase velocities therefore have the same sign, while the vertical group and phase velocities have opposite signs. Where waves progagate in the vertical, the energy always propagates in the opposite direction.

V. Composite Waves

Let $w(\mathbb{k})$ denote a plane wave with wave number $\mathbb{k}$ and $\nu = -N \sin 2\alpha$. The propagation is in the direction $\mathbb{k}$ and

of unit amplitude. Four wave number vectors are considered (Fig. 3):

$$\vec{k}_1(k_x, k_y, k_z) \quad , \quad \vec{k}_2(-k_x, -k_y, k_z),$$

$$\vec{k}_3(k_x, k_y, k_z) \quad , \quad \vec{k}_4(-k_x, k_y, k_z),$$

with $k_1 = k_2 = k_3 = k_4$, and $\nu_1 = \nu_2 = \nu_3 = \nu_4 = \nu = -N \sin 2\Omega$

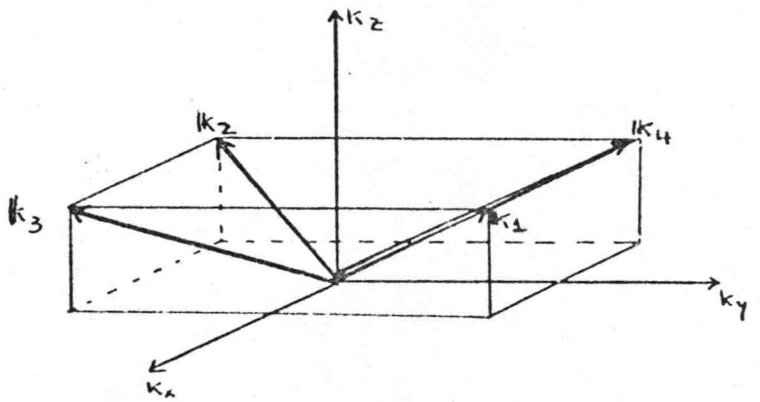

Fig. 5. Schematic of the four wave number vectors

Several combinations of the four waves are considered:

A. $W(\vec{k}_1) + W(\vec{k}_2)$

1. This combination yields the simple wave form
$\cos(k_z z + \delta_1) \cos(k_x x + k_y y + \nu t + \delta_2)$.
The amplitude varies with z and the wave propagation is in the horizontal direction ($\vec{k}_{3H}$).

2. $\bar{E}$ and $\overline{F_c}$ are additive and the energy flux density is the direction of the wave propagation (Fig. 6).

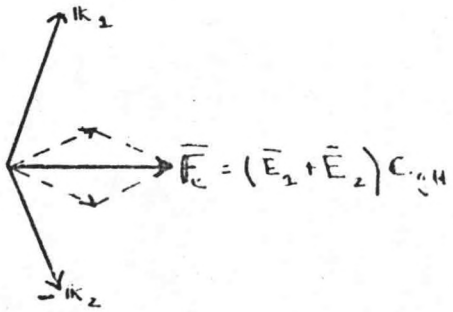

Fig. 6. Schematic of the energy flux density for the composite waves

3. The kinematics of this horizontally propagating wave ($k_y = 0$) is illustrated in Fig. 7. Since $\bar{f}_{tt} = -p_x'$, the horizontal acceleration always acts to restore the displacement to a neutral position. The largest horizontal wind perturbations ($\bar{f}_t$) are found at the equilibrium positions ($p_x' = 0$) and are directed according to the wave propagation C and the horizontal displacement occurring downstream. Since $\bar{f}_t$ and p' are positively correlated, $\overline{F_e} = \overline{f_t p'}$ is always positive indicating that $\bar{F}_e$ and C are in the same direction.

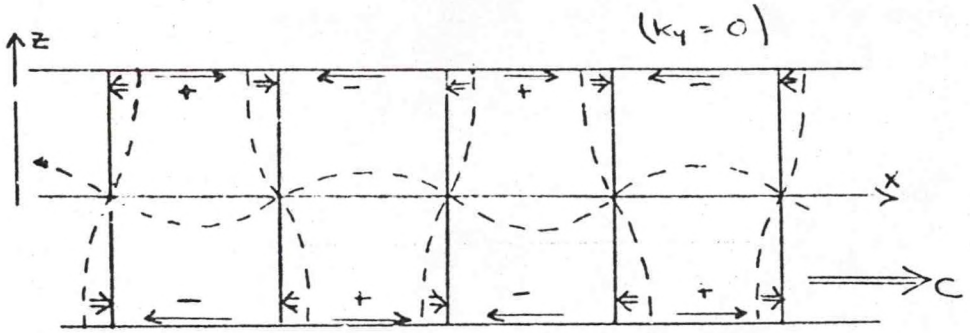

Fig. 7. Schematic of the kinematics of the horizontal wave $\omega(|k_1|) + \omega(-k_2)$ with $k_y = 0$. $+, -$ are pressure perturbations (p'); $\Leftarrow$, $\Rightarrow$ are accelerations; $\longrightarrow$, $\longleftarrow$ wave horizontal velocity.

B. $\omega(|k_1|) + \omega(|k_2|)$

1. This combination yields the simple wave form
$$\cos(k_x x + k_y y + \delta_1)\cos(k_z z + \nu t + \delta_2)$$
indicating a vertically propagating wave with amplitude which varies in x and y.

2. If $k_z > 0$, the vertical propagation is upward within the plane determined by k_1 and k_2. $\bar{F}_e$ is also vertically directed and is opposite to the propagation (Fig. 8).

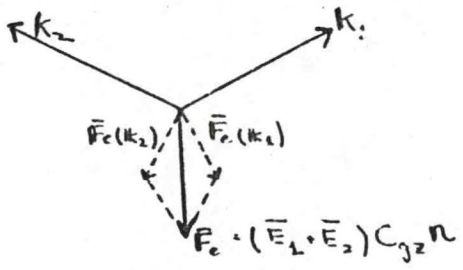

Fig. 8: Schematic of the energy flux density for the composite waves $\omega(|k_1|) + \omega(|k_2|)$.

3. The kinematics for this wave combination are illustrated in Fig. 9 for a wave propagating upward. The accelerations, both vertical and horizontal, act to restore the displacements to a neutral position. The vertical velocity, h_t, is determined by the vertical parcel displacement as the wave propagates upward with the largest vertical motion existing at an equilibrium position. Since h_t and p' are negatively correlated, $\overline{F_e} = \overline{h_t p'}$ is always less than zero, indicating that energy is propagating downward as the wave propagates up.

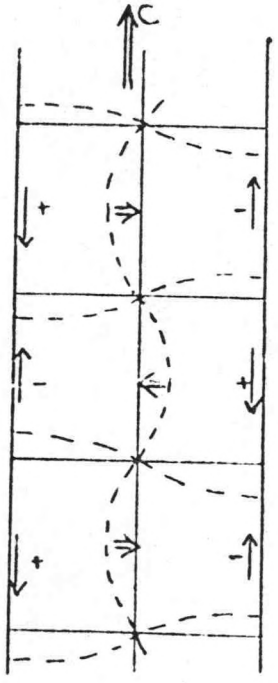

Fig. 9.

Schematic of the kinematics of the vertically propagating wave $\omega(|k_1|) + \omega(|k_2|)$. +, − pressure perturbations, ⇒ ⇐ are horizontal accelerations. ↑↓ wave vertical velocity (h_t).

Other wave combinations briefly discussed include:

C. $\omega(|k_1|) + \omega(-|k_1|)\cos(k_x x + k_y y + k_z z + \delta_2)\cos(\nu t + \delta_2)$, for which the simple wave form is a standing wave with $F_e = 0$.

D. $\omega(|k_1|) + \omega(-|k_1|) + \omega(|k_2|) + \omega(-|k_2|) + \omega(|k_3|) + \omega(-|k_3|) + \omega(|k_4|) + \omega(-|k_4|)$ yielding standing oscillations within the box. The wave form reduces to $\cos(k_x x + \delta_1)\cos(k_y y + \delta_2)\cos(k_z z + \delta_3)\cos(\nu t + \delta_4)$.

VI. Summary

This description of the basic concepts of simple gravity waves within a nonrotating fluid has produced the following important points:

A. Solutions of a two-dimensional gravity oscillation in a box are a function only of the box shape, not the area.

B. Vertical velocity is 90° out of phase with the vertical displacement.

C. Accelerations always act to restore the displacements to a neutral or equilibrium position.

D. The group and phase velocities are not the same for dispersive waves.

E. The energy flux is directed along the group velocity vector which for a plane wave is perpendicular to the direction of phase propagation.

F. For horizontally propagating waves, C_g is in the same direction as C_x with $|C_g| < |C_x|$.

G. For vertically propagating waves, C_{gz} is opposite that of C_z with $|C_{gz}| < |C_z|$.

GRAVITY OSCILLATIONS (cont'd.)

Lecturer: Dr. A. Eliassen Notes by: M. Wheldon

Date: July 10, 1974 R. Livingston

I. Pure Gravity Waves with Rotation

The model for incompressible motions, with the Boussinesq approximation, is extended to include rotation about a vertical axis. Eqs. (8) and (9) become:

$$\nabla\cdot\mathcal{S} = 0 \quad , \quad \mathcal{S}_{tt} + f\vec{m}\times\mathcal{S}_t + N^2\mathcal{S}\vec{m} + \nabla\mathcal{P}' = 0 \qquad (39)$$

For a plane wave solution:

$$\mathcal{S} = \hat{\mathcal{S}}\, e^{i(\vec{k}\cdot\vec{r} + \nu t)}$$

$$\mathcal{P}' = \hat{\mathcal{P}}\, e^{i(\vec{k}\cdot\vec{r} + \nu t)}$$

(39) becomes:

$$\vec{k}\cdot\hat{\mathcal{S}} = 0 \quad , \quad -\nu^2\hat{\mathcal{S}} + i\nu f\vec{m}\times\hat{\mathcal{S}} + N^2\hat{\mathcal{S}}\vec{m} + ik\hat{\mathcal{P}} = 0 \qquad (40)$$

$\hat{\mathcal{S}}$ is again normal to $\vec{k}$

$$\hat{\mathcal{S}} = \hat{s}_1\vec{l}_1 + \hat{s}_2\vec{l}_2 \qquad (41)$$

Unit vectors $\vec{l}_1$ and $\vec{l}_2$ form an orthogonal triad with $\vec{k}$, $\vec{l}_1$ in the plane of $\vec{m}$ and $\vec{k}$.

The following identities are readily derived from the second equation of (40):

$$\hat{s}_2 = \frac{i}{\nu} f\cos\theta\,\hat{s}_1 \qquad (42)$$

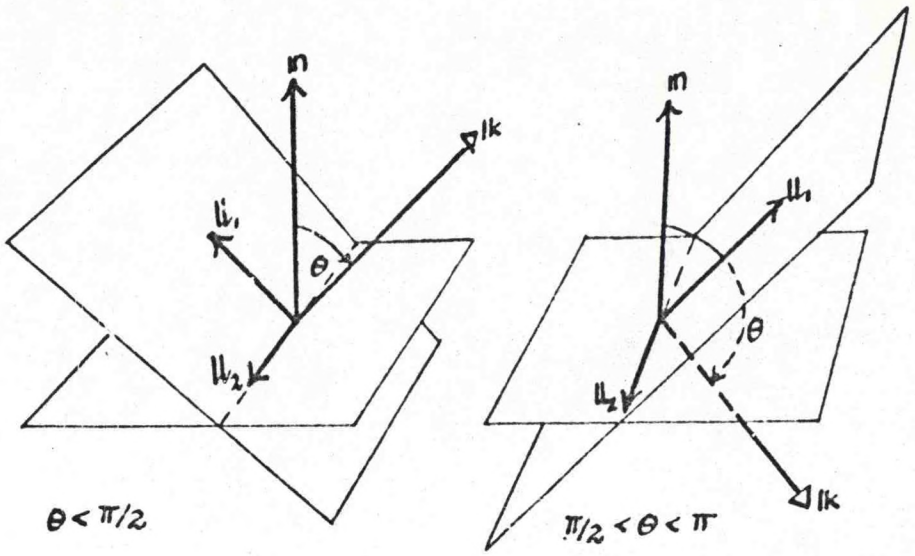

Without rotation the wave would be linearly polarized. With rotation it is elliptically polarized, with anticyclonic parcel motion.

$$\nu^2 = N^2 \sin^2\theta + f^2 \cos^2\theta = \left(N^2 k_H^2 + f^2 k_z^2\right)/K^2 \qquad (43)$$

Again we may choose $\nu < 0$. If $N > f$ than the above dispersion relation shows that $f \le |\nu| \le N$.

$$\left| \frac{\hat{s}_1}{\hat{s}_2} \right|^2 = 1 + \frac{N^2}{f^2} \tan^2\theta$$

$$\hat{P} = i \frac{N^2 - f^2}{K} \sin\theta \cos\theta \, \hat{s}_1 \qquad (44)$$

The mean wave energy density is:

$$\bar{E} = \tfrac{1}{2}\rho_0 \overline{s_t^2} + \tfrac{1}{2}\rho_0 N^2 \overline{\zeta^2}$$

$$= \frac{1}{4}\rho_0 \nu^2 \left(|\hat{s}_1|^2 + |\hat{s}_2|^2\right) + \frac{1}{4}\rho_0 N^2 |\hat{\xi}|^2 \qquad (45)$$

$$= \frac{1}{4}\rho_0 \left(\nu^2 + f^2\cos^2\theta + N^2\sin^2\theta\right)|\hat{s}_1|^2$$

$$= \frac{1}{2}\rho_0 \nu^2 |\hat{s}_1|^2$$

The first two terms in the parenthesis denote kinetic energy, and the third denotes potential energy. From the dispersion relation we see that there is no equipartion of wave energy. The final term in Eq. (14) has magnitude $\frac{1}{2}\rho_0 f^2\cos^2\theta$ for these waves.

The mean wave energy flux density is:

$$\overline{F_e} = -\frac{1}{2}\rho_0 (N^2 - f^2) c \sin\theta\cos\theta |\hat{s}_1|^2 u_1 \qquad (46)$$

The motion along u_2 does not contribute to $\overline{F_e}$, because the velocity is out of phase with pressure. Finally,

$$c_g = \frac{N^2 - f^2}{\nu K}\cos\theta \sin\theta\, u \qquad (47)$$

Again the group velocity is normal to the phase velocity, with a horizontal component in the same sense and a vertical component in the opposite sense. This would be somewhat modified if the three-dimensional rotation were used rather than the vertical component alone.

II. Gravity Waves in an Ideal Gas (Constant Composition)

$$\rho = \frac{p^{c_v/c_p}}{R\theta} = F(p, \theta)$$

$$c_s^2 = \left(\frac{\partial F}{\partial p}\right)^{-1} = \frac{c_p}{c_v} RT = \frac{c_p}{c_v}\frac{p}{\rho}$$

$$N^2 = -\frac{g}{\rho_0}\frac{\partial F}{\partial \theta}\frac{d\theta_0}{dz} = \frac{g}{\theta_0}\frac{d\theta_0}{dz} = \frac{g}{T_0}\left(\frac{dT_0}{dz} + \frac{g}{c_p}\right)$$

$$\frac{1}{\rho_0}\frac{d\rho_0}{dz} = -\frac{g}{c_s^2} - \frac{N^2}{g}$$

	c_s	N	g/c_s^2	N^2/g	β
Unit	$m\,s^{-1}$	s^{-1}	km^{-1}	km^{-1}	km^{-1}
Troposphere	320	1.2×10^{-2}	1/10	1/70	1/23
Stratosphere	290	2.2×10^{-2}	1/8.5	1/21	1/29

Typical values in the atmosphere

$\beta = \frac{1}{2}\left(\frac{g}{c_s^2} - \frac{N^2}{g}\right)$ is the parameter entering the equations of motion scaled using the mean density profile. The actual values of c_s, the speed of sound, have approximately a 10% variation about the given value in both the troposphere and stratosphere. n was calculated for an isothermal stratosphere, and a tropospheric lapse rate of about $6.5°C/km$. The Brunt-Vaisalla frequency n is two orders of magnitude greater than the Coriolis frequency, f, for which a typical value is $10^{-4}\ sec^{-1}$.

In the atmosphere it is convenient to use Eqs. (8') and (9'):

$$\nabla\cdot\tilde{\xi} - \beta\tilde{\zeta} + c_s^{-2}\tilde{p} = 0 \qquad (8')$$

$$\tilde{S}_{tt} + f \hat{m} \times \tilde{S}_t + N^2 \hat{m} \tilde{\xi} + \nabla \tilde{p} + \beta \hat{m} \tilde{\rho} = 0 \qquad (9')$$

where:

$$S = \tilde{S} \rho_0^{-1/2} \quad , \quad p' = \tilde{p} \rho_0^{1/2}$$

$$c_s^2 = \frac{c_p}{c_v} R T^0$$

$$N^2 = \frac{g}{T_0} \left(\frac{dT_0}{dz} + \frac{g}{c_p} \right)$$

$$\beta = \frac{1}{2} \left(\frac{g}{c_s^2} - \frac{N^2}{g} \right)$$

Clearly the coefficients c_s^2, N^2 and β are constant only when $\frac{dT_0}{dz} = 0$. Assuming the troposphere to be isothermal implies a value of n^2 considerably greater than observed, close to the stratospheric value. However, with a normal constant lapse rate in the troposphere, N^2 and c_s^2 will vary very slowly with height and we may use the approximation c_s^2 =constant, N^2=constant, β =constant. Then Eqs. (8',9') have solutions:

$$\tilde{S} = \hat{\tilde{S}} e^{i(k \cdot r + \nu t)} \qquad \tilde{p} = \hat{\tilde{p}} e^{i(k \cdot r + \nu t)} \qquad (43)$$

provided:

$$k_x^2 + k_y^2 = k_H^2 = (\nu^2 - f^2) \left[\frac{1}{c_s^2} + \frac{k_z^2 + \beta^2}{N^2 - \nu^2} \right]$$

The resulting waves are combined gravitational-acoustic-rotational.

Eq. (49) may be represented as a set of curves K_z^2 = constant in a diagram with coordinates K_H^2, ν^2:

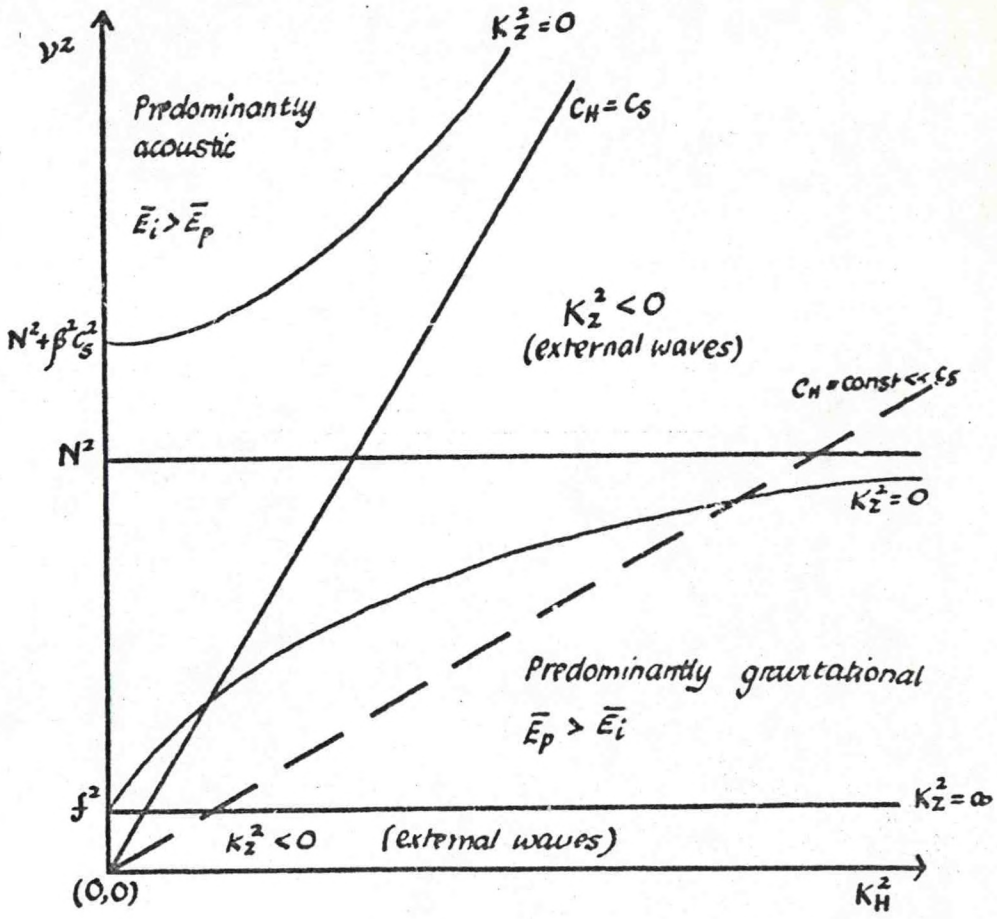

Here $K_z^2 = 0$ is represented by two branches of a hyperbola. In the area between them, $K_z^2 < 0$ and the equations can only be satisfied by exponential functions of z. These can be made to satisfy a zero condition on only one horizontal boundary and are therefore called external waves. There are also external waves for $\nu^2 < f^2$. There are two separate regions of internal waves ($K_z^2 > 0$), which have trigonometric

z-dependence and may satisfy zero conditions at two horizontal boundaries. The transition from internal to external waves across a line $k_z^2 = 0$ is of a very different nature than that across $k_z^2 = \infty$.

The ratio of mean potential to internal energy is given by:

$$\frac{\overline{E_p}}{\overline{E_i}} = \frac{N^2 c_s^2}{N^2 - \nu^2}\left(\frac{k_H^2}{\nu^2 - f^2} - \frac{1}{c_s^2}\right)$$

The two regions of internal waves have no common frequencies in the high frequency region ($\nu^2 > N^2 + \beta^2 c_s^2$), $\overline{E_i} > \overline{E_p}$. These are interpreted as acoustic waves, modified by gravity. In the low frequency region $f^2 < \nu^2 < N^2$ and $\overline{E_p} > \overline{E_i}$. These are gravity waves modified by incompressibility. In both cases there is also an influence of rotation. If the coefficients c_s^2 , N^2 and β are allowed to be slowly varying functions of height, this picture will be distorted, but will have essentially the same character.

III. The Anelastic Approximation

A straight line through the origin corresponds to a constant horizontal phase speed $c_H = -\nu/k_H$. To describe mountain lee waves we are interested in phase speeds relative to the wind satisfying $c_H \ll c_s$. Such waves are far from the predominantly acoustic regime. It is therefore appropriate to modify the equations to eliminate acoustic waves.

$\frac{\partial^2}{\partial t^2}$ of (8'): $\nabla \cdot \tilde{\xi}_{tt} - \beta \tilde{\xi}_{tt} + c_s^{-2} \tilde{p}_{tt} = 0$ (50)

$\nabla \cdot$ of (9'): $\nabla \cdot \tilde{\xi}_{tt} - f m \cdot \nabla \times \tilde{\xi}_t + N^2 \tilde{\xi}_z + \nabla^2 \tilde{p} + \beta \tilde{p}_z = 0$ (51)

Subtracting, $\nabla\cdot\tilde{\mathcal{F}}_{tt}$ drops out, and we obtain an equation containing $\nabla^2\tilde{\rho} - c_s^{-2}\tilde{\rho}_{tt}$. In pure acoustic waves, these terms are equal. In predominantly acoustic waves they are of the same order. But in slow-moving waves, $c \ll c_s$, i.e., the Mach number is small, $\left|\frac{1}{c_s^2}\tilde{\rho}_{tt}\right| \sim \frac{c^2}{c_s^2}\left|\nabla^2\tilde{\rho}\right| << \nabla^2\tilde{\rho}$, and $c_s^{-2}\tilde{\rho}_{tt}$ may be ignored versus $\nabla^2\tilde{\rho}$. This makes it plausible for the last term in (8') $(c_s^{-2}\tilde{\rho})$ or in (8) $(\rho_0^{-1} c_s^{-2} p')$ to be ignored for waves where $(c/c_s)^2 << 1$ This is not the same as setting $c_s^{-2} = 0$, since the coefficient retained. Reference to the derivation of Eq. (8) shows that the approximation is equivalent to neglecting the local time derivative of density in the continuity equation. It is the anelastic approximation. In particular it is applicable for waves whose horizontal phase speed c_H is small compared with c_s.

$$K_H^2 = \frac{\nu^2 - f^2}{N^2 - \nu^2}\left(K_z^2 + \beta^2\right) \tag{52}$$

or

$$\nu^2 = N^2\frac{K_H^2}{K^2+\beta^2} + f^2\frac{K_z^2+\beta^2}{K^2+\beta^2}$$

The dispersion relation is now linear instead of quadratic in ν^2, indicative of the loss of one regime. The diagram appropriate to (52) shows that the acoustic (high frequency) regime is completely eliminated.

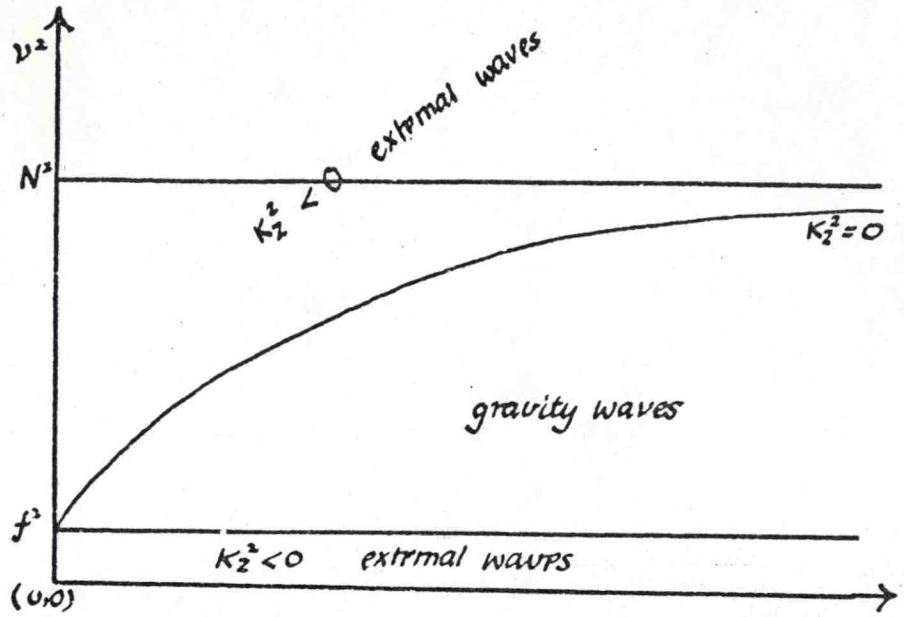

In the anelastic approximation the energy density is:

$$E = \frac{1}{2}\tilde{\xi}_t^2 + \frac{1}{2}N^2\tilde{\xi}^2 = E_k + E_p$$

should not be interpreted strictly as potential energy, since, because of the scaling transformation, it also includes some internal energy.

IV. The Approximation $\beta = 0$

If $|k_z| \gg \beta$, $L_z \ll \frac{2\pi}{\beta} \sim 150\,km$, where L_z is vertical wavelength. Then in (8'): $|\beta\tilde{\xi}| \ll |\tilde{\xi}_z|$, and in (9'): $|\beta \ln \tilde{p}| \ll |\hat{p}_z|$, so that we may ignore the β-terms. Combined with the anelastic approximation, this gives the equations:

$$\nabla \cdot \tilde{\xi} = 0 \qquad (53)$$

$$\tilde{\mathcal{S}}_{tt} + f\hat{m} \times \tilde{\mathcal{S}}_t + N^2 \hat{m}\tilde{\xi} + \nabla\tilde{p} = 0 \qquad (54)$$

These are precisely the equations which apply for an incompressible fluid using the Boussinesq approximation (39). The wave solutions for that case are also valid for an atmosphere of constant N^2, provided $k_z \gg \beta$, $c \ll c_s$ and with the substitution $\mathcal{S} = \tilde{\mathcal{S}}\rho_0^{-1/2}$, $p' = \tilde{p}\rho_0^{1/2}$. The restriction on the vertical wavelength is good for many phenomena of meteorological interest, so the approximation $\beta = 0$ is a useful one.

Care must be taken in the interpretation of these solutions. The amplitudes of $\tilde{\mathcal{S}}$ and $\tilde{p}$ are constant with height; therefore, the amplitude of $\mathcal{S}$ (and velocity $\mathcal{S}_t$) increases with height as $\rho_0^{-1/2}$, and the amplitude of p' decreases with height as $\rho_0^{1/2}$. $\left|\frac{p'}{p_0}\right| \sim \frac{\rho_0^{1/2}}{p_0} \sim \rho_0^{-1/2}$ and at a sufficiently high level $|p'| = p_0$. Similarly, parcel displacement is of increasingly large magnitude with height. The linearization in the original equation can no longer be valid above a certain level, which depends upon the wave amplitude.

With $\beta = 0$, Eq. (52) reduces to (43), valid for an incompressible, Boussinesq fluid. The wave energy flux vector is normal to $\hat{k}$, and its vertical component is opposite to k_z. If we take the equations with $\beta \neq 0$, then $\mathcal{S}$ is no longer strictly normal to $\hat{k}$, since

$$\hat{k} \cdot \tilde{\mathcal{S}} = \beta\tilde{\xi}$$

Therefore $\overline{F_e}$ is also not strictly normal to $\hat{k}$, as Eq. (13) shows that $\overline{F_e}$ must be in the direction of $\mathcal{S}$. However, the deviation is generally very small.

Literature on Acoustic-Gravity Waves

Eckart, C.: Hydrodynamics of Oceans and Atmospheres. New York, 1960.

Gossard, E. E., (1962): Vertical flux of energy into the lower ionosphere from internal gravity waves generated in the troposphere. J. Geoph. Res. 67, 745.

Tolstoy, I., (1963): The theory of waves in stratified fluids, including effects of gravity and rotation. Rev. Mod. Phys, 35, 207.

MOUNTAIN WAVES

Lecturer: Dr. A. Eliassen Notes by: R. Smith

Date: July 11, 1974 T. Curtin

I. Introduction

Internal gravity waves can be produced by many sources. Probably the best documented and the most completely analyzed are waves produced by atmospheric flow over mountains. This lecture discusses a simple model of mountain waves containing many of the elements of the real phenomena.

II. Lecture Notes

This construction of a theory of mountain waves incorporates many of the simplifying assumptions discussed in previous lectures (i.e., two-dimensional, anelastic, Boussinesq linearization). This model will, however, retain the effects of vertical shear in the mean wind. In order to isolate the effect of mountains, and to obtain steady solutions, it is required that the basic shearing stratified flow be stable and not lead spontaneously to growing disturbances. Further, a scale small enough to enable us to neglect the effects of the earth's rotation will be used for this problem. The basic flow may be in geostrophic balance, but the associated cross-flow pressure gradient will not be considered.

After making the above assumptions and transforming the variables according to

$$u = \tilde{u}\rho_0^{-1/2}, \quad w = \tilde{w}\rho_0^{-1/2}, \quad s = \tilde{s}\rho_0^{-1/2} \qquad (1)$$

$$p = \tilde{p}\rho_0^{1/2}$$

to eliminate the explicit effect of strong vertical variations of we obtain for the disturbance quantities the equations:

$$\tilde{u}_t + U\tilde{u}_x + U_z\tilde{w} + \tilde{P}_x = 0 \qquad (2)$$

$$\tilde{w}_t + U\tilde{w}_x + N^2\tilde{\rho} + \tilde{P}_z = 0 \qquad (3)$$

$$\tilde{u}_x + \tilde{w}_z = 0 \qquad (4)$$

$$\tilde{w} = \tilde{\rho}_t + U\tilde{\rho}_x \qquad (5)$$

(The symbols retain the same meaning they have had in previous lectures.) Multiplying Eqs (2), (3), and (4) by $\tilde{u}, \tilde{w}, \tilde{p}$, respectively, and adding gives:

$$E_t + (EU + \tilde{p}\tilde{u})_x + (\tilde{p}\tilde{w})_z = -U_z\tilde{u}\tilde{w} \qquad (6)$$

where:

$$E = \frac{1}{2}(\tilde{u}^2 + \tilde{w}^2) + \frac{1}{2}N^2\tilde{\rho}^2 \qquad (7)$$

is the total wave energy (i.e., kinetic plus potential).

Achievement of steady solutions ($\frac{\partial}{\partial t} = 0$) and subsequent elimination of P and S from Eqs. (2), (3), (4), and (5), we obtain a single equation for the field of vertical velocity

$$\tilde{w}_{xx} + \tilde{w}_{zz} + l^2 \tilde{w} = 0 \tag{8}$$

This is the "lee wave equation" where

$$l^2(z) = \frac{N^2}{U^2} - \frac{U_{zz}}{U} \tag{9}$$

is the "Scorer parameter."

In general, $l(z)$ will vary considerably in the vertical. The boundary conditions at the ground is that the flow follow the terrain;

$$S(x,0) = h(x) = \rho_{00}^{-1/2} \hat{h}(x) \tag{10}$$

Eq. (8) is linear with coefficients independent of x. It is possible, then, to reduce (8) to an ordinary differential equation by taking the Fourier transform:

$$\tilde{w}(x,z) = Re \int_0^\infty \hat{w}(k,z)\, e^{ikx}\, dk$$

$$\hat{h}(x) = Re \int_0^\infty \hat{h}(k)\, e^{ikx}\, dk \tag{11}$$

From (11) and (8):

$$\hat{w}_{zz} + (l^2 - k^2)\hat{w} = 0 \qquad (12)$$

while the lower boundary condition becomes, using (10) and (11)

$$\hat{w}(k,0) = ikU\hat{h}(k) \qquad (13)$$

For regions in the atmosphere where l is constant, (12) may be solved to give:

a) For $k > l$ $\quad k^2 - l^2 \equiv m^2$, $m > 0$

$$\hat{w} = A_k e^{mz} + B_k e^{-mz} \qquad (14)$$

The wave structure is exponential (i.e., external wave).

b) For $k < l$ $\quad l^2 - k^2 \equiv \lambda^2$, $\lambda > 0$

$$\hat{w} = A_k e^{i\lambda z} + B_k e^{-i\lambda z} \qquad (15)$$

The wave structure is oscillatory in z (i.e., internal).

These results are identical to the results for waves in a quiescent atmosphere if Uk here is considered to be the "intrinsic frequency" σ of the waves.

In either case [a) or b)] two complex constants must be determined The single boundary condition (13) is not sufficient: another condition is required. In case a) the solution e^{mz} may be rejected as it

has infinite energy density, hence $A_k = 0$ when $k > \ell$. The principle in case b) cannot be used because the energy densities of $e^{i\ell z}$ and $e^{-i\ell z}$ are both constant with height. Historically, four different, but equivalent, methods have been used.

1. G. Lyra (1941) required that the solution $\tilde{w}(x, z)$ have no waves on the windward side of the mountain.

2. P. Queney (1948) introduced a "Rayleigh friction" (i.e., proportional to the velocity). Eq. (15) then becomes:

$$\hat{w} = A_k e^{i\ell z - nz} + B_k e^{-i\ell z + nz}$$

where "n" is related to the friction. Here $B_k = 0$ even for small "n" to keep the solution finite.

3. E. Höiland (1951) proposed to solve the time-dependent initial value problem and determine the stationary wave which develops for large t. This was carried out by Wurtele (1953) and Palm (1953) and had the same result as the work of Lyra and Queney.

4. Eliassen and Palm (1954) used the Sommerfeldt radiation condition to select the appropriate solution. The mountain is the source of the wave energy and the wave motion may be considered as a radiation of wave energy into the infinite half-space $z > 0$. The situation here is analogous to ship-waves (except that $c_g \parallel k$)

considered in a frame moving with the ship.

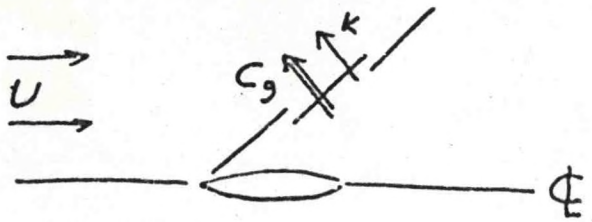

Ship Waves

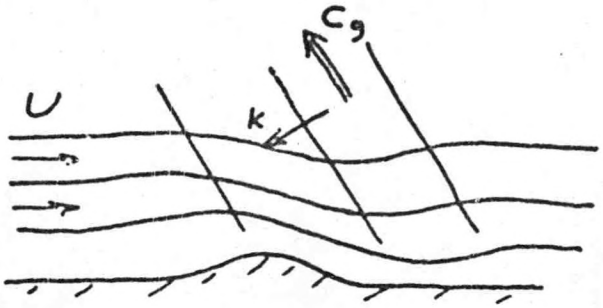

Mountain Waves

In both cases, the group velocity is directed away rather than toward the wave source.

Using Parceval's Theorem, the integrated energy flux is:

$$F = \int_{-\infty}^{\infty} \tilde{p}\tilde{w}\, dx = \pi Re \int_{0}^{\infty} \hat{p}\hat{w}^{*}\, dk \qquad (17)$$

The contribution from each wave number is k thus:

$$F^{k} = \pi Re(\hat{p}\hat{w}^{*})$$

Use of Eq. (3) gives:

$$F^{k} = \pi \frac{U}{k} Im(\hat{w}^{*}\hat{w}_{z}) \qquad (19)$$

For case a) $k > \ell$, this gives:

$$F^k = 2\pi \frac{\mu}{k} U \, Im(A_k B_k^*) \qquad (20)$$

which is zero if $B_k = 0$

For case b) $k < \ell$

$$F^k = \pi \frac{1}{k} U (|A_k|^2 - |B_k|^2) \qquad (21)$$

Here, $\hat{\omega} = A_k e^{i\lambda z}$ transfers energy up whereas $\hat{\omega} = B_k e^{-i\lambda z}$ transfers energy down. We require that all wave components transfer energy upwards, away from the source. Therefore, $B_k = 0$ for $k < \ell$. This condition is stronger than merely requiring that the net flux or the flux for each K be upward. This radiation condition can only be applied in Fourier space where the wave components are identifiable. This is equivalent, in physical space, to the condition:

$$\lim_{z \to \infty} \tilde{p}\tilde{w} \geq 0 \qquad \text{for all } x$$

but this form is difficult to use in practice.

In the Lyra-Queney solution ℓ is constant throughout the atmosphere:

$$k > \ell \,, \quad \hat{\omega}(k, z) = B_k e^{-\mu z}$$

$$\hat{\omega}(k, 0) = B_k = ikU\hat{h}(k)$$

$$k<l\,,\quad \hat{\omega}(k,z) = A_k\, e^{il z}$$

$$\hat{\omega}(k,0) = A_k = ikU\hat{h}(k)$$

The total solution consists of intregrals over the internal and external part of the spectrum.

$$\tilde{\omega}(x,z) = U\,Re\Big[\int_0^l ik\hat{h}(k)\, e^{i(lz+kx)}\,dk + \int_l^\infty ik\hat{h}(k)\, e^{-\mu z}\, e^{ikx}\,dk\Big] \qquad (23)$$

This is plotted in Fig. 1.

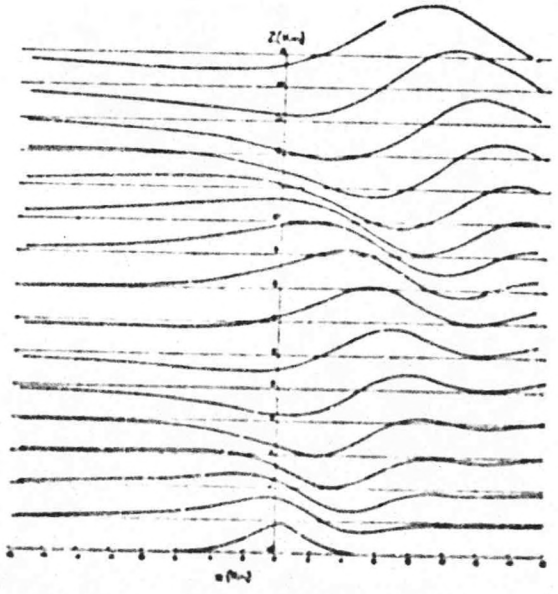

Fig. 1. Displacements of streamlines computed for an airstream for which l is approximately independent of height. (after Sawyer, 1960)

The energy and momentum flux

Suppose that $E \to 0$ when $x \to \pm\infty$ as for a wave system produced by a finite width range of mountains. Then from (6) in the steady state:

$$\frac{\partial}{\partial z}\int_{-\infty}^{\infty} \tilde{p}\,\tilde{w}\,dx = -U_z \int_{-\infty}^{\infty} \tilde{u}\,\tilde{w}\,dx \qquad (24)$$

From Eq. (2):

$$(U\tilde{u} + \tilde{p})_x + U_z \tilde{w} = 0$$

multiply by $U\tilde{u} + \tilde{p}$ and integrate to obtain

$$U_z \int_{-\infty}^{\infty} \tilde{p}\tilde{w}\,dx + U_z U \int_{-\infty}^{\infty} \tilde{u}\tilde{w}\,dx = 0$$

If $U_z \neq 0$

$$\int_{-\infty}^{\infty} \tilde{p}\,\tilde{w}\,dx = -U\int_{-\infty}^{\infty} \tilde{u}\tilde{w}\,dx \qquad (25)$$

Combining (24) and (25):

$$U\frac{\partial}{\partial z}\int_{-\infty}^{\infty} \tilde{u}\,\tilde{w}\,dx = 0$$

Therefore, when $U \neq 0$, the momentum flux

$$F_m = \int_{-\infty}^{\infty} \tilde{u}\,\tilde{w}\,dx \qquad (26)$$

is constant with height (Eliassen and Palm, 1961).

The energy flux is

$$F = -UF_m$$

so when F is upward, F_m is downward. Through the mechanism of wave resistance, the mountain acts as a sink of momentum.

Eqs. (24), (25), (26), and (27) do not depend upon ℓ^2 being constant with height, but are generally valid when $E \to 0$ for $|x| \to \infty$. Additionally, (25) is valid even where $U_z = 0$

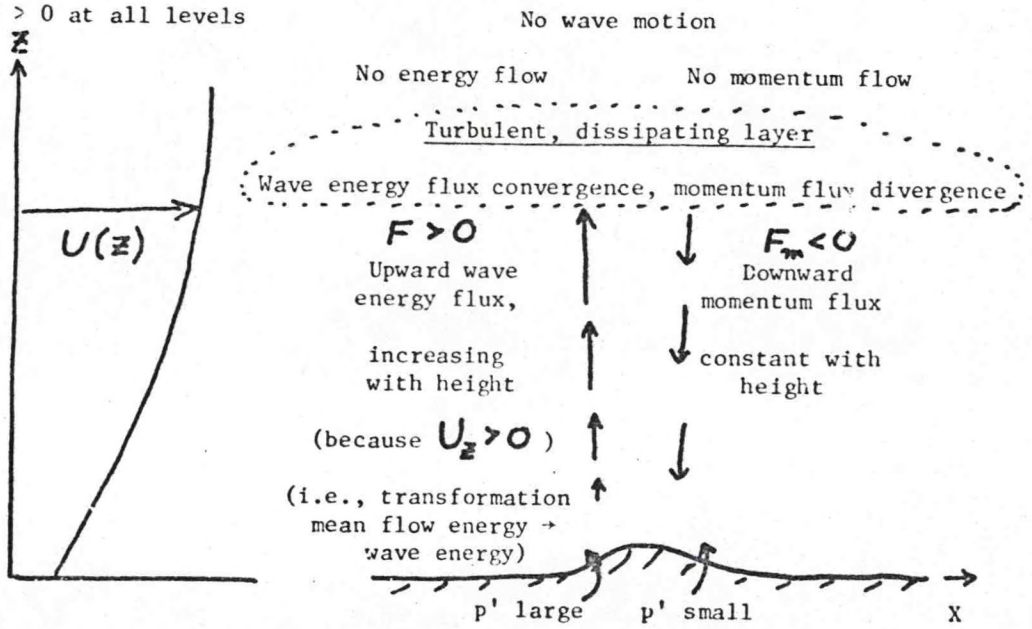

The mountain is the source of wave energy,,so p' at ground level must be larger on the windward than on the leeward side, in order for

$$\int \tilde{p}\,\tilde{w}\,dx > 0$$

In a layer with no dissipation the energy flux F will change with height in proportion to U. If U increases with height, there is a

positive flux divergence of wave energy, implying transformation from mean flow energy into wave energy.

Suppose the wave reaches a turbulent layer where the wave energy is totally dissipated to the extent that there is no wave motion above it. This layer will then be a sink of wave energy and will transform it into other kinds of energy.

Below the dissipating layer, the momentum flux is downward and constant with height, so there is no removal of momentum from the current. Momentum is deposited onto the ground through the pressure difference between the two mountain slopes. Momentum is extracted from the dissipating layer at the same rate, and this layer is therefore slowed down (Bretherton, 1969). These conditions will then set up a lateral circulation (much like the Ekman layer circulation), which through the action of the Coriolis force will redistribute the momentum vertically. In this way, the wave resistance will affect all levels.

References

Bretherton, F. P., 1969: Momentum transport by gravity waves. Quart. J. R. Met. Soc., 95, 213.

Eliassen, A. and E. Palm, 1954: Energy flux for combined gravity-sound waves. Inst. Weather and Climate Res., Norw. Acad. Sciences and Letters. Publ. 1.

_____ and _____, 1961: On the transfer of energy in stationary mountain waves. Geof. Publ., 22, No. 3.

Höiland, E., 1951: Dept. of Meteor., U.C.L.A., Report

Lyra, G.: Theone d. Stationain Leewellenshörnnug in Freier Atmosphäre. Z. Angew. Math. n. Mech., 23, 1.

Palm, E., 1953: On the formation of surface waves in a fluid flowing over a corrugated bed and on the development of mountain waves. Astrophysica Norvegica, 5, No. 3.

Queney, P., 1947: Theory of Perturbations in Stratified currents with application to airflow over mountain barriers. Univ. of Chicago, Misc. Reports No. 23.

Wurtele, M., 1953: The initial value lee wave problem for the isothermal atmosphere. Scientific Rep. No. 3, Sierra Wave Project, U.C.L.A.

AIRFLOW OVER MOUNTAINS. I.

Lecturer: Dr. A. Eliassen Notes by: K.-Y. Fung

Date: July 22, 1974 L. Gidel

A case where ℓ is constant throughout the atmosphere has been previously treated. It showed that energy flux is upward to infinity and momentum flux is downward on the lee side of a mountain. The wave motion is relatively weak at low levels and is strongly damped downstream. Scorer (1949) points out that lee waves are often strong in the lower troposphere, with many wave troughs and ridges downstream, and that this must be due to a variation of ℓ with height. This lecture takes into consideration a two layer atmosphere and investigates how it leads to wave trapping.

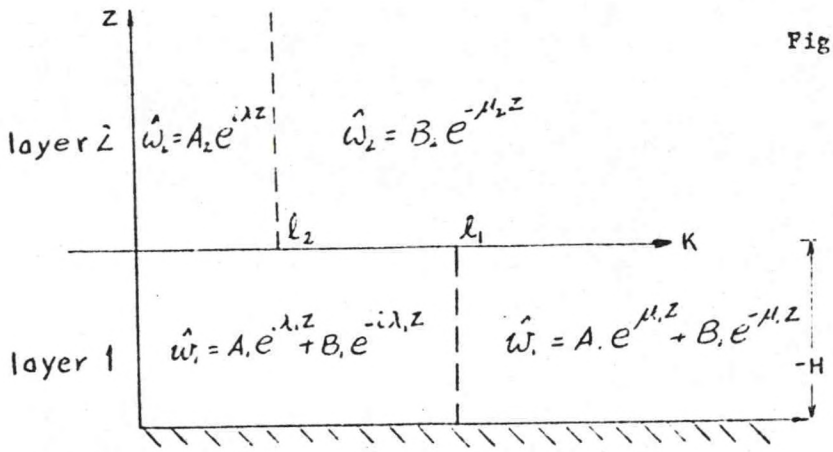

Fig. 1

where: $\lambda_1 = \sqrt{\ell_1^2 - K^2}$ $\lambda_2 = \sqrt{\ell_2^2 - K^2}$

$\mu_1 = \sqrt{K^2 - \ell_1^2}$ $\mu_2 = \sqrt{K^2 - \ell_2^2}$

Let $z = 0$ be the level separating the lower layer with Scorer number ℓ_1, from the upper layer with Scorer number ℓ_2. The solutions satisfying the transformed governing equation

$$\hat{w}_{zz} + (\ell^2 - k^2)\hat{w} = 0$$

in different regions are shown in Fig. 1. It is assumed that there are no waves coming from infinity. (This is true even if the fact the linear solution cannot be valid at all levels $z > 0$ is taken into account. At a certain height, dissipation must take place as a sink to all wave energy.) A_1 can be determined from the boundary condition at $z = -H$ and B_1, A_2, B_2, are determined by assuming $\hat{w}$ and $\frac{d\hat{w}}{dz}$ are continuous at $z = 0$. That is,

$$\hat{w}_1 = \hat{w}_2 \quad ; \quad \hat{w}_{1z} = \hat{w}_{2z} \qquad \text{at } z = 0 \qquad (32)$$

This is true provided $\ell(z)$ does not contain a δ-function or dipole at $z = 0$ (no abrupt change in θ or U with height).

Consider separately the cases $k < \ell_2$, $\ell_2 < k < \ell_1$, $k > \ell_1$:

1) $k < \ell_2$: internal motion in both layers. Applying the matching conditions (32),

$$B_1 = \frac{\lambda_1 - \lambda_2}{\lambda_1 + \lambda_2} A_1 \qquad (33)$$

$$A_2 = \frac{2\lambda_1}{\lambda_1 + \lambda_2} A_1 \qquad (34)$$

These equations give amplitude $|B_1|$, $|A_2|$ and phase ($\arg B_1$, $\arg A_2$) of the reflected (B_1) and transmitted (A_2) waves respectively in terms of the incoming wave (A_1). The energy fluxes of

the three waves are

$$\pi \frac{U(0)}{K} \lambda_1 |A_1|^2 \qquad -\pi \frac{U(0)}{K} \lambda_1 |B_1|^2$$

$$\pi \frac{U(0)}{K} \lambda_2 |A_2|^2$$

The reflection coefficient $\mathcal{R}$ is the ratio of the energy flux of the reflected wave to the incoming wave:

$$\mathcal{R} = \frac{|B_1|^2}{|A_1|^2} = \frac{(\lambda_1 - \lambda_2)^2}{(\lambda_1 + \lambda_2)^2} \tag{35}$$

and the transmission coefficient

$$\tau = \frac{\lambda_2 |A_2|^2}{\lambda_1 |A_1|^2} = \frac{4 \lambda_1 \lambda_2}{(\lambda_1 + \lambda_2)^2} = 1 - \mathcal{R} \tag{36}$$

showing that there is partial reflection. The solution in the two layers is:

$$\hat{w}_1 = \frac{2A_1}{\lambda_1 + \lambda_2} (\lambda_1 \cos \lambda_1 z + i \lambda_2 \sin \lambda_1 z) \tag{37}$$

$$\hat{w}_2 = \frac{2 \lambda_1 A_1}{\lambda_1 + \lambda_2} e^{i \lambda_2 z}$$

2) $\ell_2 < K < \ell_1$: internal wave in lower layer, external wave in the upper layer. The matching conditions give:

$$B_1 = \frac{\lambda_1 - i\mu_2}{\lambda_1 + i\mu_2} A_1 \qquad (38)$$

$$B_2 = \frac{2\lambda_1}{\lambda_1 + i\mu_2} A_1 \qquad (39)$$

Since the external wave in the upper layer cannot transfer energy, total reflection and hence trapping occurs. Here,

$$R = \frac{|B_1|^2}{|A_1|^2} = 1 \quad ; \quad Z = 0 \qquad (40)$$

Also:

$$\hat{w}_1 = \frac{2A_1}{\lambda_1 + i\mu_2} (\lambda_1 \cos\lambda_1 Z - \mu_2 \sin\lambda_1 Z) \qquad (41)$$

Nodal surfaces occur when $|\hat{w}_1| = 0$ at heights Z_n:

$$Z_n = \frac{1}{\lambda_1} \tan^{-1}\left(\frac{\lambda_1}{\mu_2}\right) \qquad (42)$$

3) $K > \ell_1$: External wave in both layers ($\mu_2 > \mu_1$)

$$B_1 = (\mu_2 + \mu_1) A_1 / (\mu_2 - \mu_1) \; ; \quad B_2 = \frac{2\mu_1 A_1}{\mu_2 - \mu_1}$$

The energy flux is zero in both layers.

$$\hat{w}_1 = -\frac{2A_1}{\mu_2 - \mu_1} (\mu_1 \cosh\mu_1 Z - \mu_2 \sinh\mu_1 Z) \qquad (43)$$

$$|\hat{w}_1| \neq 0 \qquad \text{for all} \qquad Z < 0$$

Suppose the ground is at level $Z = -H$ and the boundary condition is:

$$\hat{w}_1(K_1 - H) = i K U_0 \hat{h}(K) \qquad (44)$$

The solutions of $\hat{w}$, in three cases are:

1) from (6)

$$\hat{w}_{(1)} = i K U_0 \hat{h} \frac{\lambda_1 \cos \lambda_1 z + i \lambda_2 \sin \lambda_1 z}{\lambda_1 \cos \lambda_1 H - i \lambda_2 \sin \lambda_1 H} \qquad (45)$$

2) from (10)

$$\hat{w}_{(2)} = i K U_0 \hat{h} \frac{\lambda_1 \cos \lambda_1 z - \mu_2 \sin \lambda_1 z}{\lambda_1 \cos \lambda_1 H + \mu_2 \sin \lambda_1 H} \qquad (46)$$

3) from (12)

$$\hat{w}_{(3)} = i K U_0 \hat{h} \frac{\mu_1 \cos \mu_1 z - \mu_2 \sin \mu_1 z}{\mu_1 \cos \mu_1 H + \mu_2 \sin \mu_1 H} \qquad (47)$$

Hence:

$$w' = \int_0^{\ell_2} \hat{w}_{(1)} e^{ikx} dk + \int_{\ell_2}^{\ell_1} \hat{w}_{(2)} e^{ikx} dk + \int_{\ell_1}^{\infty} \hat{w}_{(3)} e^{ikx} dk \qquad (48)$$

If $\hat{w}_{(2)}$ does not have a pole for $\ell_2 < k < \ell_1$, then it follows from the Riemann Lebesques Lemma that

$$\lim_{|x| \to \infty} w' = 0$$

and there are no trapped waves. However, suppose that the denominator of (46) is zero for certain real values $K = K_\alpha$, $K = K_\beta$, $K =$ etc, in the internal (ℓ_2, ℓ_1) where $K_\alpha, K_\beta, \cdots$ are the roots of

$$\tan \lambda_1 H = -\frac{\lambda_1}{\mu_2} \qquad \lambda_1 = \sqrt{\ell_1^2 - K^2}$$

It can easily be seen that these are simple poles. The number of poles depends on the value $H\sqrt{\ell_1^2-\ell_3^2}$

F.g 2

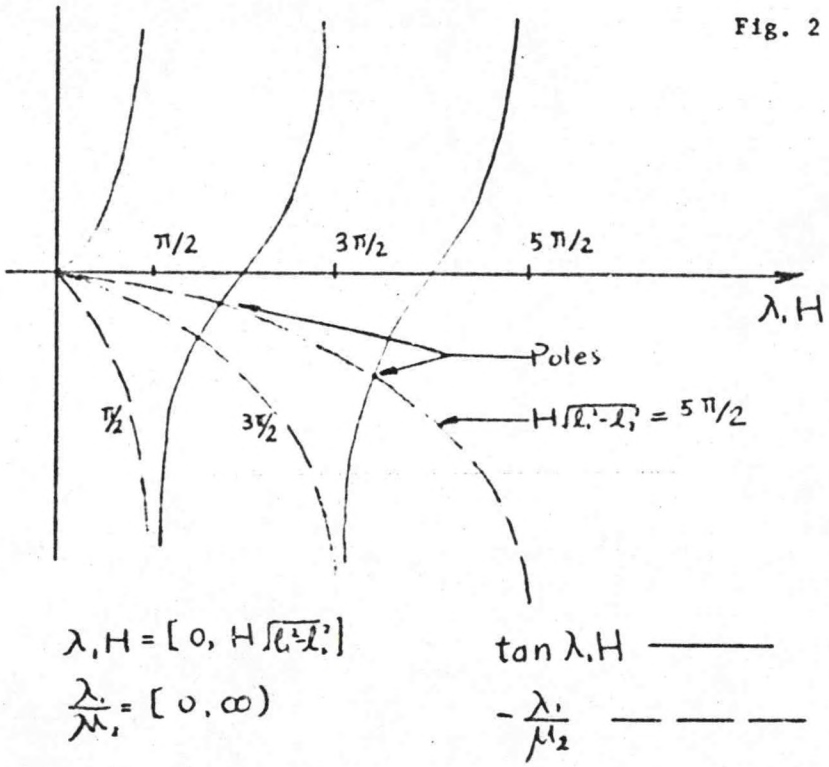

Fig. 2

As shown in Fig. 2, for $H\sqrt{\ell_1^2-\ell_3^2} < \pi/2$, there are no poles; $\frac{\pi}{2} < H\sqrt{\ell_1^2-\ell_3^2} < \frac{3\pi}{2}$, one pole; $\frac{3\pi}{2} < H\sqrt{\ell_1^2-\ell_3^2} < \frac{5\pi}{2}$ two poles; etc. $\hat{W}_1(2)$ of (48) does not have a meaning when the integral goes through the points $K = K_{\alpha,\beta}$ ... If we assume K is complex, by introducing some dissipative mechanism in the governing equation, the path of integration may be changed from the real K-axis to that shown in Fig. 3.

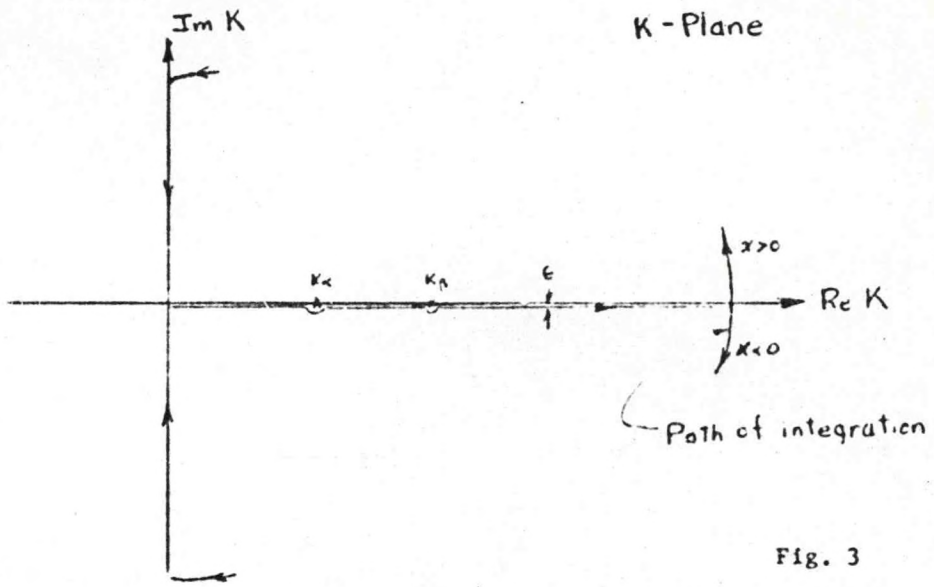

Fig. 3

Letting $\epsilon \to 0$, calculate w' using the method of contour integration and the residue theorem. For $\chi > 0$, the contour integration must be through the upper half K plane, and therefore picks up residues. For $\chi < 0$, the contour integration must be through the lower half of the K plane, and therefore picks up no residues. Thus, on the upwind side, there is no wave motion and there are infinite undamped wave trains with wave number $K_{\alpha,3,\ldots}$, on the lee side. The result for $K = K_\alpha$ is:

$$w'_{1(pole)} = Re\left\{2\pi i \frac{kU}{K_\alpha}\left(\lambda_{1\alpha}\cos\lambda_{1\alpha}3 - \mu_{2\alpha}\sin\lambda_{1\alpha}Z\right)e^{iK_\alpha\chi}\right\}$$

The trapped wave will not transport wave energy upward (it has vertical phase line, but instead the wave energy will escape horizontally downstream).

The trapped wave carries negative momentum downstream, and whenever wave energy is dissipated negative momentum is deposited.

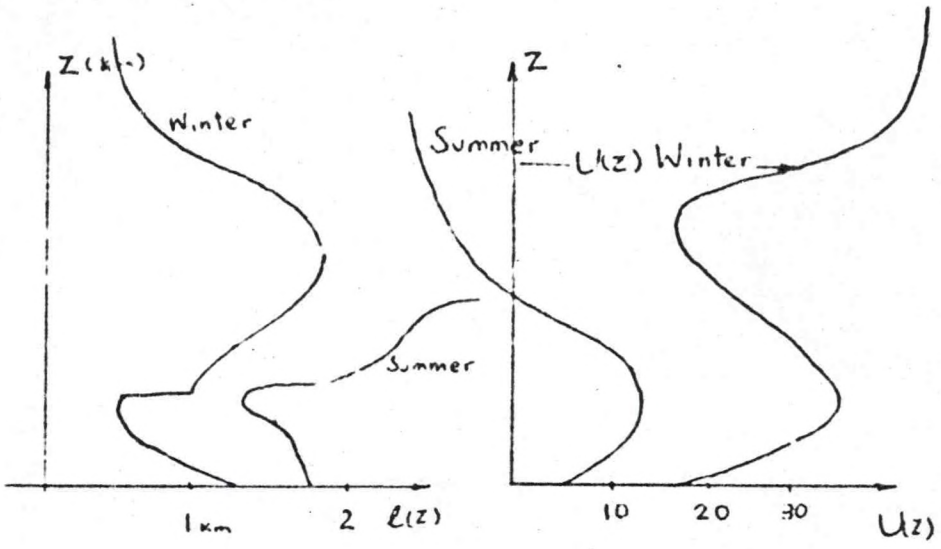

Fig. 4

Fig. 4 shows a typical variation of ℓ with height in the zone of westerlies.

The approximation ℓ =const. does not seem to be a good one anywhere. Still it is useful for quick results. Eliassen and Palm (1960) did a three layer model case. They showed that the middle layer with the smallest ℓ , effectively reflects the shortest waves. Cases where $\ell \neq$ constant have been studied. Sawyer, Palm, and Foldvik use $\ell^2 \sim e^{-\gamma z}$, leading to Bessel functions; and Kiemp and Lilly (1974) used a second order polynomials for ℓ^{-2} , with the result in terms of trigonometric and logarithmic functions.

The interface condition we have been using may not be satisfied in some cases. The kinematic boundary condition at the interface is

$$\Delta \zeta = \zeta_2 - \zeta_1 = 0$$

From

$$w = U \zeta_x$$

$$\Delta w = w_2 - w_1 = (U_2 - U_1)\, \zeta_x$$

$$= \Delta U\, \zeta_x$$

therefore $\Delta w = 0$

only if $\Delta U = 0$

Integrate the lee wave equation

$$\tilde{w}_{zz} + \tilde{w}_{xx} + \left(\frac{N^2}{U^2} - \frac{U_{zz}}{U}\right)\tilde{w} = 0$$

with respect to x. We have the equation for ζ

$$U^2 \zeta_{xx} + (U^2 \zeta_z)_z + (g \ln \theta)_z \zeta = 0$$

Integrate over a thin transition layer with respect to z

$$\Delta(U^2 \zeta_z) + \Delta(g \ln \theta)\zeta = 0$$

We obtain the second interface condition. If $\Delta U = 0$ and $\Delta \theta = 0$, then the interface conditions are

$$\Delta w = 0 \quad , \Delta w_z = 0$$

References

Scorer, R. S., 1949: Theory of airflow over mountains. Quart. J. R. Met. Soc., 86, 326.

AIRFLOW OVER MOUNTAINS II: NON-LINEAR THEORY

Lecturer: Dr. A. Eliassen Notes by: A. Friend

Date: July 23, 1974 J. Price

I. Introduction

This lecture considers the finite amplitude problem involved with airflow over mountains. The wave motions discussed have relatively short wavelength, and short time scale (Coriolis effects are not important). Vertical accelerations are also considered, and the problem is developed according to the methods of Long (1953) and Yih (1960).

II. General Development

Development begins by defining potential density, q, for which the following relations hold

$$\varrho = q\,\gamma(p) \qquad \gamma(p_r) = 1 \qquad \frac{Dq}{dt} = 0 \qquad \gamma^{-1} = \frac{d\Pi}{dp} \tag{1}$$

where p_r is a reference pressure at which the function $\gamma(p)$ equals unity, ϱ is the fluid density, $Dq/dt = 0$ expresses the conservation of q for each particle, and $\gamma^{-1} = d\Pi/dp$ is another function of pressure which is useful during the later stages of development. When the fluid is an ideal gas, the relations in (1) become:

$$q = \frac{p_r}{R\theta} \qquad \gamma = \left(\frac{p}{p_r}\right)^{c_v/c_p} \qquad \Pi = \frac{c_p}{R}\,p_r\left(\frac{p}{p_r}\right)^{R/c_p} \tag{2}$$

where c_v is the specific heat at constant volume, c_p is the specific heat at constant pressure, R is the universal gas constant, and θ is potential temperature. In the case of an incompressible fluid the

equations in (1) become:

$$\mathcal{F} = \rho \qquad \gamma = 1 \qquad \Pi = p \tag{3}$$

The solutions obtained here are derived for steady flow of an ideal gas in the xz-plane ($\partial/\partial y = 0$).

The momentum equation is then:

$$\mathbf{V}\cdot\nabla\mathbf{V} + \nabla\phi + \frac{1}{\rho}\nabla p = 0 \tag{4}$$

where $\phi = gz$ and the continuity equation is:

$$\nabla\cdot(\rho\mathbf{V}) = 0 \tag{5}$$

From (1) and the steady flow condition, we get the conservation of potential density:

$$\mathbf{V}\cdot\nabla\mathcal{F} = 0 \tag{6}$$

From (5) and (6) we have that

$$\nabla\cdot(\gamma\mathbf{V}) = 0 \tag{7}$$

and so may define a streamfunction ψ such that $\gamma\mathbf{V} = \vec{j}\times\nabla\psi$ where $\vec{j}$ is in the y direction. Vorticity is defined in the usual manner.

$$\nabla\times\mathbf{V} = \omega\vec{j} \tag{9}$$

where $\omega = \nabla\cdot\left(\frac{\nabla\psi}{\gamma}\right)$

From (4), and using the definition of Π in (1),

$$\mathbf{V}\cdot\nabla\mathbf{V} + \nabla\phi + \frac{1}{\rho}\nabla\pi = 0$$

or

$$\omega\vec{j}\times\mathbf{V} + \nabla\left(\phi + \tfrac{1}{2}V^2 + \frac{\pi}{\rho}\right) - \pi\nabla\frac{1}{\rho} = 0 \qquad (10)$$

Taking the dot product of (10) with $\mathbf{V}$ we get:

$$\mathbf{V}\cdot\omega\vec{j}\times\mathbf{V} + \mathbf{V}\cdot\nabla\left(\phi + \tfrac{1}{2}V^2 + \frac{\pi}{\rho}\right) - \mathbf{V}\cdot\left(\pi\nabla\frac{1}{\rho}\right) = 0$$

The first and third terms vanish from (6). The vector $\nabla\left(\phi + \frac{1}{2}V^2 + \frac{\pi}{\rho}\right)$ must be perpendicular to $\mathbf{V}$ and thus a function only of ψ. In fact, $\phi + \frac{1}{2}V^2 + \frac{\pi}{\rho}$ is the Bernoulli function for this system and will be defined as:

$$B(\psi) = \phi + \tfrac{1}{2}V^2 + \frac{\pi}{\rho} \qquad (11)$$

From (6) we may also deduce

$$\rho = \rho(\psi) \qquad (12)$$

From Eqs. (8) and (10):

$$-\frac{\omega}{\gamma}\nabla\psi + \nabla B - \pi\nabla\frac{1}{\rho} = 0 \qquad (13)$$

or:

$$\frac{\omega}{\gamma} + \pi\frac{d\left(\frac{1}{\rho}\right)}{d\psi} = \frac{dB}{d\psi} \qquad (14)$$

Eq. (14) is the vorticity equation relating vorticity to pressure along a streamline. Eq. (14) may also be written:

$$\frac{\omega}{\gamma} - \frac{\rho_\psi}{\rho}\left(\phi + \tfrac{1}{2}V^2\right) = \frac{1}{\rho}\frac{d(\rho B)}{d\psi} \qquad (15)$$

Assuming that the flow is straight and horizontal far upstream, and that $U_o(z)$, $\pi_o(z)$, and $\phi_o(z)$, the velocity, pressure, and potential density functions at an upstream point o are known, it may be assumed that $\rho(\psi)$ and $B(\psi)$ are also known from these conditions. Eqs. (14) and (15), then, together with (8) and (9), are differential equations for ψ. However, they also contain the unknown pressure functions π and γ.

III. The Work of Long, Yih, and Claus

Long (1953) used the vorticity equation in the form (15) for an incompressible fluid ($\gamma = 1$). Eq. (15) becomes:

$$\nabla^2\psi + \frac{\rho_\psi}{\rho}\left(\phi + \tfrac{1}{2}\nabla\psi^2\right) = \frac{1}{\rho}\frac{d(\rho B)}{d\psi} \qquad (16)$$

Long was able to integrate (16) for some special cases and verify the solutions with laboratory experiments. Long's boundary conditions were $\psi = C$ along a lower boundary of specified shape, and constant ψ along a horizontal upper boundary.

Yih (1960, 1965) introduced the transformation:

$$W' = \rho^{\frac{1}{2}} W \qquad (17)$$

with:

$$\nabla\cdot(\gamma W') = 0 \qquad W' = \vec{j}\times\frac{\nabla\psi'}{\gamma} \qquad (18)$$

$$\nabla\times W' = \omega'\vec{j} \qquad \omega' = \nabla\cdot\left(\frac{\nabla\psi'}{\gamma}\right) \qquad (19)$$

Using this transformation, Eq. (4) may be written:

$$W'\cdot\nabla W' + \rho\nabla\phi + \nabla\pi = 0$$

or:

$$\omega' \vec{J} \times \vec{V}' + \nabla(\mathcal{F}B) - \phi \nabla \mathcal{F} = 0 \qquad (20)$$

with $\mathcal{F}B = \mathcal{F}\phi + \frac{1}{2}V^2 + \Pi$. Hence

$$\frac{\omega'}{\gamma} = \frac{\partial(\mathcal{F}B)}{\partial \psi'} - \phi \frac{\partial \mathcal{F}}{\partial \psi'} \qquad (21)$$

or:

$$\nabla \cdot \left(\frac{\nabla \psi'}{\gamma} \right) = \gamma \left[\frac{\partial(\mathcal{F}B)}{\partial \psi'} - \phi \frac{\partial \mathcal{F}}{\partial \psi'} \right] \qquad (22)$$

This equation maybe integrated for atmospheric conditions if an approximation is made for the unknown function $\gamma(\mathcal{F})$. Claus (1964) approximated $\gamma(\mathcal{F})$ by setting

$$B(\psi') \approx \phi + \frac{\Pi}{\mathcal{F}(\psi')} \qquad (23)$$

and ignoring $\frac{1}{2}V^2$. This gives $\mathcal{F}$ as a function of ψ' and z. An alternate approach, which might be better, is to use hydrostatic pressure in $\gamma(\mathcal{F})$.

For some very special cases, Eq. (22) becomes a linear equation in ψ' which can be solved by standard methods. Claus (1964) computed solutions to Eq. (22) for a mountain ridge with a horizontal lid (constant ψ') as the upper boundary condition. The rationale for this boundary condition in atmospheric applications is that the tropopause, due to its strong stability, can be considered as a lid. Linear theory provides proof that this upper boundary condition is incorrect, since the lid is a total reflector, and causes the loss of the continuous spectrum of waves transfering energy upward. The only solutions

obtained are for trapped waves (if they exist).

The following figures (Yih, 1965) illustrate the dependence of Claus' solution upon compressibility and upstream functions.

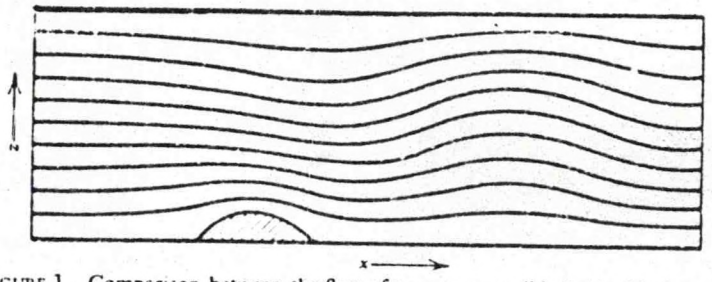

FIGURE 1. Comparison between the flow of an incompressible fluid with that of a compressible fluid. Incompressible case (after Claus, [1961 and 1964]). (*J. Fluid Mech., 19, part 2. Courtesy of the Cambridge Univ. Press.*)

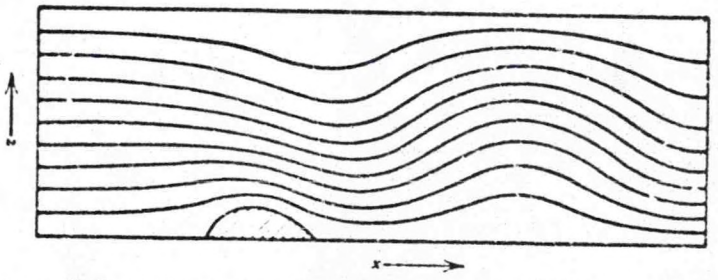

FIGURE 2. Comparison between the flow of an incompressible fluid with that of a compressible fluid. Compressible case (after Claus [1961 and 1964]). (*J. Fluid Mech., 19, part 2. Courtesy of the Cambridge Univ. Press.*)

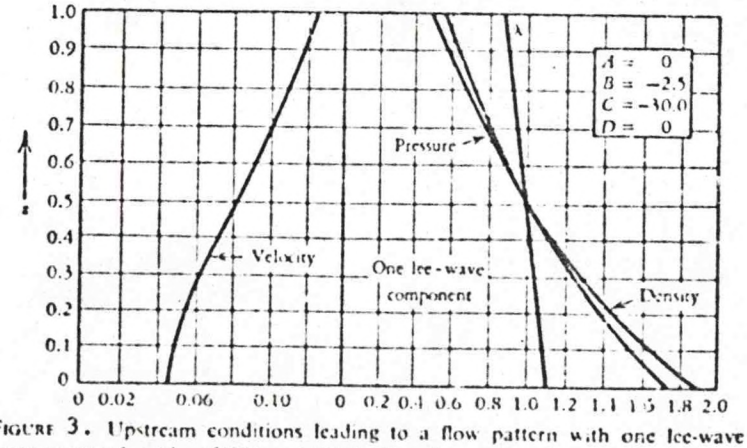

FIGURE 3. Upstream conditions leading to a flow pattern with one lee-wave component (after Claus [1961 and 1964]). The velocity is in terms of $\sqrt{gd}$, the pressure is in terms of a reference pressure p_0, and the density is in terms of a reference density ρ_0. (*J. Fluid Mech., 19, part 2. Courtesy of the Cambridge Univ. Press.*)

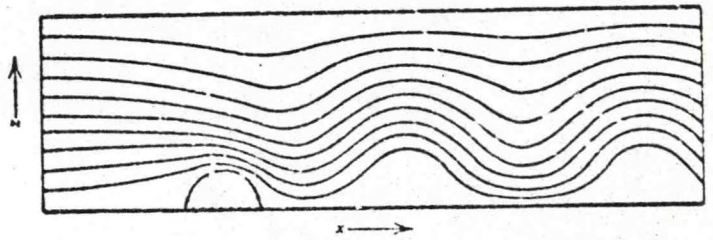

FIGURE 4. Flow pattern with one lee-wave component (after Claus [1961 and 1964]). (*J. Fluid Mech., 19, part 2. Courtesy of the Cambridge Univ. Press.*)

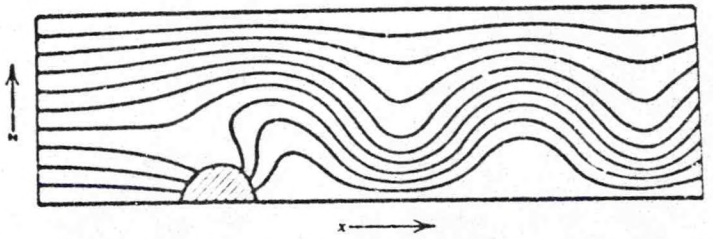

FIGURE 5. Isotherms in the flow with one lee-wave component (after Claus [1961 and 1964]). (*J. Fluid Mech., 19, part 2. Courtesy of the Cambridge Univ. Press.*)

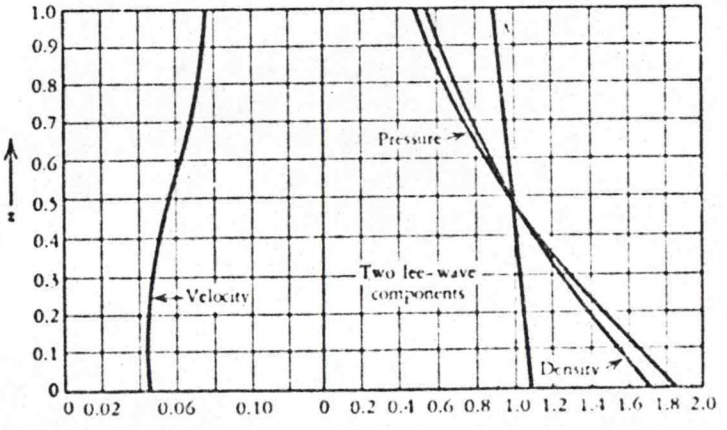

FIGURE 6. Upstream conditions leading to a flow pattern with two lee-wave components (after Claus [1961 and 1964]). The velocity is in terms of $\sqrt{gd}$, the pressure is in terms of a reference pressure p_0, and the density is in terms of a reference density ρ_0. (*J. Fluid Mech., 19, part 2. Courtesy of the Cambridge Univ. Press.*)

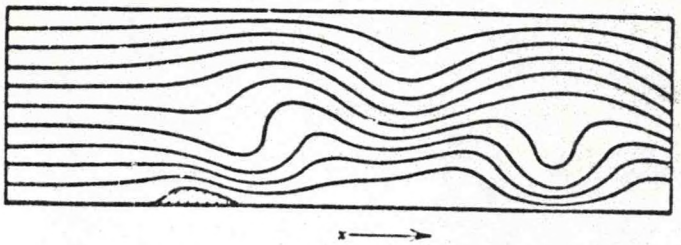

FIGURE 7. Flow pattern with two lee-wave components (after Claus [1961 and 1964]). (*J. Fluid Mech., 19, part 2. Courtesy of the Cambridge Univ. Press.*)

IV. Blocking

The steady state two-dimensional problem for a given mountain ridge, with given upstream conditions, does not always have a solution. If the upstream velocity at low levels is too weak and the static stability sufficiently strong, the low level air is not able to climb across the mountain. The term for this non-linear phenomenon is blocking. The problem must be reformulated as an initial value problem because a wave will move upstream and change the upstream conditions.

One sort of criterion for "no blocking" may be obtained from the Bernoulli equation by comparing two points on the ground streamline. One point ($z = 0$) is far upstream and the other is a point ($z = z_T$) on a mountain top. From Bernoullis's equation,

$$\frac{1}{2}U_0^2 + \frac{\pi_0}{\rho_0} = g z_T + \frac{1}{2}U_T^2 + \frac{\pi_T}{\rho_0} \qquad (24)$$

Since $\frac{1}{2}U_T^2 \geq 0$ (we assume $U_T = 0$ if blocking does occur),

$$\frac{1}{2}U_0^2 \geq g z_T - \frac{\pi_0 - \pi_T}{\rho_0} \qquad (25)$$

This criterion can be used only if an approximation can be made for the unknown π_T . One approach is to assume that π_T is hydrostatic.

Strictly speaking, blocking is a two-dimensional phenomenon which does not occur in the three-dimensional case of a limited mountain. In the three dimensional case, the low level air may move around the mountain: however, for long mountain ridges, nearly stagnant air often occurs on the upwind side. In Norway it is not unusual to have blocking with either east or west winds and dense air at low levels.

References

Claus, A., 1964: Large-amplitude motion of a compressible fluid in the atmosphere, J. Fluid Mech., 19, 267-289.

Long, R. R., 1953: Some aspects of the flow of stratified fluids. I. A theoretical investigation, Tellus, 5, 42-57.

_____, 1955: Some aspects of the flow of stratified fluids; III. Continuous density gradients. Tellus, 7, 341-357.

Yih, C.-S., 1960: Exact solutions for steady two-dimensional flow of a stratified fluid, J. Fluid Mech., 9, 161-174.

_____, 1965: Dynamics of Nonhomogeneous Fluids, MacMillan Co., New York.

MESOSCALE MOUNTAIN WAVES

Lecturer: Dr. A. Eliassen Notes by: L. W. Chang

Date: July 24, 1974 M. S. Tracton

I. The Spectrum of Mountain Waves

The general solution to the problem of airflow over mountains is discussed in order to gain insight into the nature of the solution which applies when mesoscale ($L \sim 100 - 1000$ km) mountain waves are explicitly considered.

For small disturbances of a straight baroclinic current with no horizontal wind shear and f =constant, the basic current is set as:

$$\left.\begin{aligned} \frac{\partial p_0}{\partial y} &= -fU\rho_0 \\ \frac{\partial p_0}{\partial z} &= -g\rho_0 \\ \frac{\partial U}{\partial y} &= 0 \end{aligned}\right\} \qquad (1)$$

The perturbation variables are:

$$U(z) + u'(x,z,t),\ v'(x,z,t),\ \omega'(x,z,t)$$

$$v' = \frac{dh'}{dt},\ \omega' = \frac{ds'}{dt},\ p'(x,z,t),\ \rho'(x,z,t)$$

Here $\frac{d}{dt} = \frac{\partial}{\partial t} + U\frac{\partial}{\partial x}$

The perturbation equations are:

$$\rho_0 \frac{du'}{dt} - \rho_0 fv' + \rho_0 \omega' U_z + p'_x = 0 \qquad (2)$$

$$\rho_0 \frac{dv'}{dt} + \rho_0 fu' = 0 \qquad (3)$$

$$\rho_0 \frac{dw'}{dt} + g\rho' + p'_z = 0 \qquad (4)$$

$$u_x' + w_z' = 0 \qquad (5)$$

We introduce new variables: $u'=\rho_0^{-1/2}u$, $\omega'=\rho_0^{-1/2}\omega$, $v'=\rho_0^{-1/2}v$, $\eta'=\eta\rho_0^{-1/2}$, $z'=\rho_0^{-1/2}z$, $p=\rho_0^{+1/2}p'$

Upon substitution of these new variables into Eqs. (1), (2), (3), (4), ρ_0 disappears from the perturbation equations:

$$\frac{du}{dt} - fv + U_z\omega + p_x = 0 \tag{6}$$

$$\frac{dv}{dt} + fu = 0 \tag{7}$$

$$\frac{d\omega}{dt} - fU_z\eta + N^2\zeta + p_z = 0 \tag{8}$$

$$u_x + \omega_z = 0 \tag{9}$$

The vertical component of vorticity "ω" is $\omega=\frac{\partial v}{\partial x}$, where the horizontal component of divergence $\delta=\frac{\partial u}{\partial x}$. Therefore, from Eqs. (6) and (7), we obtain, respectively, the vorticity equation and the divergence equation:

$$\frac{d\omega}{dt} + f\delta = 0 \tag{10}$$

$$n_\delta\frac{d\delta}{dt} - f\omega + n_\delta U_z\omega_x + p_{xx} = 0 \tag{11}$$

Here n_δ is equal to unity or zero. When $n_\delta = 0$, we denote the quasi-geostrophic assumption for the perturbation field.

In order to eliminate η and ζ from Eq. (8), apply "$\frac{d}{dt}$" to Eq. (8):

$$n_\omega\frac{d^2\omega}{dt^2} - fU_z v + N^2\omega + \frac{d}{dt}p_z = 0 \tag{12}$$

where:

$$n_\omega = \begin{cases} 0 & \text{quasi-hydrostatic assumption} \\ 1 & \text{non-hydrostatic assumption.} \end{cases}$$

Assuming a steady state solution ($\frac{\partial}{\partial t}=0$), apply Fourier transforms to Eqs. (10), (11), (12):

$$u = Re\int_0^\infty \hat{u}(K,z)\, e^{ikx}\, dk$$

$$v = Re\int_0^\infty \hat{v}(K,z)\, e^{ikx}\, dk$$

$$w = Re\int_0^\infty \hat{w}(k,z)\, e^{ikx}\, dk$$

We get the characteristic equation for :

$$\frac{\partial}{\partial z}\left[\left(\frac{f^2}{U^2k^2}-n_s\right)\hat{w}_z\right] - (l^2-n_w k^2)\,\hat{w}=0 \qquad (13)$$

where:

$$l^2=\frac{N^2}{U^2}-n_s\left(\frac{U_{zz}}{U}\right)$$

U, U_{zz} and l^2 are assumed to be functions of "z" only.

The property of Eq. (13) depends upon the wave number k. Under normal atmospheric conditions, N is of the order $10^{-2}\ sec^{-1}$ and $l \sim N/U$. Therefore, $f^2/U^2k^2 \sim 10^{-4}$.

We may distinguish between three cases:

A. Gravity Waves

$$k \sim \frac{N}{U}$$

In this case, non-hydrostatic, nongeostrophic assumptions must be set. $n_w = n_s = 1$ and $f^2/U^2k^2 \sim 10^{-4}$

Therefore $n_s \gg f^2/U^2k^2$ in Eq. (13). Coriolis effect can be neglected. The differential equation (13) becomes:

$$\hat{w}_{zz} + (l^2-k^2)\,\hat{w} = 0 \qquad (14)$$

This is the "lee wave equation."

B. Gravity-Inertial Waves

$k \sim \frac{f}{U}$

In this case, $\rho^2 \gg k^2$, and the quasi-static approximation $\eta_\omega = 0$ may be applied. The Eq. (13) becomes

$$\frac{\partial}{\partial z}\left[\left(1 - \frac{f^2}{\omega^2 k^2}\right)\hat{w}_z\right] + l^2 \hat{w} = 0 \qquad (15)$$

The equation has a singularity at $k = f/U$. For larger values of k, solutions generally oscillate with height, whereas for $k < f/U$, they resemble the exponential function. Due to the singularity, this case is more complicated than A, and there is very little literature concerning it.

C. Quasi-geostrophic Waves

$k \ll f/U$

Set $\eta_w = \eta_s = 0$, and obtain

$$\frac{\partial}{\partial z}\left(\frac{\hat{w}_z}{U^2}\right) - \frac{N^2}{f^2} k^2 \frac{\hat{w}_z}{U^2} = 0 \qquad (16)$$

The conclusions may be summarized in the following diagram:

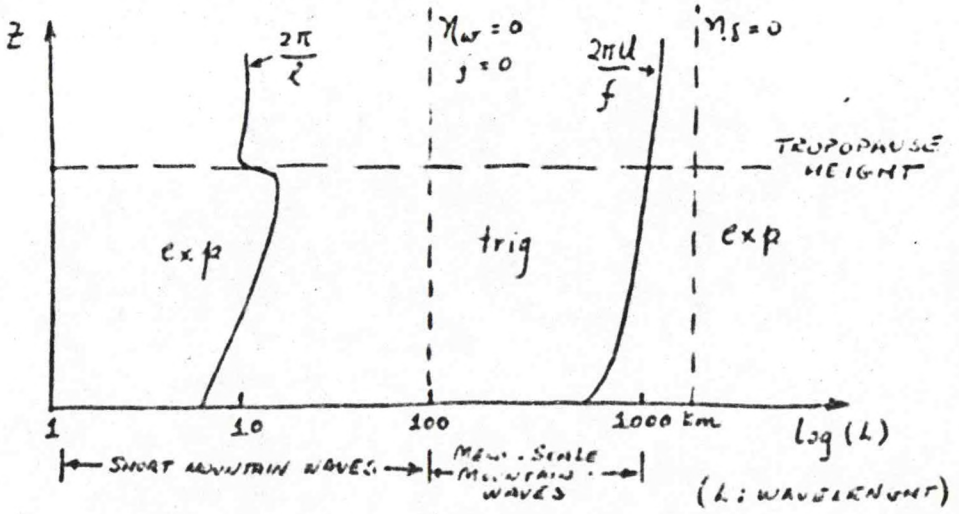

II. Properties of Mesoscale Mountain Waves

For low Mach-numbers, the steady flow of a stratified atmosphere over a mountain does not differ much from that of a stratified incompressible fluid. Consider, then, the properties of an incompressible fluid:

$$\frac{D\alpha}{dt} = 0 \quad , \qquad \alpha = \text{specific volume} \tag{17}$$

The generalization to isentropic flow of a gas is straightforward.

α is used as the vertical coordinate (equivalent to θ coordinates). The following notation applies:

$$V = \begin{pmatrix} u \\ v \end{pmatrix} \quad = \text{horizontal velocity on } \alpha \text{ surfaces}$$

$$\nabla = \begin{pmatrix} \frac{\partial}{\partial x}\big|_\alpha \\ \frac{\partial}{\partial y}\big|_\alpha \end{pmatrix} ; \quad \frac{D}{Dt} = \left(\frac{\partial}{\partial t}\right)_\alpha + V \cdot \nabla$$

$$M = \varphi + \alpha p \quad = \text{Montgomery potential} \tag{18}$$

The horizontal scale is assumed large enough ($> 10^5$ m) to allow application of the hydrostatic approximation:

$$M_\alpha = p \tag{19}$$

The continuity of mass equation is:

$$\frac{Dp_\alpha}{Dt} + p_\alpha \nabla \cdot V = 0 \tag{20}$$

while the momentum equation is:

$$\frac{DV}{Dt} + f\,k \times V + \nabla M = 0 \tag{21}$$

The basic geostrophic current $U(\alpha)$ is specified:

$$\left.\begin{aligned} fU &= -M_y \\ p &= M_\alpha \end{aligned}\right\} \Rightarrow f U_\alpha = -p_y = -M_{\alpha y} \tag{22}$$

(thermal wind equation)

Perturbation variables are functions of x, α, and t only $\left(\frac{\partial}{\partial y}=0\right)$:

$$\begin{array}{ll} U + u'(x,\alpha,t) & v'(x,\alpha,t) \\ M + m'(x,\alpha,t) & P + p'(x,\alpha,t) \end{array} \qquad (23)$$

$$\frac{d}{dt} = \frac{\partial}{\partial t} + U\frac{\partial}{\partial x} \qquad (24)$$

(Note: From this point on, primes (') will be dropped from perturbation quantities.)

The perturbation displacement in the y direction is defined as $\eta(x,\alpha,t)$:

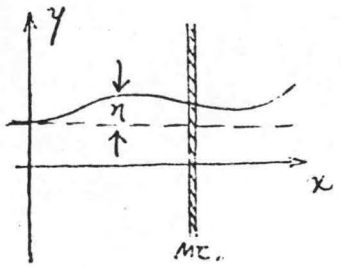

$$v = \frac{d\eta}{dt} \qquad (25)$$

The gravitational perturbation is given by:

$$q = m - \alpha p \qquad (26)$$

The perturbation equations are now:

$$\frac{du}{dt} - fv + m_x = 0 \qquad (27)$$

$$\frac{dv}{dt} + fu = 0 \qquad (28)$$

$$m_\alpha = p \qquad (29)$$

$$\frac{dp_\alpha}{dt} + p_{\alpha y} v + p_\alpha u_x = 0 \qquad (30)$$

Note:

$$-m\frac{dp_x}{dt} = -m\frac{d\dot{m}_{\alpha x}}{dt}$$

$$= -\frac{\partial}{\partial x}\left(m\frac{dm_{\alpha}}{dt}\right) + m_{\alpha x}\frac{dm_{\alpha}}{dt} + u_{\alpha} m m_{\alpha x}$$

$$= \frac{d}{dt}\left(\frac{p^2}{2}\right) + \frac{\partial}{\partial \alpha}\left(-m\frac{dp}{dt}\right) + u_{\alpha} m p_x \qquad (31)$$

If we multiply (13) by $-\rho_{\alpha} u$, (14) by $-\rho_{\alpha} v$, (15) by $-m$, and add the resulting expressions, we get the Wave Energy Equation:

$$\frac{dE}{dt} + \frac{\partial f_E^x}{\partial x} + \frac{\partial f_E^{\alpha}}{\partial \alpha} = q_E \qquad (32)$$

where: $E = \frac{1}{2}(-\rho_{\alpha})(u^2+v^2) + \frac{1}{2}p^2 \qquad (33)$

$$f_E^x = (-\rho_{\alpha}) m u; \quad f_E^{\alpha} = -m\frac{dp}{dt} \qquad (34)$$

$$q_E = -u_{\alpha} m p_x - f u_{\alpha x} m v \qquad (35)$$

The vertical eddy flux density through α-surfaces of x momentum can be written as:

$$f_m^{\alpha} = -p\varphi_x = p(m_x - \alpha p_x) \qquad (36)$$

$$= p m_x + \left(\tfrac{1}{2}\alpha p^2\right)_x$$

The lower boundary condition is specified as:

$$\varphi = \varphi_0(x,t) \quad at \quad \alpha = \alpha_B$$

i.e.,

$$m - \alpha p = \varphi_0(x,t) \quad at \ \alpha = \alpha_B \qquad (37)$$

For the steady state case: $\frac{d}{dt} = U\frac{\partial}{\partial x}$

$$\therefore v = U\eta_x \tag{38}$$

Upon integration of systems (27) - (30), with $\frac{\partial}{\partial t} = 0$ becomes:

$$U(u - f\eta) + mu = 0 \tag{39}$$

$$U^2\eta_{xx} + fu = 0 \tag{40}$$

$$m\alpha = p \tag{41}$$

$$Up_\alpha - fU_{x\alpha}U\eta + p_\alpha u = 0 \tag{42}$$

If $E \to 0$ and $m \to 0$ when $|x| \to \infty$, integration of (36) yields:

$$F_E^\alpha = \int_{-\infty}^{\infty} f_E^\alpha dx = -U\int m p_x dx = U\int p m_x dx$$

$$= -UF_m^\alpha \qquad (F_m^\alpha = \int m p_x dx) \tag{43}$$

Integration of the wave energy equation (32) yields:

$$\frac{d}{dx}F_E^\alpha = \int_{-\infty}^{\infty} q_E dx = -U_\alpha \int m p_x dx - fUU_{x\alpha}\int u\eta_x dx$$

$$= \frac{d}{d\alpha}(-UF_m^\alpha) = -\frac{d}{d\alpha}\left[U\int m p_x dx\right]$$

Consequently, when $U \neq 0$

$$\frac{d}{d\alpha}\int m p_x dx = fU_{\alpha x}\int u\eta_x dx \tag{44}$$

By Fourier transform,

$$m = Re\int_0^\infty \hat{m}(k,x)\, e^{ikx} dk$$

$$u = Re\int_0^\infty \hat{u}(k,x)\, e^{ikx} dk \tag{45}$$

$$\eta = Re\int_0^\infty \hat{\eta}(k,x)\, e^{ikx} dk$$

$$p = Re \int_0^\infty \hat{p}(k,\alpha)\, e^{ikx}\, dk \qquad (45)$$

The set of equations (39) - (42) becomes:

$$f\hat{u} = k^2 u^2 \hat{\eta} \qquad (46)$$

$$\hat{m} = -\frac{u}{f}(k^2u^2 - f^2)\hat{\eta} \qquad (47)$$

$$f u \hat{p}_x = (f^2 u u_{xx} - \rho_x k^2 u^2)\hat{\eta} \qquad (48)$$

If η is eliminated from Eqs. (47) and (48), and the result is combined with (46), we obtain:

$$\hat{m} = -\Gamma \hat{p}_x = -\Gamma \hat{m}_{xx} \qquad (49)$$

where:

$$\Gamma = \frac{u^2 - f^2/k^2}{-\rho_x + \frac{f^2}{k^2}\frac{u_{xx}}{u}} = \frac{u^2 - f^2/k^2}{\frac{g^2}{\alpha^2 N^2} + \frac{f^2}{k^2}\frac{u_{xx}}{u}} \qquad (50)$$

Γ is a function of height (i.e., α), and is not the same function of height in all cases. Further, a singularity exists at the level where

$$u^2 = f^2/k^2$$

p is continuous in space (m need not be). A differential equation for p can be derived by taking $\frac{\partial}{\partial \alpha}$ of (49). The result is

$$(\Gamma \hat{p}_x)_x + \hat{p} = 0 \qquad (50a)$$

From Eqs. (46) and (48), express $\hat{\eta}$ and $\hat{u}$ in terms of $\hat{p}$

$$\hat{\eta} = \frac{f/k^2 u}{-\rho_x + \frac{f^2}{k^2}\frac{u_{xx}}{u}}\hat{p}_x \qquad (51)$$

$$\hat{u} = \frac{u}{-P_\alpha + \frac{f^2}{k^2}\frac{u_{\alpha\alpha}}{u}}\,\hat{p}_\alpha \qquad (52)$$

From (43):

$$F_E^\alpha = -u\int_{-\infty}^{0} m\, p_x\, dx = -\pi u\, Re\int_0^\infty \hat{m}\,\hat{p}_x^*\, dk \qquad (53)$$

$$F_E^k = -\pi u\, Re\,(\hat{m}\,\hat{p}_x^*) = \pi u T\, Re\,(\hat{p}_\alpha\,(-ik\,\hat{p}^*))$$

$$= \pi u T k\, Im\,(\hat{p}_\alpha\,\hat{p}^*) \qquad (54)$$

Ricatti equation:

Define:

$$\Delta = T\,\frac{\hat{p}_\alpha}{\hat{p}} = -\frac{\hat{m}}{\hat{p}} \qquad (55)$$

Then:

$$-\Delta_\alpha = \frac{-(T\hat{p}_\alpha)_\alpha}{\hat{p}} + T\left(\frac{\hat{p}_\alpha}{\hat{p}}\right)^2 = 1 + \frac{\Delta^2}{T} \qquad (56)$$

From (54), F_E^k can be expressed in terms of Δ :

$$F_E^k = \pi u k\, Im\left(\frac{T\hat{p}_\alpha}{\hat{p}}\,\hat{p}\,\hat{p}^*\right) = \pi u k |\hat{p}|^2\, Im(\Delta) \qquad (57)$$

Consider now the solution for a layer of constant T :

a) $T > 0$

From (50a):

$$\hat{p}_{\alpha\alpha} + \frac{\hat{p}}{T} = 0 \qquad (58)$$

$$\hat{p} = Ae^{i\lambda\alpha} + Be^{-i\lambda\alpha}\,;\quad \lambda^2 = \frac{1}{T} > 0\,;\quad \lambda > 0$$

$$-k \quad \text{u} \quad (59)$$

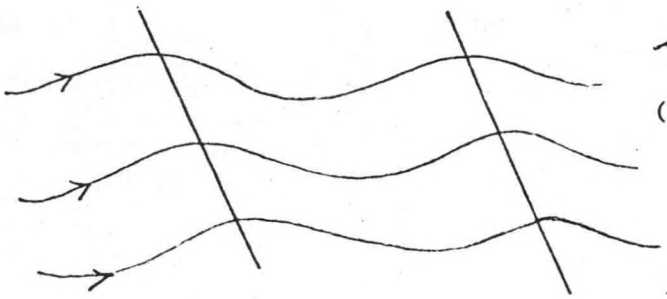

A-Wave

$$s = i\lambda\Gamma = \frac{i}{\lambda} = i\sqrt{\Gamma}$$

(carries energy upward)

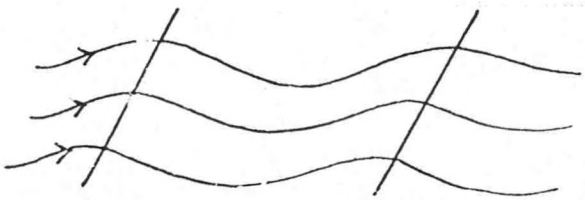

B-Wave

$$s = -i\lambda\Gamma = -\frac{i}{\lambda}$$

(carries energy downward)

b) $\Gamma < 0$

$$\hat{p} = Ae^{\mu x} + Be^{-\mu x} \; ; \; \mu^2 = -\frac{1}{\Gamma} > 0 \; ; \; \mu > 0 \qquad (60)$$

$$F_E^k = -2\pi k \frac{U}{\mu} \, \mathrm{Im}(AB^*) \qquad (61)$$

A-Wave

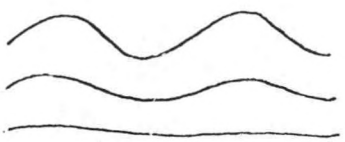

$$s = \Gamma\mu = -\frac{1}{\mu} = \sqrt{-\Gamma}$$

B-Wave

$$s = -\Gamma\mu = \frac{1}{\mu}$$

Matching conditions at interface: from (50a)

$$\Delta\hat{p} = 0 \qquad \Delta\left(\Gamma\hat{p}_x\right) = 0$$

c) Solution near the singularity $T=0$

$$u_s^2 = f^2/k^2 \qquad \alpha = \alpha_s \tag{62}$$

$$L_s = 2\pi/k_s = 2\pi \frac{u_s}{f} = 6\times 10^4 \text{ sec } u_s \tag{63}$$

(u_s = 10 m/sec: $L_s = 6\times 10^4 m$)

$$\zeta = \alpha - \alpha_s \tag{64}$$

$$T = \gamma_1 \zeta + \gamma_2 \zeta^2 + \cdots \tag{65}$$

$$\hat{p} = \zeta^r (1 + a_1 \zeta + \cdots)$$

$$(T\hat{p})_\zeta + \hat{p} = 0$$

$$r^2 = 0$$

$$\hat{p}_1 = 1 - \frac{\zeta}{\gamma_1} + \cdots ; \quad \hat{p}_2 = \hat{p}_1 \ln\zeta + b_1\zeta + b_2\zeta^2 + \cdots$$

The solution is:

$$\hat{p} = A_k(1 + F_k(\zeta))\ln\zeta + G_k(\zeta) + B_k(1 + F_k(\zeta)) \tag{66}$$

$F_k(\zeta)$ and $G_k(\zeta)$ are analytic with

$$F_k(0) = G_k(0) = 0 \tag{67}$$

and A_k and B_k are constants.

Hence:

$$\hat{p} = A_k \ln\zeta + B_k + O(\zeta\ln\zeta) \tag{68}$$

$$\hat{m} = -\gamma_1 \zeta \hat{p}_\alpha = -A_k\gamma_1 \tag{69}$$

$$\hat{n}, \hat{u} \sim \frac{1}{\zeta} \tag{70), (71}$$

Following Booker and Bretherton (1967), the singularity

$$u_s = \lim_{k_i \to 0} \left({}^{f}/_{k} + i c_i \right) \to \frac{f}{k} + u_\alpha \zeta_s$$

Thus:

$$\zeta_s = \frac{i c_i}{u_\alpha} \begin{cases} > 0 & \text{IF } u_\alpha > 0 \\ < 0 & \text{IF } u_\alpha < 0 \end{cases}$$

Hence, if $u_\alpha > 0$

$$\arg \zeta = 0 \quad \text{WHEN} \quad \zeta > 0$$

$$\arg \zeta = -\pi \quad \text{WHEN} \quad \zeta < 0$$

Therefore,

$$\arg \zeta = 0 \quad \text{WHEN} \quad \zeta > 0$$

$$\arg \zeta = -\pi \quad \text{WHEN} \quad \zeta < 0$$

and

$$\ln \zeta = \begin{cases} \ln |\zeta| \text{ WHEN } \zeta > 0 \text{ AND } u_\alpha > 0 \\ \ln |\zeta| - i\pi \text{ WHEN } \zeta < 0 \text{ AND } u_\alpha > 0 \end{cases}$$

$$\ln \zeta = \ln |\zeta| + i\pi \text{ WHEN } \zeta < 0 \text{ AND } u_\alpha < 0$$

The energy flux is

$$F_E^k = \begin{cases} \pi f \gamma_1 \, \mathrm{Im} \left(A_k B_k^* \right) & \zeta > 0 \\ \pi f \gamma_1 \left[\mathrm{Im} \left(A_k B_k^* \right) + \pi |A_k|^2 \right] & \zeta < 0, \; u_\alpha > 0 \\ \pi f \gamma_1 \left[\mathrm{Im} \left(A_k B_k^* \right) - \pi |A_k|^2 \right] & \zeta < 0, \; u_\alpha < 0 \end{cases}$$

There is flux convergence in each case.

III. Numerical Study of Mesoscale Mountain Waves

Eliassen and Rekustad (1971) have performed numerical integrations

of the equations describing air flow on the rotating earth across a mountain ridge. The width of the ridge is about 400 km. The motion is assumed to be hydrostatic and independent of the y coordinate. A nearly steady state is reached after 34 hours, showing a system of mesoscale gravity-inertial waves which are strongly damped downstream.

Two initial conditions (Fig. 2) are used to determine steady wave patterns in relation to the temperature and wind profiles of the air current.

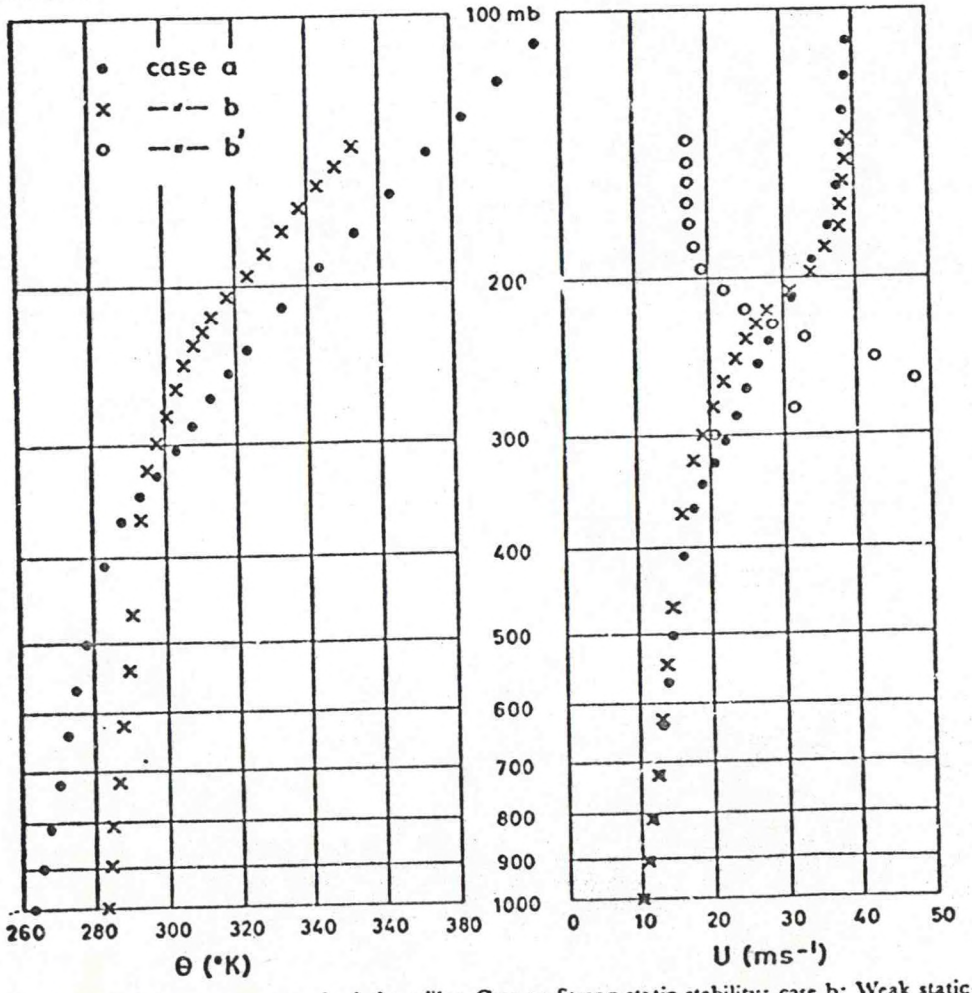

Fig. 2. Potential temperature and wind profiles. Case a: Strong static stability; case b: Weak static stability; case b': Weak static stability with a strong wind maximum near the tropopause.

Figs. 3-7 show the steady wave pattern in the plane. The conclusions that can be drawn from the numerical study are:

1) With the same mountain profile, the wave amplitudes of weak static stratification are stronger than those of strong static stratification.

2) With the same mountain profile and static stability, the wave amplitudes of linearized equations are much weaker than those of nonlinearized equations.

3) The wave pattern is quite sensitive to changes in the mountain profile.

References

Eliassen, A. and J. Rekustad, 1971; A numerical study of mesoscale mountain waves. Geofysiske Publikasjoner, XXVIII, pp. 1-13.

Booker, J. and F. Bretherton, 1967; The critical layer for internal gravity waves in a shear flow. J. Fluid Mech., 27, pp. 513-539.

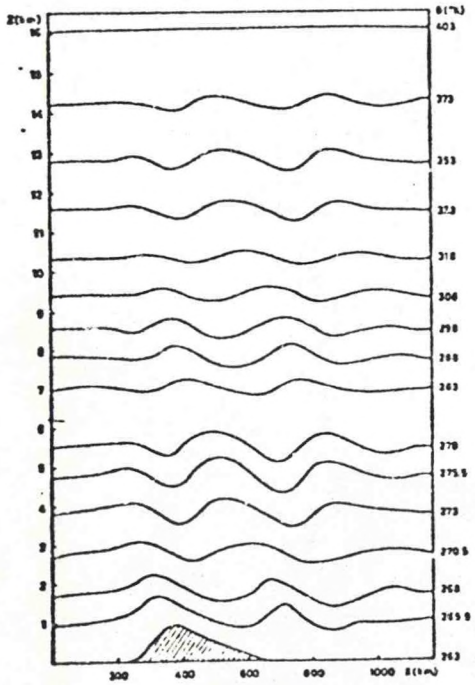

Fig. 3. Vertical cross section along the flow (xz plane) after 34.4 hours, showing mountain profile.

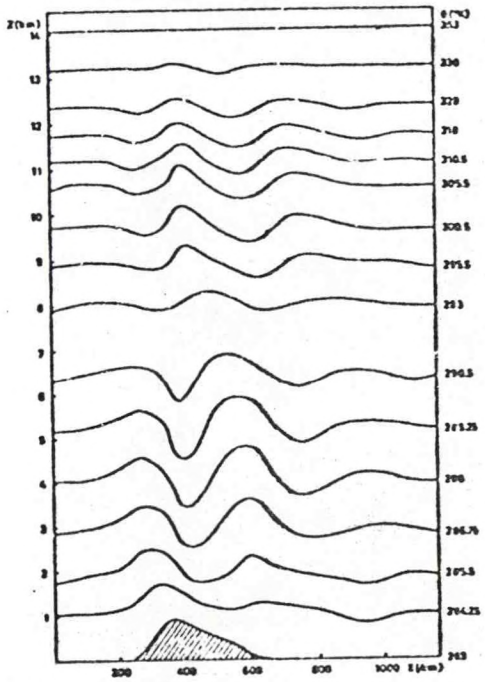

Fig. 4. Same as Fig. 3. Case b: weak static stability.

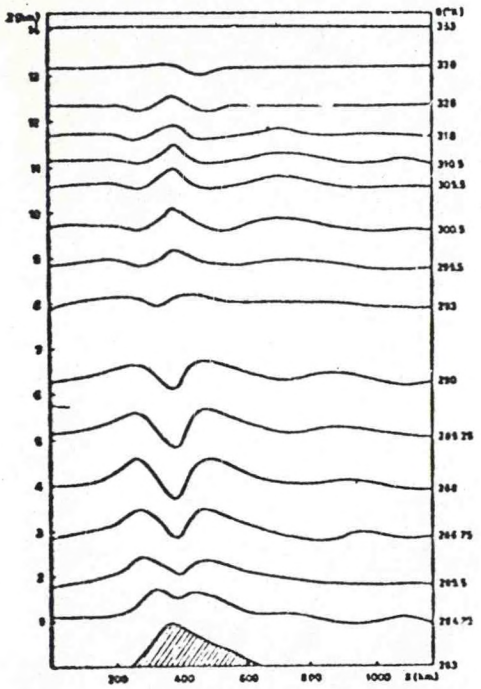

Fig. 5. Same as Fig. 3. Case b: weak static stability, equations linearized.

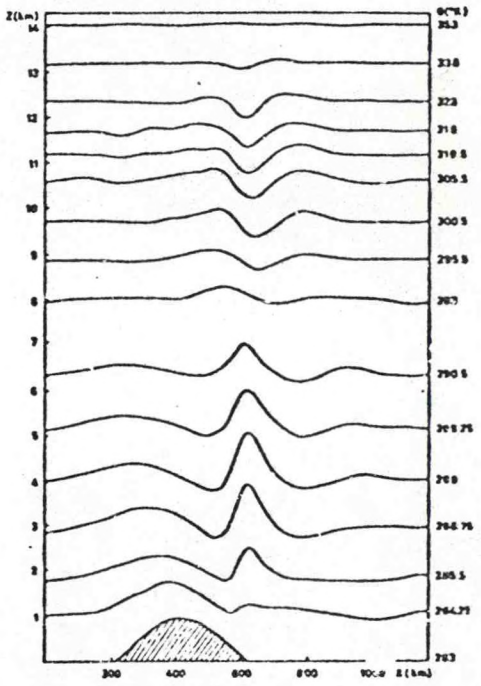

Fig. 6. Same as Fig. 3. Case b: weak static stability, symmetric mountain profile.

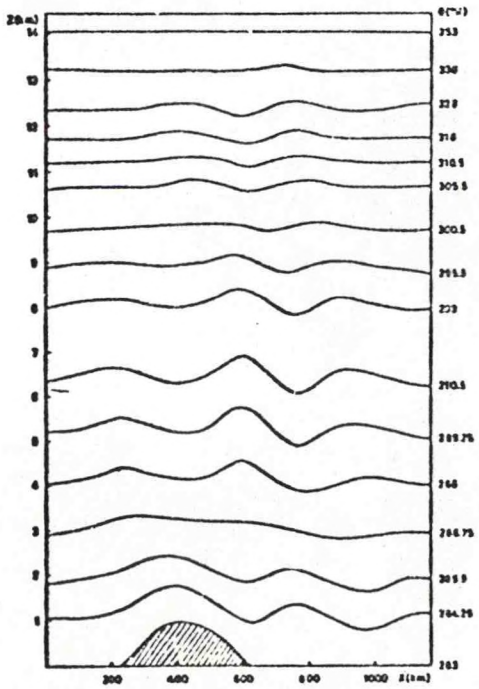

Fig. 7.
Same as Fig. 3.
Case b: Weak static stability with a wind jet. Symmetric mountain profile.

ON THE SEMI-GEOSTROPHIC APPROXIMATION WITH APPLICATION TO BAROTROPIC-BAROCLINIC INSTABILITY

Lecturer: Dr. A. Eliassen Notes by: M.J. Leach

Date: July 25, 1974 J. Fishman

I. Introduction

This lecture amplifies the work of Bleck (1973) by introducing non-geostrophic perturbations into the potential vorticity theorem. Where Bleck uses isentropic coordinates, Eliassen uses levels of constant specific volume (α) in the vertical. In either of these coordinate systems vertical advection terms can be eliminated from the mathematics. Also demonstated are some criteria for stability of flow using the semi-geostrophic approximation.

II. The Potential Vorticity Theorem in α-Coordinates

In α-coordinates, it must be assumed that the fluid is incompressible, or:

$$\frac{D\alpha}{dt} = 0$$

The fundamental definition and relationships are:

$$M = \phi + p\alpha$$

$$M_\alpha = p$$

$$M - \alpha M_\alpha = \phi$$

where: M = Montgomery potential

ϕ = geopotential

p = pressure

Thus, the potential vorticity theorem in (x, y, α, t) space is:

$$V_t + V \cdot \nabla V + f k \times V + \nabla M = 0$$

where the operator ∇ refers to the horizontal derivatives on a given α-surface.

If the absolute vorticity, Z, is defined by $Z = f + \zeta$, then potential vorticity, Q, is defined by $Q = -Z/p_\alpha$, where the conservation of potential vorticity requires:

$$\frac{dQ}{dt} = 0.$$

In his quasi-geostrophic derivation, Bleck (1973) requires:

$$\frac{\partial Q_g}{\partial t} = -V_g \cdot \nabla Q_g$$

where:

$$Q_g = \frac{f + \frac{1}{f}\nabla^2 M}{M_{\alpha\alpha}}$$

and:

Q_g = geostrophic vorticity

V_g = geostrophic wind

Following Hoskins (1972), the potential vorticity theorem is rewritten using the semi-geostrophic approximation:

$$V_t + V \cdot \nabla V + f k \times V + \nabla M = 0 \qquad (1)$$

where $\mathbf{V}$ is the geostrophic wind and $\mathbf{v}$ is the non-geostrophic wind. Solving for the components of the non-geostrophic wind of u and v, we get:

$$\left.\begin{aligned} \Delta u &= (U_y - f)(M_y + V_t) - V_y(M_x + U_t) \\ \Delta v &= (V_x + f)(M_x + U_t) - U_x(M_y + V_t), \end{aligned}\right\} \quad (2)$$

where:

$$\begin{aligned} \Delta &= (f - U_y)(f + V_x) + U_x V_y \\ &= f^2 + f J_g + U_x V_y - U_y V_x. \quad (3) \end{aligned}$$

and $\Delta \neq 0$ in order to have any meaning. Placement of u and v into the continuity equation obtains:

$$M_{xxt} + \frac{\partial}{\partial x}(M_{xx} u) + \frac{\partial}{\partial y}(M_{xx} v) = 0. \quad (4)$$

Further substitution of (2) and (3) into (4) yields:

$$\begin{aligned} &M_{xxt} + \frac{\partial}{\partial x}\left[\frac{M_{xx}}{f\Delta}\left\{(f - U_y)M_{xt} - V_y M_{yt}\right\}\right] \\ &+ \frac{\partial}{\partial y}\left[\frac{-M_{xx}}{f\Delta}\left\{U_x M_{xt} + (f + V_x)M_{yt}\right\}\right] \\ &= J_{x,y}\left[\frac{f M_{xx}}{\Delta}, \left\{M + \tfrac{1}{2}(U^2 + V^2)\right\}\right] \quad (5) \end{aligned}$$

Eq. (5) is a linear differential equation in M_t where the second order terms on the left hand side are:

$$\frac{\partial^2}{\partial \alpha^2} + \left(-\frac{M_{\alpha\alpha}}{f\Delta}\right)\left[(f-U_y)\frac{\partial^2}{\partial x^2} - V_y\frac{\partial^2}{\partial x \partial y} + U_x\frac{\partial^2}{\partial y \partial x} + (f+V_x)\frac{\partial^2}{\partial y^2}\right].$$

Since $U_x + V_y = 0$, the two terms with mixed derivatives are equal. Thus, the type of the x, y-operator in the brackets depends on the sign of $(f-U_y)(f+V_x) + U_x V_y = \Delta$. Moreover, in a statically stable atmosphere, $M_{\alpha\alpha} = P_\alpha < 0$ and since $f > 0$, then $(-M_{\alpha\alpha}/f) > 0$. Therefore, if $\Delta > 0$, Eq. (5) is elliptic. Eq. (5) can thus be solved if sufficient boundary conditions are given.

At the surface let

$$\alpha = \alpha_s(x, y, t); \quad \Phi_t = M_t - \alpha M_{t\alpha} = 0, \tag{6}$$

and at the top,

$$\alpha = \alpha_T \; ; \quad P_T = M_{t\alpha} = 0. \tag{7}$$

To get a value for α_s in Eq. (6), an advective equation is used:

$$\frac{\partial \alpha_s}{\partial t} = -u\frac{\partial \alpha_s}{\partial x} - v\frac{\partial \alpha_s}{\partial y} \tag{8}$$

in which u and v are obtained from Eq. (2) and will therefore contain M_{tx} and M_{ty}. Thus, some type of numerical method must be employed to get these values.

The kinetic energy equation can be obtained by multiplying Eq. (1) by V:

$$\frac{1}{2}V^2 + v\cdot\nabla\frac{1}{2}V^2 = -f\mathbf{k}\times v\cdot V = -v\cdot\nabla M. \tag{9}$$

The above equations can be linearized by letting $U(y, \alpha)$ represent a basic current (not to be confused with the geostrophic wind). Thus, for the basic current,

$$\left.\begin{aligned} fU &= -M_y \\ P &= M_\alpha \\ fU_\alpha &= -P_y \\ z &= f - U_y \\ Q &= \frac{f - U_y}{P_\alpha} \end{aligned}\right\} \quad (10)$$

Introduce the perturbation quantities u, v, m and p. The linearized momentum equations become:

$$u_t + Uu_x + vU_y - fv + m_x = 0 \quad (11)$$

$$v_t + Uv_x + fu + m_y = 0 \quad (12)$$

The linearized hydrostatic and continuity equations are:

$$-p + m_\alpha = 0 \quad (13)$$

$$m_{\alpha t} + Um_{\alpha x} + P_\alpha u_x + (P_\alpha v)_y = 0 \quad (14)$$

The set of equations (11 - 14) has solutions where x and t appear as a factor $e^{ik(x-ct)}$. For such a solution,

$$(U-c)u - Z\frac{v}{ik} = -m \quad (11')$$

$$fu - (U-c)k^2\frac{v}{ik} = -m_y \quad (12')$$

$$(U-c)m_{\alpha\alpha} + P_\alpha u + \left(P_\alpha \frac{v}{ik}\right)_y = 0. \quad (14')$$

Solve (11') and (12') for u and v and substitute into (14'):

$$m_{\alpha\alpha} + \left(\frac{-P_\alpha}{\Delta'} m_y\right)_y - \left[\frac{f\left(-\frac{P_\alpha}{\Delta'}\right)_y}{U-c} + \left(\frac{-P_\alpha}{\Delta'}\right)k^2\right] m = 0 \quad (16)$$

where:

$$\Delta' = fZ - (U-c)^2 k^2. \quad (15)$$

Once again, it is clear that (16) is an elliptic equation when $\Delta' > 0$.

The boundary conditions needed to solve (16) are

$$\left.\begin{aligned} \alpha &= \alpha_T(y) \quad \text{at the top} \\ \alpha &= \alpha_B(y) \quad \text{at the bottom} \end{aligned}\right\} \quad (17)$$

or some other equivalent conditions.

III. The semi-geostrophic approximation

Using perturbation equations of motion,

$$u_t + Uu_x + v U_y - fv + m_x = 0 \quad (11)$$

$$v_t + Uv_x + fu + m_y = 0 \quad (12)$$

Replacing perturbation values of u, v involved in derivatives by their respective geostrophic values

$$u_g = -\frac{1}{f} m_y \quad , \quad v_g = \frac{1}{f} m_x \quad (18)$$

yields:

$$\frac{\partial}{\partial t}\left(-\frac{1}{f} m_y\right) + U \frac{\partial}{\partial x}\left(-\frac{1}{f} m_y\right) + v U_y - fv + m_x = 0$$

$$\frac{\partial}{\partial t}\left(\frac{1}{f} m_x\right) + U \frac{\partial}{\partial x}\left(\frac{1}{f} m_x\right) + fu + m_y = 0$$

For solutions of the form

$$u = \hat{u} e^{ik(x-ct)}$$
$$v = \hat{v} e^{ik(x-ct)}$$
$$m = \hat{m} e^{ik(x-ct)}$$

one obtains, after differentiation and factoring:

$$Z\frac{v}{ik} = -\frac{1}{f}(U-c)m_y + m \qquad (11'')$$

$$fu = -m_y + \frac{1}{f}(U-c)k^2 m \qquad (12'')$$

Substituting these values for u, v into (14'), we obtain:

$$(U-c)m_{\alpha\alpha} + P_\alpha\left(-\frac{m_y}{f} + \frac{1}{f^2}(U-c)k^2 m\right) + \left[\frac{P_\alpha}{ik}\left(\frac{-ik}{Zf}(U-c)m_y + \frac{ik}{Z}m\right)\right]_y = 0$$

Using the fact that

$$Q = \frac{-Z}{P_\alpha} \qquad (19)$$

$$(U-c)m_{\alpha\alpha} - P_\alpha\left(\frac{m_y}{f} - \frac{1}{f^2}(U-c)k^2 m\right) + \left[\frac{Z}{Q}\left(\frac{(U-c)}{Zf}m_y - \frac{m}{Z}\right)\right]_y = 0$$

$$(U-c)m_{\alpha\alpha} - \frac{P_\alpha}{f}m_y + \frac{P_\alpha}{f^2}(U-c)k^2 m + \left(\frac{1}{Q}\frac{U-c}{f}m_y\right)_y - \left(\frac{1}{Q}m\right)_y = 0$$

which becomes:

$$(U-c)m_{\alpha\alpha} - \frac{P_\alpha}{f} m_y + \frac{P_\alpha}{f^2}(U-c)k^2 m + \left(\frac{1}{Qf} m_y\right)_y (U-c)$$

$$+ \left(\frac{1}{Qf} m_y\right) U_y - \left(\frac{1}{Q}\right)_y m - \frac{1}{Q} m_y = 0$$

$$(U-c)m_{\alpha\alpha} + m_y \left[-\frac{P_\alpha}{f} + \frac{U_y}{Qf} - \frac{1}{Q}\right]$$

$$+ m\left[\frac{P_\alpha}{f^2}(U-c)k^2 - \left(\frac{1}{Q}\right)_y\right] + \left(\frac{1}{Qf} m_y\right)_y (U-c) = 0$$

Look at m_y term

$$\left[-\frac{P_\alpha}{f} + \frac{U_y}{Qf} - \frac{1}{Q}\right] = \left[\frac{Z}{Qf} + \frac{U_y}{Qf} - \frac{f}{Qf}\right]$$

but $Z = f - U_y$, so the term equals zero. We now have, after dividing by $(U-c)$

$$m_{\alpha\alpha} + \left(\frac{1}{Qf} m_y\right)_y - \left[\frac{(1/Q)_y}{U-c} + \left(\frac{-P_\alpha}{f^2} k^2\right)\right] m = 0 \quad (20)$$

Multiply Eq. (20) by m^* following Rayleigh's (1880) method:

$$m_{\alpha\alpha} m^* + \left(\frac{1}{fQ} m_y\right)_y m^* - \left[\frac{(1/Q)_y}{U-c} + \left(\frac{-P_\alpha}{f^2}\right) k^2\right] m m^* = 0$$

By use of the relation

$$m_{\alpha\alpha} m^* = (m_\alpha m^*)_\alpha - m_\alpha^* m_\alpha$$

we get:

$$(m_\alpha m^*)_\alpha - |m_\alpha|^2 + \left(\frac{1}{fQ}\, m^* m_y\right)_y - \frac{1}{fQ}|m_y|^2$$

$$= \left[\frac{(1/Q)_y}{u-c} + \left(\frac{-P_\alpha}{f^2}\right)k^2\right]|m|^2 \qquad (21)$$

Integrate over the entire area in y-α space:

$$\iint\left[\left(m_\alpha m^*\right)_\alpha + \left(\frac{1}{fQ}\, m^* m_y\right)_y dy\, d\alpha =$$

$$\iint\left[|m_\alpha|^2 + \frac{1}{fQ}|m_y|^2 + \left(\frac{-P_\alpha}{f^2}\right)k^2|m|^2\right]dy\, d\alpha$$

$$+ \iint\frac{(1/Q)_y}{u-c}|m|^2\, dy\, d\alpha \qquad (22)$$

Looking at the left hand side of Eq. (22) we apply Green's Theorem in the plane and obtain:

$$\iint\left[\left(\frac{1}{fQ}\, m^* m_y\right)_y + \left(m^* m_\alpha\right)_\alpha\right]dy\, d\alpha =$$

$$\oint m^*\left(\frac{1}{fQ}\, m_y\, d\alpha - m_\alpha\, dy\right)$$

Using the fact that $(-P_\alpha)$ is a positive number, and looking at the first integral on the right hand side of Eq. (22), we see that all of the terms in the integral are positive. We therefore obtain:

$$\oint m^*\left(\frac{1}{fQ}\, m_y\, d\alpha - m_\alpha\, dy\right) = \text{Positive Number} + \iint\frac{(1/Q)_y}{u-c}|m|^2\, dy\, d\alpha \qquad (22a)$$

Now impose boundary conditions so that the upper and lower boundaries are at constant pressure, i.e., $P = M_\alpha =$ constant.

The slope of these isobaric surfaces in y-α space is:

$$\left(\frac{\partial \alpha}{\partial y}\right)_P = -\frac{P_y}{P_\alpha} = \frac{f U_\alpha}{P_\alpha} \qquad (23)$$

The boundary condition says that

$$\frac{d}{dt}(P+p) = 0 = \frac{\partial p}{\partial t} + U\frac{\partial p}{\partial x} + v\frac{\partial P}{\partial y} = iK(U-c)p + P_y v$$

from Eq. (10), $P_y = -f U_\alpha$, we can get

$$0 = ik\left[(U-c)p - f U_\alpha \frac{v}{ik}\right]$$

Substitute for v/ik from (11'') and for p from Eq. (13), yielding:

$$0 = ik\left[(U-c)m_\alpha - f U_\alpha\left(\frac{-1}{fZ}(U-c)m_y + \frac{m}{Z}\right)\right]$$

$$= ik(U-c)\left[m_\alpha + \frac{U_\alpha}{Z}m_y - \frac{f U_\alpha}{Z}\frac{m}{(U-c)}\right] \qquad (24)$$

Looking at the left hand side of the integral of Eq. (22a), we allow the perturbation to approach zero for large y.

$$\oint m^*\left(\frac{1}{fQ} m_y d\alpha - m_\alpha dy\right) = \oint m^*\left(\frac{1}{fQ} m_y \left(\frac{\partial \alpha}{\partial y}\right)_p - m_\alpha\right) dy$$

From Eq. (23),

$$\left(\frac{\partial \alpha}{\partial y}\right)_p = \frac{f U_\alpha}{P_\alpha}$$

and from Eq. (10),

$$\frac{1}{P_\alpha} = -\frac{Q}{Z}$$

which allows us to say

$$\left(\frac{\partial \alpha}{\partial y}\right)_p = -\frac{fQ U_\alpha}{Z}$$

Substitution yields:

$$\oint m^*\left(-\frac{m_y U_\alpha}{Z} - m_\alpha\right) dy$$

from the Boundary Condition Eq. (24),

$$-\frac{f U_\alpha}{Z}\frac{m}{U-c} + \frac{U_\alpha}{Z} m_y + m_\alpha = 0$$

or

$$-\frac{U_\alpha}{Z} m_y - m_\alpha = -\frac{f U_\alpha}{Z}\frac{m}{U-c}$$

The left hand side of the equation becomes:

$$\oint m^*\left(-\frac{f U_\alpha}{Z}\frac{m}{U-c}\right) dy = -\oint \frac{f U_\alpha}{Z(U-c)} |m|^2 dy$$

$$= \oint \frac{\left(\frac{\partial \alpha}{\partial y}\right)_p}{(U-c)Q} |m|^2 dy \qquad (25)$$

Hence, Eq. (22a) becomes:

$$\oint \frac{\left(\frac{d\alpha}{dy}\right)_p}{(u-c)Q} |m|^2 \, dy = \text{Positive Number} + \iint \frac{(1/Q)_y}{u-c} |m|^2 \, dy \, d\alpha$$

Rearranging

$$\iint \frac{(1/Q)_y}{(u-c)} |m|^2 dy d\alpha - \oint \frac{\left(\frac{d\alpha}{dy}\right)_p}{(u-c)Q} |m|^2 = \text{Negative Number} \quad (26)$$

Writing phase speed c in terms of its real and imaginary parts,

$$c = c_r + i c_i$$

we can say:

$$\frac{1}{u-c} = \frac{u-c^*}{|u-c|^2} = \frac{u-c_r+ic_i}{(u-c_r)^2+c_i^2} \quad (27)$$

The imaginary part of Eq. (26) must equal zero, since the negative number is pure real. Therefore:

$$c_i \left\{ \iint \frac{(1/Q)_y}{|u-c|^2} |m|^2 dy d\alpha - \oint \frac{1}{Q|u-c|^2} \left(\frac{d\alpha}{dy}\right)_p |m|^2 dy \right\} = 0 \quad (28)$$

In the case of unstable waves, $c_i > 0$, and therefore

$$\iint \frac{(1/Q)_y}{|u-c|^2} |m|^2 dy d\alpha - \oint \frac{1/Q}{|u-c|^2} \left(\frac{d\alpha}{dy}\right)_p |m|^2 dy = 0 \quad (29)$$

Now, considering the real part of Eq. (26) yields:

$$\iint \frac{u(1/Q)}{|u-c|^2} |m|^2 dy d\alpha - \oint \frac{u\,1/Q}{|u-c|^2} \left(\frac{d\alpha}{dy}\right)_p |m|^2 dy = \text{Negative} \quad (30)$$

Suppose that $(\partial\alpha/\partial y)_p = 0$, i.e., on the upper and lower boundaries α is constant. Therefore, from Eq. (29) we see that $(1/Q)_y$ must be of either sign or zero throughout the region. From Eq. (30), $(1/Q)_y$ must be predominantly positive where U is small and negative where U is large. Similar results and derivations can be found in Charney and Stern (1962) and Pedlosky (1964), however, based upon a different utilization of the geostrophic approximation.

References

Bleck, R., 1973: Numerical forecasting experiments based on conservation of potential vorticity on isentropic surfaces. J. Appl. Meteor, 12, 737-752.

Charney, J., and M. E. Stern, 1962: On the stability of internal baroclinic jets in a rotating atmosphere. JAS, 19, 159-172.

Hoskins, B. J., 1972: Non-Boussinesq effects and further development in a model of upper tropospheric frontogenesis. Quart. J. of Roy. Meteor. Soc., 98, 532-541.

Pedlosky, J., 1964: The stability of currents in the atmosphere and the ocean: Part I. JAS, 21, 201-219.

Rayleigh, Lord, 1880: On the stability, or instability, of certain fluid motions. Scientific papers, 3, Cambridge University Press, 594-596.

FORCED LATERAL CIRCULATION IN A STRAIGHT BAROCLINIC CURRENT WITH APPLICATION TO FRONTOGENESIS

Lecturer: Dr. A. Eliassen Notes by: K.-Y. Fung

J. Cahir

Date: July 29, 1974

I. System of Coordinates

The set x, y, p, as shown, is chosen as coordinates. In order to study the lateral circulation, we assume no variation in the x direction, i.e., $\frac{\partial}{\partial x} = 0$. The conservative quantities in this system are:

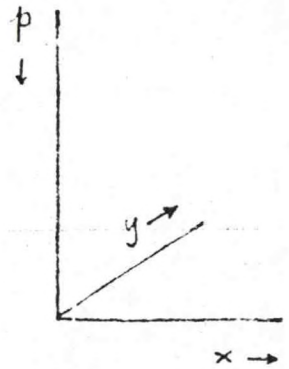

A. Absolute x-momentum (or spin), defined as:

$$S = u - fy$$

It is assumed for the moment that f is a constant. If f is not constant, $\int^{y} f\,dy'$ is used instead of fy. The conservation of absolute x-momentum can be written in the form,

$$\frac{DS}{Dt} = \frac{Du}{Dt} - fv = 0 \qquad (1)$$

B. Potential temperature:

$$\frac{D\theta}{Dt} = 0 \qquad (2)$$

The steady state current $U(y,p)$, spin $S(y,p)$, and absolute vorticity z satisfy:

$$fU = -\phi_y \qquad (3)$$

$$\alpha = \gamma\theta = -\phi_p \qquad (4)$$

or combining:

$$f u_p = \gamma \theta_y \tag{5}$$

which is the thermal wind relation.

Here:

$$\alpha = \theta \frac{d\pi}{dp} = \theta \gamma(p)$$

$$\gamma(p) = \frac{R}{p_r} \left(\frac{p}{p_r}\right)^{-c_v/c_p}$$

p_r is a reference pressure and partial deriviatives are subscripted.

$$S = U - fy \tag{6}$$

$$S_p = U_p \; ; \quad S_y = U_\eta - f = -\Sigma \tag{7}$$

The potential vorticity Q can be expressed in a simple manner:

$$Q = \frac{\alpha}{g}\left[\left(f - \partial U/\partial z\right)\frac{\partial \theta}{\partial y} + \frac{\partial U}{\partial z}\frac{\partial \theta}{\partial y}\right] = \frac{\alpha}{g}\frac{\partial(S,\theta)}{\partial(z,y)}$$

$$= \frac{\alpha}{g}\frac{\partial(S,\theta)}{\partial(p,y)}\frac{\partial(p,y)}{\partial(z,y)} = \frac{\partial(S,\theta)}{\partial(p,y)} \tag{8}$$

Suppose the system is perturbed in such a way that parcels are displaced (η, π) from their original position and at the same time receive an increment of spin ΔS

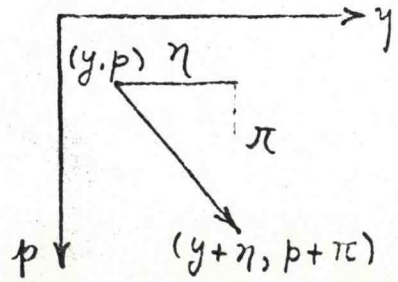

and of potential temperature $\Delta\theta$. The perturbed quantities u', ϕ', s', θ', corresponding to their steady state quantities U, $\dot{\psi}$, S, θ respectively, satisfy:

$$\eta_{tt} = -fu' - \phi_y' = -fs' - \phi_y' \tag{9}$$

$$-\alpha' - \phi_p' = -\gamma\theta' - \phi_p' \tag{10}$$

Since the total spin and potential temperature are conserved:

$$S(y+\eta, p+\pi) + s' = S(y,p) + \Delta s$$

$$\theta(y+\eta, p+\pi) + \theta' = \theta(y,p) + \Delta\theta$$

Expanding s', θ' to the first order,

$$s' = -\eta S_y - \pi S_p + \Delta s \tag{11}$$
$$= u'$$

$$\theta' = -\eta\theta_y - \pi\theta_p + \Delta\theta \tag{12}$$

The perturbed quantities may be inserted into Eqs (9) and (10):

$$\eta_{tt} = fS_y\eta + fS_p\pi - \phi_y' - f\Delta s \tag{13}$$

$$0 = \gamma\theta_y\eta + \gamma\theta_p\pi - \phi_p' - \gamma\Delta\theta \tag{14}$$

The displacements also satisfy the continuity equation, integrated over time from the initial disturbance.

$$\eta_y + \pi_p = 0 \tag{15}$$

Thus the displacement must be circulating in the y-p plane.

II. Free Oscillations

An example of the application of the above equations to fluid flow problems is the case where: $\Delta\Delta = \Delta\theta = 0$, free oscillations. Along closed streamlines, the fundamental mode of oscillation with frequency ν makes the second time derivative $\frac{\partial^2}{\partial t^2} = -\nu^2$. Integration along a closed streamline produces: $\oint (13)dy + \oint (14)dp$ leading to

$$-\nu^2 \oint \eta\, dy = \oint \left[(fS_y \eta + fS_p \pi)\, dy + (\gamma\theta_y \eta + \gamma\theta_p \pi)\, dp \right] \tag{16}$$

This is an application of Hoiland's formula.

Along a streamline the relation $\frac{dp}{dy} = \frac{\pi}{\eta} \equiv \xi$ holds and (16) can be written:

$$-\nu^2 \oint \eta\, dy = \oint \left[fS_y + (fS_p + \gamma\theta_y)\xi + \gamma\theta_p \xi^2 \right] \eta\, dy \tag{17}$$

$$\nu^2 = \frac{\oint R\eta\, dy}{\oint \eta\, dy} \tag{18}$$

where:

$$R = -fS_y - (fS_p + \gamma\theta_y)\xi - \gamma\theta_p \xi^2 \tag{19}$$

$\nu^2 > 0$ is required for all stable oscillations. R positive for all ξ would therefore be a sufficient condition for stable oscillations. From the thermal wind relation, $fS_p = \gamma\theta_y$. R definitely positive implies that:

$$-fS_y > 0\,; \quad -\gamma\theta_p > 0 \tag{20}$$

$$(-fS_y)(-\gamma\theta_p) - (-fS_p)(-\gamma\theta_y) > 0 \tag{21}$$

$(-fS_y) > 0$ represents rotational stability, $-\gamma\theta_p > 0$ represents static stability, and $-fS_p = -\gamma\theta_y$ represents baroclinicity of the fluid. (20) may be combined to give:

$$f\gamma Q > 0 \quad \text{or} \quad Q > 0 \tag{22}$$

Therefore it is sufficient to have positive potential vorticity in order for a fluid to be stable with respect to lateral overturnings.

If $\Delta\lambda$ and $\Delta\theta$ are not equal to zero in general, the question arises: what are the displacements that lead to a new equilibrium state? In equilibrium, the acceleration term η_{tt} is zero. From Eqs. (13) and (14) we have:

$$\frac{\partial}{\partial p}\left[fS_y\eta + fS_p\pi - f\Delta\lambda\right] = \frac{\partial}{\partial y}\left[\gamma\theta_y\eta + \gamma\theta_p\pi - \gamma\Delta\theta\right] \tag{23}$$

The integrated form of the continuity equation (15) suggests the displacement function ψ' satisfying:

$$\eta = -\psi'_p \quad ; \quad \pi = \psi'_y \tag{24}$$

Eq. (23) becomes:

$$\frac{\partial}{\partial p}\left[-fS_y\eta'_p + fS_p\psi'_y\right] + \frac{\partial}{\partial y}\left[\gamma\theta_y\psi'_p - \gamma\theta_p\psi'_y\right]$$
$$\equiv L(\psi') = f\frac{\partial\Delta\lambda}{\partial p} - \gamma\frac{\partial\Delta\theta}{\partial y} \equiv F \tag{25}$$

where F represents the forcing, which may be a differential force along vertical lines, or differential heating or cooling in isobaric

surfaces. Eq. (25) is elliptic if:

$$(-fS_y)(-\gamma\theta_p) - (-fS_p)(-\gamma\theta_y) = f\gamma Q > 0 \qquad (25)$$

Again, $Q > 0$ is necessary for the system to remain in equilibrium to the forcing.

The operator L determines the extent of the horizontal and vertical direction of the lateral circulation produced by a disturbance ($\Delta\lambda$ or $\Delta\theta$). If $\gamma\theta_y = fS_p = 0$ and $fS_y, \gamma\theta_p$ are constants, L becomes:

$$(-fS_y)\frac{\partial^2}{\partial p^2} + (-\gamma\theta_p)\frac{\partial^2}{\partial y^2}$$

The coordinate can be stretched until the coefficients are equal. We then have a Laplacian operator which is isotropic in the vertical plane, and may therefore estimate the ratio of the vertical to horizontal extent of streamlines (H/L, say) for a localized disturbance by setting:

$$\frac{fS_y}{H^2} = \frac{\gamma\theta_p}{L^2}$$

$$\left(\frac{H}{L}\right)^2 = \frac{fS_y}{\gamma\theta_p} = \frac{-fZ_1}{-\gamma\rho g\theta_z} = \frac{fZ}{N^2}$$

Further, if $F < 0$ everywhere in a region bounded by a streamline C, Ψ has a maximum inside C. Therefore, the flow is indirect. If $F > 0$, Ψ has a minimum inside C, and the flow is direct.

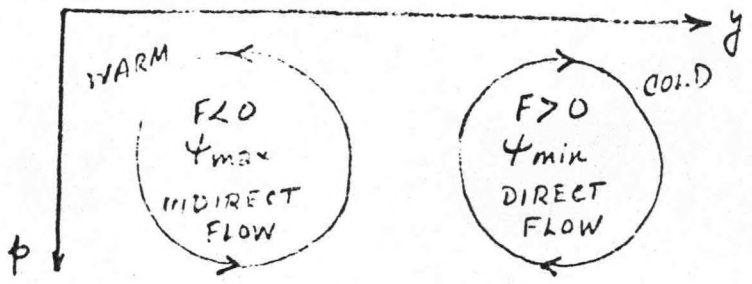

In coordinates (y, p), the operator in Eq. (25) is oblique, and has mixed derivatives y'_{yp}. However, when transformed into coordinates (s, p) or (y, θ), the operator becomes rectilinear and much simpler.

In coordinates (s, p),

$$Q = \frac{\partial(\theta, s)}{\partial(p, y)} = \frac{\partial(\theta, s)}{\partial(p, s)} \frac{\partial(p, s)}{\partial(p, y)} = \frac{\theta_p}{y_s} \qquad (27)$$

The thermal wind equation (5) becomes:

$$f y_p + r\theta_s = 0$$

$$\left(\frac{\partial}{\partial p}\right)_y = \frac{1}{y_s}\left(y_s \frac{\partial}{\partial p} - y_p \frac{\partial}{\partial s}\right) \qquad (28)$$

$$\left(\frac{\partial}{\partial y}\right)_p = \frac{1}{y_s} \frac{\partial}{\partial s}$$

$L(\psi')$ becomes:

$$-y_s L(\psi') = f\psi'_{pp} + (rQ\psi_s')_s \qquad (29)$$

In coordinates y, θ :

$$Q = \frac{S_y}{p_\theta} \tag{30}$$

The thermal wind equation is:

$$f S_\theta + \gamma p_y = 0 \tag{31}$$

$$\frac{\partial}{\partial p}\Big)_\gamma = \frac{1}{p_\theta}\frac{\partial}{\partial \theta}$$

$$\frac{\partial}{\partial y}\Big)_p = \frac{1}{p_\theta}\left(p_\theta \frac{\partial}{\partial y} - p_y \frac{\partial}{\partial \theta}\right)$$

$L(\psi')$ beomes:

$$-p_\theta \, L(\psi') = (f Q \psi_\theta')_\theta + (\gamma \psi_y)_y \tag{32}$$

The coordinate systems (p, S) and (y, θ) are equivalent in the sense that they both simplify the operator L.

III. Forced Oscillations

Suppose the forcing F goes on as a continuous process, and the variation in time is sufficiently slow. We may still ignore η_{tt} in (13) and assume that the current is always balanced. The response of the current to the continuous forcing is a lateral circulation, whose velocity v and ω may be expressed by a stream function:

$$v = -\psi_p \quad ; \qquad \omega = \psi_y \tag{33}$$

Using the same technique as before, we find:

$$L(\psi) = \frac{\partial F}{\partial t} = f \frac{\partial}{\partial p}\left(\frac{\partial \Delta \lambda}{\partial t}\right) - \gamma \frac{\partial}{\partial y}\left(\frac{\partial \Delta \theta}{\partial t}\right) \qquad (34)$$

This is Eq. (25) differentiated with respect to t. $\partial(\Delta\lambda)/\partial t$ is a momentum added per unit time, or a force. $\partial(\Delta\theta)/\partial t$ is the increase of θ per unit time, or the heat source.

In any kind of quasi-geostrophic or filtered numerical prediction scheme, the non-divergent velocity field may be prescribed. This implies a vertical circulation which can be diagnosed by an ω-type equation. The ω-type equation in turn, implies changes in the geostrophic field by divergence and the concomitant necessity for the calculation of advection by the divergent wind. (34) is a special case of a generalized ω-equation, with $\partial\omega/\partial x = 0$, involving tilting and non-geostrophic advection.

Differential temperature advection acts very much like a heat source. Thus, Bergeron's deformation field, concentrating the isotherms, gives a direct circulation as does a shearing advection. T. W. Sawyer (1956) was the first to compute the lateral circulation in a frontal zone resulting from a Bergeron-type differential advection. His equation was equivalent to:

$$L(\psi) = 2f\gamma O_y V_y \qquad (35)$$

where, on the right-hand-side, the differential heating is replaced by differential advection due to stretching along the front (u_x) or

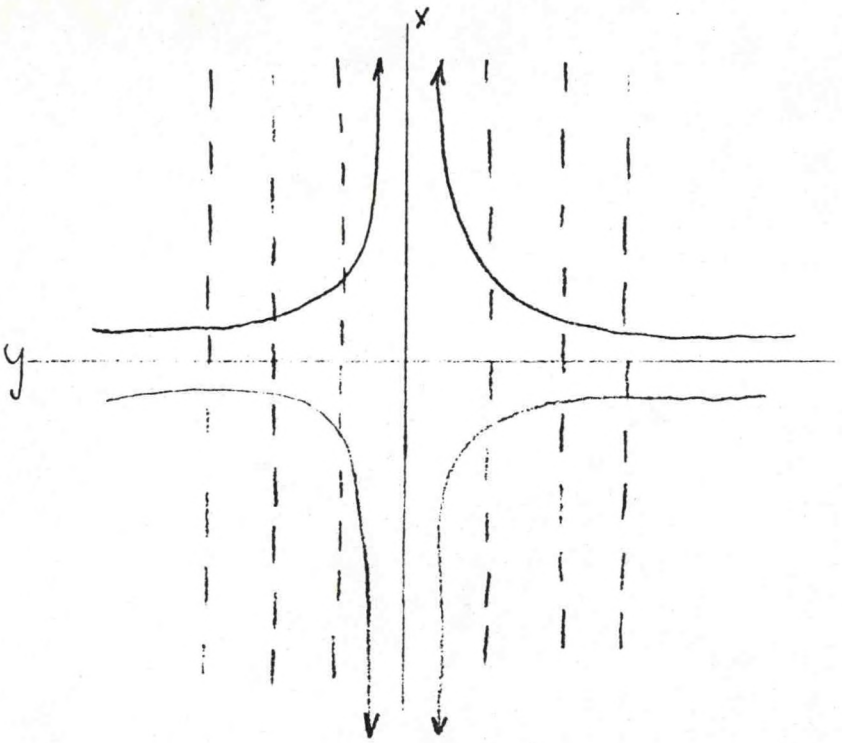

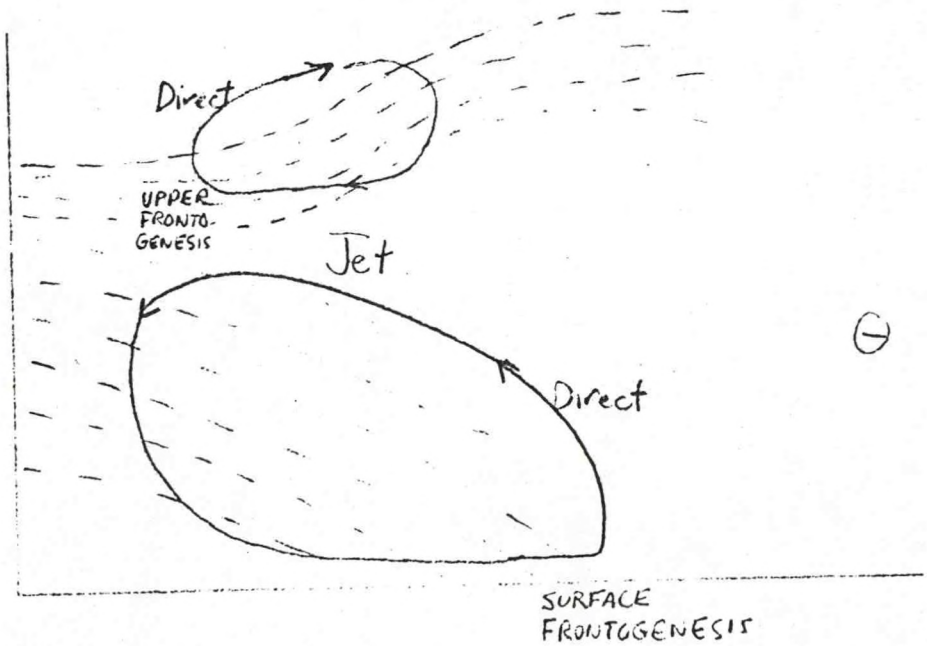

BERGERON - SAWYER CASE

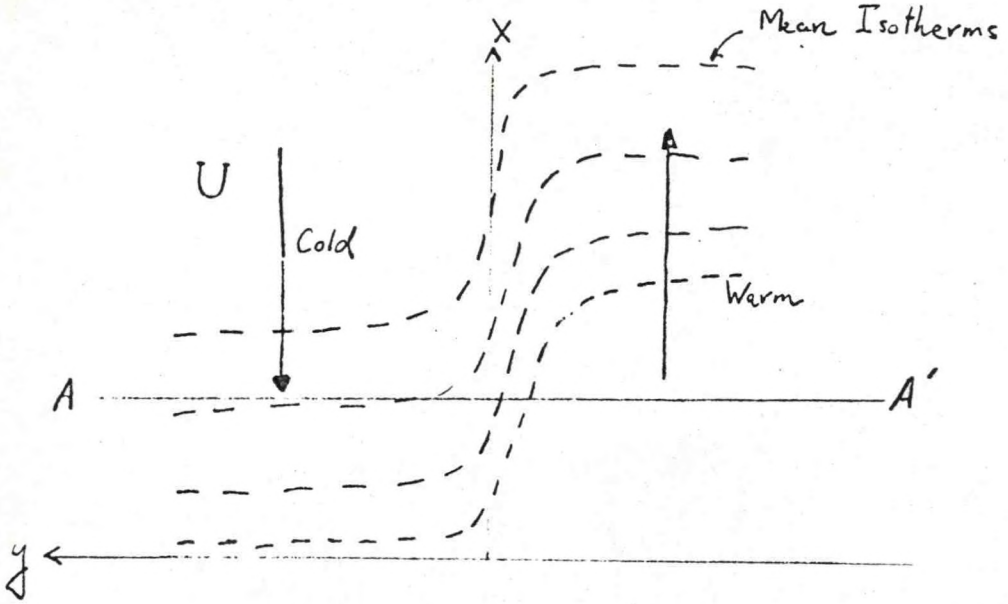

Shearing Advection. Thermal Wind Crosses Front From Cold to Warm Side

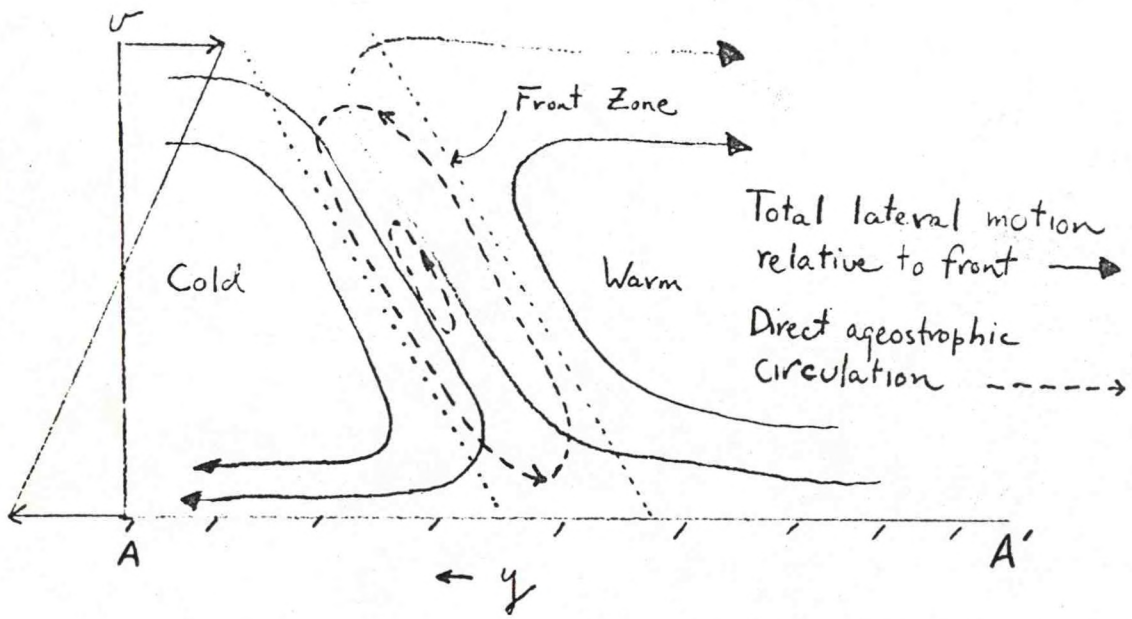

compression in the cross-front direction ($V_y = -U_x$) Eliassen (1962) generalized the equation to:

$$L(\Psi) = -2\gamma\,(\theta_y U_x - \theta_x U_y)$$
$$= 2f\,(U_p V_y - U_y V_p) \qquad (36)$$

Here, the stream function is that of the velocity field. The first part of the RHS term represents Bergeron forcing; the second is shearing advection.

References

Bergeron, T., 1928: Über die Dreidimensional Verknüpfende Wetteranalyse. Geof. Publ., 5, No. 6.

Sawyer, J. S., 1956: The vertical circulation at meteorological fronts and its relation to frontogenesis. Proc. Roy. Soc. A., 234, 346.

Eliassen, A., 1962: On the vertical circulation in frontal zones. Geof. Publ., 24, (Vilhelm Bjerknes Centennial Volume), p. 147.

Journal of the Meteorological Society of Japan Vol. 49, Special Issue

VII. EKMAN LAYER

On the Ekman Layer in a circular Vortex

By Arnt Eliassen

University of Oslo, Blinden, Norway
(Manuscript received 1 March, 1971)

Abstract

The system under study is an Ekman boundary layer in a circular vortex bounded by a plane horizontal surface which rotates around the axis in an absolute sense. It is found that the vertical motion forced by a turbulent Ekman layer near the axis will tend to zero with the radius. In contrast, it is known from the Greenspan-Howard theory that the vertical motion is constant near the axis in the laminar case. Implications for the spin-up mechanism and for the structure of typhoons are pointed out.

Lecture given on July 30, 1974

1. Introduction

Since the early works of Ekman and Taylor, the Ekman layer has been a familiar concept in geophysics. Their theories apply to straight geostrophic currents, and the diffusion of momentum is assumed to be balanced by the Coriolis force due to the cross-isobaric flow, or, in other words, by the advection of the earth's momentum due to the cross-isobaric flow. This is valid under the condition that the Rossby number is small, so that the absolute momentum of the air motion does not deviate much from that of the earth.

Taylor (1916) incorporated a slip boundary condition at the bottom of the Ekman layer, where the stress was set proportional to the square of the relative wind; this gives a complete determination of the velocity field in the Ekman layer, including the angle between the surface wind and the isobars.

The Ekman layer is known to play an essential role in a circular vortex such as a tropical cyclone. In this case the classical theory does not directly apply, partly because of the restrictions imposed by the circular geometry, and partly because the Rossby number is large, i.e. the absolute angular velocity of the air motion with respect to the axis of the vortex is much larger than that of the underlying surface.

Greespan and Howard (1963) studied the laminar Ekman layer in a vortex for small Rossby numbers. Using a non-slip boundary condition at the lower boundary, they found that the vertical motion at the top of the Ekman layer is nearly constant in the central part of the vortex, including the axis itself (see also Greenspan (1968), eq. (2.3.9) on p. 31).

On the other hand, Ooyama (1969), Rosenthal (1970), Sundqvist (1970) and Yamasaki (1968), in their numerical simulation experiments of the development of tropical cyclones, all obtained results which indicate the existence of a more or less pronounced central eye, with almost no ascending motion in the center itself and the maximum at some distance from the center. These authors all used Taylor's slip boundary condition appropriate for a turbulent Ekman layer.

Thus the distribution of the vertical motions in these experiments (and in a real typhoon) differs considerably from what is obtained for a laminar Ekman layer. The difference may be due to the effect of condensation heat, but it is also conceivable that it is due to the use of different boundary conditions.

The present paper aims at throwing some light on this question. The Ekman layer for a vortex in a homogeneous-incompressible fluid is studied, partly using the non-slip boundary condition at the bottom surface, and partly using the slip condition appropriate for turbulent conditions. The two cases are found to differ considerably.

2. Heuristic analysis of the Ekman layer

Consider a homogeneous and incompressible fluid of density ρ and kinematic viscosity ν, performing a circular vortex motion with respect to a vertical axis z. Let r denote distance from the axis, and t time. The motion is considered as axially symmetric, so that all variables are functions of r, z and t.

Let $\omega(r, t)$ be the absolute angular velocity with respect to the axis z, and let $v(r, z, t)$ and $w(r, z, t)$ denote the radial and vertical components, respectively, of a "meridional" circulation superimposed upon the vortex motion, as shown in the figure below.

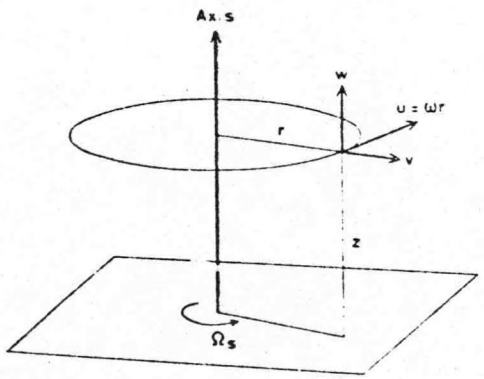

The fluid is assumed to be bounded below by a solid surface $z=0$, which rotates with the constant absolute angular velocity Ω_s.

The Rossby number, defined as

$$\mathrm{Ro}=\frac{|\omega-\Omega_s|}{\Omega_s} \tag{2.1}$$

is tentatively assumed small, so that the motion is one of almost rigid rotation.

The upper boundary is taken either as a horizontal surface of symmetry, or as a free surface at $z=H$. In the latter case, we assume that the "local" Froude number $\omega^2 r^2/gH$, where g is the acceleration of gravity, is everywhere small, so that H may be considered constant in space and time. Moreover, H is assumed to be large enough so that the Ekman number, defined as

$$E=\frac{\nu}{\Omega_s H^2} \tag{2.2}$$

is small.

We shall consider a motion without excessive inertia waves or oscillations. Under these conditions, an Ekman boundary layer is known to develop next to the lower boundary; its thickness δ is of the order

$$\delta=\left(\frac{\nu}{\Omega_s}\right)^{\frac{1}{2}}=E^{\frac{1}{2}}H \tag{2.3}$$

Within the Ekman layer, ω and v both vary with height; the advection of angular momentum is nearly balanced by diffusion. Above the Ekman layer, gradients are small, and the angular momentum remains very nearly constant for each fluid particle. In the absence of inertia oscillations, the material surfaces of constant angular momentum in this region must have the shape of vertical cylinders at all times. Therefore ω and v do not change with height: we shall denote their values above the Ekman layer by capital letters, and write

$$\omega=\Omega(r, t), \quad v=V(r, t) \text{ when } z>\delta \tag{2.4}$$

Conservation of absolute angular momentum for $z>\delta$ gives

$$\left(\frac{\partial}{\partial t}+V\frac{\partial}{\partial r}\right)(\Omega r^2)=0$$

or

$$\frac{\partial \Omega}{\partial t}=-V\left(\frac{2\Omega}{r}+\frac{\partial \Omega}{\partial r}\right) \tag{2.5}$$

With H constant, the kinematic boundary contition requires

$$w=0 \qquad \text{at } z=0 \text{ and } z=H \tag{2.6}$$

Moreover, it follows from (2.6) and the condition of incompressibility that

$$\int_0^\delta v\,dz+\int_\delta^H v\,dz=0.$$

In the second integral, v has the constant value V. Denoting the first integral by Q:

$$Q(r, t)=\int_0^\delta v\,dz \tag{2.7}$$

we obtain

$$(H-\delta)V=-Q \tag{2.8}$$

From the condition of incompressibility, it also follows that w above the Ekman layer is a linear function of z:

$$w=\frac{H-z}{r}\frac{\partial}{\partial r}(rV), \quad z>\delta \tag{2.9}$$

of (2.20)

$$\frac{\tau}{\rho}\approx C_1|\Omega-\Omega_s|(\Omega-\Omega_s)r^2 \qquad (2.22)$$

where $C_1=\kappa^2 C$.

From (2.11), we obtain in this case

$$Q\simeq-\frac{C_1}{2}\frac{|\Omega-\Omega_s|(\Omega-\Omega_s)}{\Omega_s}r^2 \qquad (2.23)$$

Again we take the case of solid rotation, i.e. $\partial\Omega/\partial r=0$. Substituting (2.23) into (2.8) and (2.10), we obtain

$$V\simeq\frac{C_1}{2}\frac{|\Omega-\Omega_s|(\Omega-\Omega_s)}{\Omega_s}\frac{r^2}{H} \qquad (2.24)$$

$$W\simeq\frac{3}{2}C_1\frac{|\Omega-\Omega_s|(\Omega-\Omega_s)}{\Omega_s}r \qquad (2.25)$$

Equation (2.5) becomes

$$\frac{\partial\Omega}{\partial t}\simeq-C_1\frac{\Omega}{\Omega_s}|\Omega-\Omega_s|(\Omega-\Omega_s)\cdot\frac{r}{H}$$

$$\simeq-C_1|\Omega-\Omega_s|(\Omega-\Omega_s)\frac{r}{H} \qquad (2.26)$$

or, integrated from the initial value Ω_0:

$$\frac{1}{|\Omega-\Omega_s|}\simeq\frac{1}{|\Omega_0-\Omega_s|}+C_1\frac{r}{H}t \qquad (2.27)$$

Thus, for the turbulent Ekman layer, $V\sim r^2$ and $W\sim r$. We cannot speak of a "spin-up time" in this case, since the spin-up or spin-down is not described by an exponential function. It will be seen from (2.27) that the time required for a certain adjustment of the angular velocity will be inversely proportional to r; thus, at the axis there is no spin-up or spin-down at all.

3. The Structure of the circular Ekman layer in the vicinity of the axis of the vortex

The results of the preceding section are obtained from a very crude analysis of the Ekman layer. Below a more rigorous approach to the same problem will be made.

Our objective is to determine the vertical velocity W at the top of the Ekman layer as a function of r under semi-steady conditions. Since W is not sensitive to a change of H, we may just as well consider the limiting case $H\to\infty$ (or $E\to 0$). In this case, the spin-up or spin-down will be infinitely slow, and the motion may be considered strictly stationary.

The following scaling will be used:

$$[t]=\Omega_s^{-1},\quad [r]=[z]=\left(\frac{\nu}{\Omega_s}\right)^{\frac{1}{2}}=\delta \qquad (3.1)$$

The other quantities will be scaled accordingly; thus

$$[v]=[w]=\delta\cdot\Omega_s,\quad [\omega]=\Omega_s \qquad (3.2)$$

When nothing else is said, all quantities below are assumed to be scaled in this way.

The steady-state dynamic equations may be written

$$\frac{\partial}{\partial r}(rv)+r\frac{\partial w}{\partial z}=0 \qquad (3.3)$$

$$v\frac{\partial}{\partial r}(\omega r^2)+w\frac{\partial}{\partial z}(\omega r^2)=\frac{\partial^2\omega}{\partial z^2}r^2 \qquad (3.4)$$

$$v\frac{\partial v}{\partial r}+w\frac{\partial v}{\partial z}+(\Omega^2-\omega^2)r=\frac{\partial^2 v}{\partial z^2} \qquad (3.5)$$

The first of these is the condition of incompressibility. The second expresses balance between advection and vertical diffusion of absolute angular momentum (ωr^2). The third is the equation of motion in the radial direction, with the horizontal pressure force expressed as ($-\Omega^2 r$). Ω is the angular velocity required if the centrifugal forces shall balance the horizontal pressure force. Since the density is constant, the hydrostatic equation requires that the horizontal pressure force, and hence Ω, does not change with height:

$$\frac{\partial\Omega}{\partial z}=0 \qquad (3.6)$$

The boundary conditions at the top are

$$\omega\to\Omega,\quad v\to 0,\quad \text{when}\quad z\to\infty \qquad (3.7)$$

At the lower boundary, there is first the kinematic condition

$$w=0\quad\text{when}\quad z=0 \qquad (3.8)$$

The form of the remaining boundary conditions at the lower boundary will depend upon whether the Ekman layer is laminar or turbulent.

In the laminar case,

$$\omega=1,\quad v=0\quad\text{when}\quad z=0 \qquad (3.9)$$

In the turbulent Ekman layer, the boundary conditions are instead:

The value of w at $z=\delta$ is, according to (2.8)

$$w_{z=\delta}=W(r,t)=-\frac{1}{r}\frac{\partial}{\partial r}(rQ) \qquad (2.10)$$

Thus, if Q is known, V, W and $\partial\Omega/\partial t$ may be determined from (2.8), (2.10), and (2.5).

To obtain an estimate of Q, we must make use of the balance of forces within the Ekman layer. In a frame of reference rotating with the lower boundary surface, the radial velocity v gives rise to a Coriolis force $-2\Omega_s\rho v$ per unit volume in azimuthal direction. Integrated over the Ekman layer, this amounts to $-2\Omega_s\rho Q$. Under quasi-stationary conditions, this force per unit horizontal area is approximately balanced by the viscous stress $(-\tau)$ from the underlying surface in azimuthal direction. Hence

$$Q=-\frac{\tau}{2\Omega_s\rho} \qquad (2.11)$$

To proceed further, τ must be related to the motion field. This will be done separately for the laminar Ekman layer and for the turbulent Ekman layer.

In any case, however, it is clear that τ will, ceteris paribus, not depend upon H. As a consequence, neither Q nor W will depend upon H, as will be seen from (2.11) and (2.10).

A. *The laminar Ekman layer.*

Under laboratory conditions, laminar Ekman layers may be produced. In this case, ν must be interpreted as the molecular kinematic viscosity, and a non-slip condition applies at the lower boundary; hence

$$\omega_{z=0}=\Omega_s \qquad (2.12)$$

The surface stress is

$$\frac{\tau}{\rho}=\nu r\left(\frac{\partial\omega}{\partial z}\right)_{z=0} \qquad (2.13)$$

and a reasonable estimate of τ, apart from a quasi-constant factor of order unity, is

$$\frac{\tau}{\rho}\simeq\nu\frac{\Omega-\Omega_s}{\delta}r \qquad (2.14)$$

Then, from (2.11),

$$Q\simeq-\frac{1}{2}\delta\cdot(\Omega-\Omega_s)\cdot r \qquad (2.15)$$

This expression may be substituted in (2.8) and (2.10).

solid rotation above the Ekman layer, i.e. $\partial\Omega/\partial r=0$. From (2.8)

$$V\simeq\frac{1}{2}\frac{\delta}{H}(\Omega-\Omega_s)r \qquad (2.16)$$

from (2.10)

$$W\simeq\delta\cdot(\Omega-\Omega_s) \qquad (2.17)$$

and from (2.5)

$$\frac{\partial\Omega}{\partial t}\simeq-\frac{\delta}{H}\Omega(\Omega-\Omega_s)\approx-\frac{\delta}{H}\Omega_s(\Omega-\Omega_s) \qquad (2.18)$$

and hence

$$\Omega-\Omega_s\simeq(\Omega_0-\Omega_s)e^{-\frac{\delta}{H}\Omega_s t} \qquad (2.19)$$

We note that V in this case is proportional to r, whereas W is independent of r. The spin-up or spin-down process is described by (2.19), and the spin-up time is seen to be

$$\frac{H}{\delta}\Omega_s^{-1}=E^{-\frac{1}{2}}\Omega_s^{-1}.$$

These results are in agreement with the theory of Greenspan and Howard (1963).

B. *The turbulent Ekman layer.*

In vortices in the atmosphere or the ocean, the Ekman layer is turbulent. The coefficient ν must then be replaced by a coefficient of eddy viscosity K, which varies in space. In a crude theory, this variation may be ignored, except near the lower boundary where K tends systematically towards zero as the boundary is approached. This situation is usually treated by introducing a shallow "Prandtl-layer" of variable K underneath the Ekman layer, such that most of the wind shear in the entire boundary layer takes place in the Prandtl-layer. Let ω_p denote the angular velocity at the top of the Prandtl-layer; then the stress near the surface may be expressed approximately as

$$\frac{\tau}{\rho}=C|\omega_p-\Omega_s|(\omega_p-\Omega_s)r^2 \qquad (2.20)$$

where C is a drag coefficient appropriate to the level in question. We now assume that

$$\frac{\omega_p-\Omega_s}{\Omega-\Omega_s}=\kappa \qquad (2.21)$$

is quasi-constant (this would be true if the ratio were only slightly smaller than unity).

$$\frac{\partial \omega}{\partial z}=C(\omega-1)\sqrt{(\omega-1)^2r^2+v^2}$$

$$\text{when} \quad z=0 \qquad (3.10)$$

$$\frac{\partial v}{\partial z}=Cv\sqrt{(\omega-1)^2r^2+v^2}$$

We shall assume the solution to be analytic near the axis, and that vorticity and divergence exist also at $r=0$. This may be achieved by expressing ω, v and w as power series in r:

$$\omega(r,z)=\omega_0(z)+\omega_1(z)r+\omega_2(z)r^2+\cdots$$

$$\frac{1}{r}v(r,z)=v_0(z)+v_1(z)r+v_2(z)r^2+\cdots$$

$$w(r,z)=w_0(z)+w_1(z)r+w_2(z)r^2+\cdots \qquad (3.11)$$

Substituting these expressions into (3.3–5) and collecting terms of the lowest power in r, we obtain (with primes denoting differentiation with respect to z):

$$\left.\begin{aligned}&2v_0+w_0'=0\\&2v_0\omega_0+w_0\omega_0'=\omega_0''\\&v_0^2+w_0v_0'+\Omega_0^2-\omega_0^2=v_0''\end{aligned}\right\} \qquad (3.12)$$

From (3.7):

$$\omega_0\to\Omega_0, \quad v_0\to 0 \quad \text{when} \quad z\to\infty \qquad (3.13)$$

From (3.8):

$$w_0=0, \text{ when} \quad z=0 \qquad (3.14)$$

A. *The laminar Ekman layer.*

In the laminar case, the zero-order equations are supplemented by (3.9), which give

$$\omega_0=1, \quad v_0=0 \quad \text{when} \quad z=0 \qquad (3.15)$$

The equations (3.12–15) form a non-linear system, which may be solved by linearization for small Rossby numbers, i.e.

$$|\Omega_0-1|\ll 1, \quad |\omega_0-1|\ll 1, \quad \left|\frac{v_0}{r}\right|\ll 1.$$

The linearized system is

$$\left.\begin{aligned}&2v_0+w_0'=0\\&2v_0=(\omega_0-\Omega_0)''\\&-2(\omega_0-\Omega_0)=v_0''\\&\omega_0-\Omega_0\to 0, \ v_0\to 0, \ \text{when} \ z\to\infty\\&\omega_0=1, \ v_0=0, \ w_0=0, \ \text{when} \ z=0\end{aligned}\right\} \qquad (3.16)$$

with the solution

$$\left.\begin{aligned}\omega_0&=\Omega_0-(\Omega_0-1)e^{-z}\cos z\\v_0&=-(\Omega_0-1)e^{-z}\sin z\\w_0&=(\Omega_0-1)(1-e^{-z}(\cos z+\sin z))\end{aligned}\right\} \qquad (3.17)$$

This solution is identical with the steady-state solution given by Greenspan (1968) on the basis of the theory of Greenspan and Howard (1963), although the scaling is different.

The vertical motion at the top of the Ekman layer is seen to be

$$W=w_{0(z\to\infty)}=\Omega_0-1 \qquad (3.18)$$

or, in dimensional units

$$W=\delta\cdot\Omega_s\left(\frac{\Omega_0}{\Omega_s}-1\right)=\delta(\Omega_0-\Omega_s) \qquad (3.19)$$

in complete agreement with the result of the heuristic analysis (2.17).

B. *The turbulent Ekman layer.*

In the turbulent case, the zero-order equation (3.12–14) must be supplemented by the zero-order boundary conditions obtained from (3.10); they are

$$\omega_0'=0 \quad v_0'=0, \quad \text{when} \quad z=0 \qquad (3.20)$$

The system (3.12, 13, 14, 20) has the following solution

$$\omega_0=\Omega_0=\text{const}, \quad v_0=0, \quad w_0=0 \qquad (3.21)$$

representing a solid rotation all the way down to the surface. It is noteworthy that (3.21) satisfies the *non-linear* system of equations and is thus not restricted to small Rossby numbers ($\Omega_0-1\ll 1$). The author has not been able to prove that (3.21) is the only solution. However, in the linearized case for small Rossby numbers, it is easy to show that no other solution exists.

On the basis of (3.21), we now proceed to the first order equations, by collecting terms of next-lowest power in r from eqs. (3.3–5), (3.7), (3.8), and (3.10). The first-order equations will automatically be linear, even if the Rossby number is not small. They are

$$\left.\begin{aligned}&3v_1+w_1'=0\\&2\Omega_0v_1=\omega_1''\\&2\Omega_0(\Omega_1-\omega_1)=v_1''\\&\omega_1\to\Omega_1, \quad v_1\to 0 \quad \text{when} \quad z\to\infty\\&\left.\begin{aligned}&w_1=0\\&\omega_1'=C\Omega_0\sqrt{(\Omega_0-1)}\\&v_1'=0\end{aligned}\right\} \ \text{when} \quad z=0\end{aligned}\right\} \qquad (3.22)$$

The solution is readily found to be

$$\left.\begin{aligned} \omega_1 &= \Omega_1 + \frac{C}{2}\frac{|\Omega_0-1|(\Omega_0-1)}{\sqrt{\Omega_0}}e^{-\sqrt{\Omega_0}z} \\ &\quad\times(\sin\sqrt{\Omega_0}z-\cos\sqrt{\Omega_0}z) \\ v_1 &= -\frac{C}{2}\frac{|\Omega_0-1|(\Omega_0-1)}{\sqrt{\Omega_0}}e^{-\sqrt{\Omega_0}z} \\ &\quad\times(\sin\sqrt{\Omega_0}z+\cos\sqrt{\Omega_0}z) \\ w_1 &= \frac{3}{2}C\frac{|\Omega_0-1|(\Omega_0-1)}{\Omega_0} \\ &\quad\times(1-e^{-\sqrt{\Omega_0}z}\cos\sqrt{\Omega_0}z) \end{aligned}\right\} \quad (3.23)$$

Thus the series for the velocity field (3.11) will begin as follows

$$\left.\begin{aligned} u &= \omega r = \Omega_0 r + \omega_1 r^2 + \cdots \\ v &= v_1 r^2 + \cdots \\ w &= w_1 r + \cdots \end{aligned}\right\} \quad (3.24)$$

This represents a solid rotation with a superimposed Ekman spiral. The latter tends to zero as r^2 when $r\to 0$, so that sufficiently close to the axis, only the solid rotation remains. It is noteworthy that this result holds *also for large Rossby numbers* ($\Omega_0 \gg 1$). The thickness of the Ekman boundary layer described by (3.23) is seen to be $\Omega_0^{-1/2}$ or in dimensional units (with K in stead of ν)

$$\delta_0 = \left(\frac{K}{\Omega_0}\right)^{\frac{1}{2}} \quad (3.25)$$

The boundary layer thickness is thus independent of Ω_s.

The limiting value of the vertical velocity as $z\to\infty$ is

$$W = W_1 r = \frac{3}{2}C\frac{|\Omega_0-1|(\Omega_0-1)}{\Omega_0}r \quad (3.26)$$

or, in dimensional units

$$W = \delta\cdot\Omega_s\frac{3}{2}C\frac{\frac{\Omega_0}{\Omega_s}-1\left|\left(\frac{\Omega_0}{\Omega_s}-1\right)\right.}{\left(\frac{\Omega_0}{\Omega_s}\right)}\frac{r}{\delta}$$

$$= \frac{3}{2}C\frac{|\Omega_0-\Omega_s|(\Omega_0-\Omega_s)}{\Omega_0}r \quad (3.27)$$

in qualitative agreement with (2.25).

Thus we have corroborated the result of section 2, that the vertical motion at the top of a *turbulent* Ekman layer in the vicinity of the axis will tend to zero with r. In the turbulent case, the "Ekman layer suction" is therefore inefficient near the axis, and must have a maximum at some radial distance from it.

4. Conclusion

The results presented in the preceding sections may perhaps have a bearing on the structure of tropical cyclones, in particular the existence of the central eye. It is true, of course that the vertical circulation in a typhoon is maintained largely by the large amount of condensation heat released in the ascending currents. On the other hand, it is quite conceivable that the Ekman layer has a controlling influence on the *location* of the ascending currents where condensation heat is released. Since the turbulent Ekman layer has been shown to suppress ascending motions near the axis, it is tempting to draw the conclusion that the eye structure with the main ascending currents taking place outside the eye is a result of an Ekman layer control. A consequence of this would be that the eye is not readily reproducible in laboratory vortices with laminar Ekman layer.

Acknowledgement

The author wishes to thank Dr. Philip D. Thompson for helpful comments.

References

Greenspan, H. P. and L. N. Howard, 1963: On a time-dependent motion of a rotating fluid. J. Fluid Mech. **17**, p. 385.

Greenspan, H. P., 1968: The theory of rotating fluids. Cambridge University Press.

Ooyama, K., 1969: Numerical simulation of the life cycle of tropical cyclones. J. Atm. Sci. **26**, p. 3.

Rosenthal, S. L., 1970: A circularly symmetric primitive equation model of tropical cyclone development containing an explicit water vapor cycle. Monthly Weather Rev. **98**, p. 643.

Sundqvist, H., 1970: Numerical simulation of the development of tropical cyclones with a ten-level model. Part I. Tellus XXII, p. 359.

Taylor, G. I., 1916: Skin friction of the wind on the earth's surface. Proc. Roy. Soc. A, XCII, p. 196.

Yamasaki, M., 1968: Numerical simulation of tropical cyclone development with the use of primitive equations. J. Met. Soc. Japan **39**, p. 187.

END

DATE

FILMED

1-16-76

NTIS